University of Reading

Structural and Physical Properties of Chalcogenide Materials for Thermoelectric Applications

A thesis submitted for the degree of Doctor of Philosophy

School of Chemistry, Food & Pharmacy

Panagiotis Mangelis

September 2017

Declaration

I confirm that this is my own work and the use of all material from other sources has been properly and fully acknowledged.

Panagiotis Mangelis

To my family.

Acknowledgements

I would like to express my sincere acknowledgments to the people and the institutions that supported and helped me during my Ph.D course and contributed to the completion of the work presented in this thesis.

First and foremost, I am grateful to my supervisors, **Prof Anthony V. Powell** and **Dr Paz Vaqueiro**. Without their support, guidance and expertise, I would not have been able to start and complete the work of my thesis.

I would like to thank EPSRC and the University of Reading for the financial support.

Special thanks go to:
The solid state chemistry group of the University of Reading, especially **Gabin**, **Andreas**, **Jesus**, **Sarah**, **John**, **Seb** and **Son** for their help and friendship.

Alex Aziz for his friendship and the band structure calculations which are included in Chapter 4, supporting the investigation on shandite sulphides.

Prof Jean-Claude Jumas for performing Mössbauer Spectroscopy measurements and analysis for six samples of the series $Co_{3-x}Fe_xSn_2S_2$.

Dr Ron Smith and **Dr Ivan Da Silva** for their assistance with powder neutron diffraction experiments on POLARIS and GEM diffractometers.

The Chemical Analysis Facility for the access to X-ray diffraction and thermal analysis measurements and especially **Mr Nick Spencer** for his help and support during X-ray diffraction measurements.

Mr Mark McClemont for his friendship and the countless silica tubes he prepared for the synthesis of my samples.

Mr Gary Yeo, this kind and helpful man, for his important assistance, fixing the instruments and always keeping the hot-press in a good condition.

Last but not least, I cannot forget the help and support of my friends, **Vangelis**, **Antonis**, **Carly**, **Mary** and especially **Christos**, during the period of the writing-up of my thesis, where I had some health issues.

Abstract

Investigations of structural and thermoelectric properties of shandite-type sulphides and diamond-like quaternary chalcogenides have been carried out.

Electron and hole doping is investigated in $Co_3Sn_2S_2$ through the chemical substitution of cobalt by its neighbouring elements. The synthesis of two series, $Co_{3-x}Ni_xSn_2S_2$ ($0 \leq x \leq 3$) and $Co_{3-x}Fe_xSn_2S_2$ ($0 \leq x \leq 0.6$) is described. Powder neutron diffraction experiments have been carried out for both series, while ^{119}Sn and ^{57}Fe Mössbauer spectroscopy measurements have been conducted for $Co_{3-x}Fe_xSn_2S_2$ ($0 \leq x \leq 0.6$). The materials become more metallic with increasing nickel content, while the substitution of Co by Fe induces a metal-to-*n*-type-semiconductor transition, and an increase in the thermoelectric figure-of-merit (ZT) is achieved to a maximum of 0.2 at 525 K. Further improvement in ZT is achieved by the simultaneous substitution at the transition metal and main-group metal sites. In the series $Co_{2.667}Fe_{0.333}Sn_{2-y}In_yS_2$ ($0 \leq y \leq 0.7$), the materials become more semiconducting with increasing In content and a marked increase in the Seebeck coefficient is observed. $Co_{2.667}Fe_{0.333}Sn_{1.4}In_{0.6}S_2$ exhibits ZT = 0.28 at 473 K.

The quaternary chalcogenides A_2ZnCQ_4 (*A* = Cu, Ag; *C* = Sn, Ge; *Q* = S, Se) were synthesized and investigated using powder neutron diffraction. Rietveld analysis reveals that all phases crystallize in the kesterite structure at room temperature and the Cu-containing compounds exhibit partial Cu/Zn disorder in the z = 0.25 and 0.75 planes. For Cu_2ZnGeS_4, an irreversible phase transition is observed at 1123 K from the kesterite to the wurtzite-stannite structure. For $Cu_2ZnGeSe_4$, the cations in z = 0.25 and 0.75 planes become fully disordered at 473 K, while simultaneously, Cu vacancies are created. Hole doping in $Cu_{2+x}ZnGe_{1-x}Se_4$ ($0 \leq x \leq 0.15$) results in a marked decrease in electrical resistivity, increasing the ZT to 0.18 at 573 K.

Table of Contents

Chapter 1 - Introduction

The increased requirements for energy consumption (an increase by 44 % between 2006 and 2030)[1], as well as the demand for the reduction of environmental impacts and greenhouse gas emissions, have led to an explosion of research on sustainable energy technologies and new materials for energy harvesting. Climate change and the decrease of fossil fuel reserves make this need ever more urgent. From the point of view of materials, extensive efforts are made for the manufacture of more efficient and environmentally friendly systems for power generation and energy storage, such as batteries,[2] fuel cells,[3] supercapacitors,[4] solar cells[5] and thermoelectrics.[6] Thermoelectric devices are able to provide considerable energy savings applied in technologies where the waste heat can be exploited and used to create the required temperature gradient. The great benefit is that heat is converted directly to electrical power and consequently, it is a sustainable energy technology. Globally, almost the 66 % of energy consumption is emitted to the environment as waste heat. Theoretically, thermoelectrics can have a wide range of applications for energy harvesting in either large- or small-scale technologies. Any combustion engine in industry, power plants, automobiles, domestic heating systems or even electric devices and computers which emit waste heat can play the role of the heat source. Practically, the low efficiencies and the relatively high production cost of the current thermoelectric materials limit their applications to very specific fields where other parameters such as the nature of the application and reliability are more important.[7] For instance, thermoelectric devices have been used as power generators in deep space probes, as cooling systems on laboratory equipment, on temperature- and climate-control applications, as well as on portable coolers. Recent developments of thermoelectric materials enhance the expectations that in the future more efficient and less expensive devices will be commercialized and thermoelectric technology will play a crucial role in the sustainable energy sector.[8]

1.1 Thermoelectricity

1.1.1 Thermoelectric devices

A thermoelectric device is comprised of a number of modules; each of which consists of multiple thermoelectric couples. A couple is made of two semiconducting materials, an *n*- and a *p*-type. A typical thermoelectric couple is illustrated in Figure 1.1. The application of a temperature gradient across a thermoelectric couple causes the diffusion of charge carriers: electrons and holes. As a result, an electric field is created, providing an electrical potential. Connecting the couple with an external circuit, an electrical current can be produced. The heat source determines the temperature range in which the couple is going to work. The operation of a thermoelectric couple is based on the Seebeck effect which is described below. Conversely, if a voltage is applied between the ends of thermoelectric couple, then a temperature difference will be created providing cooling at the one junction. This operation is based on the Peltier effect.

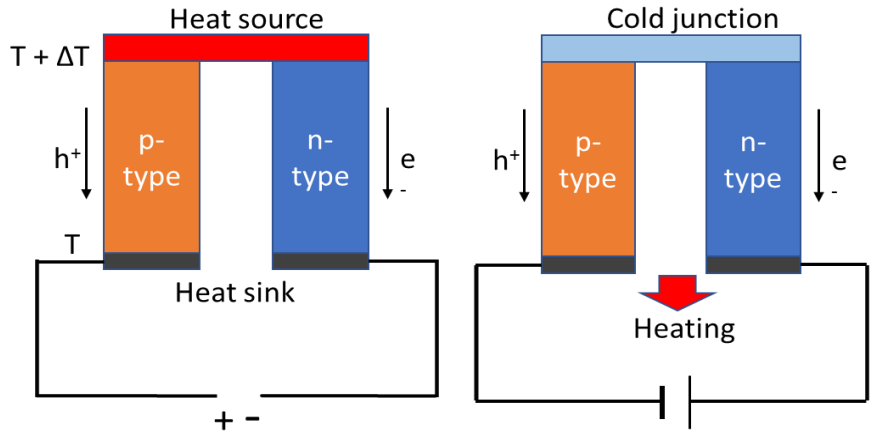

Figure 1.1 Typical thermoelectric couple in power generation mode (left) and cooling mode (right)

1.1.2 Thermoelectric Principles

1.1.2.1 Seebeck effect

In Figure 1.2 two dissimilar conductors, a and b, are connected electrically in series but thermally in parallel. When the two junctions, A and B, have different temperatures, then a voltage is developed between the ends, C and D.

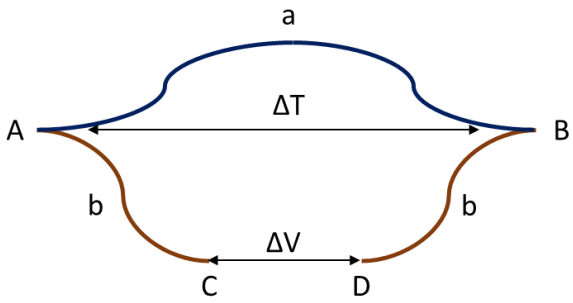

Figure 1.2 Illustration of a thermocouple

The flow of charge carriers due to the temperature difference ΔT is called the Seebeck effect. The voltage ΔV is proportional to the temperature difference and can be expressed by the Equation 1.1

$$\Delta V = S_{ab} \Delta T \qquad (1.1)$$

S_{ab} is the Seebeck coefficient for the materials a and b and is measured in μV K^{-1}.

1.1.2.2 Peltier effect

Conversely, if a voltage is applied across the ends C and D, then an electrical current will flow through the circuit. As a result, one of two junctions is heated with a heating rate q (dQ / dt) while the other junction is cooled with a rate –q. The direction of the current determines which of the two junctions is heated. This is called the Peltier effect. The heating rate q is proportional to the current I which flows through the dissimilar conductors

$$\pi_{ab} = I / q \qquad (1.2)$$

where π_{ab} is the Peltier coefficient.

1.1.3 Thermoelectric Efficiency and Figure of Merit, ZT

Essentially, a thermoelectric device is a heat engine and as a result its operation is based on the thermodynamic laws. Therefore, assuming that the device is an ideal engine without heat losses, the efficiency can be expressed as the electrical power produced over the amount of heat absorbed at the hot junction (Equation 1.3).

$$\Phi = \frac{\text{elecrical power generated}}{\text{heat power absorbed at hot junction}} \quad (1.3)$$

Ignoring contact resistance, the maximum efficiency of a thermoelectric couple is equal to the product of the Carnot efficiency η_c and the factor γ which is related to the properties of the materials from which the thermocouple is fabricated

$$\Phi = \eta_c \gamma \quad (1.4)$$

where

$$\eta_c = (T_H - T_C) / T_H \quad (1.5)$$

$$\gamma = [(1 + Z_c\bar{T})^{1/2} -1] / [(1 + Z_c\bar{T})^{1/2} + T_C/T_H] \quad (1.6)$$

$$\bar{T} = (T_H + T_C)/2.$$

Z_c is the figure of merit of the thermocouple and can be expressed as

$$Z_c = (S_a - S_b)^2 / [(\kappa_a/\sigma_a)^{1/2} + (\kappa_b/\sigma_b)^{1/2}]^2 \quad (1.7)$$

where κ_a, κ_b and σ_a, σ_b are the thermal and electrical conductivities of the materials a and b respectively.[9] The figure-of-merit for a material is given in units of K^{-1} by the Equation 1.8

$$Z = S^2 \sigma / \kappa \quad (1.8)$$

where the numerator $S^2\sigma$ is called the power factor. From the above equations, we can conclude that the efficiency of a thermocouple depends on the temperature difference as well as the figure-of-merit. A more useful measure for the performance of thermoelectric materials is the dimensionless figure-of-merit which embodies the temperature dependence (Equation 1.9).

$$Z T = S^2 \sigma T / \kappa \quad (1.9)$$

Current thermoelectric devices with a ZT of 0.8 can exhibit an efficiency around 6 %.[10] Although, new nanostructured materials such as superlattices, nanowires and quantum

dots have been reported the last years with high thermoelectric performances,[6,11] their synthesis process (atomic layer deposition processes) is very expensive and slow which makes them unsuitable for large-scale commercialization.[11]

1.2 Physical property requirements for thermoelectric materials

Equation 1.9 shows clearly that the efficiency of a thermoelectric material depends on three physical properties: the electronic conductivity, the thermal conductivity and the Seebeck coefficient. High thermoelectric performance requires the unusual combination of high electronic conductivity associated with metallic phases, together with a high Seebeck coefficient and a low thermal conductivity, characteristics of non-metallic materials in order to maximize the figure-of-merit. The problem is that these three properties are interdependent which prevents their simultaneous optimization. The improvement of one parameter is accompanied with the deterioration of at least one of the other two. For instance, when an increase is achieved in electrical conductivity, the Seebeck coefficient is reduced, while it is also possible to cause an increase in the thermal conductivity. This happens because the aforementioned electrical and thermal properties depend in a different way on other fundamental parameters such as charge carrier concentration, n, and charge carrier mobility, μ. Equation 1.10 shows the relation of electrical conductivity with these parameters

$$\sigma = n\, e\, \mu \tag{1.10}$$

where e is the electronic charge. Therefore, an increase in the charge carrier concentration improves the electrical conductivity of the material (assuming that charge carrier mobility is not reduced greatly). However, an increase in charge carrier concentration decreases the Seebeck coefficient. For metals or degenerate semiconductors, the dependence of the Seebeck coefficient on the charge carrier concentration is given by Equation 1.11.[12]

$$S = \frac{8\pi^2 k_B^2}{3eh^2} m^* T \left(\frac{\pi}{3n}\right)^{2/3} \tag{1.11}$$

where k_B is the Boltzmann constant, e the electronic charge, h the Planck constant, m* the charge carrier effective mass and T the temperature. Assuming in the material a

mixed conduction mechanism, both electron and hole conductivities, σ_e and σ_h, contribute to the overall Seebeck coefficient (Equation 1.12)[13]

$$S = \frac{\sigma_h S_h - |\sigma_e S_e|}{\sigma_h + \sigma_e} \qquad (1.12)$$

where S_e and S_h are the partial Seebeck coefficients of electrons and holes respectively. The dominant charge carrier determines the sign of overall Seebeck coefficient value. The thermal conductivity of a solid defines how easily the material permits the transport of heat flow across it when there is a temperature gradient between the ends of the solid. The heat quantity transferred per unit time per unit area, q, is determined by the temperature gradient dT/dx and is given by the formula

$$q = - \kappa \, dT/dx \qquad (1.13)$$

The constant of proportionality κ is the thermal conductivity of the material and is measured in W m^{-1} K^{-1}.

There are two contributions to the thermal conductivity: conduction electrons and lattice vibrations (phonons). Therefore, the total thermal conductivity κ is the sum of electron and phonon contributions, κ_e and κ_L,

$$\kappa = \kappa_e + \kappa_L \qquad (1.14)$$

The thermal conductivity is closely related to the number of free electrons. The heat transfer can be explained by the model of the free-electron gas. At the hot side, the kinetic energy of free electrons is higher than that one at the cold side. This causes the transfer of electrons through collisions to the cold side. The higher the concentration of free electrons, the more collisions that will occur, resulting in a larger thermal conductivity. In metals, where the concentration of conduction electrons is large, both the electronic and thermal conductivity are high. The latter is determined mainly by the electron contribution: $\kappa \approx \kappa_e$.[14] The Wiedemann – Franz Law (Equation 1.15) shows the ratio between the two conductivities.

$$\kappa_e = L_0 \, \sigma \, T \qquad (1.15)$$

where L_0 is the Lorentz number and T the temperature. The Lorentz number is a proportionality constant which is dependent on the charge carrier concentration and varies between materials. For metals, $L_0 = 2.44\times10^{-8}$ W Ω K^{-2}.

Another factor which plays an important role in the total thermal conductivity is the number of phonons. Phonons are the quantum particles which are generated by the waves of lattice vibrations corresponding to the energies of these waves. In semiconductors and insulators, where the number of charge carriers is limited, it is possible the phonon contribution to dominate in the total thermal conductivity. The reduction of lattice contribution through phonon scattering is one of the key strategies in order to improve the thermoelectric performance, as it is explained later in Section 1.5.2. Figure 1.3 illustrates the dependence of the key thermoelectric parameters as a function of charge carrier concentration.

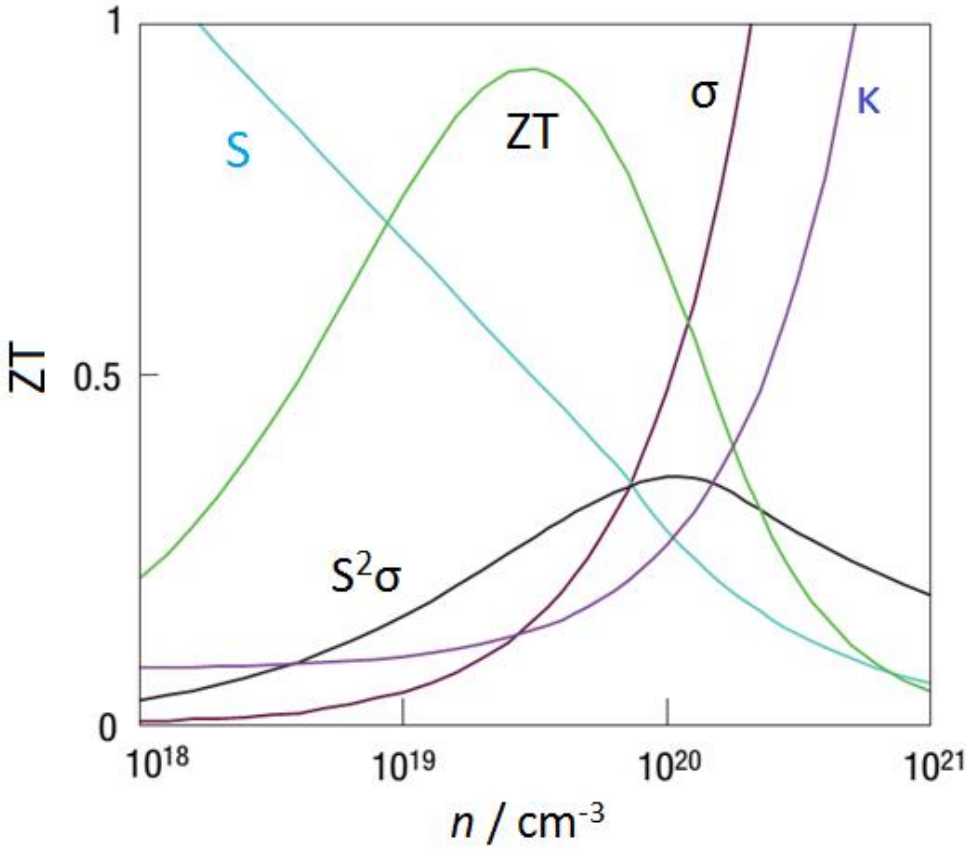

Figure 1.3 Dependence of the key thermoelectric properties electrical conductivity σ, Seebeck coefficient, S, thermal conductivity, κ, power factor, $S^2\sigma$, and the figure of merit, ZT, as a function of charge carrier concentration n.[12]

The interdependence of these parameters limits the optimization of thermoelectric performance in the semiconducting region. Consequently, metals are not appropriate materials for thermoelectric applications due to low Seebeck coefficient values and high electron thermal conductivities. On the other hand, although insulators exhibit a large Seebeck coefficient, they are not able to conduct electricity. The ideal charge carrier concentration for which the figure of merit is maximized, ranges between $10^{19} – 10^{20}$ cm^{-3}.

1.3 Crystal Structure

The understanding of the crystal structure is the key for the investigation of a material as the structural arrangement and the electronic configuration of atoms affect largely the physical properties of the solid. A crystal structure is described by its unit cell which is repeated along the three dimensions. The atomic bonds are determined by the atom positions and the type of the unit cell. There are five types of bonds: the strong ionic, covalent and metallic bonds, and the weak hydrogen bond and van der Waals' forces.

1.3.1 Low-dimensional structures

Low-dimensional materials have attracted special interest because of their unique physical properties and their potential use in a wide range of technological applications such as energy storage and conversion devices, lasers and photodectors.[15] Anisotropic chemical bonding can reduce the dimensionality of a structure. For instance, a two-dimensional structure is characterized by strong interatomic bonds in the two crystallographic directions and a much weaker interaction in the third one. Low-dimensional materials can possess morphologies such as flakes (2-dimensional) or ribbons and nanotubes (1-dimensional).

A wide range of two-dimensional layered structures exist in the literature including graphite, transition-metal phosphates and transition-metal dichalcogenides. They consist of one or more layers of strongly bonded elements which are separated by van der Waals' gaps. These structures are of particular interest because they are able to intercalate guest species into these gaps. The intercalation of guest species in transition-metal dichalcogenides, MX_2 (M: transition metal; X: S, Se, Te), has produced marked improvements in their thermoelectric performance. The MX_2 slabs are formed by either edge-sharing octahedra or edge-sharing trigonal prisms, building a XMX stacking sequence.[16] TiS_2 is a typical example of a layered disulphide with the space group

$P\bar{3}m1$. The structure consists of layers of edge-sharing TiS_6 octahedra (Figure 1.4) stacked along the *c* axis and separated by a van der Waals' gap. The van der Waals gap contains vacant octahedral and tetrahedral sites which can host a wide range of guest species. The intercalation of small amounts of cobalt in Co_xTiS_2 ($0.04 \leq x \leq 0.08$) has improved the ZT to 0.3 at 573 K which corresponds to an increase of 25% over that of TiS_2.[17]

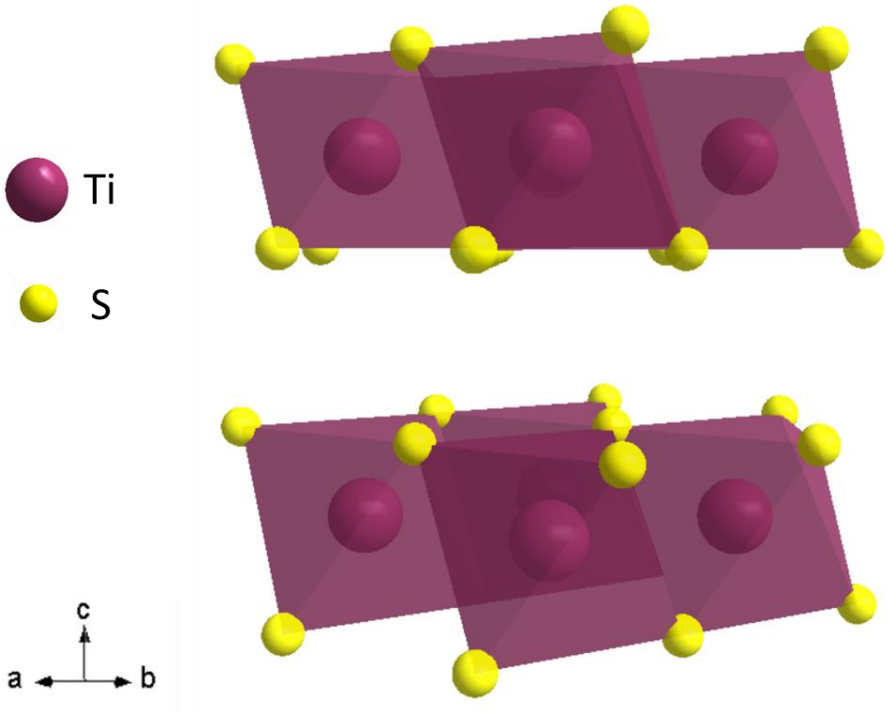

Figure 1.4 Layered structure of TiS_2.

1.3.2 Superstructures

The term of superstructure is used when an additional arrangement is superimposed on a crystal structure, forming a larger unit cell. Metal-atom, magnetic or vacancy ordering are three possible causes for the formation of a superstructure. A characteristic example investigated in this work, is the formation of different superstructures which depend on the possible cation ordering in the quaternary chalcogenides with the general formula A_2ZnCQ_4 (where *A* = Cu, Ag; *C* = Ge, Sn; *Q* = S, Se). Calculations[18] have indicated for this group, the existence of two potential fully ordered superstructures, the stannite and kesterite (Fig. 1.5), which are derived from zinc-blende (ZB) and wurtzite (W) type structures. These superstructures are discussed in detail in Section 1.10.2 and Chapter 5.

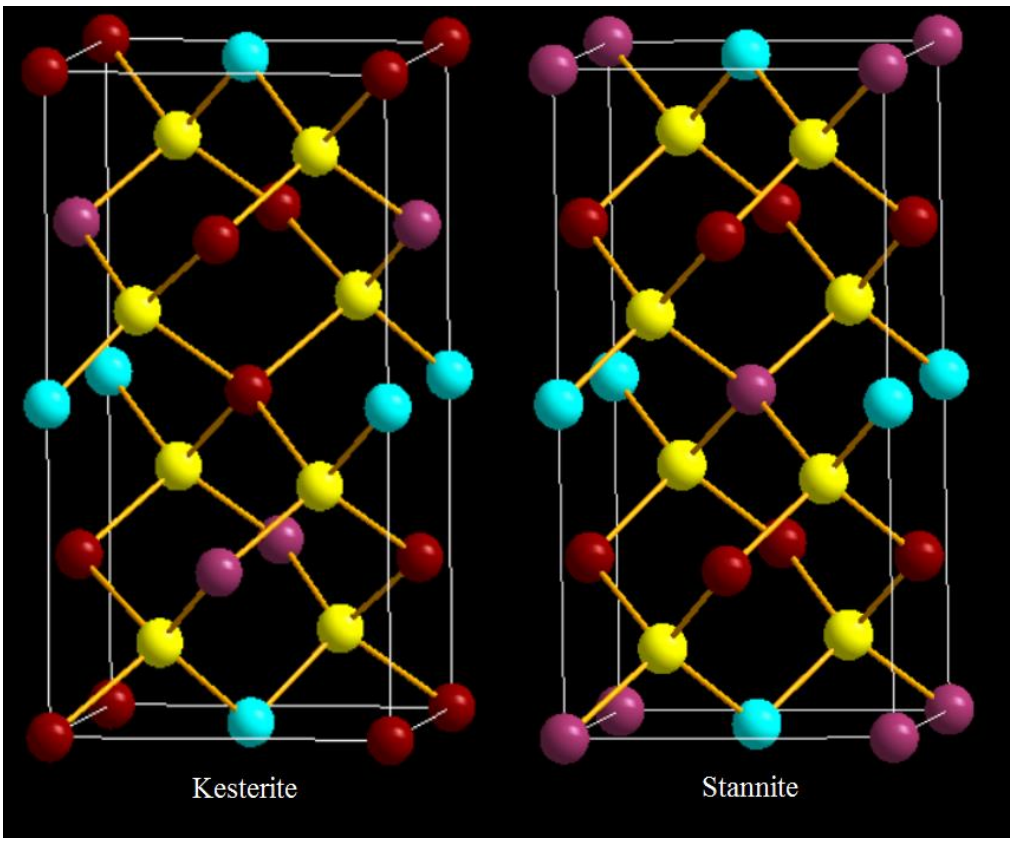

Figure 1.5 The kesterite (*I-4*) and stannite (*I-42m*) superstructures of the zinc-blend phase of A_2ZnCQ_4. Yellow spheres denote *Q* anions. The *A*, Zn and *C* cations are illustrated by red, grey and turquoise spheres respectively.

1.4 Electronic structure

The ability to understand the electronic structure of a material is crucial for its investigation and the strategy which must be applied in order to improve its thermoelectric performance. The physical properties of a solid are related directly with its electronic structure. In solid state chemistry, band theory and density-of-states constitute the theoretical background to describe the electronic structure and account for the electrical behavior of materials.

1.4.1 Band theory and density of states

As the number of atomic orbitals increases in molecules, this results in a larger combination of energy states and a larger number of molecular orbitals (Figure 1.6 (c)). The increase of molecular orbitals lowers the gap between successive energy levels. In a

solid, an infinite chain of atoms creates an infinite number of molecular orbitals and consequently, the energy gap is so small, that the energy states can be assumed as a continuous band with a finite width (Figure 1.6 (d)).

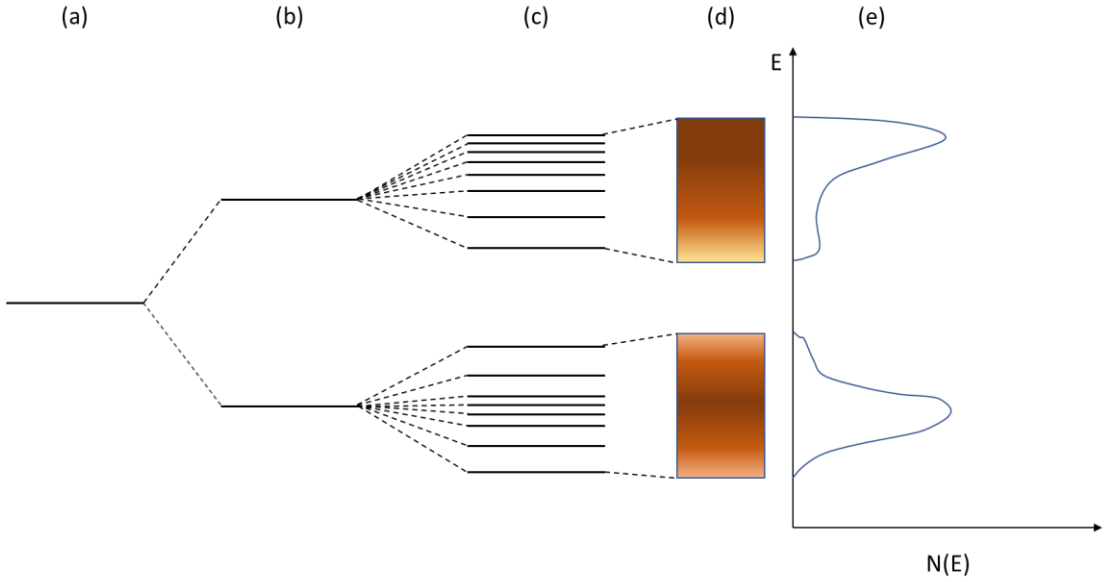

Figure 1.6 Energy states of (a) an atom, (b) a small molecule, (c) a large molecule and (d) a solid. Darker regions correspond to higher concentrations of energy states. (e) the density of states corresponding to (d).

The density of states is defined as the number of energy levels which exist over the energy range $E + \Delta E$.[19] The regions between the filled energy bands which are empty of molecular orbitals, correspond to energy gaps. The energy which separates the completely filled valence band and the empty or partially occupied conduction band is termed the band gap, E_g. The band gap together with the Fermi energy determine the conduction mechanism of a material. The Fermi energy, E_F, is defined as the energy state of the highest occupied orbital of a material at the temperature of absolute zero, 0 K. At higher temperatures, energy states above the Fermi level can be occupied, while others below E_F are unoccupied. In semiconductors and insulators, the Fermi energy is located in the band gap between the valence and the conduction band. The magnitude of E_g determines the electrical behavior of the solid (Figure 1.7). A large band gap corresponds to an insulating material, while the material is characterized as a

semiconductor if E_g is small and thermally excited electrons can jump from the valence to conduction band. In a metal, there is no band gap and free electrons can move in the electronic structure, providing high values of electrical conductivity.

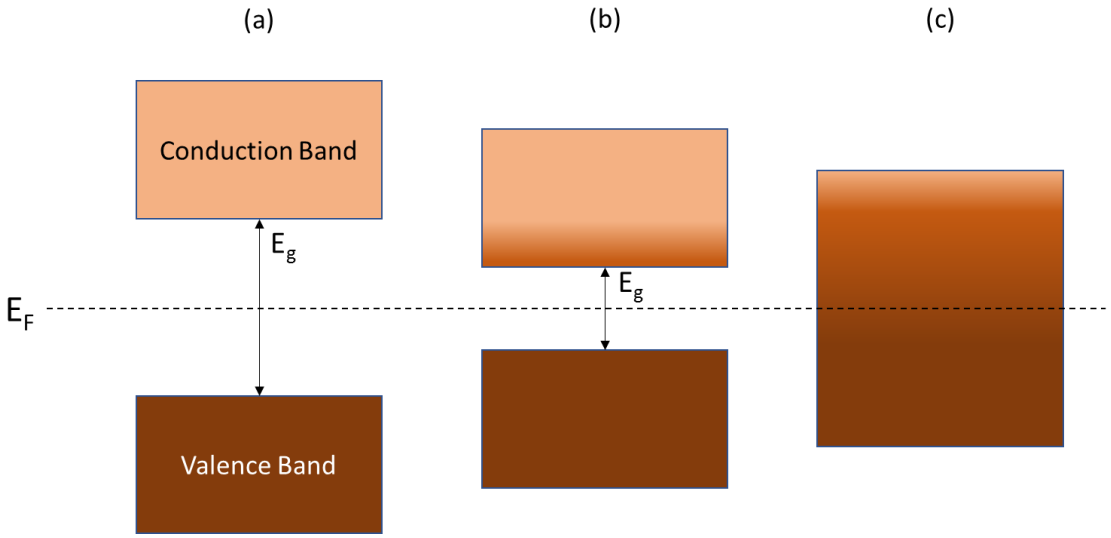

Figure 1.7 Illustration of the conduction and valence bands in (a) insulators, (b) semiconductors and (c) metals. The band gap, E_g, and Fermi energy, E_F, are shown.

1.4.2 Conduction mechanisms

In order to specify the electronic properties of a material, it is important to understand the conduction mechanisms. Electronic conductors such as metals and semiconductors can possess two types of charge carriers: electrons and holes. There is another category of conductors (ionic conductors) where ions can play the role of charge carriers. Ionic conductors often have 'open' structures with neighboring vacancies or van der Waals gaps in order to provide sufficient ion mobilities.[20] These materials attract high interest for applications such as batteries.

In the field of thermoelectrics, candidate materials with good thermoelectric properties are localized in the semiconducting region (Section 1.2, Figure 1.3). Semiconductors can be described as intrinsic or extrinsic. In intrinsic semiconductors, the number of thermally (or optically) excited electrons in the conduction band is equal to the number of holes in the valence band and the Fermi level is localized in the band gap between the

conduction and valence band (Figure 1.8 (a)). In extrinsic semiconductors, the number of charge carriers depends on the levels of doping. Through electron doping the Fermi level is shifted near to the conduction band and donor levels are created below the conduction band, providing excited electrons. The majority of charge carriers are electrons and the semiconductor is characterized as *n*-type (Figure 1.8 (b)).

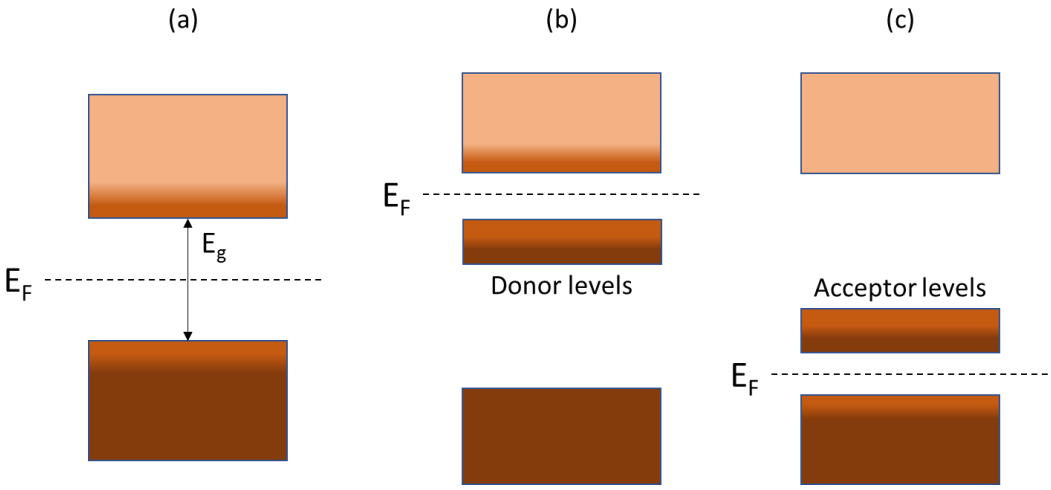

Figure 1.8 Schematic of the valence and conduction bands of (a) an intrinsic semiconductor, (b) a *n*-type semiconductor and (c) a *p*-type semiconductror.

In hole doped semiconductors, the Fermi level is localized near to the valence band. Electrons are promoted to acceptor levels, leaving behind a high concentration of holes in the valence band. In this case, the semiconductor is characterized as *p*-type (Figure 1.8 (c)).

1.5 Strategies to improve the efficiency of thermoelectric materials

There are several strategies to improve the efficiency of thermoelectric materials such as doping, intercalation and nano-compositing. The choice (or the combination) of strategies which will target to maximize the overall performance, the thermoelectric figure of merit, depends on the structural characteristics of the material. Chemical substitution is one of the main strategies to optimize the thermoelectric properties which are described in Section 1.2. The optimization of charge carrier concentration is the key

for the increase of figure of merit and depends on the type of doping (electron or hole) which must be applied.

1.5.1 Improvement of the Seebeck coefficient – Mott relation

Materials with highly structured density of states close to the Fermi level present particular interest for investigations of their thermoelectric performance. Appropriate doping of these materials can potentially lead to a marked increase in Seebeck coefficient. The absolute value of the Seebeck coefficient can be determined at a specific temperature T through the Mott relation[21] (Equation 1.16).

$$S = \left(\frac{\pi^2 k^2 T}{3e}\right)\left(\frac{d\ln[\sigma(E)]}{dE}\right)_{E=E_F} \qquad (1.16)$$

where k is the Boltzmann constant, E_F the Fermi level and e the electronic charge. The Seebeck coefficient depends on the derivative $d\ln[\sigma(E)]/dE$ at the Fermi level, where $\sigma(E)$ is the electrical conductivity which is proportional to the density of states. Therefore, the Seebeck coefficient is dependent strongly on the slope of the density of states at the Fermi level (Figure 1.9). The tuning of the Fermi level on a pronounced sharp peak in the density of states can have a large impact in the magnitude of the Seebeck coefficient.

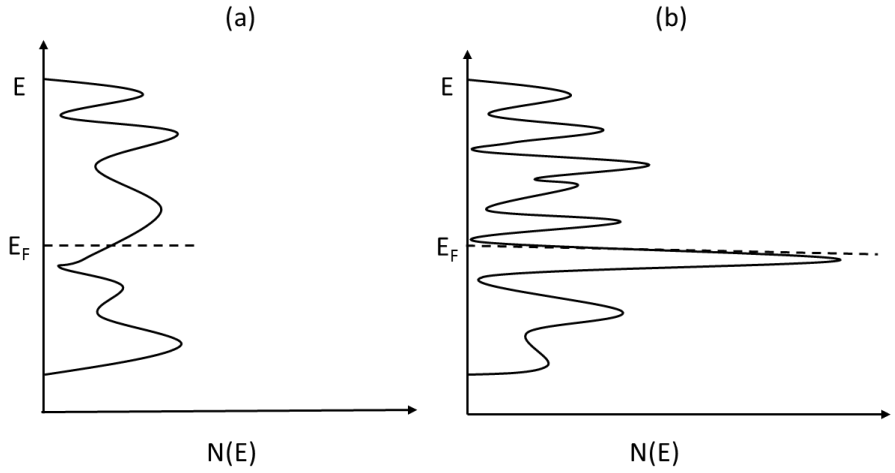

Figure 1.9 Density of states of two hypothetical materials with a small (a) and large (b) $d[\ln\sigma(E)]/dE$ at the Fermi level.

1.5.2 Reduction of lattice thermal conductivity - Phonon scattering

As was mentioned in Section 1.2, the thermal conductivity has electronic and phonon contributions. The electronic contribution is related directly to the electronic conductivity and as a result it cannot be reduced without affecting the ability of the material to conduct electricity. For this reason, efforts are largely focused on the reduction of lattice thermal conductivity through the phonon scattering in the crystal structure.

One of the design strategies which is investigated extensively the last years, is the phonon glass-electronic crystal approach. The characteristic of this group of materials is that they conduct electrical current like a crystal and conduct heat like a glass. Materials such as skutterudites[22] and clathrates[23] possess cage-like structures which contain void spaces. These vacancies can host weakly bound atoms or molecules which are able to 'rattle'. The localized vibrational modes associated with the 'rattlers' have the Einstein vibrating behavior and can cause a great reduction in lattice thermal conductivity.[24]

The phonon spectrum has a wide range of wavelengths which correspond to different mean free paths (mfp). This means that there are different types of phonon scattering which contribute in the weakening of lattice vibrations within the material. Combining sources of scattering on all relevant length scales, from atomic-scale lattice disorder and nanoscale precipitates to mesoscale grain boundaries, a great reduction in lattice thermal conductivity can be achieved.[25] The disorder inside the unit cell can be increased by introducing point defects such as vacancies, substituted and interstitial atoms or by alloying. These differences in mass, size and interatomic forces play an important role in the scattering of phonons with short mfp.[26] For example, alloying Bi_2Te_3 with isoelectronic ions reduces thermal conductivity without affecting electrical conductivity, while the rare earth chalcogenide $La_{3-x}Te_4$ exhibits low values of thermal conductivity (below 0.5 $Wm^{-1}K^{-1}$) because its structure contains a high number of vacancies.[12] Nanoscale inclusions in bulk materials can scatter phonons with short and medium mfp, reducing effectively the lattice thermal conductivity. Introducing 2-10 nm SrTe nanocrystals into the bulk Na-doped PbTe, an increase in ZT (~1.7 at 800 K) is achieved.[27] An additional decrease in κ_L can be accomplished by scattering the phonons with long mean free path at the grain boundaries of crystallites. Improvements in thermoelectric performance through grain-boundary phonon scattering have been reported for Na-doped PbTe[25] and alloys of Bi_2Te_3.[28]

Phonon scattering is also created at the interfaces of layered structures. For instance, layered cobalt oxides are quite interesting complex structures where distinct regions provide different functions. The region with the electron – crystal structure determines the electron conductivity, while the thermal conductivity is determined by the phonon – glass region which is composed of a heavily disordered structure. Therefore, phonon and electron transport are independently controlled.[12] Na_xCoO_2 is a complex material where CoO_2 nanosheets possess a strongly correlated electron system serving as electronic transport layers, while Na^+ nanoblock layers create phonon scattering effects because Na^+ ions are randomly located in interlayer sites and are highly disordered.[29]

1.5.3 Nanostructured thermoelectric materials

Recent studies have highlighted that low-dimensional structures of thermoelectric materials can improve the figure-of-merit significantly. As the dimensionality is reduced and the size of the system reaches the scale of nanometers, new physical phenomena arise, providing the opportunity for the three key properties, Seebeck coefficient, electrical and thermal conductivity, to vary more independently.[30]

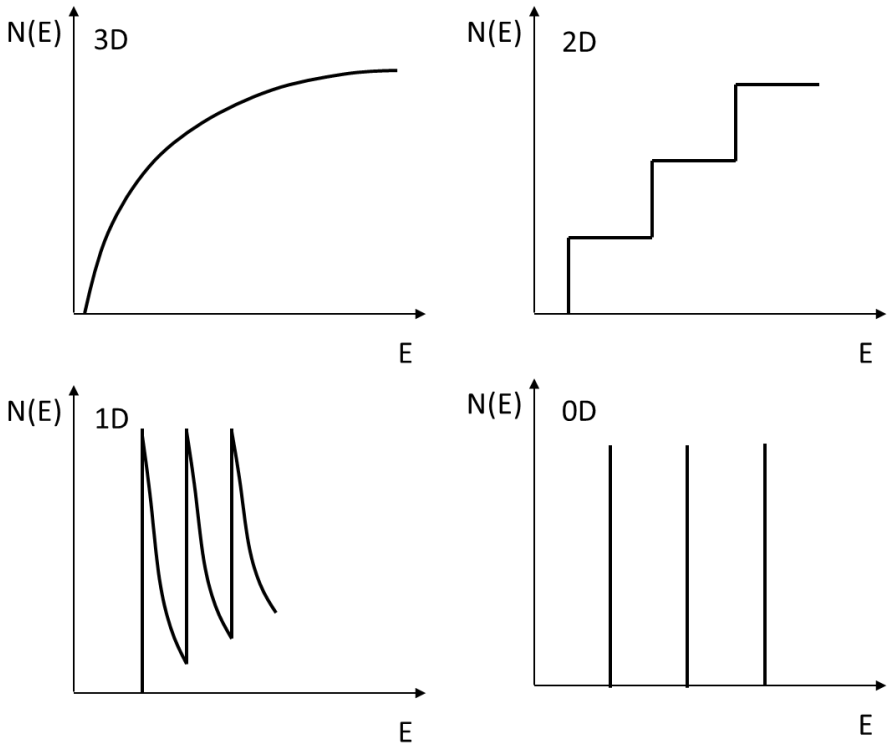

Figure 1.10 The density of states for bulk 3D crystalline semiconductors, 2D quantum wells, 1D quantum wires, 0D quantum dots.[30]

The reduction of dimensionality causes quantum-confinement effects which may create a more structured density of states, N(E), with sharp variations (Figure 1.10). This provides the opportunity for a large dlnσ(E)/dE close to the Fermi level and consequently an increase of Seebeck coefficient, without necessarily affecting the electrical conductivity.

Another benefit of nanostructuring is the numerous interfaces which enhance phonon scattering. In a polycrystalline material, the number of grain boundaries increases as the size of the particles get smaller to nanoscale. Phonons are scattered effectively only when their mean free path (mfp) is larger than the spacing of interfaces. Scattering effects act upon electrons as well. Consequently, an improved thermoelectric performance requires phonons to be scattered more effectively than electrons. Therefore, a nanostructure needs to have interfaces whose spacing is larger than the mfp of electrons but also shorter than that of phonons. As a result, the electronic conductivity will not be impaired as much as the lattice thermal conductivity is reduced. For example, a dramatic reduction in thermal conductivity due to phonon scattering effects has been reported in one-dimensional silicon nanowires, achieving a high increase in thermoelectric performance with ZT = 0.6 at room temperature[31] and ZT ≈ 1 at 200 K.[32]

1.6 State-of-the-art thermoelectric materials

State-of-the-art thermoelectric materials can be classified into three groups depending on the temperature range in which they are employed. Their performance depends directly on the operating temperature (Figure 1.11). For this reason, thermoelectric applications at different temperatures require different groups of materials. The most widely used thermoelectric materials for commercial applications which operate at temperatures up to 450 K are alloys of Bi_2Te_3 and Sb_2Te_3.[12] These materials are used for the construction of thermoelectric refrigerators. PbTe alloys[12] and TAGS[33] are suitable for temperatures up to 900 K. *n*-type compositions of PbTe exhibit a ZT around 0.8 at 673 K while the *p*-type alloy $(GeTe)_{0.85}(AgSbTe_2)_{0.15}$, known as TAGS, can possess a maximum ZT above 1.2. The latter has been employed in long-life thermoelectric generators. Thermoelectric materials for high-temperature applications are *n*- and *p*-type SiGe alloys which were firstly fabricated by NASA and can operate at temperature ranges up to 1300 K, exhibiting superior mechanical strength.[34]

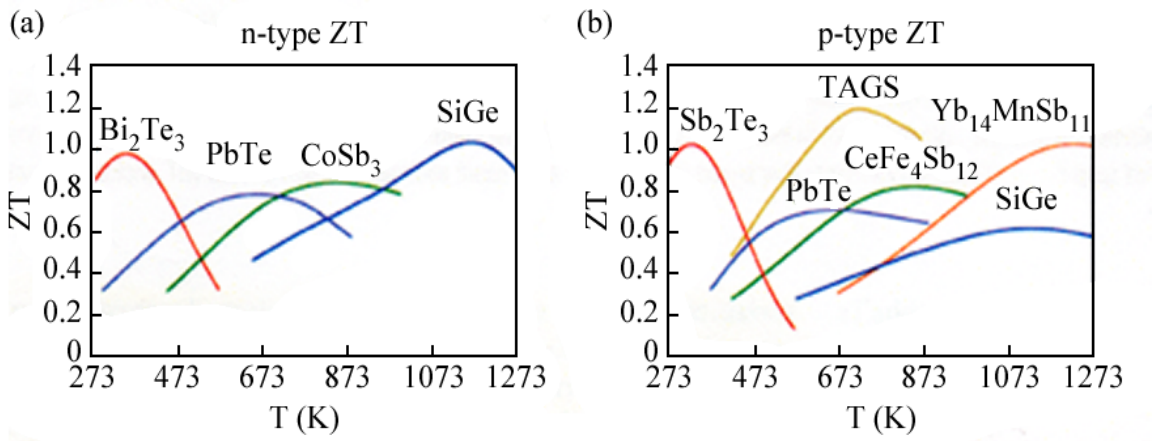

Figure 1.11 Figure of merit, ZT, of state-of-the-art *n*-type (a) and *p*-type (b) thermoelectric materials as a function of temperature. [12]

1.6.1 Bismuth Telluride

Bi_2Te_3 was one of the first thermoelectric materials which were investigated in the 1950's. It was discovered that alloying of Bi_2Te_3 with Sb_2Te_3 and Bi_2Se_3 provided an enhanced power factor as well as a decrease in thermal conductivity. In the 1960's the *p*-type alloy $Bi_xSb_{2-x}Te_3$ with $x \approx 1$ was reported with a ZT = 0.75 at 300K.[35] After decades of research the alloys of Sb_2Te_3 and Bi_2Se_3 have been established as the state-of-art thermoelectric materials for applications close to room temperatures. The structures of Sb_2Te_3 and Bi_2Se_3 are similar to that of Bi_2Te_3. The Bi_2Te_3 structure is described in the space group $R\bar{3}m$ and consists of double layers of $BiTe_6$ octahedra which are stacked perpendicular to the *c* axis, in an ABC sequence (Figure 1.12).[36] The Te-Bi bonds have an ionic-covalent character, while between the double layers there are van der Waals gaps. As a result, Bi_2Te_3 exhibits highly anisotropic properties. [37]

Both *n*-type and *p*-type alloys of Bi_2Te_3 possess a figure of merit, $ZT \approx 1$ with *p*-type alloys reaching the highest values. Typically, thermoelectric devices which operate between 200 and 400 K, are fabricated from *p*-type alloys, $Bi_xSb_{2-x}Te_{3-y}Se_y$ with $x \approx 0.5$, $y \approx 0.12$ and *n*-type, $Bi_2(Se_yTe_{1-y})_3$ with $y \approx 0.05$.[38] The *p*-type alloy $(Bi_2Te_3)_{0.25}(Sb_2Te_3)_{0.72}(Sb_2Se_3)_{0.03}$ exhibits the highest figure of merit (ZT = 1.14) which has ever been reported in any bulk material at 300 K.[39] However, thin film materials offer great opportunities for ZT enhancements. *p*-type Bi_2Te_3/Sb_2Te_3 superlattices demonstrate the best ZT value to date close to 2.4, while *n*-type $Bi_2Te_3/Bi_2Te_{2.83}Se_{0.17}$ superlattices reach a ZT near to 1.4.[38]

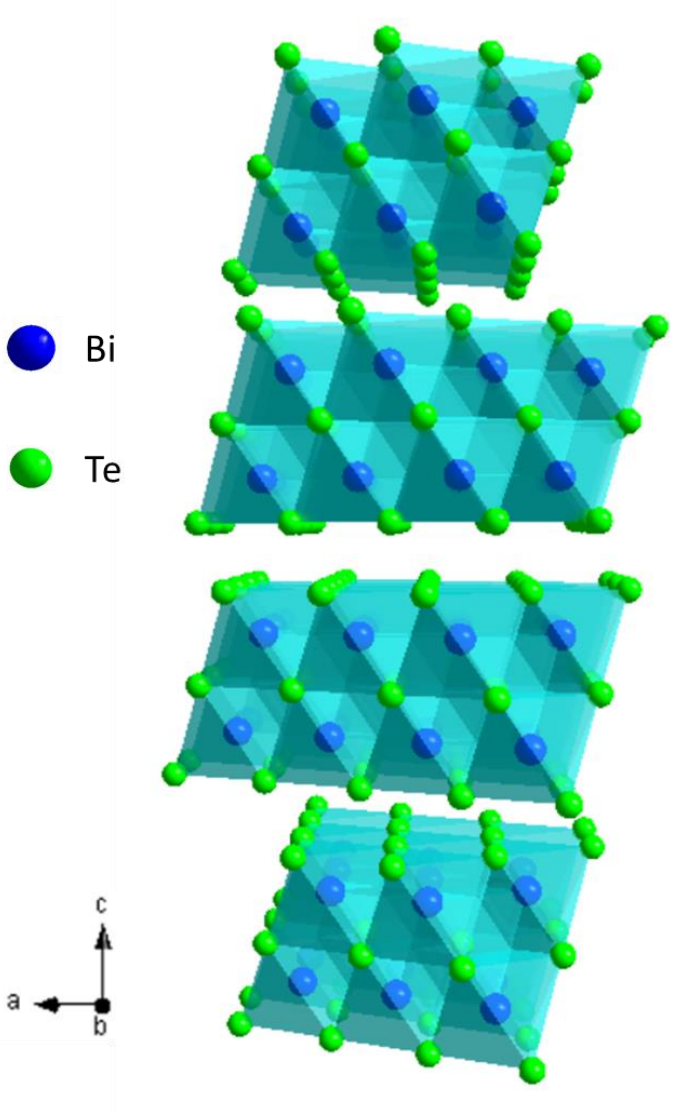

Figure 1.12 Structure of Bi_2Te_3

1.7 Challenges

Practically, there are many obstacles and challenges which should be overcome for thermoelectric materials to become economically viable and provide commercial applications for power generation. High cost and low efficiency are the main factors which prevent their commercialization. Common commercial thermoelectric materials such as Bi_2Te_3 alloys are very expensive for large-scale device fabrication. The reason is that tellurium is a scarce element (earth abundance ≈ 0.001 ppm)[48] and its cost is getting higher. In addition, their efficiency is relatively low, ZT ≈ 1. The above challenges combined with the significant opportunities of electricity harvesting from waste heat have led to an explosion of research on new materials exhibiting the benefits overleaf:

- ✓ earth-abundant
- ✓ free from tellurium,
- ✓ relatively cheap,
- ✓ low production cost,
- ✓ non-toxic,
- ✓ appropriate for commercial applications (sufficient mechanical strength, reliability),
- ✓ high thermoelectric performance.

1.8 Te-free chalcogenide thermoelectric materials

Te-free chalcogenides, sulphides and selenides, have attracted great interest as potential thermoelectric materials. The advantage of these compounds is that sulphur (earth abundance ≈ 420 ppm) and selenium (earth abundance ≈ 0.05 ppm) are more abundant and consequently less expensive elements than the scarce tellurium.[48] Moreover, sulphides are environmentally friendlier than tellurides because they are non-toxic. The discovery of Te-free sulphides and selenides with good thermoelectric properties at temperatures close to ambient is one of the main targets of research in thermoelectrics.

1.8.1 Bi_2S_3

Bi_2S_3 is the sulphide analogue of the commercial Bi_2Te_3 and has been receiving attention over the last two decades as a candidate thermoelectric material. The structure of Bi_2S_3 is different to that of Bi_2Te_3, consisting of one-dimensional $[Bi_4S_6]$ ribbons which extend infinitely along the *b*-axis (Figure 1.13).[40] Bi_2S_3 is a semiconductor with a relatively large band gap of 1.30 eV.[41] The promising features of this material are a relatively high Seebeck coefficient, around -325 $\mu V\ K^{-1}$, at ambient temperature and a thermal conductivity 25 % lower than that of Bi_2Te_3. However, the much lower electrical conductivity of $10^{-4}\ \Omega^{-1}\ cm^{-1}$ results in a poor ZT of 0.05 at room temperature.

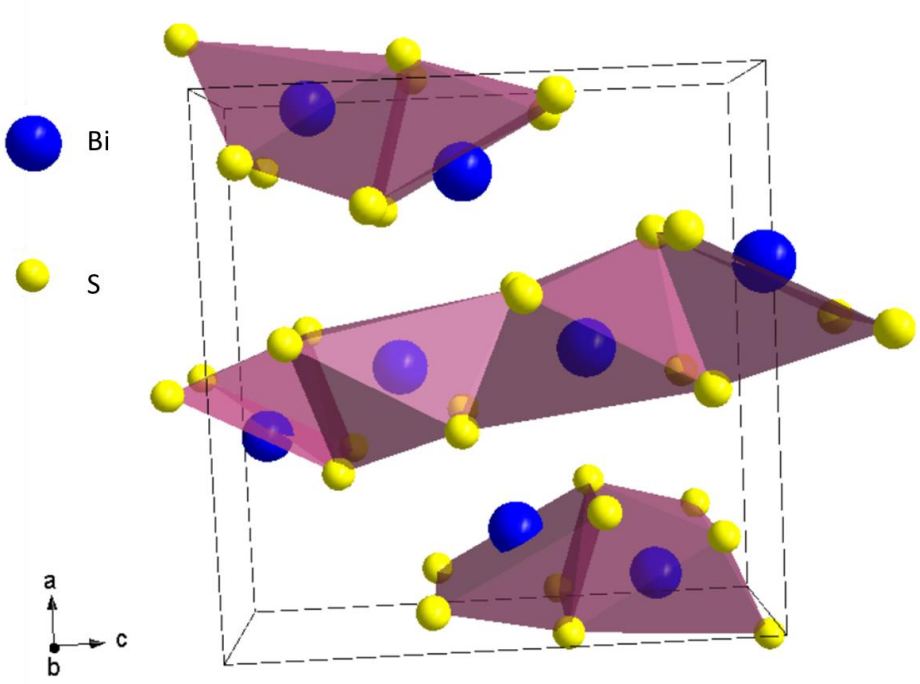

Figure 1.13 One-dimensional structure of Bi_2S_3

Many attempts have been carried out to improve the thermoelectric performance of Bi_2S_3.[42] By increasing the number of sulphur vacancies, the electrical conductivity of $Bi_2S_{2.90}$ was raised by 2 orders of magnitude and the ZT was improved to 0.11 at 523 K.[43] A great improvement was achieved by doping with 0.5 mol % $BiCl_3$, increasing the power factor over a broad temperature range and reaching a maximum ZT of around 0.6 at 760 K, which is the highest reported value for this material.[44]

1.8.2 Lead sulfides and selenides

To date a wide range of PbTe-based both *p*-type (e.g. $AgPb_mSn_nSbTe_{m+n+2}$, $PbTe_{1-x}Se_x$, $NaPb_mSbTe_{m+2}$, PbTe−SrTe and PbTe−PbS) and *n*-type materials (e.g. $AgPb_mSbTe_{m+2}$, $Pb_{1-x}Sn_xTe$−PbS, PbTe−CdTe and PbTe−Ag_2Te) have been fabricated with optimized thermoelectric properties. However, these materials contain the scarce tellurium which is forbidden for large-scale applications. For this reason, the sulphide, PbS, and selenide, PbSe, analogues have been studied as alternative thermoelectric materials.[45] All lead chalcogenides possess the rock salt structure where Pb and *Q* occupy the cation and anion sites respectively (Figure 1.14). A recent study of the PbS−PbTe system demonstrated promising improvements in their thermoelectric properties.[46] This achievement lead to new investigations on Te-free PbS-based compounds. In 2011, it

was discovered that the combination of nanoprecipitates of Bi_2S_3 and Sb_2S_3 second phases with doping of $PbCl_2$ can improve dramatically the ZT for *n*-type PbS (from 0.4 to 1.1 at 923 K).[47] Table 1.1 summarizes recent examples of high performance Pb-based chalcogenides with the best ZT values.

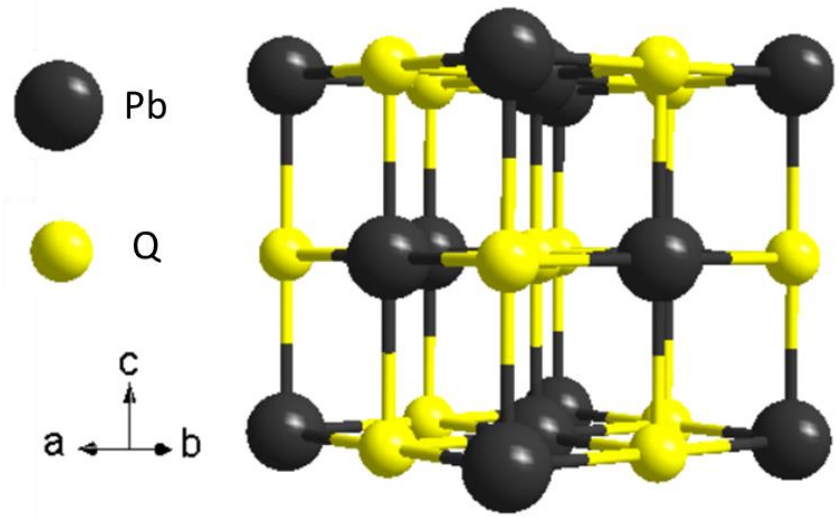

Figure 1.14 Structure of Pb*Q* (*Q* = Te, Se, S)

Table 1.1 - State-of-art Pb-based chalgogenide thermoelectrics. The band gap, E_g, the maximum ZT and the optimum operating temperature are presented. [45]

Pb*Q* *Q* =Te, Se, S	E_g (eV)	*n*-type ZT	*p*-type ZT
PbTe	0.31	$AgPb_{18}SbTe_2$ 1.8 at 800 K[49]	PbTe+12%PbS +2%Na 1.8 at 800 K[50]
PbS	0.41	PbS+1%Bi_2S_3 +1%$PbCl_2$ 1.1 at 923 K[47]	PbS+3%SrS +2.5%Na 1.2 at 923 K[45]
PbSe	0.28	PbSe+12%PbS +0.3%$PbCl_2$ 1.3 at 900 K[51]	$Pb_{0.993}Na_{0.007}Se$ 1.2 at 850 K[52]

1.8.3 Chevrel selenides

The Chevrel phases are described by the formula $M_xMo_6Q_8$ ($1 \leq x \leq 4$, Q = S, Se or Te). From this category of materials, selenides are emerging as the most promising thermoelectrics because they are anticipated to exhibit lower thermal conductivity than the sulphide counterparts and higher temperature stability than the tellurides.[53] The phase of nominal composition $Cu_4Mo_6Se_8$ ($Cu_{3.1}Mo_6Se_8$) is one of the best-performing *p*-type Chevrel phase thermoelectrics at high temperatures, exhibiting a ZT of around 0.6 at 1000 ^oC.[54] The Mo_6Se_8 unit consists of a slightly distorted [Mo_6] octahedral cluster capped on its faces by eight Se atoms arranged in a cube. The packing of Mo_6Se_8 forms vacant cavities throughout the structure providing sites for intercalated ions. The intercalation of 'rattling' Cu atoms decreases the thermal conductivity significantly and enhances the thermoelectric performance of the material. Along the *c* axis, the clusters are separated by the four Cu atoms in adjacent sheets. Interlayer connections are created solely by Cu-Se bonds. Each Cu atom is coordinated by 3 Se atoms (Figure 1.15).[55]

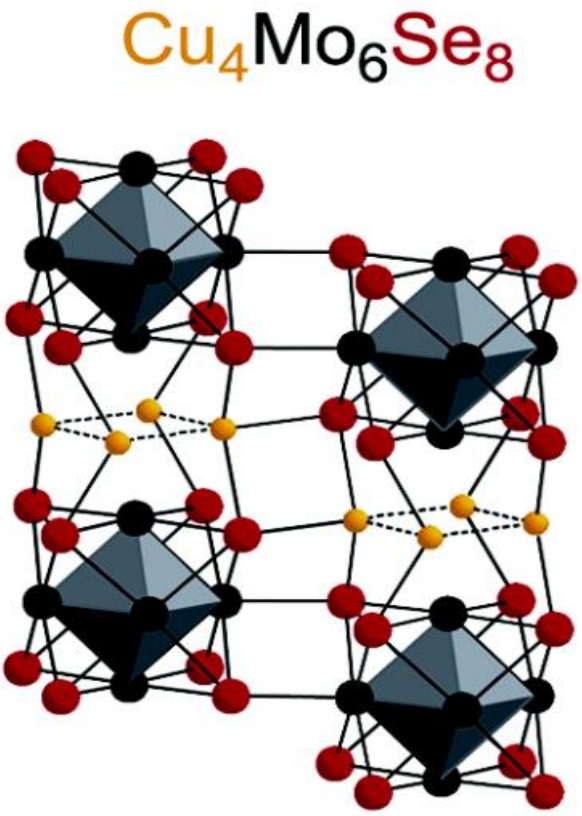

Figure 1.15 Structure of $Cu_4Mo_6Se_8$.[55]

1.8.4 Rare earth sulphides

Rare-earth sulphides have shown promising thermoelectric properties at high temperatures. The benefit of these materials is that their structure contains a relatively large number of vacancies. These compounds possess the cubic Th_3P_4-type structure termed the γ-phase. The cell of cubic Th_3P_4-type structure consists of 28 sites, 12 cations and 16 anions. In each cell, the rare-earth atoms occupy only 32/3 of the 12 available sites which means that 4/3 sites remain vacant.[56] Filling these vacancies with additional rare-earth atoms can either increase electron density or reduce lattice thermal conductivity. The ternary sulphides $SmGd_{1.02}S_3$, $LaGd_{1.02}S_3$ and $NdGd_{1.02}S_3$ exhibit an optimized ZT of 0.3, 0.4 and 0.51 at 950 K respectively,[57,58] while the best thermoelectric performance has been reported for the $LaS_{1.42}$ with a ZT = 0.75 at 1273 K.[59]

1.8.5 Copper-containing chalcogenides

There is a wide range of Te-free, copper-containing chalcogenides which have been investigated for their thermoelectric properties in recent years. Tetrahedrite and bornite minerals are two low-cost families due to their availability as natural minerals. Doped tetrahedrite sulphides with the general formula $Cu_{10}M_2Sb_4S_{13}$ (*M* = Mn, Fe, Co, Ni, Cu, Zn) have been studied recently.[60] These materials exhibit a low lattice thermal conductivity because of their complex cubic structure which contains 58 atoms in the unit cell. The quaternary chalcogenides Cu_2BCQ_4 (*B* = Cd, Zn; *C* = Sn, Ge; *Q* = S, Se) also exhibit promising thermoelectric properties. They are reviewed extensively in Section 1.9.2 and Chapter 5. Other Te-free candidate thermoelectrics are the chalcopyrite $CuFeS_2$[61] and the high-performance binary copper sulphides and selenides $Cu_{2-x}Q$ (*Q* = S, Se).[62, 63] Table 1.2 summarizes the figure of merit of a range of copper chalcogenides and substituted derivatives.

Table 1.2 Te-free Copper-containing chalcogenides, their maximum ZT and the optimal operating temperature.

Compound	ZT	Optimal Temperature
$Cu_{10.5}NiZn_{0.5}Sb_4S_{13}$[64]	> 1	723 K
$Cu_{11}ZnSb_4S_{13}$[66]	~ 1	723 K
$Cu_{11}MnSb_4S_{13}$[65]	1.13	575 K
$Cu_{11.5}Co_{0.5}Sb_4S_{13}$[66]	0.98	673 K
$Cu_{11.5}Fe_{0.5}Sb_4S_{13}$[65]	0.95	700 K
Cu_5FeS_4[67]	0.4	700 K
$Cu_{5.04}Fe_{0.96}S_4$[67]	0.5	700 K
$Cu_{0.96}Co_{0.04}FeS_2$[61]	0.22	675 K
$Cu_{1.97}S$[62]	1.7	1000 K
β-phase Cu_2Se[63]	~ 1.6	973 K

1.9 Materials investigated in this work

Sulphides and selenides with promising thermoelectric properties and the potential for further improvement are investigated in this work. The shandite $Co_3Sn_2S_2$ is a pseudo-two-dimensional mixed-metal sulphide with interesting physical properties. Different types of doping are carried out to target an increase in Seebeck coefficient and a reduction in thermal conductivity. Research is also conducted on quaternary chalcogenides with the general formula A_2ZnCQ_4 (A = Cu, Ag; C = Sn, Ge; Q = S, Se). This group of materials has attracted a lot of interest in many fields of technology including thermoelectrics. Especially selenide compounds have shown a substantial thermoelectric performance. Efforts are performed to improve the figure of merit of $Cu_2ZnGeSe_4$. The structures of the investigated materials are described below.

1.9.1 The shandite $Co_3Sn_2S_2$

Sulphides with the general formula $M_3M'_2S_2$ crystallize in the shandite structure and contain transition metal atoms (M = Co, Ni, Rh, Pd) and elements from III and IV group (M'=Sn, In, Pb, Tl). The structure of $Co_3Sn_2S_2$ is illustrated in Figure 1.16. The Co and Sn(2) atoms form layers with a kagome topology. The Sn(1) atoms are located in

interlayer sites and coordinated by six cobalt atoms forming a trigonal antiprismatic configuration. The sulphur atoms occupy interlayer positions capping trigonal arrays of cobalt atoms.

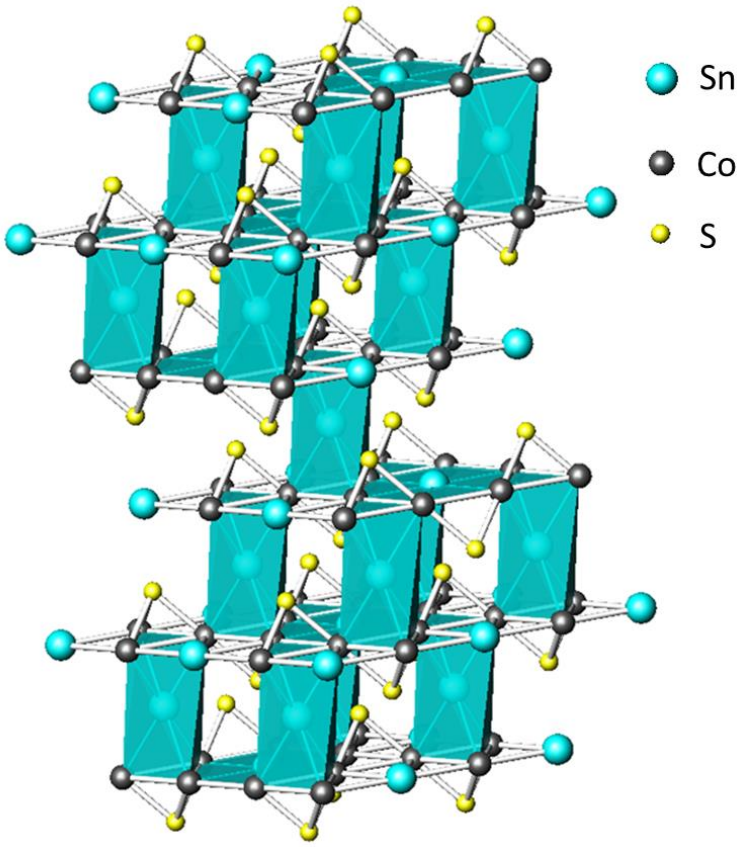

Figure 1.16 The shandite structure of $Co_3Sn_2S_2$ with the space group $R\bar{3}m$.

$Co_3Sn_2S_2$ is ferromagnetic (T_C = 176 K) and has been described as a type I_A half-metal.[68] The unusual combination of a metal-like electrical conductivity and a Seebeck coefficient of *ca*. -48 μV K^{-1} at 300 K has attracted particular interest.[69] This relatively high value can be explained by the fact that narrow sharp peaks are observed in the density of states in the vicinity of the Fermi level (Section 1.5.1, Figure 1.17). Figure 1.17 shows the relative contributions of atoms to the density of states, as calculated by Dedcov et al..[70] The region around the Fermi level is formed predominantly by the *3d* orbitals of transition metal atoms and the energy gap is relatively narrow at 300 meV.

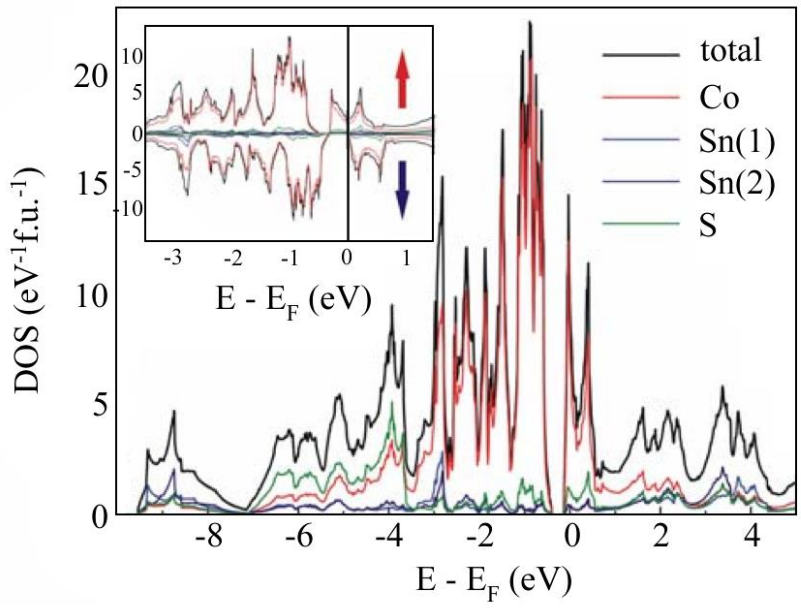

Figure 1.17 Density of states for the $Co_3Sn_2S_2$ shandite.[70]

1.9.2 Quaternary chalcogenides

The quaternary chalcogenides with the general formula A_2BCQ_4 where *A*, *B*, *C* are elements from groups 11, 12 and 14 respectively and *Q* = S or Se, are generally wide-gap *p*-type semiconductors with relatively high Seebeck coefficients. The interesting characteristic of this family of materials is that they exhibit low thermal conductivities due to their particular natural distorted crystal structure. These compounds crystallize in the zinc-blende-derived structures, the stannite with space group $I\bar{4}2m$ and kesterite with space group $I\bar{4}$ (Figure 1.5). In the kesterite structure, *A* and *B* atoms alternate on the *z* = 0.25 and *z* = 0.75 planes, perpendicular to *c* axis, in the *2c* and *2d* Wyckoff sites respectively, while *A* and *C* atoms form layers perpendicular to the *c* axis at *z* = 0, 0.5, occupying *2a* and *2b* Wyckoff sites respectively. In the stannite model, all *A* atoms occupy the *4d* site and are located in the *z* = 0.25 layer, whereas *B* and *C* cations form planes perpendicular to the *c* axis at *z* = 0, 0.5. *C* cations occupy the same Wyckoff site *2b* in both structural models. Essentially, in the stannite structure the two distinct sites *2c* and *2d* are occupied by the same cation, transforming into a single site, *4d*. In both zinc-blende structures, anion atoms are coordinated tetrahedrally by different cations (2 A^+, 1 B^{2+} and 1 C^{4+} cations), forming diverse interatomic distances.[71] This natural distorted structure enhances the phonon scattering, resulting in the reduction of lattice thermal conductivity. However, these materials 'suffer' from low electrical conductivities. Appropriate hole doping through chemical substitution is a typical

strategy to increase the number of charge carriers and the electrical conductivity and as a result to improve the thermoelectric figure-of-merit. Table 1.3 summarizes some of the quaternary compounds and their substituted derivatives which have been investigated recently for their thermoelectric properties.

Table 1.3 Quaternary chalcogenides A_2BCQ_4 with optimized thermoelectric properties at the optimal operating temperature.

Compound	*T / K*	*ρ / mΩ cm*	*S / μV K^{-1}*	*κ / W m^{-1} K^{-1}*	*ZT*
$Cu_2ZnSnSe_4$[72]	700	4.4	156	2.11	0.18
$Cu_{2.10}Zn_{0.90}SnSe_4$[72]	700	1.2	112	1.55	0.45
$Cu_2ZnSn_{0.90}In_{0.10}Se_4$[71]	700	6.9	215	1.25	0.37
$Cu_2ZnGa_{0.05}Sn_{0.95}Se_4$[75]	700	10	~ 220	~ 0.55	0.39
Cu_2ZnSnS_4[72]	700	189	355	1.21	0.039
$Cu_{2.10}Zn_{0.90}SnS_4$[72]	700	7.6	211	1.12	0.36
$Cu_2CdSnSe_4$[72]	700	31.9	298	1.01	0.19
$Cu_{2.10}Cd_{0.90}SnSe_4$[72]	700	5.3	156	0.49	0.65
$Cu_2CdGeSe_4$[73]	723	125	389	0.53	0.16
$Cu_{2.1}Cd_{0.9}GeSe_4$[73]	723	13.9	226	0.64	0.42
$Cu_2ZnGeSe_4$[74]	673	12.5	185	1.0	~ 0.18
$Cu_2ZnGe_{0.9}In_{0.1}Se_4$[74]	673	~ 5.7	185	1.25	0.33

1.10 Aims of the Project

The aim of the present work is the synthesis and research of cost-efficient and environmentally friendly materials as possible candidates for thermoelectricity generation. Efforts will be carried out to improve the thermoelectric performance of promising sulphides and selenides. Doping strategies through chemical substitution are applied to target a tuning of electrical and thermal transport properties in order to optimize the thermoelectric figure of merit of the materials. The project includes solid state synthesis methods, structural characterization using X-ray and neutron diffraction and physical property measurements. This work seeks an enhancement of thermoelectric efficiency of tellurium-free materials in order to establish a more competitive position in the market of thermoelectrics and to arise opportunities for large-scale applications for waste-heat recovery.

Chapter 2 - Experimental techniques

2.1 Synthesis

2.1.1 Sealed tube method at high temperatures

Solid-state synthesis was carried out in the absence of air by using the sealed tube method at high temperatures. This method was used to avoid the reaction of either reactants or products with oxygen and the subsequent formation of oxide impurities. In addition, due to the fact that all synthesized samples in this project contain sulfur and selenium, the evacuation in the tube reduces the risk of a possible explosion of the tube, because of the increase of vapor pressure of sulfur and selenium at high temperatures. The tubes were made of fused silica because this material has a high melting point and remains relatively inert even at high temperatures. Stoichiometric mixtures of carefully weighted reactants were ground by using an agate pestle and mortar to create a homogeneous powder of small well-mixed particles. This ensures that the surface contact area of reactants is maximized and as a result the diffusion distance of reactant atoms or ions is minimized. For the synthesis of sulphide compounds, sulphur flakes, which had been dried previously under vacuum, in order to remove possible traces of moisture, were used as reactants. The fused silica tubes were sealed under a vacuum of $< 10^{-3}$ mbar using a vacuum line. The solid-state reactions were carried out by one or more firings at elevated temperatures, each for a few days, using a furnace. Intermediate regrinding between firings was used to make the samples homogeneous fine powders in order to ensure a complete reaction. The reaction progress after each firing was checked by powder X-ray diffraction. It was necessary for each firing a slow heating rate to be applied in order to prevent the rapid increase of vapor pressure of sulphur and selenium, while a slow cooling rate enables the gases to reintegrate into the powder without condensing on the wall of the tube. The exact synthesis conditions for each compound are described separately in the appropriate sections.

2.1.2 Mechanical alloying

Mechanical alloying has been established as an alternative solid state synthesis process over the last 40 years. In this method, high energy ball milling is used to mix and grind powdered reactant elements or compounds in order to synthesize new phases. In 1970, Benzamin's team firstly developed this technique, successfully synthesizing dispersion

strengthened superalloys.[76] Various products have been synthesized by mechanical alloying, including intermetallic compounds, alloys, ceramics, nanocrystalline metals and nanocomposites.[77] During the milling process, the powder is trapped between either colliding balls or balls and the walls of the jar. The collisions among balls and walls create high amounts of energy which are transferred to the reagents and cause a repeated fracturing and welding of the powder. The energy transfer depends on a number of parameters. These include the type of mill, the rotational speed of the jar, the milling duration and temperature, the size, the number and the type of the balls and whether the milling is carried out dry or with the addition of an inert liquid (wet milling).[78]

In the work reported here, a Retsch PM100 planetary ball mill was used for the mechanical alloying of the quaternary selenide, $Ag_2ZnSnSe_4$. This type of mill is appropriate for laboratories because it can provide high speeds and its size is relatively small. A stainless, steel jar of 25 ml and 30 stainless steel balls of 6 mm were used for the synthesis of 5 g product.

2.2 Powder X-ray diffraction

For almost a century, X-ray diffraction has been the principal technique for the structural characterization of crystalline materials. In the electromagnetic spectrum X-ray radiation is located between the ultraviolet and γ-rays with a range of wavelengths close to 10^{-10} m (1 Å). The most standard method of X-ray production comes from the collision of high-energy electrons with a metal target, usually Cu. A heated tungsten filament produces the electron beam which, subsequently, is accelerated by a high electrical voltage (~ 30 kV). The energy of accelerated electrons is sufficient to cause the ionization of the 1*s* electrons of Cu. This results in the transition of 2*p* or 3*p* electrons to 1*s* orbital in order to fill the vacancy. The transition occurs with the simultaneous emission of X-ray photons. The most intense radiation, $K_{\alpha,}$ is released by the 2*p* electron transition with a wavelength of 1.5418 Å, while 3*p* electron transition emits the K_β radiation (1.3922 Å). Ni foil is able to filter out white and K_β radiation, giving the K_α beam. In fact, the K_α emission occurs as a closely spaced doublet, $K_{\alpha1}$ and $K_{\alpha2}$. The weaker $K_{\alpha2}$ is removed by a crystal monochromator, leaving in the incident beam only the desired $K_{\alpha1}$ (1.54051 Å).[79]

The fact that the wavelength of X-ray radiation is similar to interatomic distances (~ 2-3 Å) of crystal structures, enables the diffraction of X-rays. When the incident beam strikes a crystalline solid, the atoms or ions play the role of secondary point sources, re-

radiating and scattering the X-rays. Constructive interference occurs in specific directions where the diffracted beams are parallel with each other. In most cases the beams are not in phase, resulting in destructive interferences. In order to have constructive interference, the conditions must satisfy Bragg's law. Assuming that the crystal structure consists of planes of atoms, and that the planes may be considered to act as semi-transparent mirrors, when X-ray beams strike a plane, a percentage of radiation is diffracted, while the remaining is transmitted and may be diffracted by the next lattice layer. For example, the first beam in Figure 2.1 is diffracted at O by the second lattice plane while the second beam is reflected at L by the third plane. It is evident that the second beam travels an extra distance KLN in the crystal compared to the distance of the first beam. According to Bragg's law, this additional distance which is related to the d-spacing between two adjacent layers, d_{hkl}, must be equal to an integer number of wavelengths, λ (Equation 2.1). There is a correlation between the inter-plane d-spacing of a crystalline solid and its unit cell. A number of equations which depend on the geometry of the crystal structure can describe directly this relationship (Appendix A) and as a result the characteristics of the unit cell can be determined.

$$KL = LN = d_{hkl} \sin\theta$$
$$KLN = 2\, d_{hkl} \sin\theta$$
$$n\lambda = 2\, d_{hkl} \sin\theta \qquad (2.1)$$

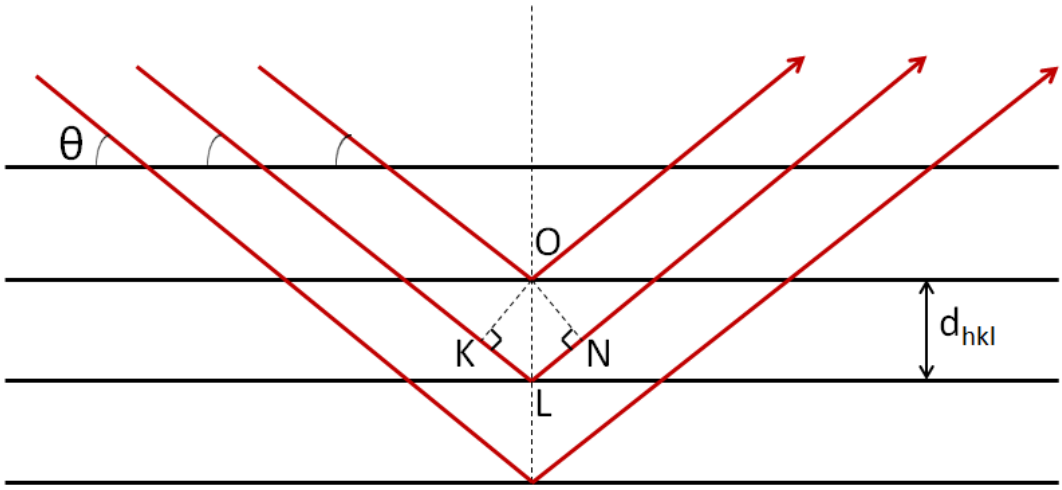

Figure 2.1 Diagram of X-ray diffraction by adjacent lattice planes in a crystalline solid.

X-ray diffraction measurements were carried out for samples in powder and pellet form using a Bruker D8 Advance powder diffractometer, operating with Ge-monochromated Cu $K\alpha_1$ radiation with a wavelength of $\lambda = 1.5406$ Å and a LynxEye linear detector. The powdered samples were ground thoroughly with an agate pestle and mortar. The resulting fine powders were subsequently loaded into a recessed PMMA polymer sample holder leaving at the top of the holder a flat surface. Data for purity and phase identification analysis were typically collected over the angular range $5 \leq 2\theta/^{\circ} \leq 85$ counting for 1.2 sec at each step of 0.02762 ˚ in detector position. On occasions, where the quantity of the powder was limited, a flat plate of single crystal silicon was used as a sample holder to which a few mg of the sample were stuck using a little Vaseline.

Initial evaluation of the data was carried out using the ICDD-PDF database of EVA software package.[80] The experimental data were compared to patterns of known compounds in order to determine the phase or the phases present in the sample. Once the desired material had been produced as a single phase, X-ray diffraction data were collected over the extended range $10 \leq 2\theta\ (^{\circ}) \leq 120$ with higher counting times in order to improve the statistical quality of the data. For the shandite compounds, a step of 0.018° was used, counting for 3.6 sec at each step of the detector, while a step of 0.049° with a counting time of 4 sec / step were used for the quaternary chalcogenides A_2ZnBQ_4 (A = Cu, Ag; B = Sn, Ge; Q = S, Se). Rietveld refinements were carried out using the General Structure Analysis System[81] (GSAS) software package.

2.3 Powder Neutron Diffraction

Neutron diffraction exhibits some essential differences compared with X-rays, providing specific advantages. The main difference is in the scattering process. In the case of X-ray diffraction, the electron cloud of atoms scatters the photon beam, while the nucleus is responsible for the scattering of neutrons. For this reason, neutron scattering is not dependent strongly on the atomic number of the atoms and as a result the scattering can be effective for both light and heavy elements, producing precise data for the position of light atoms, such as hydrogen. In addition, X-rays cannot distinguish neighboring elements in the periodic table with similar atomic numbers, such as Fe, Co and Ni. However, these atoms have different neutron scattering factors (Table 2.1), allowing a more detailed structural analysis and the observation of superlattice phenomena such as metal-atom ordering. Moreover, due to the fact that neutrons have

spin, they carry magnetic moments which can interact with those of atoms. This provides information for the magnetic properties of the material and the investigation of magnetic ordering.[82]

Table 2.1 Neutron diffraction scattering lengths of elements for which metal-atom ordering investigations conducted.[83]

Element	Bound coherent scattering length / fm
Fe	9.45
Co	2.49
Ni	10.3
Cu	7.718
Zn	5.680
Ge	8.185
Ag	5.922
Sn	6.225

Powder neutron diffraction experiments were carried out at the ISIS facility of Rutherford Appleton Laboratory using two multibank diffractometers, GEM and POLARIS, which are located on Target Station 1 (Figure 2.2). Pulsed neutron beams are generated through the spallation process where a heavy metal target is bombarded by high energy protons. Initially, hydrogen anions are produced using an electrical discharge and are accelerated by a linear accelerator of 70 MeV, reaching 37 % of the speed of light. H^- ions pass through an alumina window which removes two electrons, producing protons. These are accelerated by a 800 MeV synchrotron with a circumference of 163 m. This increases the proton speed to 84 % of the speed of light. The proton beam is then extracted as a pulsed beam at 50 Hz and is directed in two target stations. After the collision of high-energy protons with the heavy metal target, neutrons are produced to supply the various instruments which are located around each of the two target stations. As neutrons are directed to the instruments, they pass through a window which adjusts the width and the height of the beam.

Samples were contained in vanadium cans because this element scatters neutrons weakly and as a result it does not contaminate greatly the data of the investigated material. The specific peaks which come from vanadium (Table 2.2) are usually excluded during the data analysis process by the Rietveld method, which is explained later.

Table 2.2 Neutron scattering lengths of vanadium.

hkl	*d-spacing (Å)*	I_{rel}
110	2.1423	1000
200	1.5149	243
211	1.2369	388.46
220	1.0712	517.75
310	0.9581	647.44

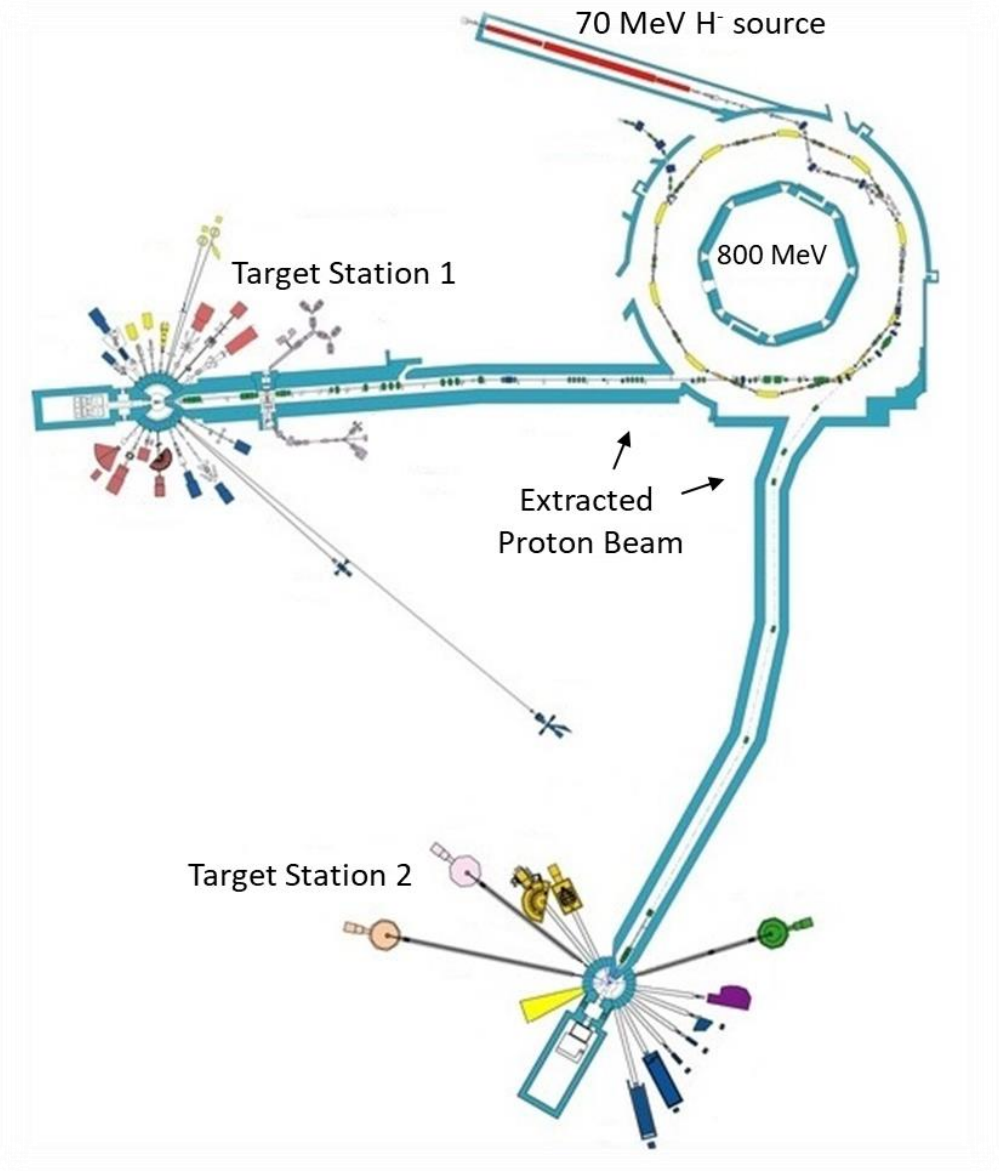

Figure 2.2 Layout of ISIS facility.[84]

2.3.1 The GEM diffractometer

The General Materials (GEM) diffractometer consists of a large array of ZnS/^{6}Li scintillator detectors with an area of 7.270 m^2 and a range of scattering angles from 1.2˚ to 171.4˚ (Figure 2.3). The instrument has a long flight of path of 17 m, providing a high resolution in reciprocal-space with an optimum value of $\Delta Q/Q$ = 0.34% at back-scattering angles.

Powder neutron diffraction data are collected in time-of-flight by the seven detector banks (details in Table 2.3). For room temperature measurements, the samples were loaded into 6 mm diameter thin-walled vanadium cans. The high temperature measurements were conducted using an aluminium furnace, whose the vanadium chamber had been evacuated previously. The powders had been sealed under vacuum (~ 10^{-4} mbar) in high purity quartz ampoules which were placed in 8 mm diameter vanadium cans. The investigation of structural characterization of all samples was carried out using data collected from bank 3 to bank 7. The measurements from banks 5 and 5X as well as banks 6 and 7 were combined to make two single data sets.

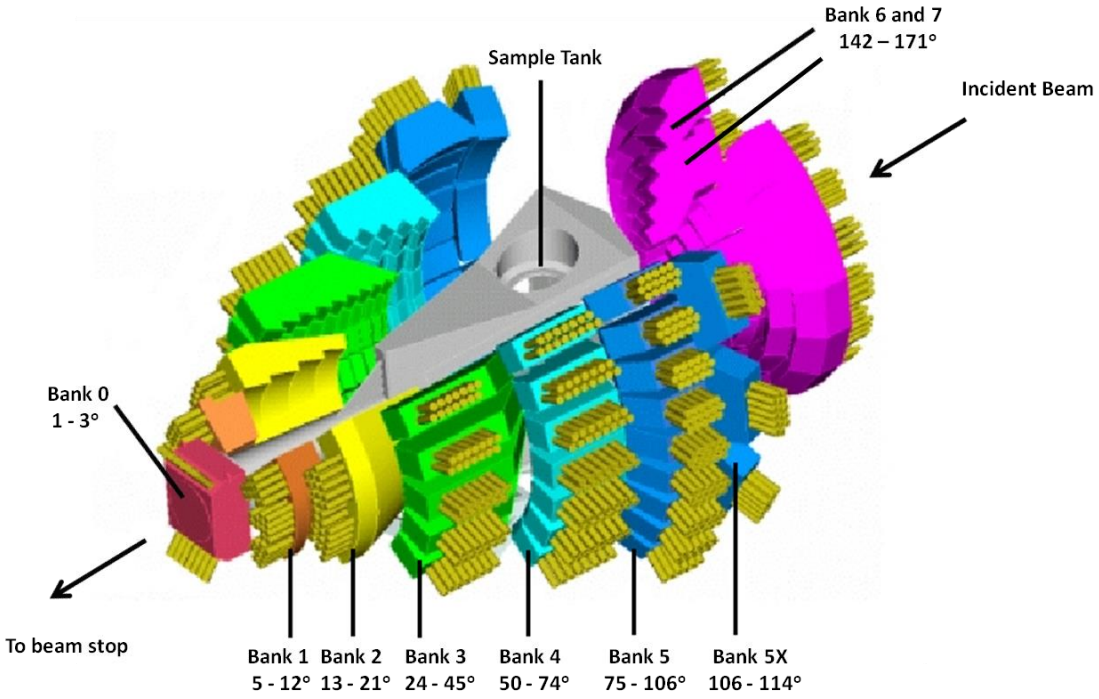

Figure 2.3 GEM diffractometer.[85]

Table 2.3 Detector bank parameters of the GEM diffractometer.[86]

Bank	1	2	3	4	5	5X	6	7
2θ / °	5-12	13-21	24-45	50-74	79-104	105-113	142-149	149-169
Δd/d / %	4.7	2.4	1.7	0.79	0.51	0.51	0.34	0.35
d range / Å	2-30	1-14	0.8-7	0.7-4	0.5-2.5		0.3-1.7	

2.3.2 The POLARIS diffractometer

In 2012, the POLARIS diffractometer (Figure 2.4) was upgraded, increasing the detector coverage and improving the incident beam collimation. The upgraded version has a primary flight path of 14 m and 6 detector banks which can cover a range from 6 to 168˚ (Table 2.4).[87] The benefit of the instrument is that provides a high intensity neutron flux and as a result sufficient experimental data can be collected in a relatively short time period even for samples with a small amount of powder. Rietveld refinements were carried out using experimental data from bank 4 and the single data set from the combination of measurements from bank 5 and bank 6.

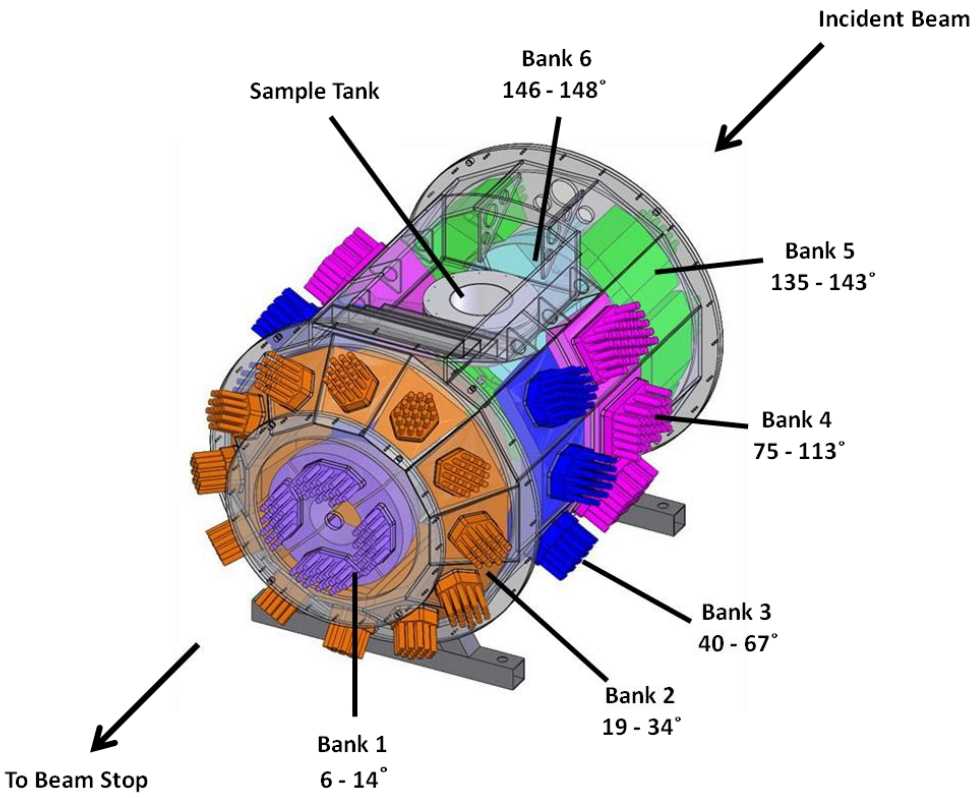

Figure 2.4 Detector banks of POLARIS diffractometer.[88]

Table 2.4 Detector bank parameters of POLARIS.[87]

Bank	1	2	3	4	5	6
2θ / °	6-14	19-34	40-67	75-113	135-143	146-168
Δd/d / %	> 2.7	1.2-1.9	0.85	0.51	0.30	
d_{max} / Å	19.6	8.7	7.0	0.2	2.7	

2.4 Rietveld Refinement

The analysis of both powder X-ray and powder neutron diffraction data was carried out by the Rietveld method[89,90] using the General Structure Analysis System (GSAS) software[81] package through the EXPGUI user interface. This method uses the least square approach to refine an initial structural model against the experimental data in order to fit as well as possible with the collected diffraction pattern. Mathematically, during the least-square process, the quantity which must be minimized is the residual S_y (Equation 2.2).

$$S_y = \sum_i w_i (y_i - y_i calc)^2 \qquad (2.2)$$

where

y_i = the experimental intensity of the i step

$y_i calc$ = the calculated intensity of the i step

$w_i = 1 / y_i$

The programme requires three types of data: a structural model, an instrument parameter file and the experimental data. A successful Rietveld refinement need high quality diffraction data and a good starting structural model, otherwise the analysis process may fail. A range of parameters are refined to improve the goodness-of-fit between the predicted model and the experimental profile. Following initial refinement of scale factors and background parameters, lattice parameters were refined in order to improve the correspondence in the position of the peaks between the calculated and experimental data. Subsequently, the atomic coordinates, thermal parameters and

occupancy factors, all of which affect the peak intensities were introduced as variables into the refinement, before finally allowing the peak shape profile coefficients to refine. For both X-ray and neutron diffraction refinements the peak shape was modelled using a pseudo-Voigt function[91,92] which mixes Gaussian and Lorentzian functions.

There are several numeral criteria of fit, R-values, which indicate the quality of a refinement. The most important is the weighted profile R factor (R_{wp}) which shows the percentage of residual between the experimental data and the calculated model. Therefore, the goal for a successful refinement is to achieve a value for R_{wp} as low as possible.

$$R_{wp} = \sqrt{\frac{\sum_i w_i(y_i - y_i calc)^2}{\sum_i w_i y_i^2}} \quad (2.3)$$

The minimum R_{wp} value which is reachable using a certain number of refinement parameters, *P*, is the R_{exp}.

$$R_{exp} = \sqrt{\frac{N-P}{\sum_i^N w_i y_i^2}} \quad (2.4)$$

where *N* is the number of experimental observations. The goodness of fit (χ^2) is the ratio between the R_{wp} and R_{exp} and should be higher but near to 1.[90]

$$\chi^2 = (R_{wp} / R_{exp})^2 \quad (2.5)$$

2.5 Sample consolidation

Physical property measurements require the densification of the powdered samples into circular pellets with high densities. All samples were consolidated by hot-pressing using a hot-press manufactured in house. Each sample was placed inside a graphite mould which was loaded with graphite dies (Figure 2.5). Graphite foils were placed between the dies and the sample to avoid contact with the dies and facilitate the removal of the pellet. The whole system was heated by cartridge heaters which were able to reach temperatures up to 750 ˚C. The desired temperature was programmed by a temperature controller which was connected with the system by a thermocouple, while the pressure was applied using a hydraulic press. After hot-pressing, the resulting pellets were polished carefully by using silicon carbide paper in order to remove any residue of the graphite foils from the surface of the sample.

Subsequently, the density of the pellets was measured by the buoyancy method which is based on Archimedes' Principle. The weights of the samples were measured in air and water by using an AE Adam PW 184 instrument with an uncertainty of *ca.* 5 %. The dimensions of the pellets which were measured with an electronic caliper, had a diameter of *ca*. 12.7 mm and a thickness of *ca.* 2mm.

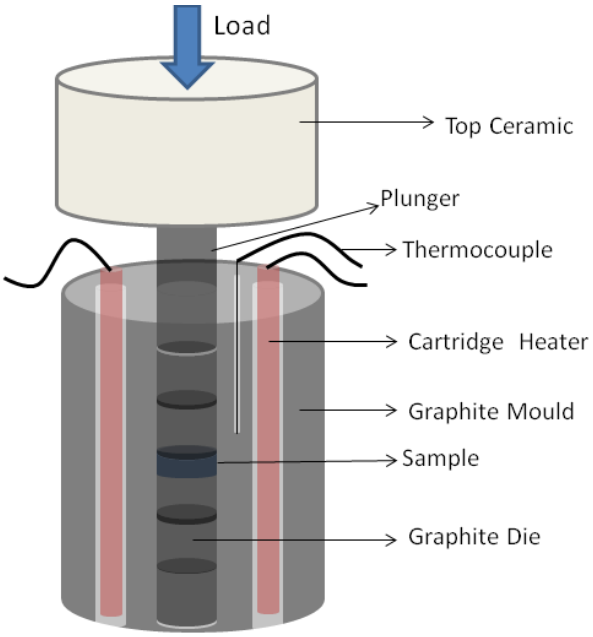

Figure 2.5 Hot-pressing system with cartridge heaters.

2.6 Ingot fabrication

To measure Seebeck coefficient at low temperatures, ingots were fabricated by cutting the pellets with a diamond saw. The pellets were attached by molten wax to a ceramic block. The diamond saw was equipped with a blade which rotated at 100 rpm. The blade was aligned with an outline of the ingot drawn previously on the surface of the pellet. Cutting the pellets at 4 different positions formed rectangular ingots with dimensions *ca.* 10.7 x 3 x 1.8 mm^3. The residual wax which was stuck on the ingots, was removed by polishing with silicon carbide paper.

2.7 Physical property measurements

2.7.1 Electrical transport property measurements

The ability of a material to resist the flow of electrical current is defined by the electrical resistivity which is the inverse of electrical conductivity. Therefore, as can be observed in Equation 2.6, the electrical resistivity is related directly to the concentration, n, and mobility, μ, of charge carriers:

$$\rho = \frac{1}{\sigma} = \frac{1}{\sigma_e + \sigma_h} = \frac{1}{n_e\, e\, \mu_e + n_h\, e\, \mu_h} \tag{2.6}$$

where n_e and n_h are the electron and hole concentration respectively, e is the elementary charge and μ_e and μ_h the electron and hole mobility respectively.

If the material is *n*-type, the electrical conductivity is dominated by electrons, while if the majority of charge carriers are holes, it is *p*-type. The trend of electrical resistivity in the temperature change gives valuable information for the behavior of the measured material, characterizing it as either metallic or non-metallic.

Information about the type of material can be derived by the measurement of Seebeck coefficient which is the measure of electrical voltage which is produced by a temperature gradient across the material. The sign of the measured values is determined by the majority of charge carriers; positive values indicate holes as dominant carriers, while electrons are responsible for negative values.

2.7.1.1 Electrical resistivity and Seebeck coefficient measurements

Using the Linseis LSR3-800 instrument, measurements of the electrical resistivity and Seebeck coefficient were made over the temperature range $300 \leq T / K \leq 625$ in 10 K steps. The hot-pressed samples with the aforementioned circular-pellet shape and dimensions were placed between the upper and lower blocks and in contact with two platinum electrodes (Figure 2.6). The furnace chamber was filled with He gas (1.1 bar). The primary furnace held the chamber at a selected temperature, while a second heater heated the lower side of the pellet, thereby creating a temperature gradient. To measure the Seebeck coefficient, two probes equipped with thermocouples were in contact with the upper and lower sides of the pellet measuring the temperatures T_1 and T_2, as well as the voltage difference. The distance between the two thermocouples was measured at 7.8 mm and a temperature gradient of 50 K was applied. The electrical resistivity

measurement was based on the four-terminal method. The two platinum electrodes supplied a constant current of 100 mA and the two thermocouples measured the voltage gradient dV. The uncertainty of the measurements is around 5 %.

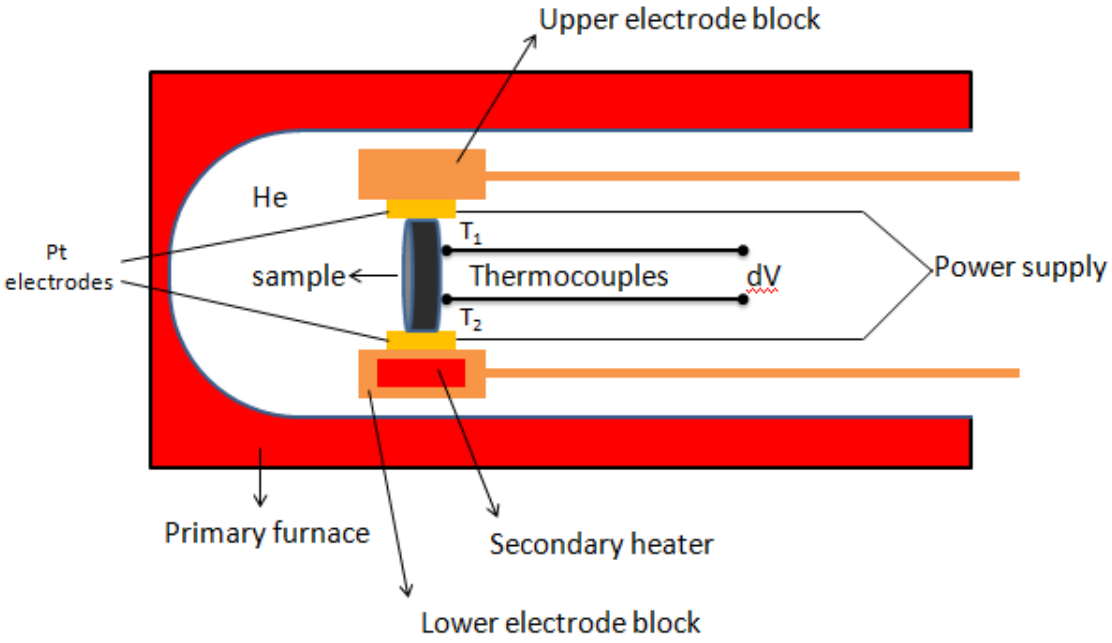

Figure 2.6 Schematic illustration of LSR3-800.

2.7.1.2 Seebeck coefficient measurements at low temperatures

Low-temperature Seebeck coefficient measurements were conducted for the shandite $Co_{3-x}Ni_xSn_2S_2$ ($0 \leq x \leq 3$) over the range $100 \leq T / K \leq 350$ in 10 K steps using an in-house instrument equipped with a close-cycle refrigerator (CCR) (Figure 2.7). The system was cooled by an Advance Research System Inc. ARS-2HW compressor and was isolated from the environment under vacuum. Each ingot was attached on a holder made of copper, using silver paste. A small heater was close to one edge of the sample in order to supply it with heat, providing the necessary temperature gradient. Two thermocouples which were each connected to a LakeShore-331 controller measured the temperature at the hot and cold side of the sample. The cold side of sample holder was attached to the main stick of the instrument. This was equipped with a heater which was responsible for the general heating of the instrument. A second LakeShore-331

controlled the temperature of the instrument. Two 50 µm copper wires attached by silver paint to the ends of the ingot were connected to a Keithley 2182A nanovoltmeter which measured the voltage drop ΔV. The Seebeck coefficient was determined by applying a temperature gradient ΔT across the sample and measuring the corresponding voltage ΔV. The slope ΔV / ΔT determines the Seebeck coefficient. The uncertainty of Seebeck coefficient measurements at low temperatures is *ca.* 5 %.

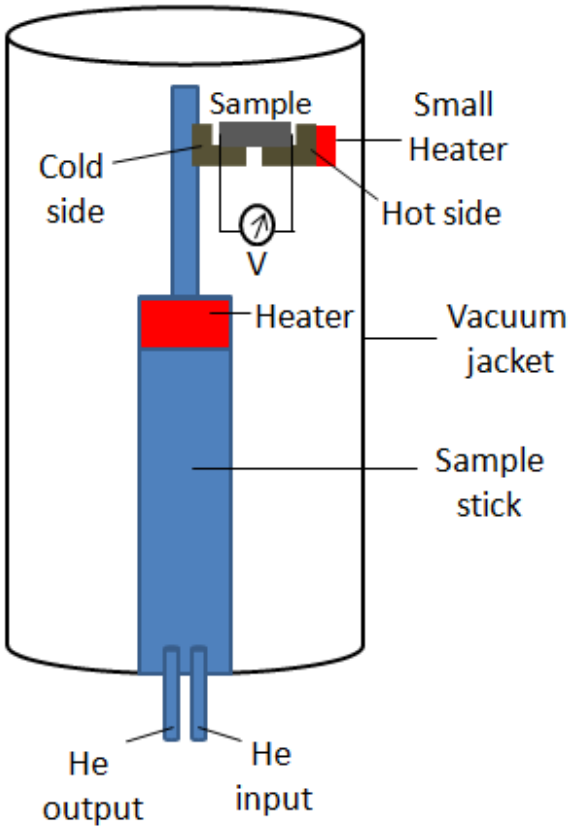

Figure 2.7 Illustration of the CCR in-house instrument.

2.7.2 Thermal transport property measurements

Thermal diffusivity measurements were conducted on circular-shaped pellets which had a diameter of 12.5 – 12.7 mm and a thickness of 1.8 – 2.0 mm. The measurements were carried out using a Netzsch LFA 447 Nanoflash instrument over the temperature range $300 \leq T / K \leq 573$ in steps of 25 K with an uncertainty of *ca*. 5 %. A software-controlled automatic sample changer allows measurement of up to 4 samples at the same time. The instrument operates with the light flash technique. The xenon flash lamp, the sample holder and the InSb IR detector are installed vertically (Figure 2.8). In each step of

25 K, 3 shots of flash light incident on the bottom surface of the sample while the IR detector measures the temperature rise on the top surface. The top and bottom surfaces of pellets were coated with a graphite layer in order to enhance the absorption of laser energy and the emission of IR radiation to the detector.

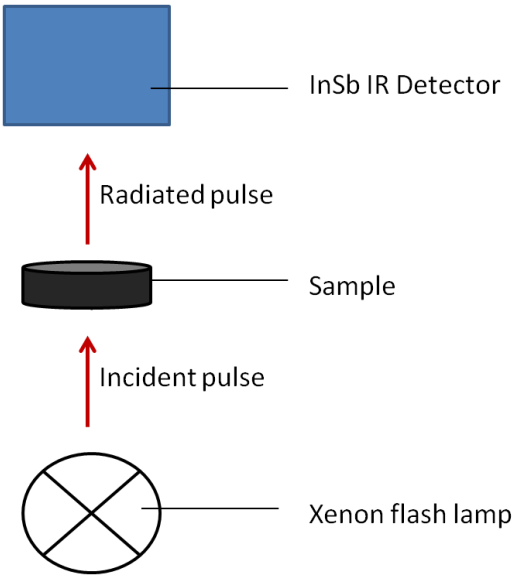

Figure 2.8 Schematic of Netzsch LFA 447 Nanoflash instrument.

The commercial software, Proteus®, was used to carry out the analysis of the measured temperature / time function and calculate the thermal diffusivity, α, according to Equation 2.8, where K_x is a dimensionless constant, L the thickness of the pellet, through which the heat is transferred and t_x the percentage of temperature increase at a specific time. The determination of the specific heat was achieved using the comparison method. The same measurement conditions were applied for a Pyroceram 9606 sample, a reference material of known heat capacity. Finally, the results of thermal diffusivity α and heat capacity C_p allowed the determination of thermal conductivity κ of the sample using the Equation 2.9, where ρ is the density of the material which had been previously determined using the Archimedes method.

$$\alpha = \frac{K_x \, L^2}{t_x} \tag{2.8}$$

$$\kappa = \alpha \; C_p \; \rho \tag{2.9}$$

The electronic contribution, κ_{el}, was determined using the Wiedemann-Franz law, and subsequently, the lattice contribution, κ_L, was determined as the difference between κ and κ_{el}. The fact that all samples of the investigated series (shandite sulphides and $Cu_{2+x}ZnGe_{1-x}Se_4$) are either metallic or semiconducting with low electrical resistivity, allowed the use of Lorentz number, $L_0 = 2.44\times10^{-8}$ W Ω K^{-2}, for the calculation of electronic contribution.

2.8 ^{119}Sn and ^{57}Fe Mössbauer Spectroscopy

This technique was discovered by Rudolf Mössbauer in 1958 (Nobel Prize in Physics, 1961) and is based on the recoilless nuclear resonance absorption of γ radiation.[93] Mössbauer spectroscopy is a highly sensitive technique which explores the changes in the energy states of nuclei which interact with their chemical environment. Three types of nuclear interactions occur: isomers shifts, quadropole and magnetic interactions. A typical Mössbauer spectrometer is illustrated schematically in Figure 2.9. The source must be of the same isotope as the atoms which are going to be investigated in the sample. The decay of radioactive isotopes emits gamma radiation which is aligned by a collimator before striking the solid sample. The source is in movement, back and forwards periodically. The transmitted γ ray is collected by a detector which measures the intensity of the beam.

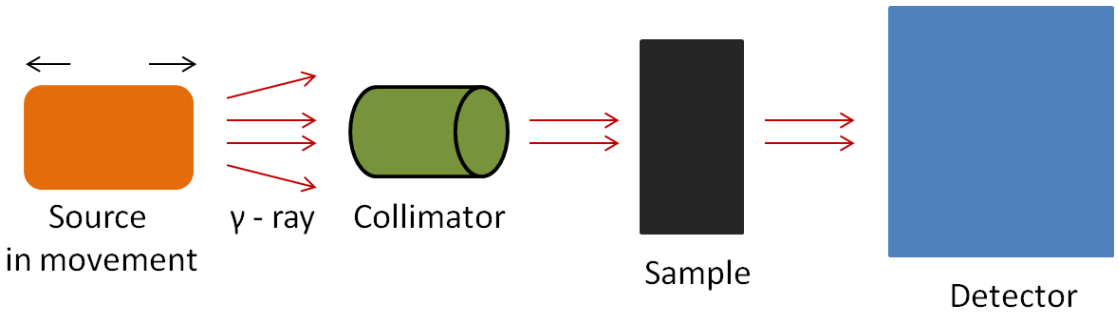

Figure 2.9 Mössbauer Spectroscopy instrument.

^{119}Sn and ^{57}Fe Mössbauer experiments were conducted on the series $Co_{3-x}Fe_xSn_2S_2$ to investigate the oxidation state of tin and iron atoms. The experiments were carried out at the University of Montpellier by Professor Jean-Claude Jumas. The ^{119}Sn and ^{57}Fe Mössbauer spectroscopic data were recorded in transmission mode and in constant acceleration mode using as sources ^{119}Sn embedded in a $CaSnO_3$ matrix and ^{57}Co (Rh)

with nominal activity of 925 MBq, respectively. The velocity scales were calibrated with the magnetic sextet of a high-purity α-Fe foil as the reference absorber, using ^{57}Co (Rh) as the source. The absorbers containing 1 – 2 mg cm^{-2} of ^{119}Sn or 0.2 - 0.1 mg cm^{-2} of ^{57}Fe were prepared inside a glove box under argon atmosphere, by mixing the powder samples with Apiezon grease held between two Kapton films. The sample holder was sealed to prevent air contact. The hyperfine parameters δ (isomer shift) and ΔE_q (quadrupole splitting) were determined by fitting Lorentzian profiles to the experimental spectra, using a least-squares method. The resulting errors in the hyperfine parameters are found to be smaller than 0.01 mm s^{-1} for the different $Co_{3-x}Fe_xSn_2S_2$ compounds. The isomer shift values for the ^{119}Sn spectra are given relative to δ values of a $BaSnO_3$ spectrum recorded at room temperature, whilst the ^{57}Fe data are expressed relative to α-Fe.

2.9 Thermal analysis

Thermal analysis techniques are used for the investigation of phase changes which are related to temperature changes. Thermogravimetric analysis (TGA) tests the thermal stability of a solid, measuring the weight of the sample as the temperature is increased, at a controlled rate. The differential scanning calorimetry (DSC) technique monitors the flow of heat absorbed or released by the solid as a function of temperature. TGA and DSC measurements were carried out simultaneously for the quaternary $Cu_2ZnGeSe_4$ selenide using a TA Instruments SDT Q600 instrument. Powder of *ca*. 20 mg was placed in a pan made of alumina and was heated under nitrogen flow up to 500 ˚C.

Chapter 3- Electron and hole doping in shandite $Co_3Sn_2S_2$

3.1 Introduction

In 2013, Corps *et al.*[94] demonstrated that substitution of tin by indium in $Co_3Sn_{2-x}In_xS_2$ ($0 \leq x \leq 2$) enhances the thermoelectric performance by tuning E_F within narrow *d*-bands (Figure 1.17). $Co_3Sn_2S_2$ has 47 valence electrons which occupy 24 of 31 bands. E_F crosses the half-occupied 24th band which is mainly of Co 3*d* character. Since indium provides one electron less than tin, substitution of Sn reduces the number of valence electrons by one electron for each unit increase in In content, shifting E_F to sharp peaks in the Co 3*d* states. As a result, E_F is localized in a more pronounced curvature in the density of states (DOS) and according to Mott relation,[21] this gives a high rise of Seebeck coefficient. At room temperature $Co_3Sn_{1.15}In_{0.85}S_2$ exhibits a ZT of 0.2, which represents an almost 3-fold increase over that of $Co_3Sn_2S_2$.

Magnetic susceptibility measurements have revealed that the substitution of Co by Ni in $Co_{3-x}Ni_xSn_2S_2$ ($0 \leq x \leq 3$) suppresses the ferromagnetic order at $x > 0.2$.[95] Band structure calculations[96] have indicated that the E_F of $Ni_3Sn_2S_2$ is moved to higher energies within 3*d* states. Mössbauer and X-ray photoelectron spectroscopy (XPS) experiments have shown that $Ni_3Sn_2S_2$ is a metal with the valence electron configuration: $(Ni^0)_3(Sn(1)^{2+})(Sn(2)^{2+})(S^{2-})_2$.[97] However, there is not a clear conclusion for the oxidation states in the cobalt end-member phase, $Co_3Sn_2S_2$. ^{119}Sn Mössbauer spectroscopy[98] appears to rule out Sn(II) and Sn(IV) states, while Umetani et al[99] suggest for cobalt a mixture of Co(0) and Co(II). Recently, XPS data for $Co_3Sn_{2-x}In_xS_2$ indicate for cobalt a zero-valent state, while for sulfur, an oxidation state which approaches zero.[100] However, the Bader charge analysis of DFT calculations suggest for sulfur a net negative charge of *ca*. 0.7. In addition, ^{119}Sn Mössbauer spectra revealed for the two tin sides an oxidation state which tends toward zero.

In 2015, Sakai et al.[101] revealed a new solubility limit for $Co_{3-x}Fe_xSn_2S_2$ under high-pressure (HP) and high-temperature (HT) conditions. Samples with $x < 0.6$ showed impurities of < 10 vol %, while clear increases of additional phases SnS and FeS were observed in samples with $x \geq 0.6$. The Fe solubility limit x_{max} rises from below $x = 0.6$ up to $x = 1.0$ following HP and HT heat treatments. The ferromagnetic transition temperature is reduced as a function of iron composition (for $x = 1$, $T_C = 68(3)$ K). At ambient pressure, growth of single crystals of $Co_{3-x}Fe_xSn_2S_2$ with $x_{max} = 0.53$ has also

been reported.[102] Recently, has been suggested that T_C decreases with iron content in a similar fashion to that observed in indium-substituted shandites, indicating that the electron count is a key parameter in determining the magnetic ground state of the material.[103]

Here, the effect of electron and hole doping on the thermoelectric properties of $Co_3Sn_2S_2$ is investigated through the chemical substitution of the transition metal atom, Co, by its neighboring elements, Ni and Fe, respectively. Two series, $Co_{3-x}Ni_xSn_2S_2$ ($0 \leq x \leq 3$) and $Co_{3-x}Fe_xSn_2S_2$ ($0 \leq x \leq 0.6$), have been synthesized and characterized initially by X-ray diffraction. In an effort to explore further the effect of cobalt substitution in the structure, neutron diffraction experiments were carried out for both series. Mössbauer spectroscopy data were obtained and analyzed for the iron substituted series, while the thermoelectric properties for both series are also presented and discussed. The results of the present work have been published in the Journal of Solid State Chemistry.[104]

3.2 Synthesis

All samples of $Co_{3-x}M_xSn_2S_2$ (M = Ni: $0 \leq x \leq 3$; M = Fe: $0 \leq x \leq 0.7$) were prepared by the sealed tube method at high temperatures, Section 2.1.1. Appropriate mixtures of elemental nickel (Alfa Aesar, powder, 99.9%), cobalt (Alfa Aesar, powder, 99.8%), tin (Sigma-Aldrich, powder, ≥ 99%), iron (Sigma-Aldrich, powder, 99.9%) and sulphur (Sigma-Aldrich, flakes, 99.99%) were ground with an agate pestle and mortar. The resulting powders were sealed in silica tubes under vacuum < 10^{-3} mbar. Two firings were carried out: at 500 ˚C and 700 ˚C, each for 48 h, with an intermediate grinding. A heating / cooling rate of 0.5 ˚C min^{-1} was used.

3.3 Structural characterization

3.3.1 Powder X-ray diffraction

The collection of powder X-ray diffraction data was carried out as described in Section 2.2. Rietveld refinements were carried out using as the initial structural model the lattice parameters and atomic coordinates of the cobalt end-member phase described in the space group $R\bar{3}m$.[1] Following the refinement of the scale factor, the background parameters were refined using the reciprocal interpolation function. Subsequently, zero point, lattice parameters, atomic coordinates of the sulphur atom and thermal parameters

were introduced into the refinement. The profile coefficients were initially refined individually and at the end simultaneously, until convergence of the refinement was achieved. For a given composition, the refinement was initiated using the refined model of the previous composition for the initial structural model. The thermal parameters of Co and its neighboring elements, Ni and Fe, were constrained to be equivalent, while site occupancy factors were set at their nominal values.

3.3.1.1 Powder X-ray diffraction for $Co_{3-x}Ni_xSn_2S_2$ ($0 \leq x \leq 3$)

Powder X-ray diffraction data reveal that all samples of $Co_{3-x}Ni_xSn_2S_2$ are single phases over the entire range of composition ($0 \leq x \leq 3$) (Figure 3.1).

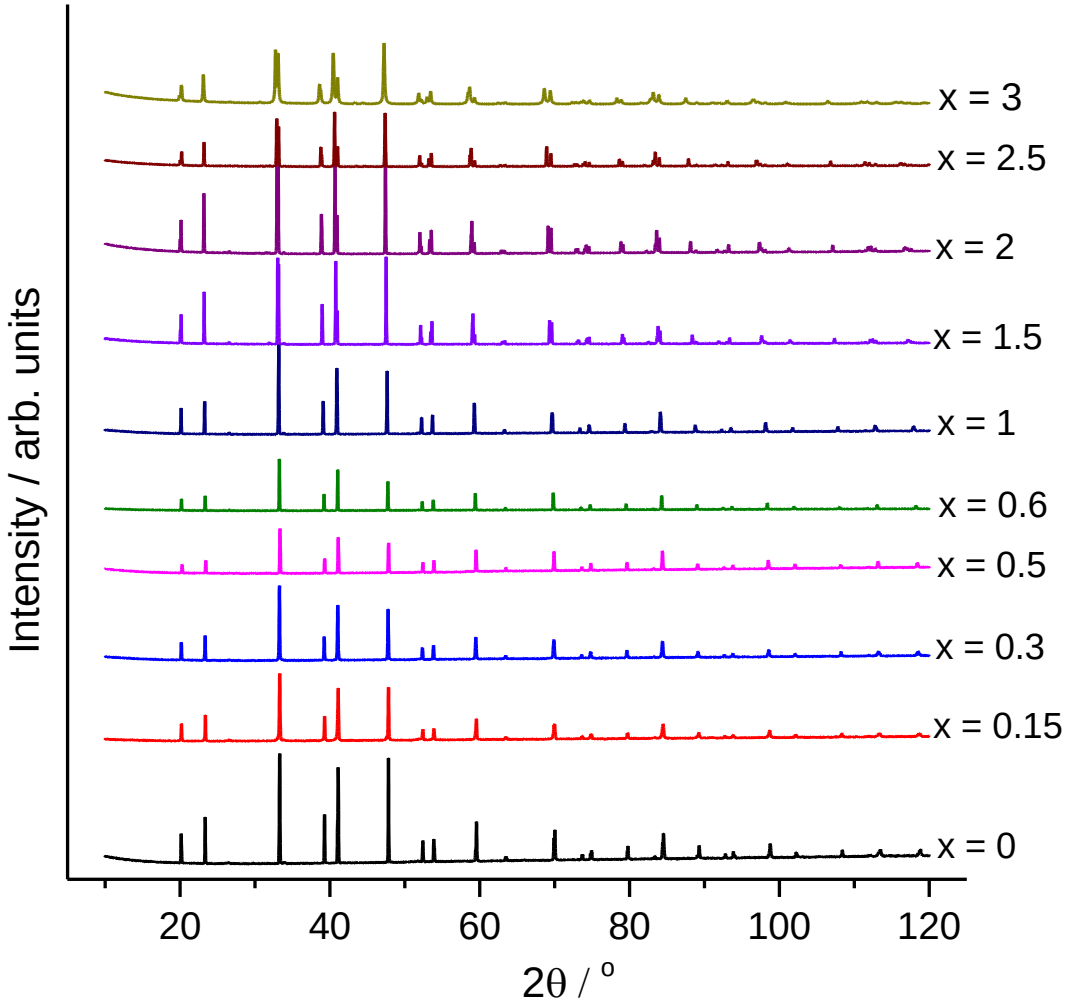

Figure 3.1 Powder X-ray diffraction data for $Co_{3-x}Ni_xSn_2S_2$ ($0 \leq x \leq 3$) over the range $10 \leq 2\theta / ° \leq 120$.

Figures 3.2 up to 3.5 present the results of Rietveld refinements for four representative compositions (x = 0, 1, 2, 3), while the remaining patterns are illustrated in Appendix B. The Rietveld refinements showed that the experimental patterns for all samples are well described in the space group $R\bar{3}m$ ($1.1 \leq \chi^2 \leq 2.0$, $2.5 \leq R_{wp}$ / % ≤ 8.0). Only in the nickel end-member phase traces of Ni_3Sn_2 (~ 1.3 wt %) are observed.

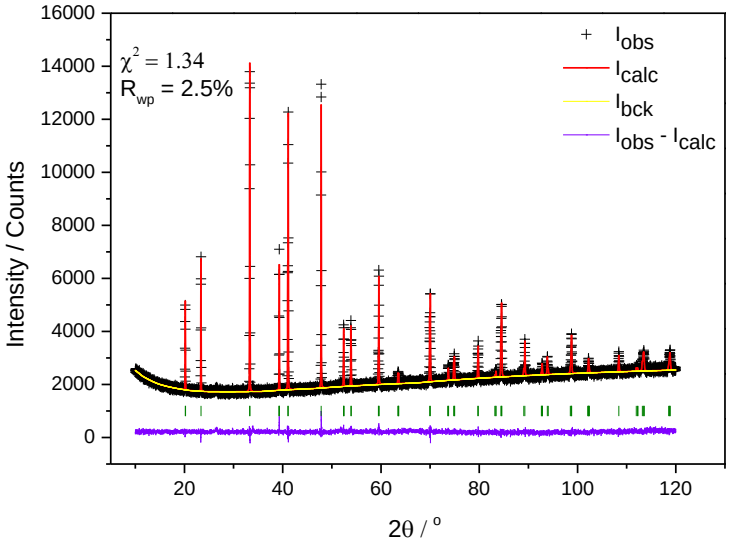

Figure 3.2 Rietveld refinement of $Co_3Sn_2S_2$ using X-ray diffraction data. Observed (black crosses), refined (red solid lines) and difference (blue bottom line) profiles. Reflection positions are marked by olive lines.

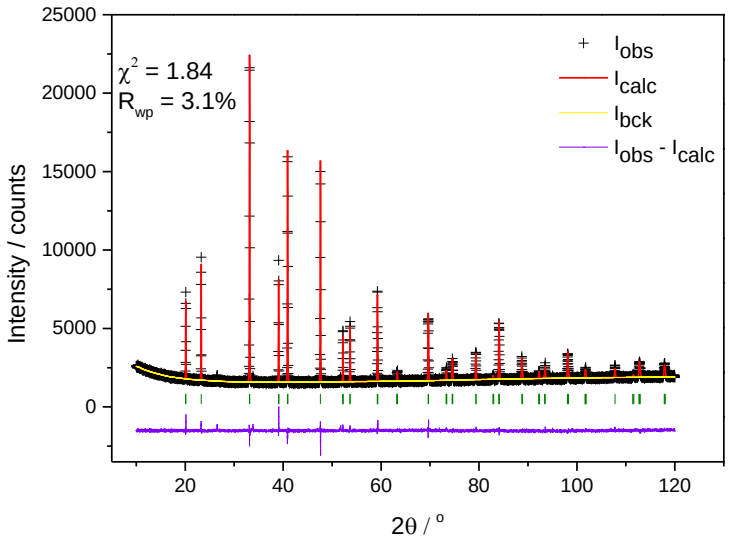

Figure 3.3 Rietveld refinement for $Co_2NiSn_2S_2$ using X-ray diffraction data. Observed (black crosses), refined (red solid lines) and difference (blue bottom line) profiles. Reflection positions are marked by olive lines.

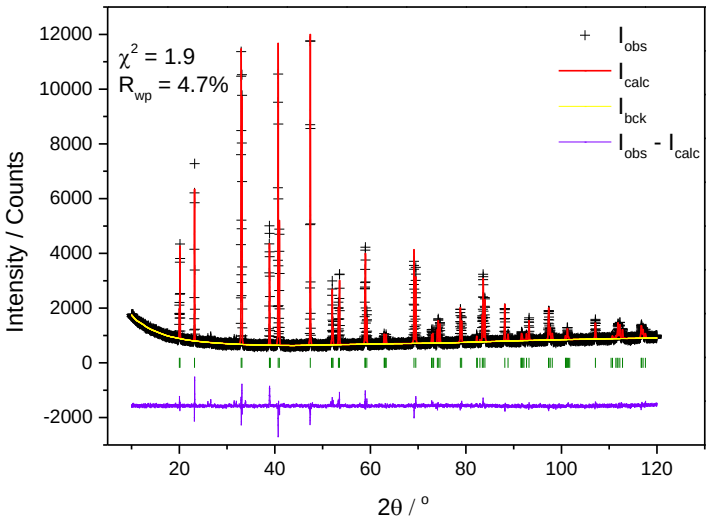

Figure 3.4 Rietveld refinement for $CoNi_2Sn_2S_2$ using X-ray diffraction data. Observed (black crosses), refined (red solid lines) and difference (blue bottom line) profiles. Reflection positions are marked by olive lines.

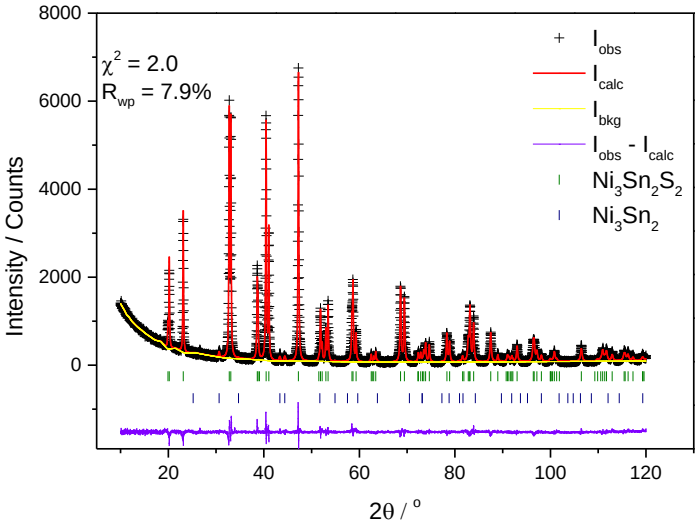

Figure 3.5 Rietveld refinement for $Ni_3Sn_2S_2$ using X-ray diffraction data. Observed (black crosses), refined (red solid lines) and difference (blue bottom line) profiles. Olive markers correspond to the $Ni_3Sn_2S_2$ phase, while navy markers denoted Ni_3Sn_2 present in trace amounts (~ 1.3 wt %).

The refined lattice parameters (Figure 3.6) reveal that the substitution of cobalt by nickel causes an increase of *ca*. 1.9 % in the lattice parameter, *a*, corresponding to an expansion of the kagome lattice, whilst the *c* lattice parameter is not affected greatly by substitution, exhibiting a broad weak maximum at x = 2.5.

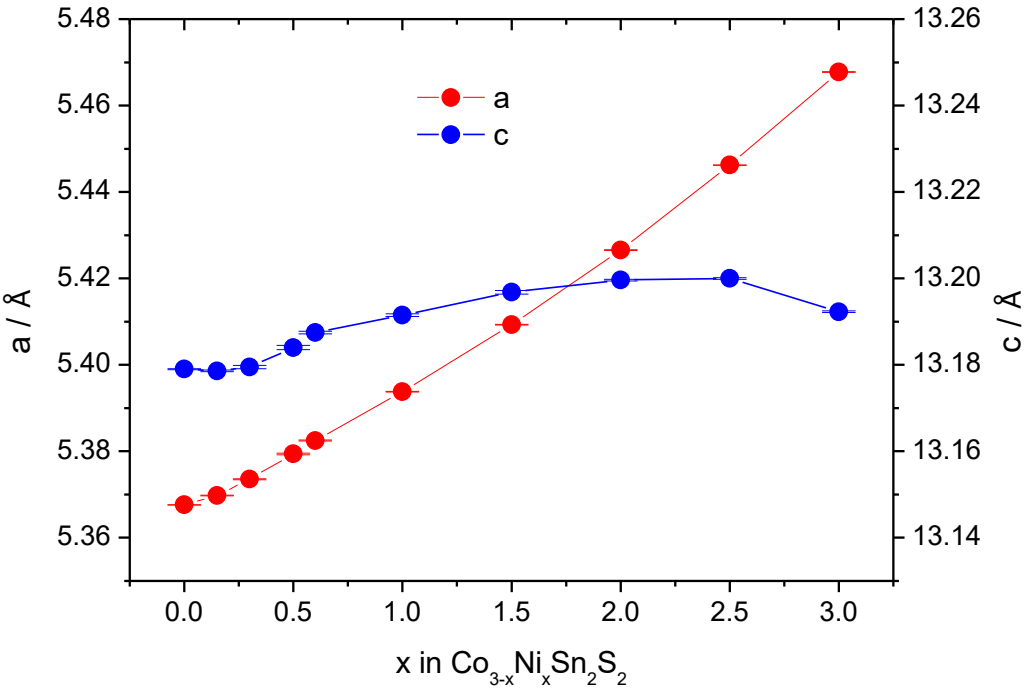

Figure 3.6 Lattice parameters determined by powder X-ray diffraction, for the series $Co_{3-x}Ni_xSn_2S_2$ ($0 \leq x \leq 3$).

3.3.1.2 Powder X-ray diffraction for $Co_{3-x}Fe_xSn_2S_2$ ($0 \leq x \leq 0.7$)

X-ray diffraction data for the series $Co_{3-x}Fe_xSn_2S_2$ reveal that the single phase region extends only to x = 0.6 (Figure 3.7), with impurities of SnS and FeS being identified at higher level of substitution (x = 0.7). In Figures 3.8 and 3.9, the patterns of Rietveld refinements are presented for two representative compositions (x = 0.3, 0.6). The remaining patterns are illustrated in Appendix C. In this case, the structural model provides a good description ($1.1 \leq \chi^2 \leq 1.7$, $2.5 \leq R_{wp}$ / % ≤ 3) of the experimental profiles.

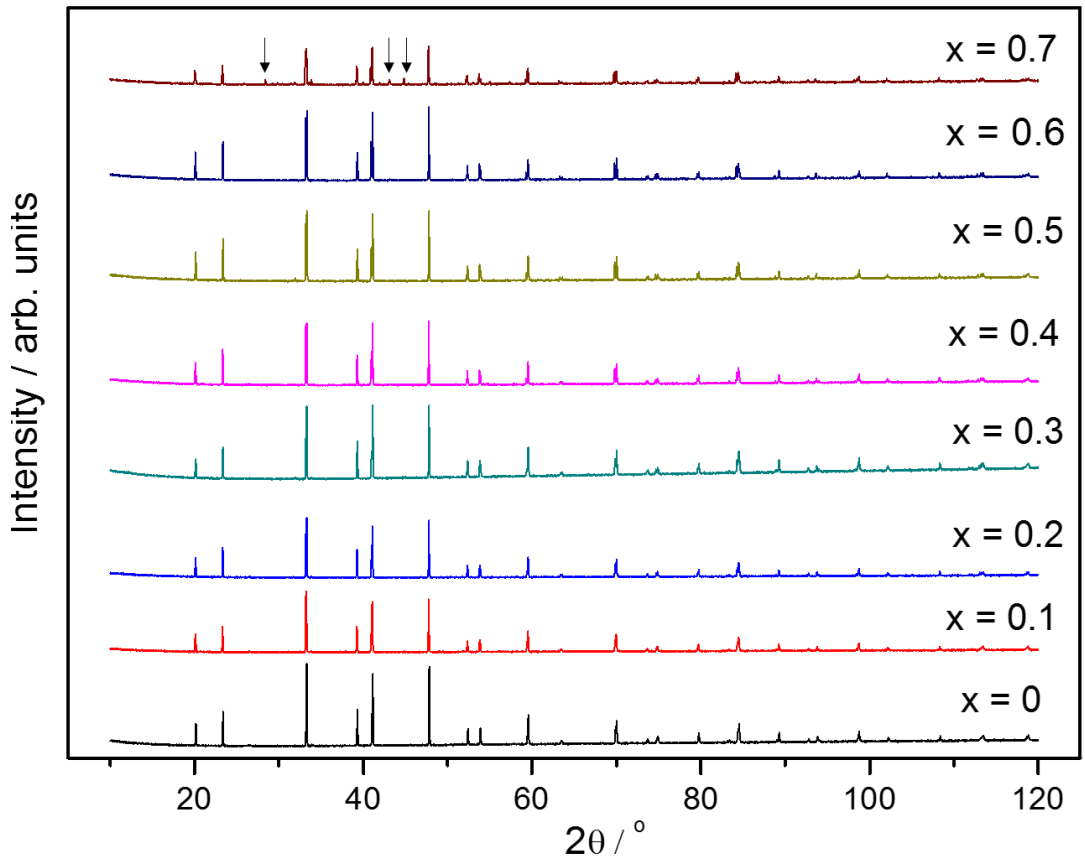

Figure 3.7 Powder X-ray diffraction data for $Co_{3-x}Fe_xSn_2S_2$ ($0 \leq x \leq 0.7$) over the range $10 \leq 2\theta / ° \leq 120$. The arrows show the impurity peaks on the pattern of x = 0.7.

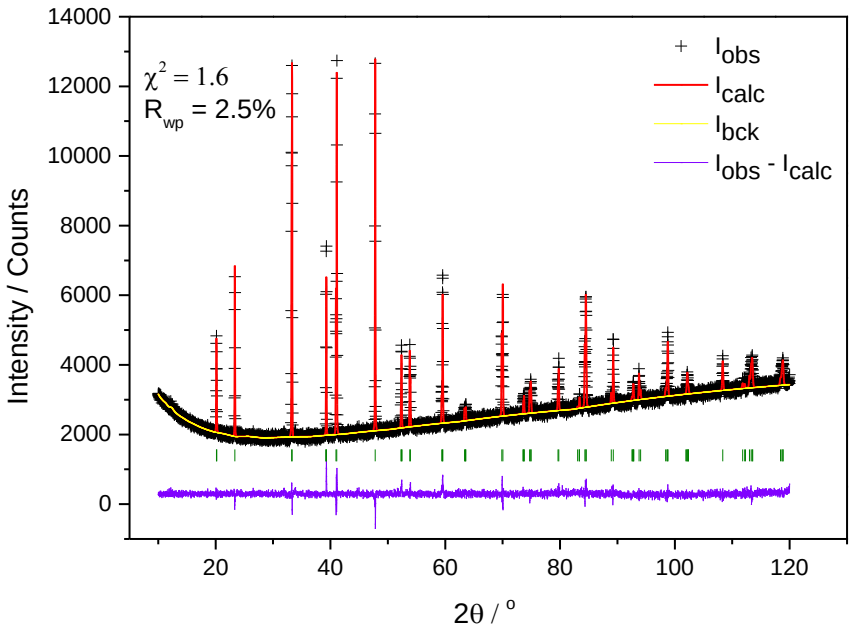

Figure 3.8 Rietveld refinement for $Co_{2.7}Fe_{0.3}Sn_2S_2$ using X-ray diffraction data. Observed (black crosses), refined (red solid lines) and difference (blue bottom line) profiles. Reflection positions are marked by olive lines.

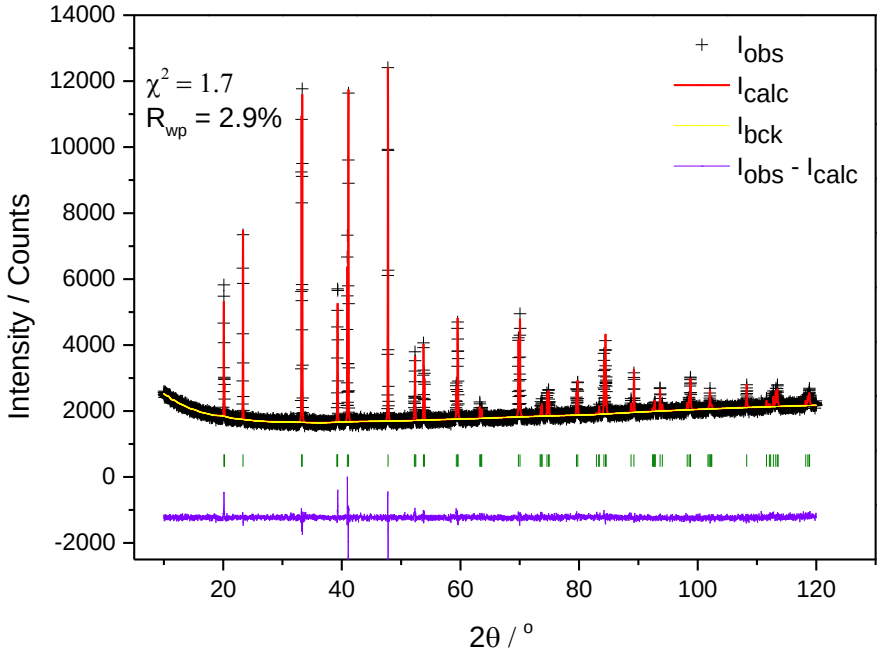

Figure 3.9 Rietveld refinement for $Co_{2.4}Fe_{0.6}Sn_2S_2$ using X-ray diffraction data. Observed (black crosses), refined (red solid lines) and difference (blue bottom line) profiles. Reflection positions are marked by olive lines.

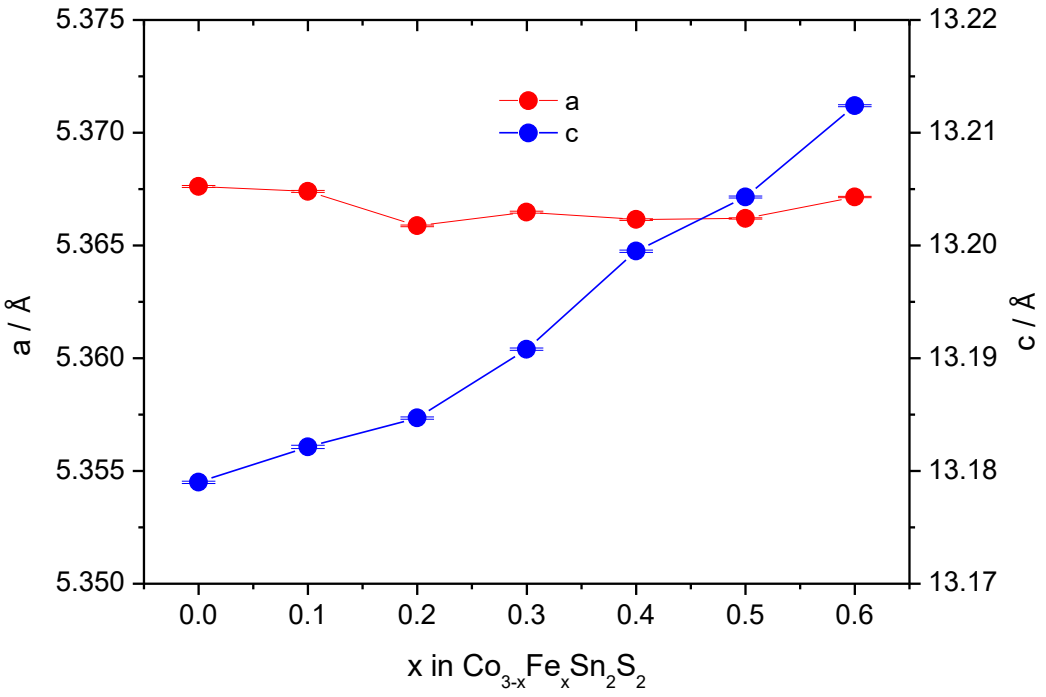

Figure 3.10 Lattice parameters determined by powder X-ray diffraction, for the series $Co_{3-x}Fe_xSn_2S_2$ ($0 \leq x \leq 0.6$).

The Rietveld analysis for the series $Co_{3-x}Fe_xSn_2S_2$ ($0 \leq x \leq 0.6$) showed that iron substitution does not affect the *a* lattice parameter, which is almost invariable with the increase of iron content, while the *c* lattice parameter exhibits a slight increase, ~ 0.3 % (Figure 3.10). The compositional dependence of lattice parameters is comparable to that in single crystals.[102]

3.3.2 Powder Neutron diffraction

Powder neutron diffraction experiments for $Co_{3-x}Ni_xSn_2S_2$ and $Co_{3-x}Fe_xSn_2S_2$ were carried out using the GEM diffractometer at the ISIS Facility, Rutherford Appleton Laboratory. Neutron diffraction data provide good contrast between the neighbouring transition-metal atoms present (Table 2.1), enabling full structural characterization to be performed including investigation of the possibility of transition-metal ordering.

3.3.2.1 Powder neutron diffraction for $Co_{3-x}Ni_xSn_2S_2$ ($0 \leq x \leq 3$)

Powder neutron diffraction data were collected at room temperature for ten samples in the series $Co_{3-x}Ni_xSn_2S_2$ ($0 \leq x \leq 3$) and for two samples (x =1, 2) at high temperatures, up to the synthesis temperature. Multibank Rietveld refinements were conducted using the GSAS software package and data from the high-resolution bank 6 ($2\theta = 154^\circ$), bank 5 ($2\theta = 91^\circ$), bank 4 ($2\theta = 63^\circ$) and bank 3 ($2\theta = 35^\circ$). The refined lattice parameters and atomic coordinates from the X-ray data analysis were used for the initial structural model. The refinement was initiated using data from the highest resolution bank. Scale factor and background parameters were firstly refined. The background was modelled using the reciprocal interpolation function. The refinement of lattice parameters, atomic coordinates and thermal parameters followed. At the end, appropriate profile coefficients were also refined. The thermal parameters of the transition-metal atoms were constrained to be equal and site occupancy factors were fixed at their nominal values. Once convergence was achieved, data from the other banks were introduced sequentially. Each time where a new data set was added, all refined parameters were fixed. From the new detector bank, firstly the scale factor and the background were refined. The refinement of diffractometer constants DIFA and DIFC followed in order to adjust with the highest resolution bank. Subsequently, the aforementioned constants were fixed and all parameters were refined again including in the refinements the new detector bank. This procedure was repeated three times in order to include the data sets from the four detector banks. All parameters were ultimately refined simultaneously,

and convergence was achieved. The resulting multibank Rietveld refinements of the series $Co_{3-x}Ni_xSn_2S_2$ ($0 \leq x \leq 3$) are illustrated in Figures 3.11 to 3.14 and Appendix D. The low values of R_{wp} ($1.9 \leq R_{wp}$ / % ≤ 3.7) confirm the space group $R\bar{3}m$. The Rietveld analysis reveals that throughout the series $Co_{3-x}Ni_xSn_2S_2$ ($0 \leq x \leq 3$) substitution occurs in a disordered fashion, with no ordering of cobalt and nickel atoms being observed. The structural model is described by 4 independent crystallographic atomic positions (Table 3.1). The refined lattice parameters and *z* atomic coordinate of sulphur atom are presented in Table 3.2, while the refined isotropic thermal parameters are presented in Table 3.3. Table 3.4 presents selected bond lengths and angles.

Table 3.1 Atomic coordinates of $M_3Sn_2S_2$ (*M* : transition metal atom).

Atom	**Wyckoff Site**	**x**	**y**	**z**
Sn(1)	3(a)	0	0	0
Sn(2)	3(b)	0	0	0.5
M	9(d)	0.5	0	0.5
S	6(c)	0	0	Table 3.2

Table 3.2 Refined lattice parameters, *z* atomic coordinate of S and the calculated volume of the unit cell for the series $Co_{3-x}Ni_xSn_2S_2$ ($0 \leq x \leq 3$).

x	**a /Å**	**c/Å**	**S(z)**	**V/ Å^3**
0	5.37235(4)	13.1972(2)	0.28324(5)	329.869(3)
0.333	5.37543(4)	13.1878(2)	0.28350(6)	330.012(3)
0.666	5.38523(5)	13.1931(2)	0.28347(6)	331.349(2)
1	5.39455(4)	13.1949(2)	0.28353(7)	332.541(2)
1.333	5.40490(3)	13.2012(1)	0.28332(6)	333.979(2)
1.666	5.41405(3)	13.1963(1)	0.28320(7)	334.988(4)
2	5.42703(2)	13.20538(9)	0.28288(7)	336.827(2)
2.333	5.43886(2)	13.20156(8)	0.28254(7)	338.198(2)
2.666	5.45074(2)	13.19735(9)	0.28221(9)	339.569(2)
3	5.47088(2)	13.20904(8)	0.28217(8)	342.386(2)

Table 3.3 Refined isotropic thermal parameters for the series $Co_{3-x}Ni_xSn_2S_2$ ($0 \leq x \leq 3$).

x	*M*[a] Uiso/Å²	Sn(1) Uiso /Å²	Sn(2) Uiso /Å²	S Uiso /Å²
0	0.523(8)	0.54(3)	0.60(3)	0.42(2)
0.333	0.608(7)	0.66(3)	0.72(3)	0.48(2)
0.666	0.743(5)	0.81(3)	0.89(3)	0.60(2)
1	0.793(6)	0.88(4)	0.89(4)	0.60(2)
1.333	0.809(5)	1.00(3)	0.83(3)	0.64(2)
1.666	0.857(4)	1.03(2)	0.91(2)	0.69(2
2	0.905(5)	1.04(2)	0.94(2)	0.69(2)
2.333	0.898(4)	1.01(2)	0.96(2)	0.68(2)
2.666	0.929(5)	1.03(2)	0.95(2)	0.67(2)
3	0.957(5)	0.96(2)	0.97(2)	0.68(2)

[a] where *M* represents the transition-metal site containing a mixture of cobalt and nickel.

Table 3.4 Selected bond distances and angles from powder neutron diffraction refinements against powder neutron diffraction data for $Co_{3-x}Ni_xSn_2S_2$ ($0 \leq x \leq 3$).

x	*M*-*M*/Sn(2) (Å) x 6	*M*-Sn(1) (Å) x 6	*M*-Sn(1)-*M* (º) x 3
0	2.68618(2)	2.69131(3)	59.874(1)
0.333	2.68771(2)	2.69054(3)	59.931(1)
0.666	2.69261(2)	2.69289(3)	59.993(1)
1	2.69727(2)	2.69468(3)	60.064(1)
1.333	2.70245(1)	2.69728(2)	60.127(0)
1.666	2.70703(1)	2.69814(2)	60.218(0)
2	2.71352(1)	2.70154(1)	60.293(0)
2.333	2.71943(1)	2.70301(1)	60.402(0)
2.666	2.72537(1)	2.70443(1)	60.513(0)
3	2.73544(1)	2.70940(1)	60.637(0)

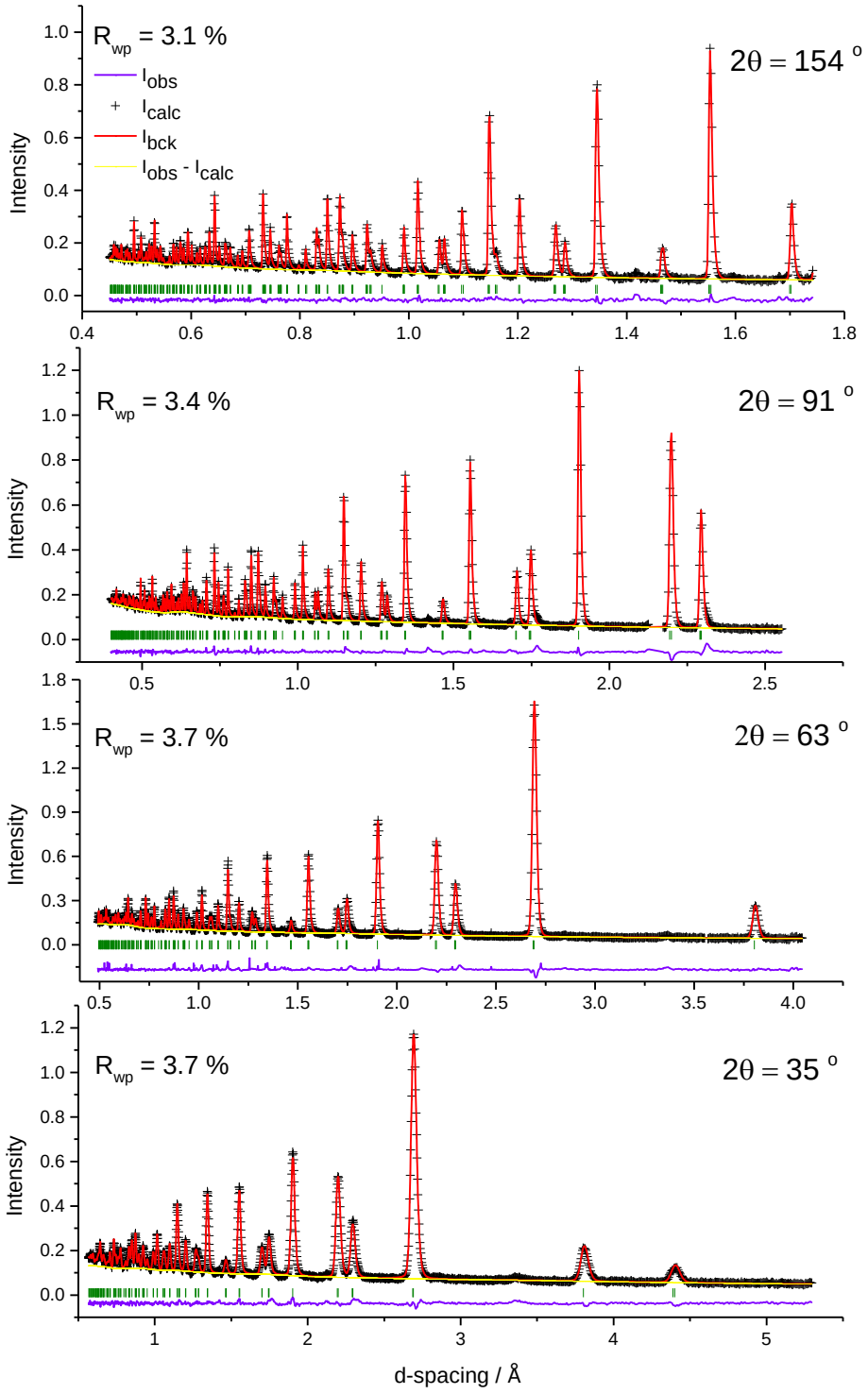

Figure 3.11 Multibank Rietveld refinement for $Co_3Sn_2S_2$ using powder neutron diffraction data collected at room temperature ($\chi^2 = 2.6$). Observed (black crosses), refined (red solid lines) and difference (blue bottom line) profiles. Reflection positions are marked by olive lines.

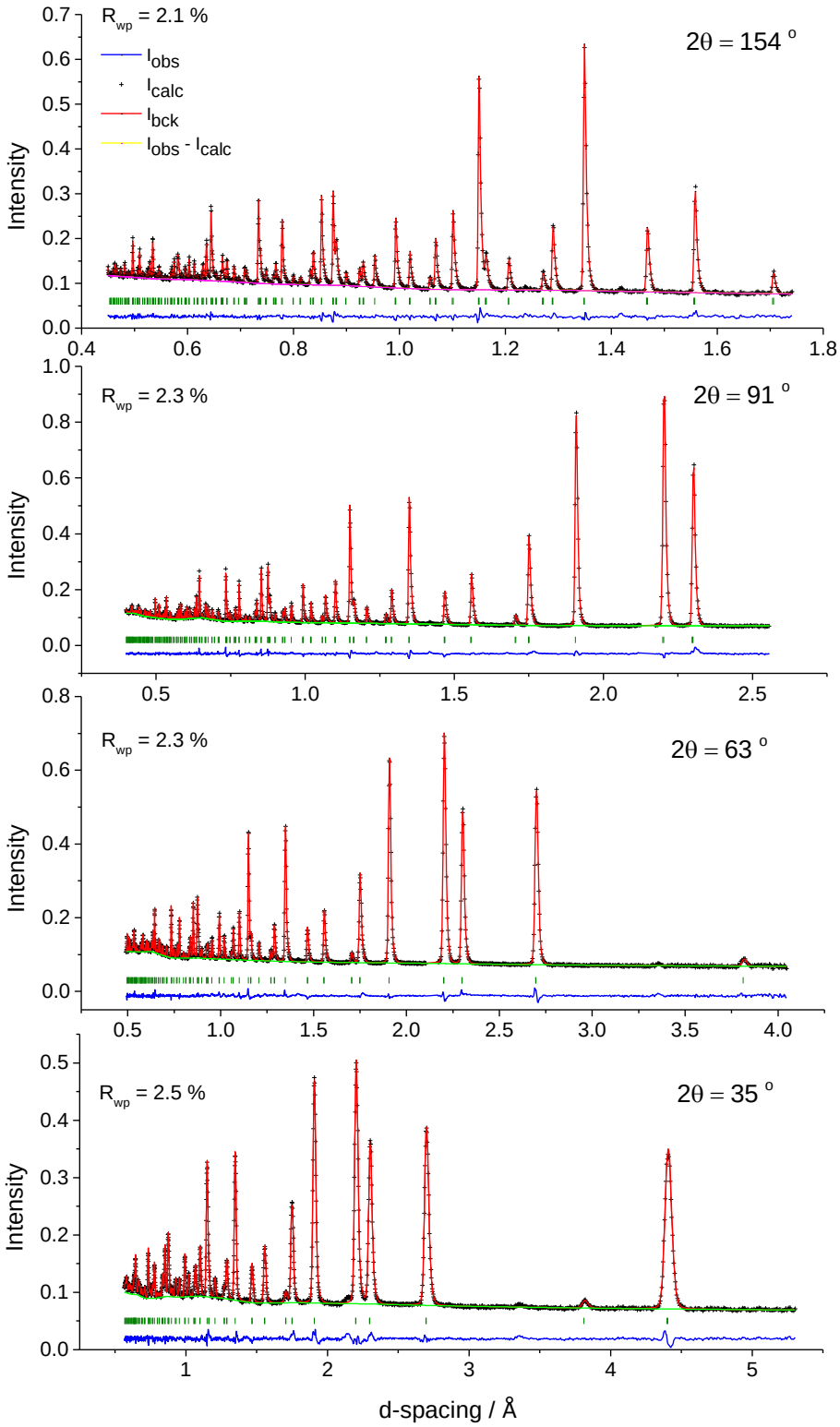

Figure 3.12 Multibank Rietveld refinement for $Co_2NiSn_2S_2$ using powder neutron diffraction data collected at room temperature (χ^2 = 2.3). Observed (black crosses), refined (red solid lines) and difference (blue bottom line) profiles. Reflection positions are marked by olive lines.

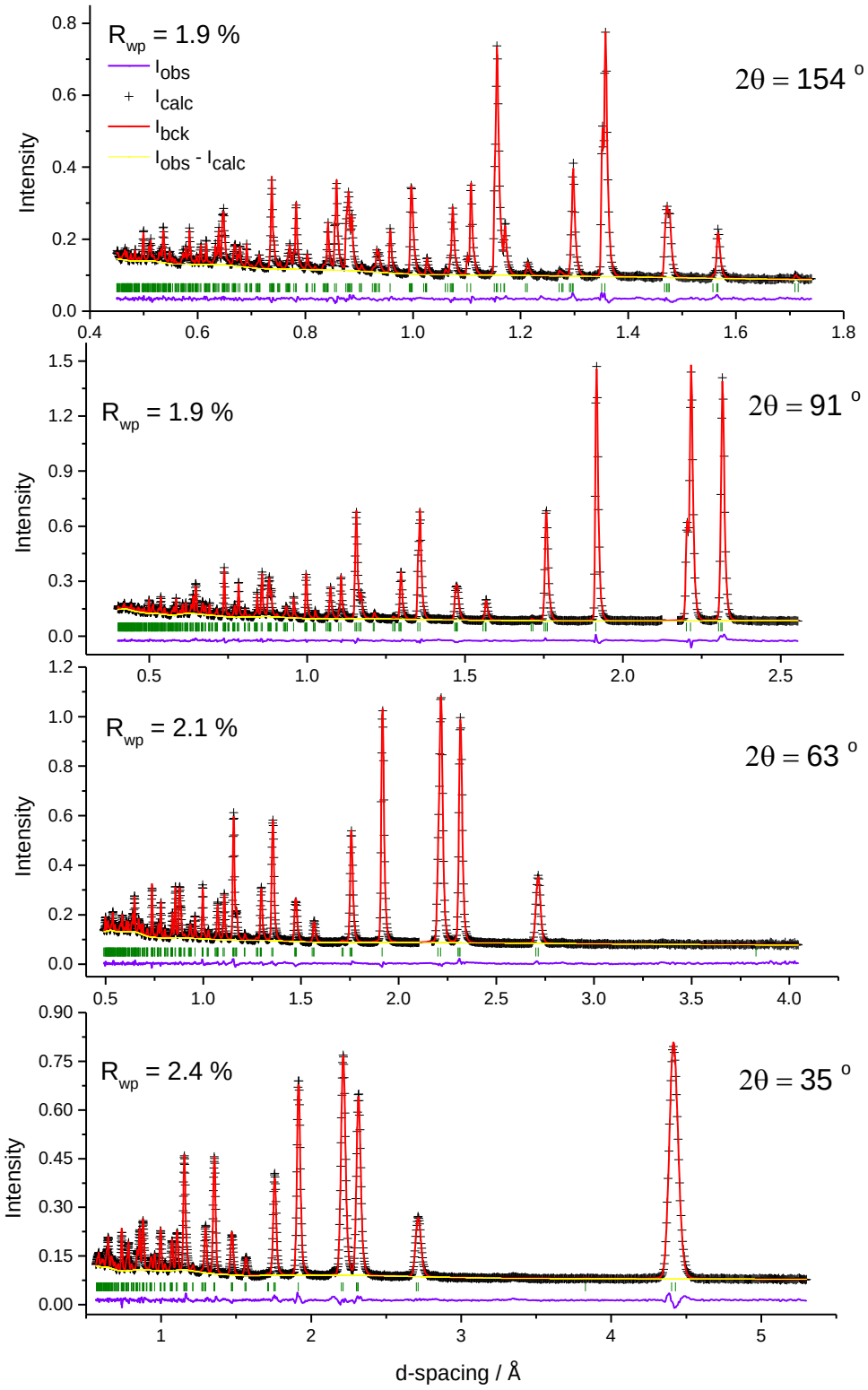

Figure 3.13 Multibank Rietveld refinement for $CoNi_2Sn_2S_2$ using powder neutron diffraction data collected at room temperature (χ^2 = 2.4). Observed (black crosses), refined (red solid lines) and difference (blue bottom line) profiles. Reflection positions are marked by olive lines.

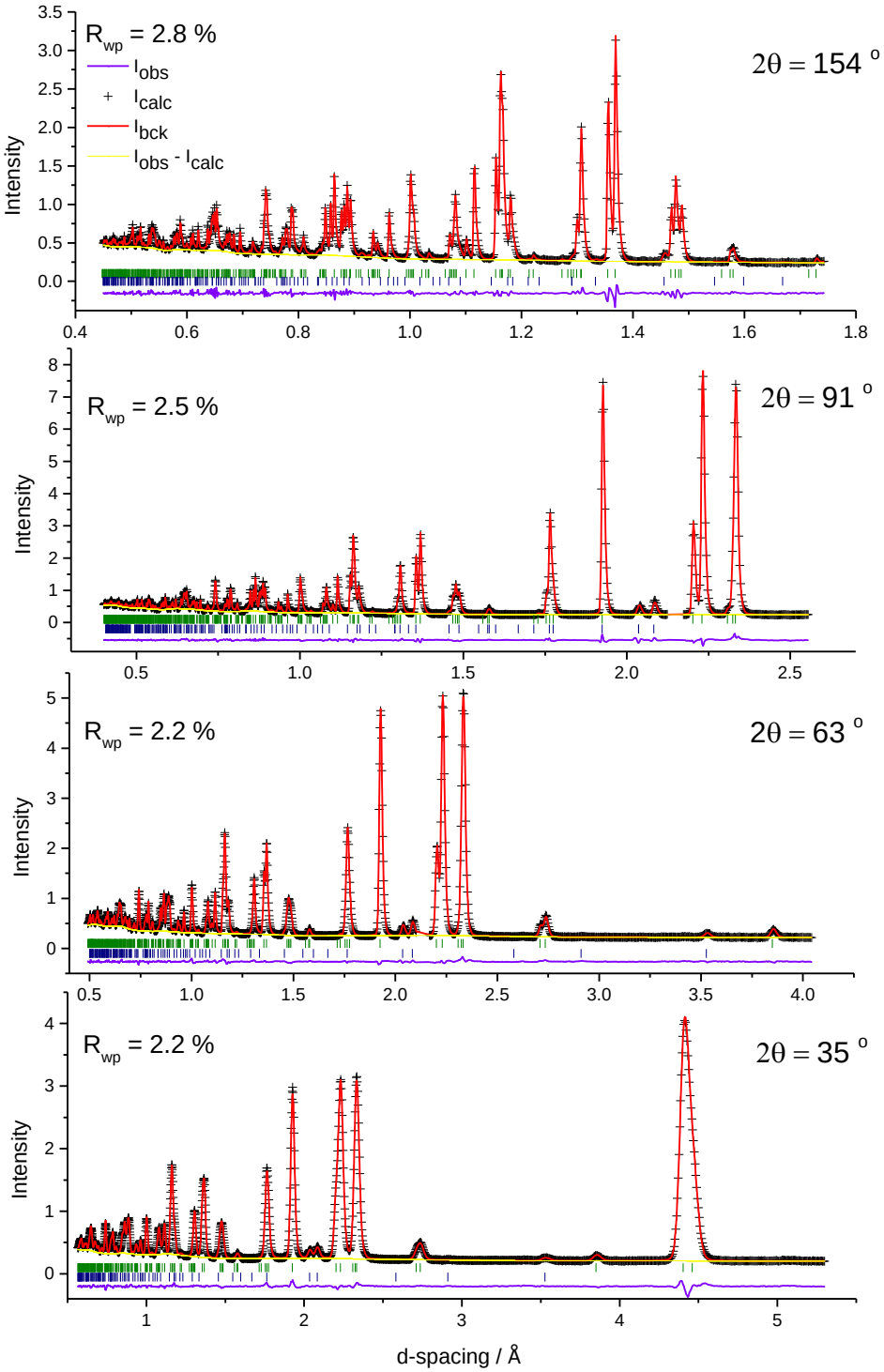

Figure 3.14 Multibank Rietveld refinement for $Ni_3Sn_2S_2$ using powder neutron diffraction data collected at room temperature (χ^2 = 6.8). Observed (black crosses), refined (red solid lines) and difference (blue bottom line) profiles. Reflection positions of $Ni_3Sn_2S_2$ phase are indicated by olive markers, while navy markers denote traces of Ni_3Sn_2 (~ 3.7 wt%).

The increase in *a* lattice parameter across the series $Co_{3-x}Ni_xSn_2S_2$ ($0 \leq x \leq 3$), mirrors the increase in the unit cell volume of *ca*. 3.8%. Moreover, the expansion of the kagome layer with increasing nickel content is clearly reflected in the increase of the intralayer *M*–*M* and *M*–Sn(2) distances. A simultaneous increase of *M*–Sn(1)–*M* angles with Ni content - where the two transition metal (*M*) atoms are located in the same layer - also results from the expansion of the kagome layer. A similar trend is also observed in the interlayer *M*–Sn(1) distances.

The substitution of cobalt by nickel increases the electron count by three electrons across the series. As discussed in Section 3.1, E_F crosses the half-occupied 24th band which is of mainly Co 3*d* character.[93] According to recent DFT calculations for In substitution,[100] at energies just above E_F, the main contribution to the electronic DOS in the end-member phase $Co_3Sn_2S_2$ arises from Co-based d_{xy} and $d_{x^2-y^2}$ orbitals. These states contribute primarily to the in-plane interactions. Previous investigations[100] suggest that these interactions have anti-bonding character. The increased electron count throughout the series results in the progressive filling of the 24th and 25th bands, consistent with the DOS calculations of $Ni_3Sn_2S_2$ by Gütlich et al.,[97] which confirm that the *d*-orbitals in the other end-member phase $Ni_3Sn_2S_2$ are fully occupied. The addition of electrons to $d_{xy}/d_{x^2-y^2}$ states increases the antibonding character of *M*–Sn(2) interactions, thereby weakening the bonds within the kagome layers, leading to the observed increase in *a* lattice parameter and increase in bond distances *M*–*M*/Sn(2) (Table 3.4).

The analysis of neutron diffraction data of two samples, $Co_2NiSn_2S_2$ and $CoNi_2Sn_2S_2$, as a function of temperature demonstrates that the disordered arrangement of transition-metal atoms which was observed at room temperature remains. No structural phase transition or degradation of the samples occur and the structures continue to be well described in the space group $R\bar{3}m$ up to their synthesis temperature. In Figures 3.15 to 3.18, neutron diffraction data of $Co_2NiSn_2S_2$ collected by the four detector banks are presented as a function of temperature. The shift of the peaks to higher values of d-space with the increase of temperature reflects the thermal expansion of the unit cell. The increase of lattice parameters with the rise of temperature (Figure 3.19) results in a volume increase of *ca.* 4%. The neutron diffraction data and refined lattice parameters as a function of temperature for $CoNi_2Sn_2S_2$ are presented in Appendix E. Up to 873 K, an increase of *ca.* 3% is observed in its unit cell volume.

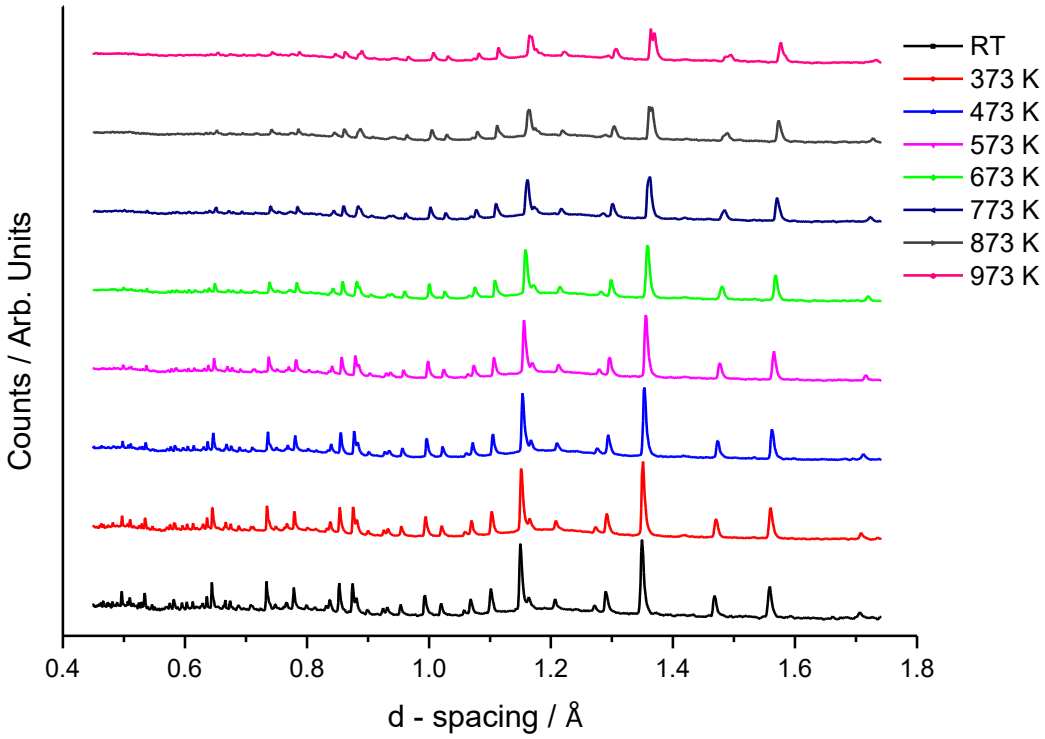

Figure 3.15 Neutron diffraction data of $Co_2NiSn_2S_2$ from bank 6 of 154˚ at elevated temperatures.

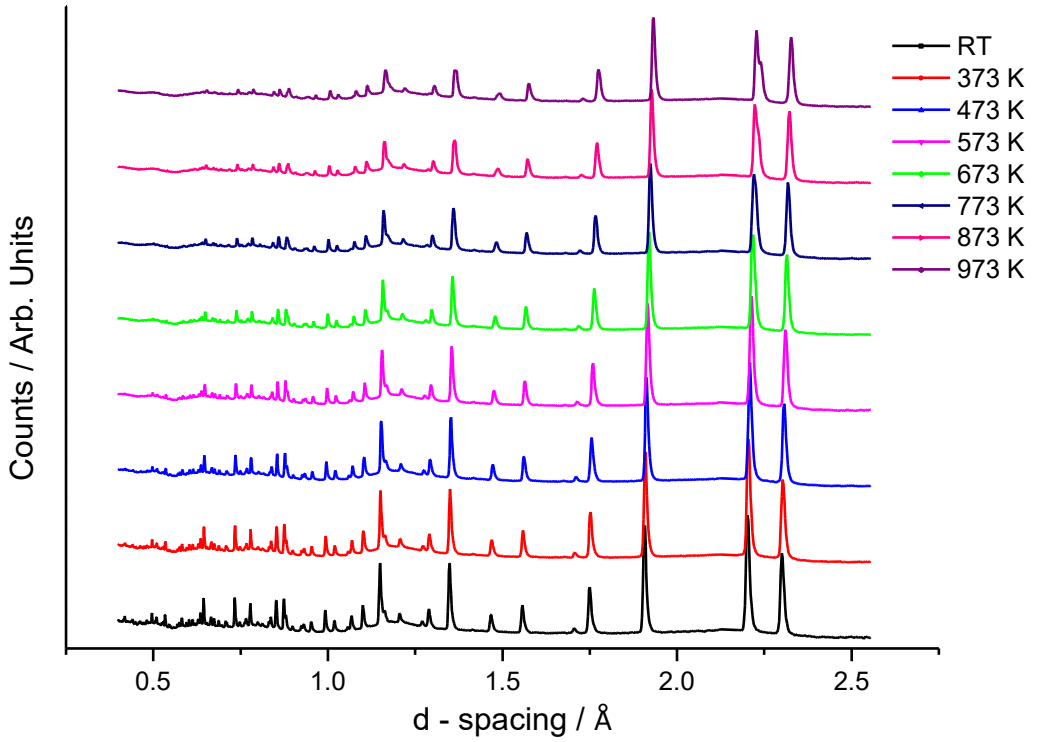

Figure 3.16 Neutron diffraction data of $Co_2NiSn_2S_2$ from bank 5 of 91˚ at elevated temperatures.

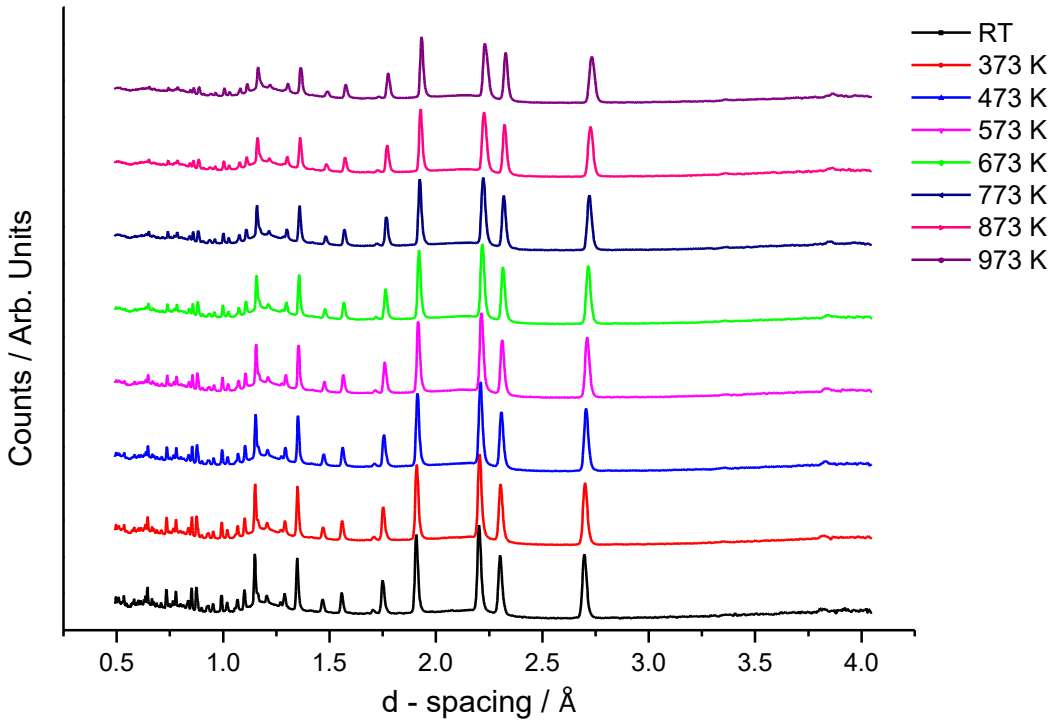

Figure 3.17 Neutron diffraction data of $Co_2NiSn_2S_2$ from bank 4 of 63˚ at elevated temperatures.

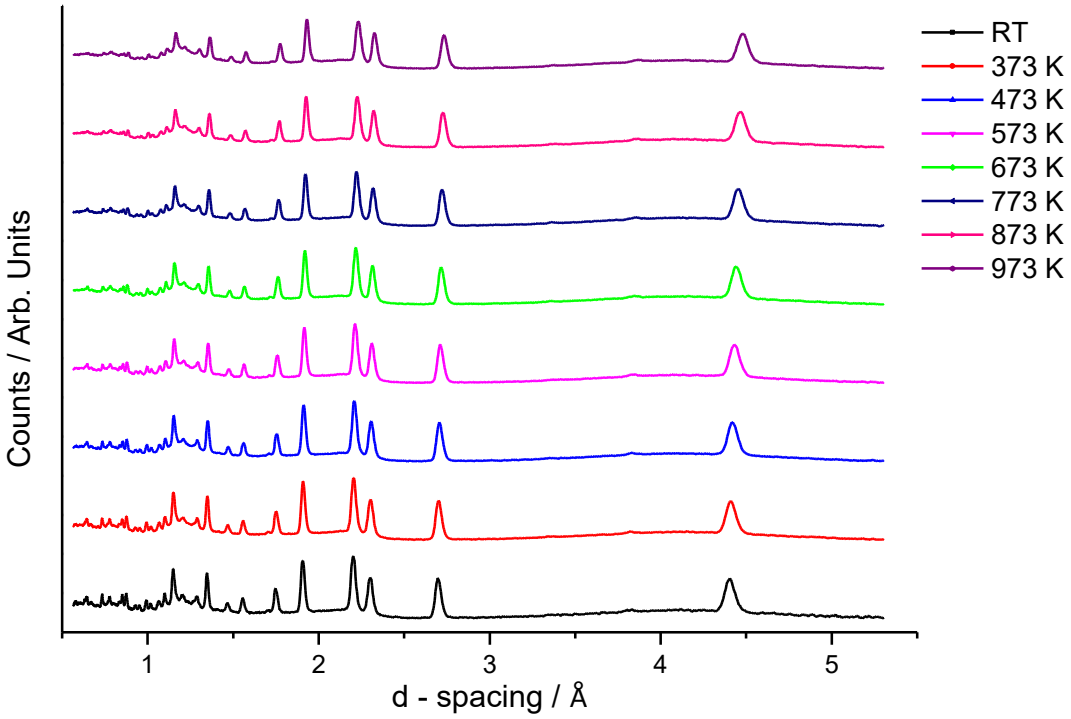

Figure 3.18 Neutron diffraction data of $Co_2NiSn_2S_2$ from bank 3 of 35˚ at elevated temperatures.

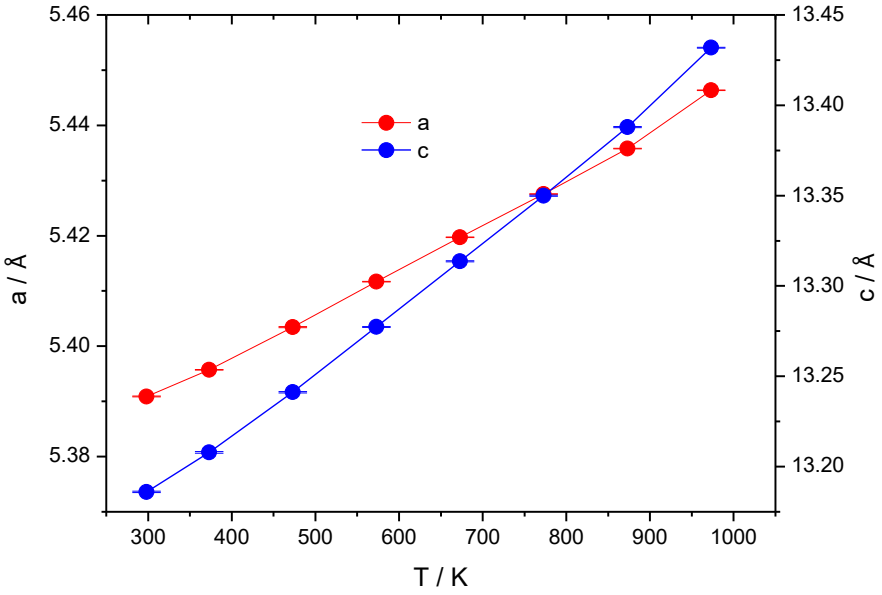

Figure 3.19 Lattice parameters of $Co_2NiSn_2S_2$ as a function of temperature.

3.3.2.2 Powder neutron diffraction for $Co_{3-x}Fe_xSn_2S_2$ ($0 \leq x \leq 0.6$)

Powder neutron diffraction data were collected at room temperature for two iron substituted samples (x = 0.3, 0.6) using the GEM Xpress service. Multibank Rietveld refinements were conducted using the GSAS software package and data from the bank 5 (2θ = 91˚), bank 4 (2θ = 63˚).and bank 3 (2θ = 35˚). The refinement process was analogous to that outlined in Section 3.3.2.1, using the parameters obtained by the refinements from X-ray diffraction data for the initial structural model. The multibank Rietveld refinements of $Co_{2.7}Fe_{0.3}Sn_2S_2$ and $Co_{2.4}Fe_{0.6}Sn_2S_2$ are presented in Figures 3.20 and 3.21 respectively. For both refinements, convergence was achieved after the simultaneous refinement of all parameters identified in Section 3.3.2.1. The values of R_{wp} (5.6 % ≤ R_{wp} ≤ 8.4 %) and χ^2 (1.1) indicate a good agreement of the structural model with the experimental profiles. A trace amount of FeS (< 1%) which was not evident in the powder X-ray diffraction data, was revealed by neutron diffraction.

The Rietveld refinements of two iron substituted samples indicate a fully disordered fashion at the transition metal site. The refined lattice parameters of the unit cell and *z* atomic coordinate of sulphur atom for materials in the series $Co_{3-x}Fe_xSn_2S_2$ ($0 \leq x \leq 0.6$) are presented in Table 3.5. The refined isotropic thermal parameters are presented in Table 3.6, while Table 3.7 presents selected bond lengths and angles. In the series $Co_{3-x}Fe_xSn_2S_2$ ($0 \leq x \leq 0.6$), the decrease in *a* lattice parameter is offset by the increase in *c* lattice parameter. As a result, there are not great differences in the volume of the

unit cell. $Co_{2.4}Fe_{0.6}Sn_2S_2$ exhibits the longest *M*-Sn(1) bond distance, reflecting the slightly increased spacing between the kagome sheets.

Table 3.5 Refined lattice parameters, *z* atomic coordinate of S and the calculated volume of the unit cell for $Co_{3-x}Fe_xSn_2S_2$ ($0 \leq x \leq 0.6$).

x	a /Å	c/Å	S(z)	V/ Å^3
0	5.37235(4)	13.1972(2)	0.28324(5)	329.869(3)
0.3	5.36605(7)	13.1961(4)	0.2826(1)	329.069(6)
0.6	5.36602(6)	13.2122(3)	0.2823(1)	329.467(6)

Table 3.6 Refined isotropic thermal parameters for $Co_{3-x}Fe_xSn_2S_2$ ($0 \leq x \leq 0.6$).

x	*M* Uiso/Å^2	Sn(1) Uiso /Å^2	Sn(2) Uiso /Å^2	S Uiso /Å^2
0	0.523(8)	0.54(3)	0.60(3)	0.42(2)
0.3	0.46(1)	0.31(4)	0.37(5)	0.31(3)
0.6	0.47(1)	0.39(1)	0.24(1)	0.22(3)

Table 3.7 Selected bond lengths and angles from powder neutron diffraction refinements of $Co_{3-x}Fe_xSn_2S_2$ ($0 \leq x \leq 0.6$).

x	*M*-*M*/Sn(2) (Å) x 6	*M*-Sn(1) (Å) x 6	*M*-Sn(1)-*M* (º) x 3
0	2.68618(2)	2.69131(3)	59.874(1)
0.3	2.68303(3)	2.69011(5)	59.826(1)
0.6	2.68301(3)	2.69230(4)	59.772(1)

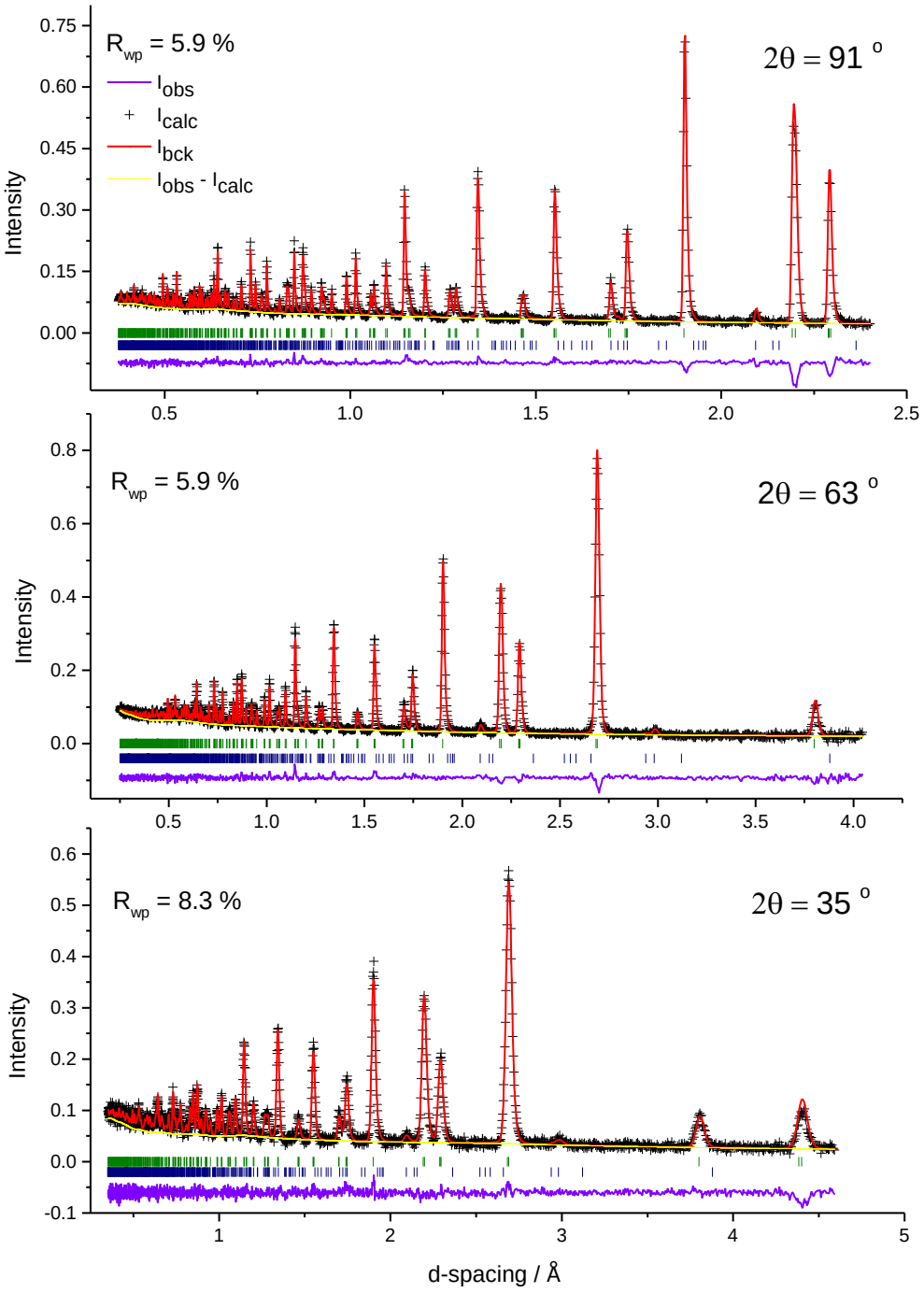

Figure 3.20 Multibank Rietveld refinement for $Co_{2.7}Fe_{0.3}Sn_2S_2$ using powder neutron diffraction data collected at room temperature (χ^2 = 1.1). Observed (black crosses), refined (red solid lines) and difference (blue bottom line) profiles. Reflection positions of shandite phase are indicated by olive markers, while FeS (~ 0.6 wt %) is indicated by navy markers.

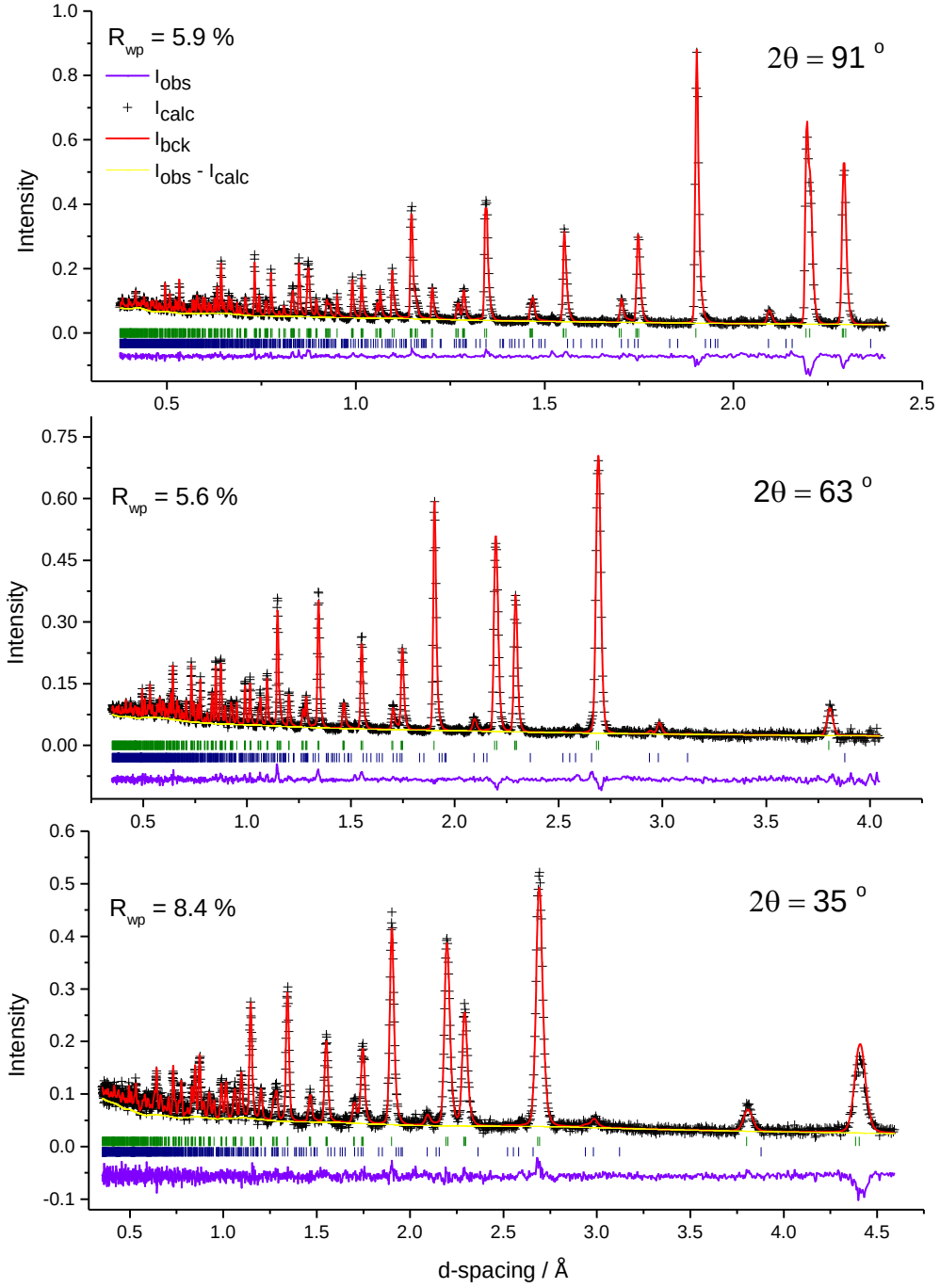

Figure 3.21 Multibank Rietveld refinement for $Co_{2.4}Fe_{0.6}Sn_2S_2$ using powder neutron diffraction data collected at room temperature (χ^2 = 1.1). Observed (black crosses), refined (red solid lines) and difference (blue bottom line) profiles. Reflection positions of the shandite phase are indicated by olive markers, while FeS (~ 0.9 wt %) is indicated by navy markers.

3.4 Mössbauer Spectroscopy in $Co_{3-x}Fe_xSn_2S_2$ ($0 \leq x \leq 0.6$)

^{119}Sn and ^{57}Fe Mössbauer data were collected on six powdered samples of $Co_{3-x}Fe_xSn_2S_2$ ($0 \leq x \leq 0.6$) at the University of Montpellier by Professor Jean-Claude Jumas. The techniques for both ^{119}Sn and ^{57}Fe Mössbauer experiments are described in Section 2.8.

3.4.1 ^{119}Sn Mössbauer Spectroscopy

^{119}Sn Mössbauer measurements of all six iron-substituted samples show the same peak doublet consisting of two broad peaks of comparable intensity (Figure 3.22 and Appendix F). The peaks were fitted using a least squares process and a Lorentzian peak shape. The doublet has two components associated with the two tin crystallographic sites in the structure. The assignment of the signal to each site was made on the basis of isomer shift values (δ).

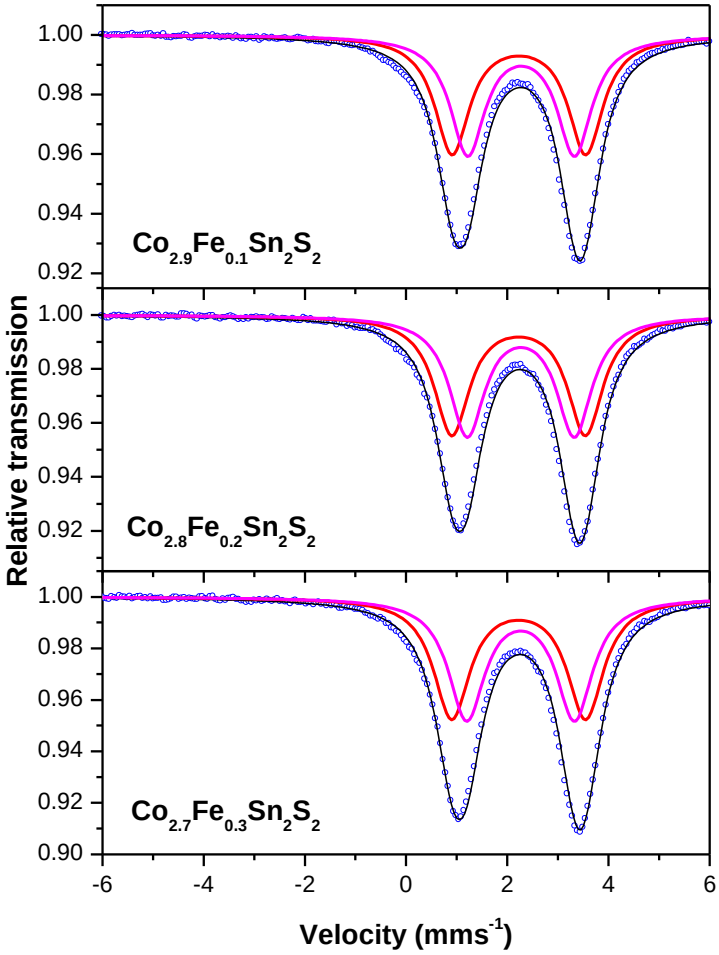

Figure 3.22 ^{119}Sn Mössbauer spectroscopy data collected at room temperature for the samples $Co_{3-x}Fe_xSn_2S_2$ ($0.1 \leq x \leq 0.3$).

Data from all ^{119}Sn Mössbauer measurements are presented in Table 3.8. The fitted peak with the largest quadrupole splitting is attributed to the Sn(2) atoms at the intralayer kagome site as this has the most distorted crystallographic environment, while the smaller quadrupole splitting values are assigned to Sn(1) trigonal antiprismatic interlayer sites. The values of the isomer shift (δ) for the Sn(2) site for all iron-substituted samples lie in a narrow range between 2.11 and 2.13 mm s^{-1}, while those of interlayer Sn(1) site lie between 2.16 and 2.18 mm s^{-1}. These values are comparable to those reported for tin alloys and intermetallics such as α-Sn^0 (2.1 mm s^{-1}), Sn^0Mg_2 (δ = 1.8 mm s^{-1}) and β-Sn^0 (2.6 mm s^{-1}).[105] Moreover, no change is observed in the isomer shift values of both tin sites with those of Co-end-member phase reported by Corps et al..[100] These observations drive to the conclusion that iron substitution does not affect the local electronic structure of two tin sites, which retain their low oxidation state, tending toward zero.

Table 3.8 Isomer Shifts (δ), Quadropole Splitting (Δ), Line Width (Γ) for ^{119}Sn Mössbauer spectroscopy of $Co_{3-x}Fe_xSn_2S_2$ ($0 < x \leq 0.6$).

X	*δ (mm/s)*	*Δ (mm/s)*	*Γ (mm/s)*	*Contribution (%)*	*Assignement (%)*
0.1	2.13 (1)	2.64 (2)	0.83 (1)	50	Sn(2)
	2.18 (1)	2.10 (2)	0.84 (5)	50	Sn(1)
0.2	2.12 (1)	2.64 (1)	0.85 (1)	50	Sn(2)
	2.17 (1)	2.12 (1)	0.85 (1)	50	Sn(1)
0.3	2.12 (1)	2.64 (1)	0.87 (1)	50	Sn(2)
	2.16 (1)	2.13 (1)	0.87 (1)	50	Sn(1)
0.4	2.12 (1)	2.66 (1)	0.84 (1)	50	Sn(2)
	2.16 (1)	2.12 (1)	0.84 (1)	50	Sn(1)
0.5	2.12(1)	2.66 (1)	0.82 (1)	50	Sn(2)
	2.17 (1)	2.11 (1)	0.82 (1)	50	Sn(1)
0.6	2.11 (1)	2.65 (1)	0.84 (1)	50	Sn(2)
	2.16 (1)	2.11 (1)	0.84 (1)	50	Sn(1)

3.4.2 ^{57}Fe Mössbauer Spectroscopy

^{57}Fe Mössbauer spectra throughout the series $Co_{3-x}Fe_xSn_2S_2$ ($0 < x \leq 0.6$) exhibit a doublet in which the two peaks are of unequal intensity. Least squares fitting of peaks with a Lorentzian peak shape reveals that the doublet is composed of two overlapping contributions. Representative ^{57}Fe data for $Co_{3-x}Fe_xSn_2S_2$ ($0.4 < x \leq 0.6$) are presented in Figure 3.23, with the remaining spectra provided in Appendix F, while hyperfine parameters are presented in Table 3.9.

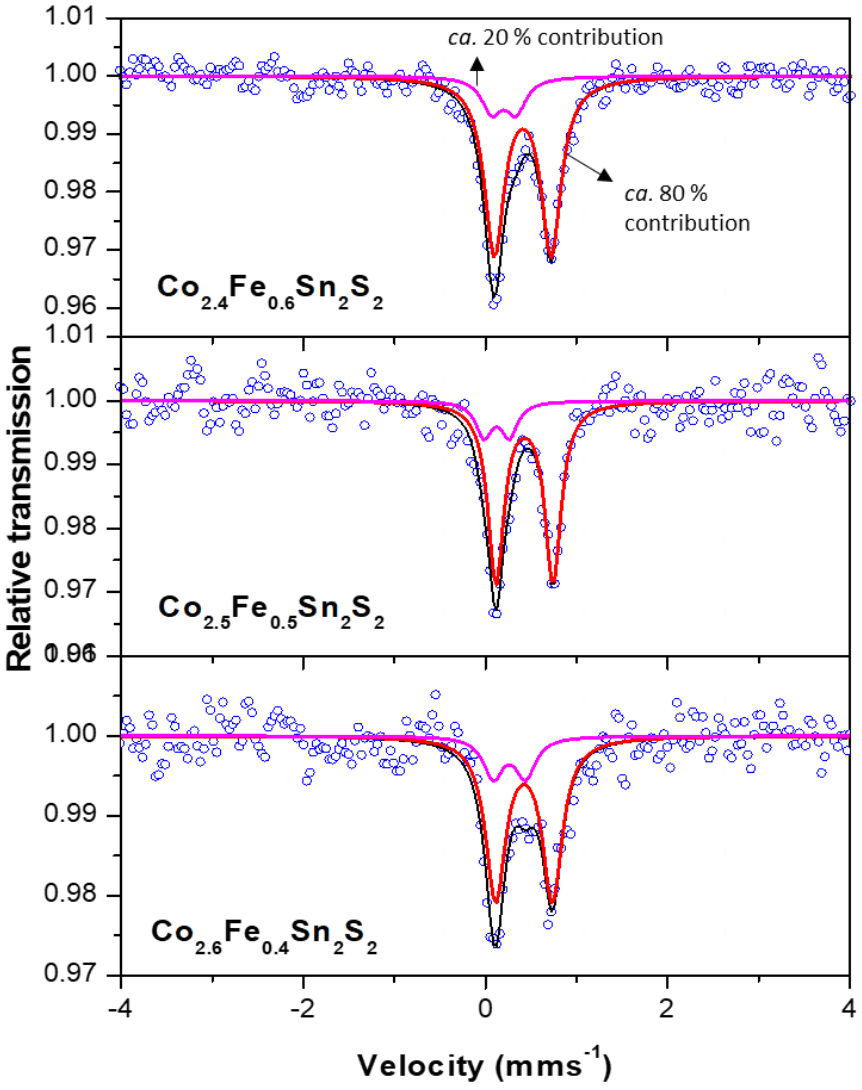

Figure 3.23 ^{57}Fe Mössbauer spectroscopy data for three samples of the series $Co_{3-x}Fe_xSn_2S_2$ ($0.4 \leq x \leq 0.6$). Points denote experimental data and the full lines signify the fit to the two overlapping doublets with contributions *ca.* 80 % and *ca.* 20 %, and the overall fit (black line).

Table 3.9 Isomer Shifts (δ), Quadropole Splitting (Δ), Line Width (Γ) and Contribution of each line to the ^{57}Fe Mössbauer Spectra of $Co_{3-x}Fe_xSn_2S_2$ ($0 < x \leq 0.6$).

X	*δ* *(mm s^{-1})*	*Δ* *(mm s^{-1})*	*Γ* *(mm s^{-1})*	*Contribution (%)*
0.1	0.41(1)	0.62(1)	0.20(5)	85
	0.13(4)	0.44(5)	0.20(5)	15
0.2	0.40 (1)	0.63 (1)	0.24 (5)	76
	0.27 (3)	0.16 (4)	0.24 (5)	24
0.3	0.44 (2)	0.62 (3)	0.28 (1)	81
	0.27 (7)	0.27 (11)	0.28 (1)	19
0.4	0.42 (3)	0.62 (5)	0.26 (9)	80
	0.26 (11)	0.35 (19)	0.26 (9)	20
0.5	0.430 (5)	0.629 (8)	0.20 (4)	84
	0.10 (3)	0.35 (4)	0.20 (4)	16
0.6	0.410 (5)	0.624 (8)	0.27 (4)	84
	0.20 (2)	0.27 (3)	0.27 (4)	16

The more intense doublet with a relative contribution of *ca*. 80 %, exhibits an isomer shift in the range 0.40 - 0.44 mm s^{-1} and a quadrupole splitting of 0.62 – 0.63 mm s^{-1}. The corresponding ranges for the weaker doublet with a contribution of *ca*. 20 % are 0.10 - 0.27 mm s^{-1} and 0.16 – 0.44 mm s^{-1} respectively. The observation of two doublets is perhaps surprising given the location of iron at a single crystallographic 9(*d*) site. The neutron diffraction data excluded the possibility for the iron atoms to occupy one of the tin sites, either 3(*a*) or 3(*b*). Furthermore, powder X-ray and neutron diffraction data did not show any impurity phases at a level that would give rise to a signal of the magnitude *ca*. 20 % for the second doublet. It is suggested here that the two doublets in the ^{57}Fe Mössbauer spectra must come from different local environments of the iron substituent. Within the kagome layers, each iron atom is surrounded by two tin and four transition-metal atoms. The powder neutron diffraction revealed that the substitution of Co by Fe occurs in a disordered fashion. This means that the transition-metal neighbours can be either cobalt or iron. Probability calculations were carried out by Prof Anthony Powell and Dr Paz Vaqueiro for the determination of local electronic environment of Fe atoms in the kagome layer (Appendix G). The calculations indicate that at low levels of substitution, the probability for an iron atom to be surrounded by

four cobalt neighbours is *ca*. 0.84. The next most likely environment, in which one of the cobalt neighbours has been replaced by an iron atom, has a probability of *ca.* 0.15. This suggests that the doublet with $\delta = 0.40 – 0.44$ mm s^{-1} corresponds to the first case where iron atoms are coordinated only by cobalt and tin atoms, whilst the weaker doublet is assigned to the second local environment with one iron neighbour. The relative probabilities for $x \leq 0.2$ are in a good agreement with the contributions of the two doublets. For $x > 2$, a deviation is observed between the calculated probabilities and the contributions of the two doublets, suggesting that the distribution of iron atoms in the kagome layer is no longer purely statistical.

The isomer shift values of the more intense doublet ($\delta = 0.40 – 0.44$ mm s^{-1}) compare favourably with that of the structurally related intermetallic, FeSn (0.41 mm s^{-1}),[106] which contains similar kagome layers to those in $Co_{3-x}Fe_xSn_2S_2$. In addition, they are close to the isomer shifts of 0.42[107] and 0.43[108] mm s^{-1} which have been reported for $KFeS_2$. These values are assigned to Fe^{3+}. The assignment of the weaker doublet is less clear since the isomer shifts for different oxidation states overlap. The low isomer shift values may be related with Fe-Fe interactions. The marcasite phase, FeS_2, exhibits comparable isomer shifts for Fe^{2+} (0.23[109] and 0.277[110] mm s^{-1}), whilst Mössbauer spectra for the ferric ions in natural single crystals of α-$CuFeS_2$[111] and the chalcopyrite-related $TlFeS_2$[112] have yielded isomer shifts of 0.24 and 0.18 mm s^{-1} respectively. Benedetto et al[113] have also reported isomer shifts in the range 0.25 – 0.30 mm s^{-1} for Fe^{3+} ions in the solid solution Cu_2FeSnS_4-Cu_2ZnSnS_4. According to the aforementioned data, a mixed Fe^{2+}/Fe^{3+} oxidation state could be possible in $Co_{3-x}Fe_xSn_2S_2$ ($0 < x \leq 0.6$). However, the principal conclusion is that iron is localized in two different electronic environments with a non-zero formal oxidation state. The previous study of Corps et al[100] concluded that in $Co_3Sn_{2-x}In_xS_2$ series, cobalt atoms exhibit a near-zero oxidation state while a slight electron transfer occurs between the main-group element and sulphur atoms. In the series $Co_{3-x}Fe_xSn_2S_2$ the tin atoms retain the near-zero oxidation state of cobalt-end-member phase, while the two sub-spectra for iron atoms suggest a non-zero, possibly mixed, oxidation state. This requires electron transfer from iron to sulphur in addition to that arising from the main-group element.

3.5 Hot-pressing

All samples of the shandite family were hot-pressed for 25 min at 60 bar and 720 ˚C according to the process which was described in Section 2.5. All samples were ball-milled at 350 rpm for 1 hour prior to consolidation. The densities of the resulting pellets

which were determined by the Archimedes method, were *ca.* 98 % of the crystallographic value.

3.6 Electrical Transport Properties

3.6.1 Electron doping in $Co_{3-x}Ni_xSn_2S_2$ ($0 \leq x \leq 3$)

3.6.1.1 Electrical Resistivity

Electrical resistivity measurements were carried out on circular pellets of samples $Co_{3-x}Ni_xSn_2S_2$ ($0 \leq x \leq 3$) over the temperature range $300 \leq T / K \leq 625$ as described in section 2.7.1.1. The results are presented as a function of temperature in Figure 3.24. The electrical resistivity for all samples in the $Co_{3-x}Ni_xSn_2S_2$ series exhibits a positive $d\rho/dT$ indicating metallic behaviour. The increase in nickel composition markedly reduces the electrical resistivity of the material, as evidenced by comparison of data collected at constant temperature (Figure 3.25). It is notable that $Ni_3Sn_2S_2$ reaches a resistivity of 0.04 mΩ cm which is almost an order of magnitude lower than the value of $Co_3Sn_2S_2$.

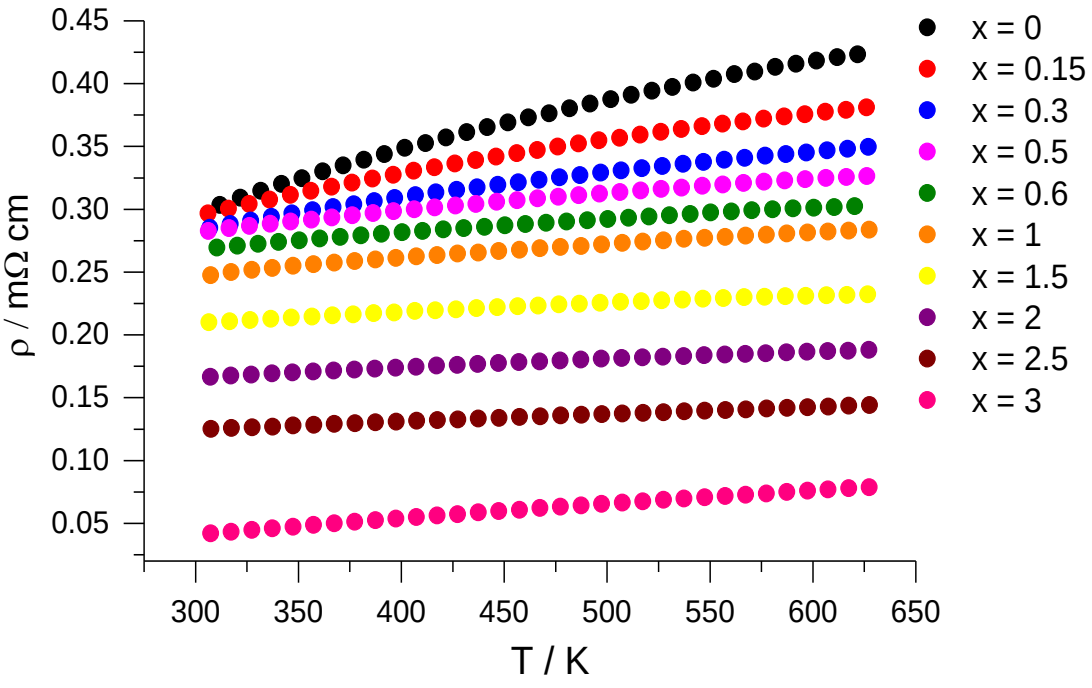

Figure 3.24 Electrical resistivity measurements as a function of temperature for $Co_{3-x}Ni_xSn_2S_2$ ($0 \leq x \leq 3$) over the temperature range $300 \leq T / K \leq 625$.

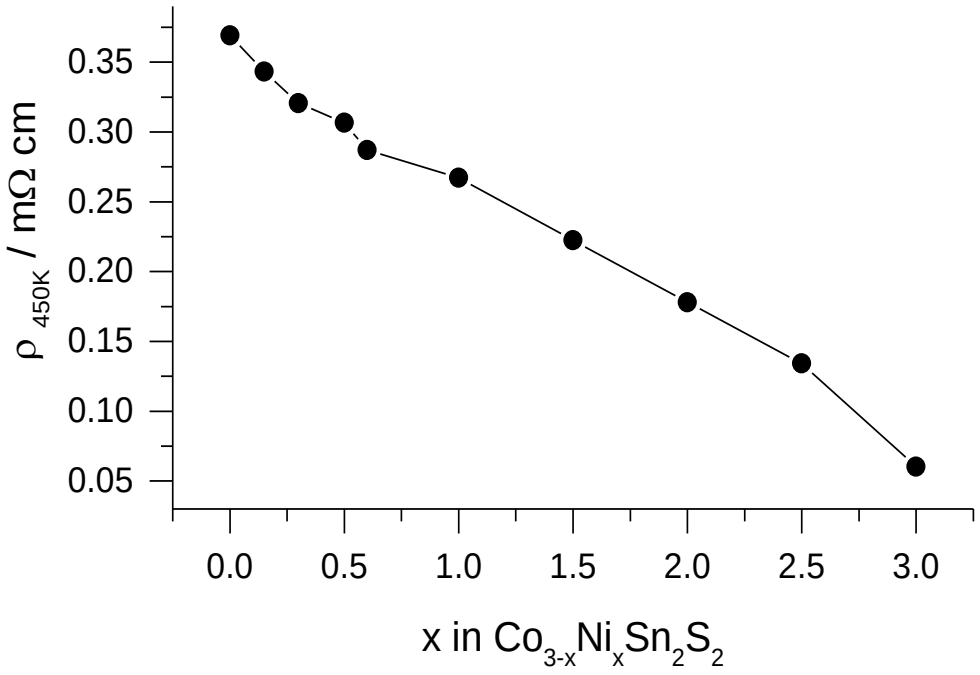

Figure 3.25 The electrical resistivity of $Co_{3-x}Ni_xSn_2S_2$ as a function of Ni composition at 450 K.

3.6.1.2 Seebeck Coefficient

Seebeck coefficient measurements for the series $Co_{3-x}Ni_xSn_2S_2$ ($0 \leq x \leq 3$) are presented in Figure 3.26. As can be observed, the values of Seebeck coefficient for all samples are negative throughout the composition range $0 \leq x \leq 3$, indicating that electrons are the main charge carriers and consequently all compositions are *n*-type materials. In addition, the absolute value of the Seebeck coefficient, $|S|$, increases almost linearly with temperature, consistent with the metallic behaviour indicated by the resistivity data. Figure 3.27 demonstrates that the absolute value of the Seebeck coefficient decreases with increasing Ni composition, exhibiting a minimum value at x = 2.5. Data are also presented for low temperature measurements (Figure 3.28) which were conducted according to the experimental procedure of Section 2.7.1.3. These measurements also show that $|S|$ is reduced with increasing Ni content, while the almost linear S(T) behaviour seen at high temperatures is continued to low temperatures for all Ni-substituted phases. The mismatch in data in the two temperature ranges is due to the use of two different instruments.

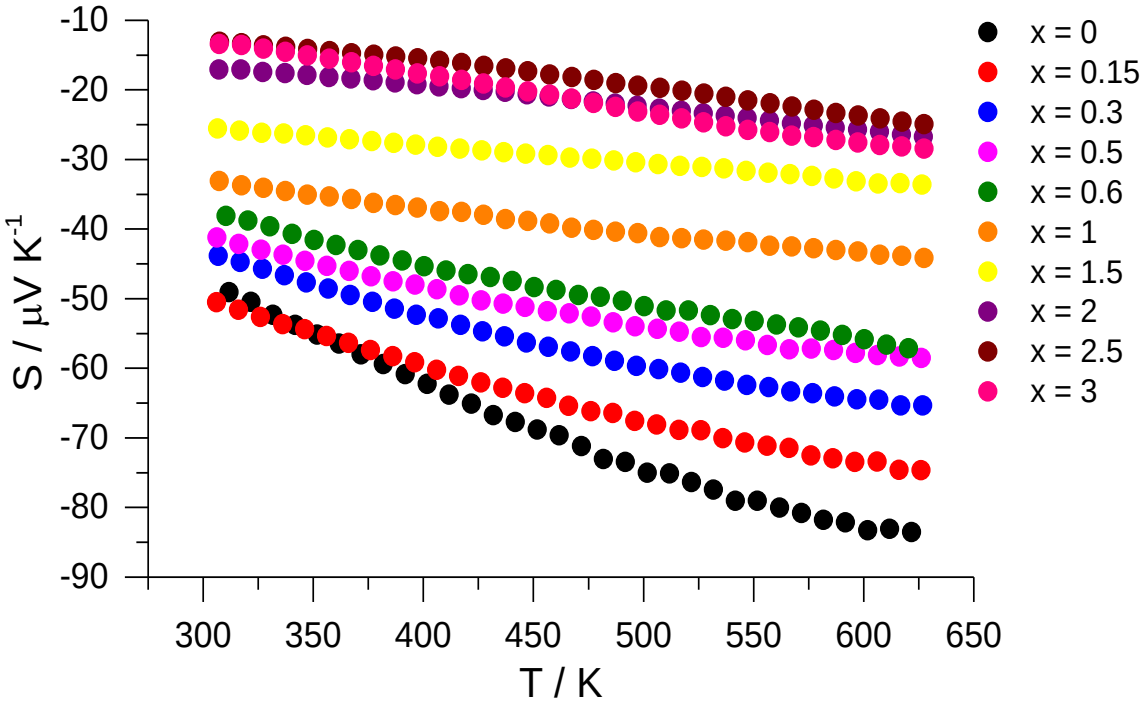

Figure 3.26 Seebeck coefficient measurements as a function of temperature for $Co_{3-x}Ni_xSn_2S_2$ ($0 \leq x \leq 3$) over the temperature range $300 \leq T / K \leq 625$.

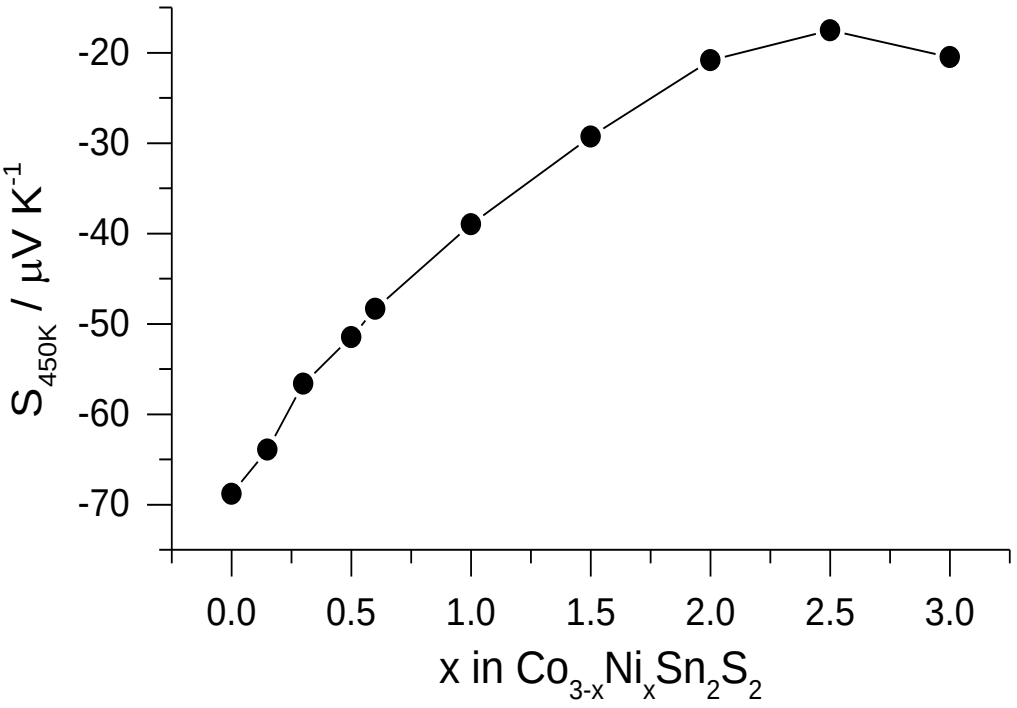

Figure 3.27 Seebeck coefficient of $Co_{3-x}Ni_xSn_2S_2$ as a function of Ni content at 450 K.

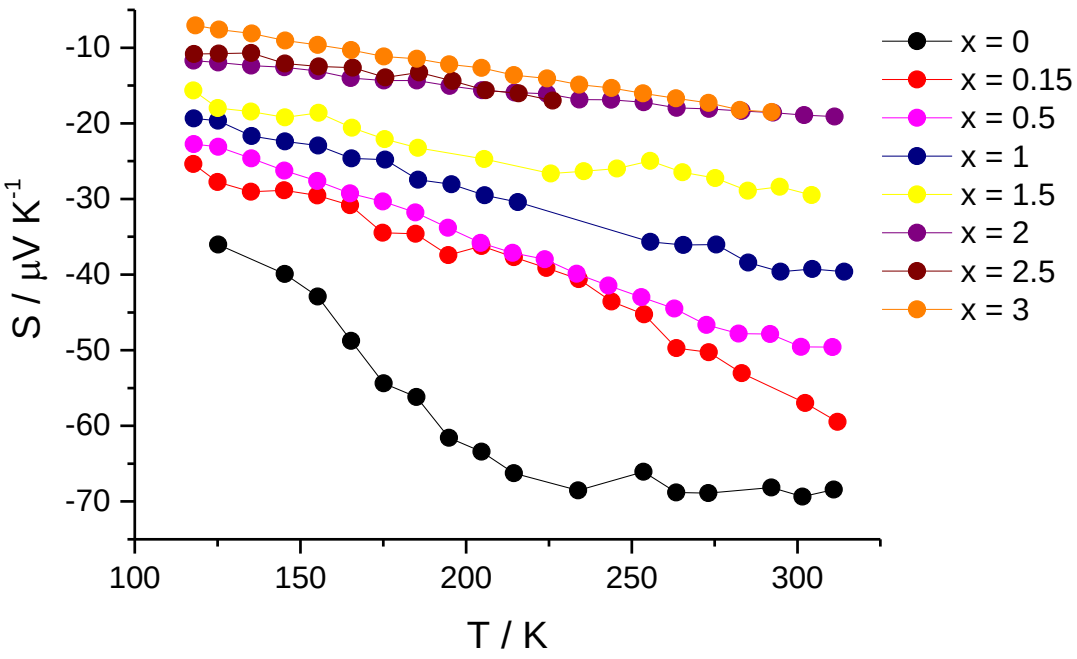

Figure 3.28 Seebeck coefficient measurements as a function of temperature for $Co_{3-x}Ni_xSn_2S_2$ ($0 \leq x \leq 3$) over the temperature range $115 \leq T / K \leq 315$.

3.6.2 Hole doping in $Co_{3-x}Fe_xSn_2S_2$ ($0 \leq x \leq 0.6$)

3.6.2.1 Electrical Resistivity

Electrical resistivity data for the series $Co_{3-x}Fe_xSn_2S_2$ ($0 \leq x \leq 0.6$) are presented in Figure 3.29, while Figure 3.30 shows the variation of resistivity with iron composition at a constant temperature. Hole doping results in a markedly different behaviour to that described for $Co_{3-x}Ni_xSn_2S_2$ in Section 3.5.2.2. In this case, electrical resistivity increases with increasing iron content. Up to $x = 0.4$, the material exhibits metallic behavior as $\rho(T)$ shows a positive temperature dependence, while for $x \geq 0.5$, the material appears to exhibit a semiconducting behaviour.

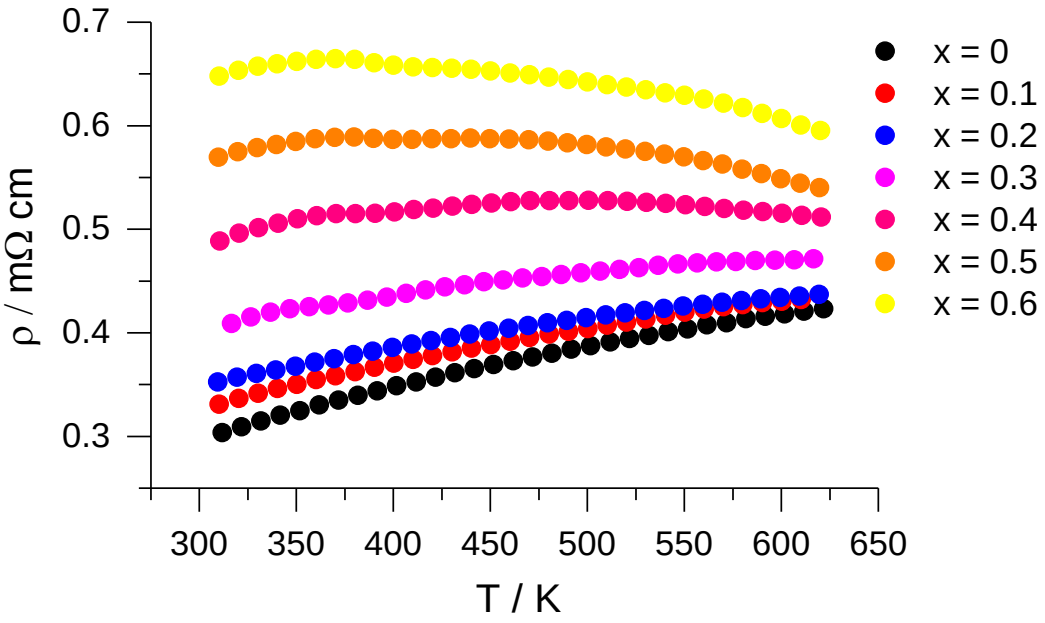

Figure 3.29 Electrical resistivity measurements as a function of temperature for $Co_{3-x}Fe_xSn_2S_2$ ($0 \leq x \leq 0.6$) in the temperature range $300 \leq T / K \leq 625$.

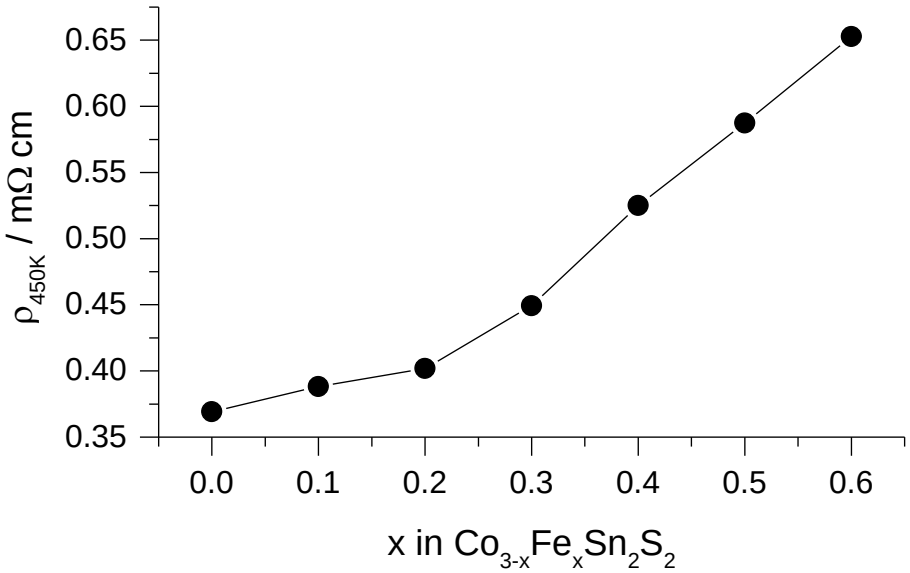

Figure 3.30 Electrical resistivity of $Co_{3-x}Fe_xSn_2S_2$ as a function of Fe content at 450 K.

3.6.2.2 Seebeck coefficient

Seebeck coefficient data for the series $Co_{3-x}Fe_xSn_2S_2$ ($0 \leq x \leq 0.6$) are presented in Figure 3.31. The negative values demonstrate the retention of n-type character. As is evident from Figure 3.32, at a constant temperature, $|S|$ increases with increasing iron content. It is noteworthy that the most iron-rich sample, $Co_{2.4}Fe_{0.6}Sn_2S_2$, exhibits the highest values of $|S|$, reaching 81.5 μV K^{-1} close to room temperature: an increase of 66 % from that of the Co-end-member phase.

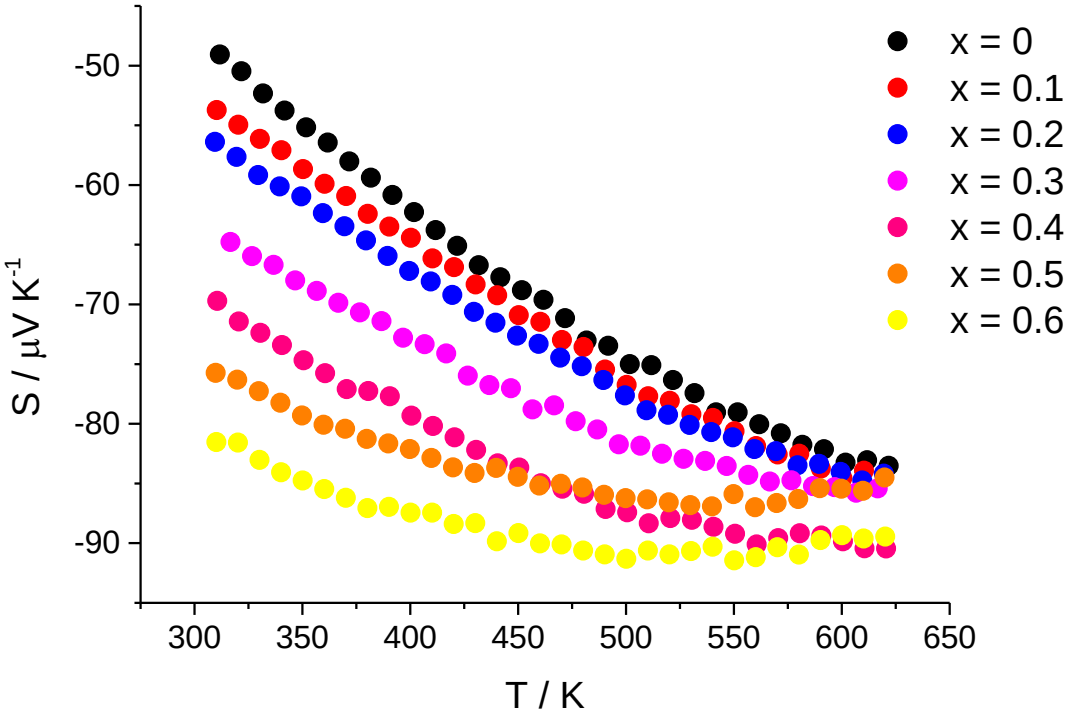

Figure 3.31 Seebeck coefficient measurements as a function of temperature for $Co_{3-x}Fe_xSn_2S_2$ ($0 \leq x \leq 0.6$) in the temperature range $300 \leq T / K \leq 625$.

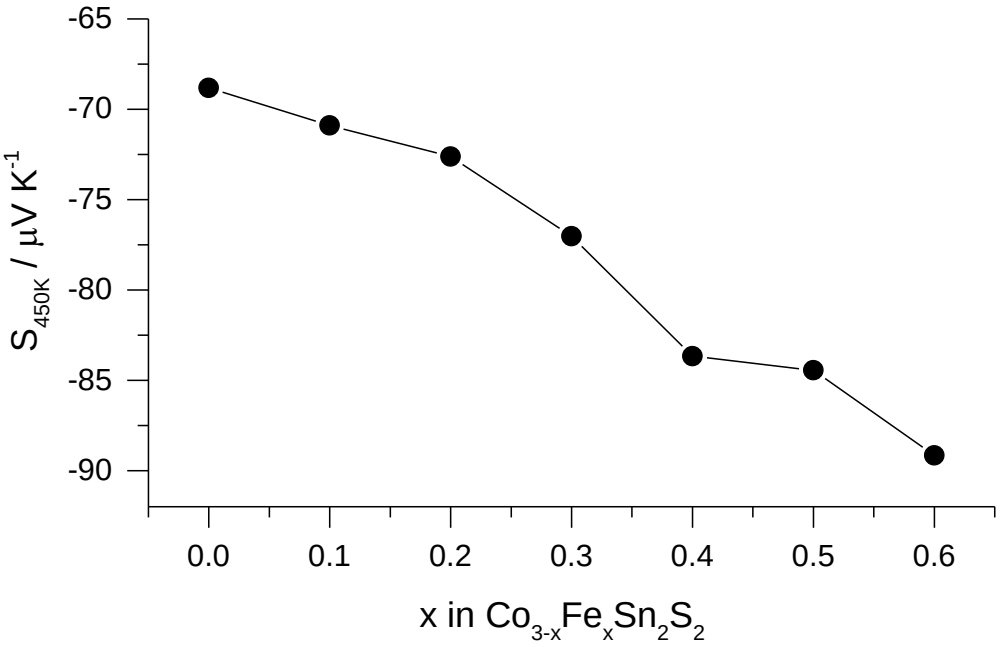

Figure 3.32 Seebeck coefficient data of $Co_{3-x}Fe_xSn_2S_2$ with Fe content at 450 K.

3.7 Thermal conductivity

Measurements of the thermal conductivity, κ, were carried out for both investigated series, $Co_{3-x}Ni_xSn_2S_2$ ($0 \leq x \leq 3$) and $Co_{3-x}Fe_xSn_2S_2$ ($0 \leq x \leq 0.6$), as described in Section 2.7.2. By using the Wiedemann-Franz law together with the electrical resistivity data of Section 3.5, the electronic contribution to the thermal conductivity, κ_{el}, was determined and by subtraction, the lattice contribution, κ_L.

3.7.1 Electron doping in $Co_{3-x}Ni_xSn_2S_2$ ($0 \leq x \leq 3$)

Thermal conductivity data for the series $Co_{3-x}Ni_xSn_2S_2$ are presented in Figure 3.33. The total thermal conductivity remains effectively constant up to a composition of x =1, whilst for higher nickel contents there is a rise in thermal conductivity which becomes particularly marked as x = 3 is approached. The electronic contribution for all samples of the series is increased slightly with temperature, whilst $\kappa_L(T)$ shows a negative temperature dependence. The sharp increase in κ for $Ni_3Sn_2S_2$ arises from the large electronic contribution, reflecting the particularly low electrical resistivity of this metallic phase.

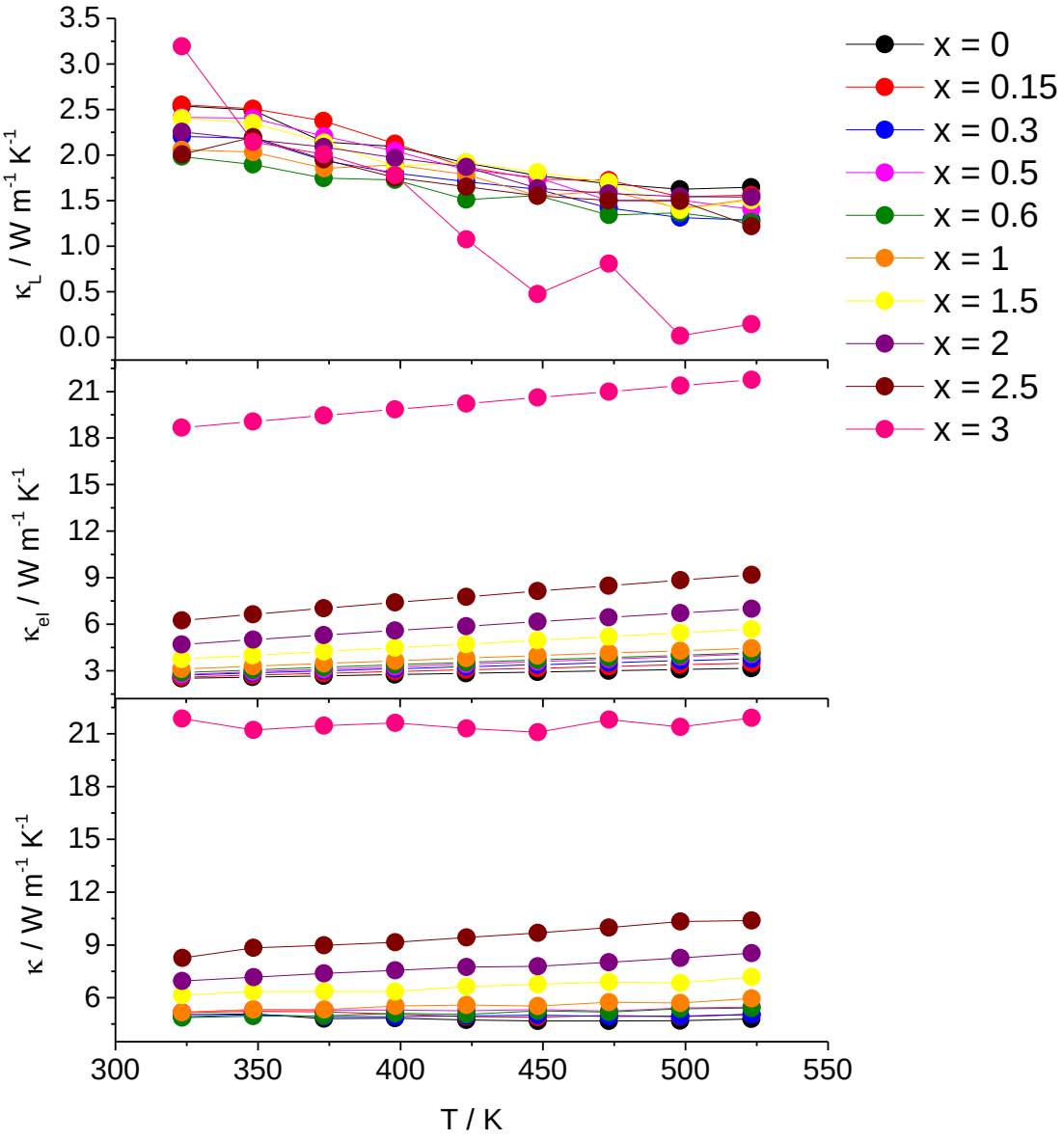

Figure 3.33 Thermal conductivity κ (bottom), electronic contribution, κ_e, (middle) and lattice contribution, κ_L, (top) as a function of temperature for $Co_{3-x}Ni_xSn_2S_2$ ($0 \leq x \leq 3$).

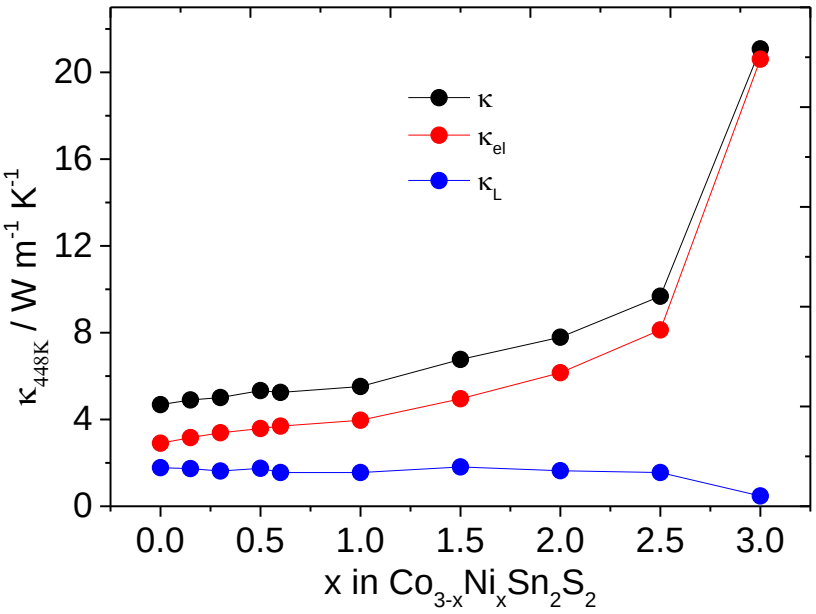

Figure 3.34 Compositional dependence of κ, κ_{el} and κ_L in $Co_{3-x}Ni_xSn_2S_2$ ($0 \leq x \leq 3$) at the constant temperature of 448 K.

In Figure 3.34 κ, κ_{el} and κ_L are presented at the constant temperature of 448 K as a function of Ni content. This analysis indicates that the thermal conductivity is determined predominantly by the electronic contribution, while the lattice contribution is almost independent of the composition of nickel. This is consistent with an increase in charge carrier concentration on nickel substitution and the absence of any appreciable mass fluctuation scattering owing to the similar atomic masses of nickel and cobalt.

3.7.2 Hole doping in $Co_{3-x}Fe_xSn_2S_2$ ($0 \leq x \leq 0.6$)

The thermal conductivity of $Co_{3-x}Fe_xSn_2S_2$ falls on substitution with iron (Figure 3.35) with the lowest value at room temperature (at x = 0.5) reduced by 32 % from that of $Co_3Sn_2S_2$. The electronic and lattice contributions to the thermal conductivity show opposing temperature dependences. The electronic contribution, κ_{el}, at constant temperature decreases almost linearly with increasing iron content (Figure 3.36), whilst κ_L is effectively compositionally invariant, consistent with the absence of mass fluctuation scattering for elements whose atomic masses differ by only 1 amu.

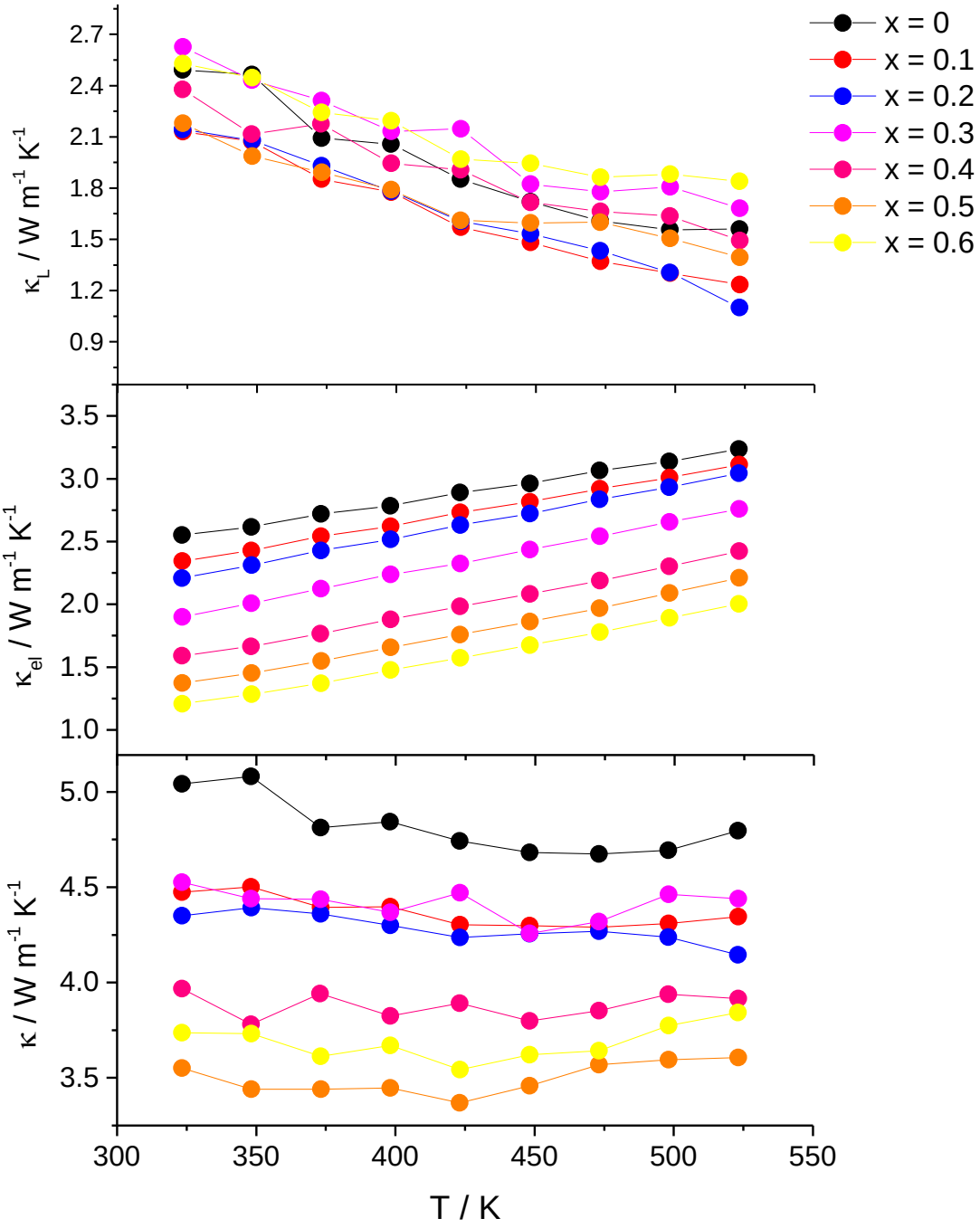

Figure 3.35 Thermal conductivity κ (bottom), electronic contribution, κ_e, (middle) and lattice contribution, κ_L, (top) as a function of temperature for $Co_{3-x}Fe_xSn_2S_2$ ($0 \leq x \leq 0.6$).

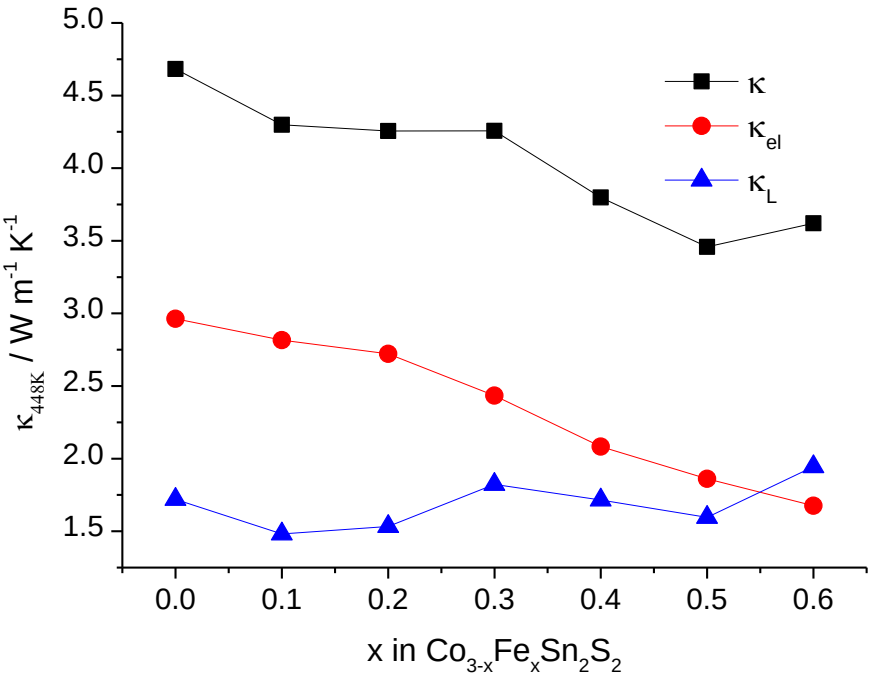

Figure 3.36 Compositional dependence of κ, κ_{el} and κ_L in $Co_{3-x}Fe_xSn_2S_2$ ($0 \leq x \leq 0.6$) at the constant temperature of 448 K.

3.8 Thermoelectric Properties

Electrical resistivity, Seebeck coefficient and thermal conductivity measurements were used to determine the thermoelectric power factor (S^2/ρ) and thermoelectric figure of merit ZT of the samples.

3.8.1 Power factor and ZT for $Co_{3-x}Ni_xSn_2S_2$ ($0 \leq x \leq 3$)

The simultaneous decrease of resistivity and |*S*| contributes to an overall reduction in the power factor of the material (Figure 3.37). However, the Ni-end-member phase exhibits a higher power factor than that of the other materials with $x \geq 1$, due to the extremely low resistivity of the sample. Electron doping through nickel substitution increases the metallic character of the materials, as evidenced by the decrease observed in both the resistivity and Seebeck coefficient, leading to a transition from the half-metallic, $Co_3Sn_2S_2$, to the metallic $Ni_3Sn_2S_2$ phase. Electron doping through substitution of cobalt by nickel does not improve the TE figure-of-merit, ZT (Figure 3.38). The marked decrease in |S| is principally responsible for the reduction in ZT, whilst for $x > 1$ the increased κ also contributes to the observed reduction in ZT.

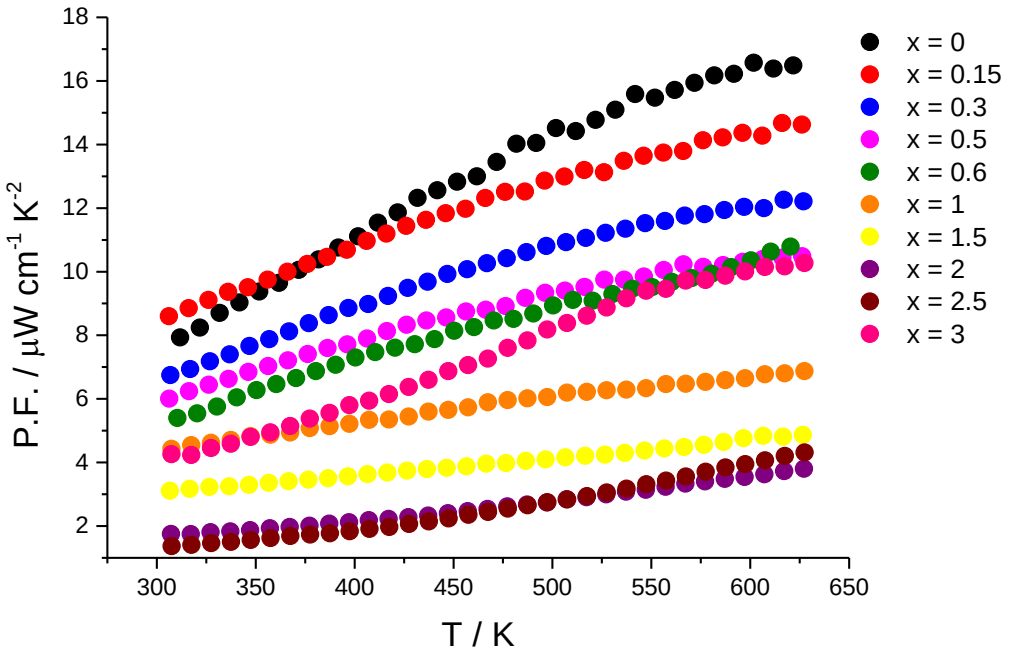

Figure 3.37 Power factors (P.F.) for $Co_{3-x}Ni_xSn_2S_2$ ($0 \leq x \leq 3$) in the temperature range $300 \leq T / K \leq 625$.

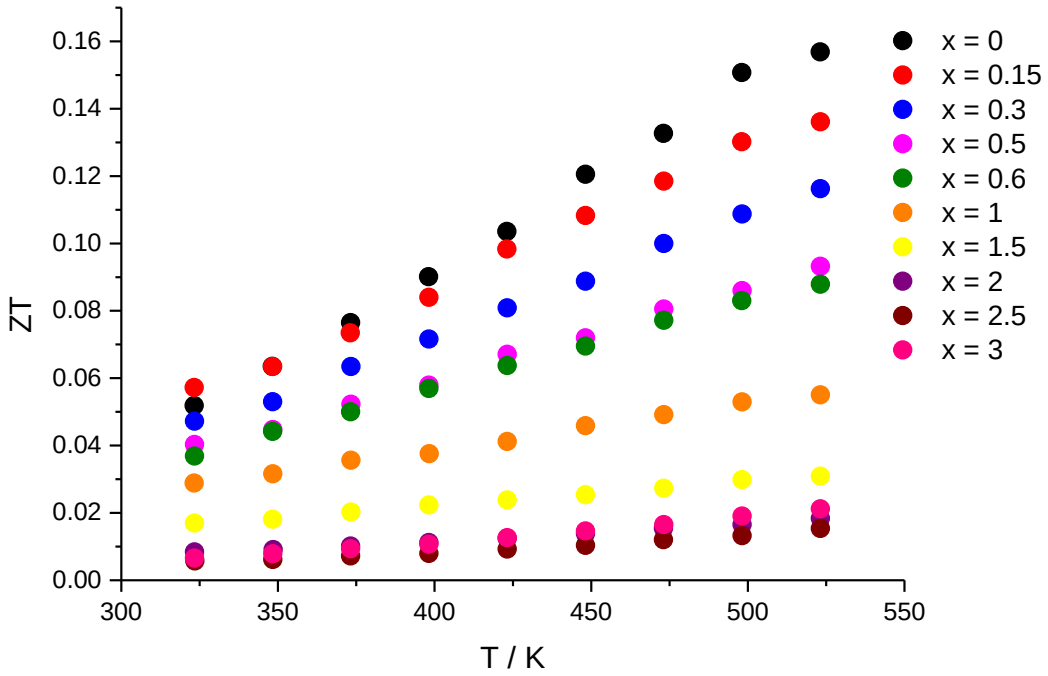

Figure 3.38 The figure-of-merit, ZT, for $Co_{3-x}Ni_xSn_2S_2$ ($0 \leq x \leq 3$) as a function of temperature.

3.8.2 Power factor and ZT for $Co_{3-x}Fe_xSn_2S_2$ ($0 \leq x \leq 0.6$)

The increase in Seebeck coefficient across the series is sufficient to offset the reduction in electron conductivity and results in an increase of the power factor (Figure 3.39) particularly at temperatures close to ambient. $Co_{2.4}Fe_{0.6}Sn_2S_2$ attains a power factor of 10.3 μW cm^{-1} K^{-2} at 310 K, which corresponds to an increase of 29% from that of the end-member $Co_3Sn_2S_2$. Hole doping causes the depopulation of the 24th *d*-band, as cobalt is replaced by the one less electron iron, and moves E_F downwards in energy, possibly to a region of the DOS where there is a greater curvature and hence a larger derivative of the DOS, which may be responsible for the increase in $|S|$. The combination of the reduction in thermal conductivity and the increase in power factor results in the increase of the figure-of-merit of $Co_{3-x}Fe_xSn_2S_2$ ($0 \leq x \leq 0.6$) (Figure 3.40). The greatest differences in ZT are observed at low temperatures. It is remarkable that at 350 K, $Co_{2.5}Fe_{0.5}Sn_2S_2$ exhibits ZT = 0.11, which is double that of $Co_3Sn_2S_2$. At 525 K, the maximum value of 0.2 is exhibited by $Co_{2.6}Fe_{0.4}Sn_2S_2$ and corresponds to an increase of *ca.* 22% from that of $Co_3Sn_2S_2$.

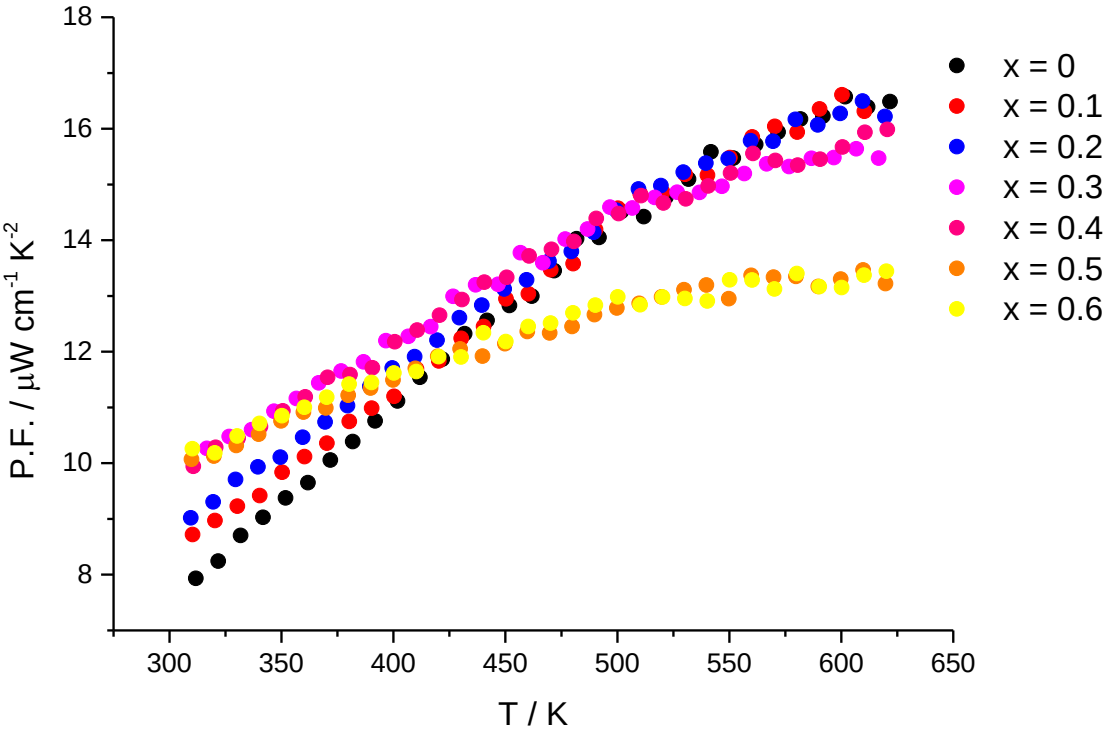

Figure 3.39 Power factors (P.F.) for $Co_{3-x}Fe_xSn_2S_2$ ($0 \leq x \leq 0.6$) in the temperature range $300 \leq T / K \leq 625$.

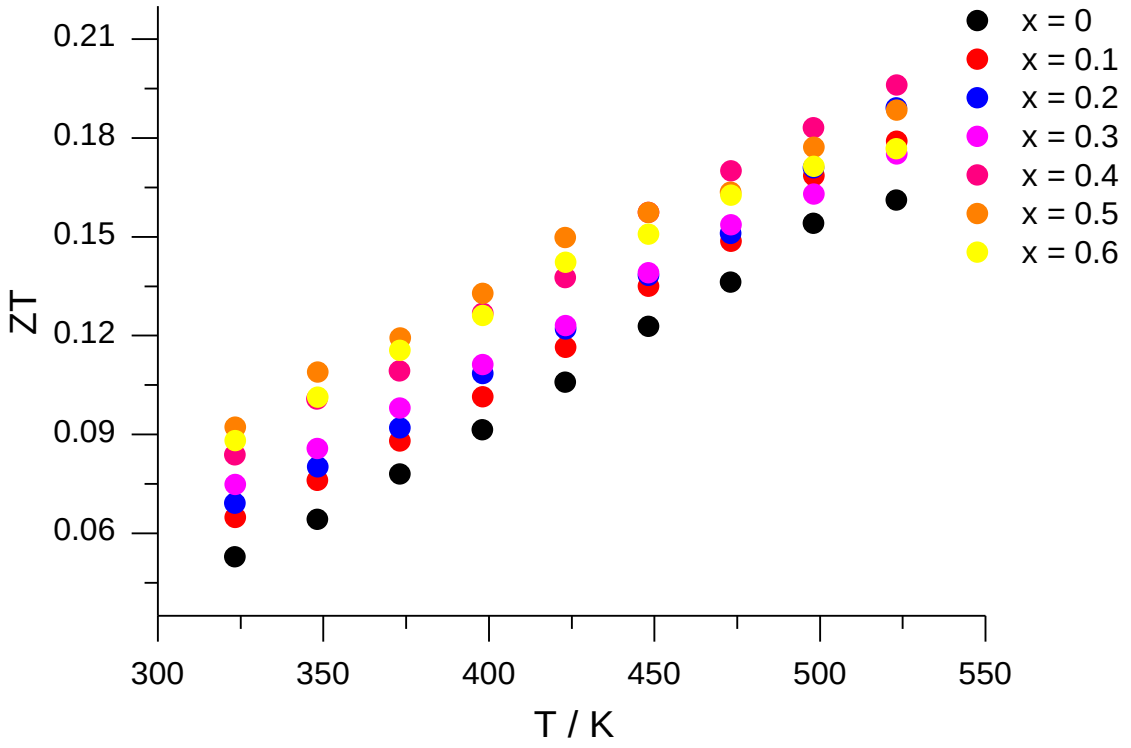

Figure 3.40 The figure-of-merit, ZT, for $Co_{3-x}Fe_xSn_2S_2$ ($0 \leq x \leq 0.6$) as a function of temperature.

3.9 Conclusions

In this chapter, electron and hole doping in the shandite $Co_3Sn_2S_2$ was achieved through the chemical substitution of Co, by its neighbouring elements, Ni and Fe. In the case of Ni substitution single phases are observed throughout the composition range ($0 \leq x \leq 3$), whilst Fe substitution occurs over the more limited range of ($0 \leq x \leq 0.6$). X-ray and neutron diffraction data reveal that the replacement of cobalt by nickel causes an expansion in the kagome layer while iron substitution causes a small increase of spacing between the kagome layers, enhancing the two-dimensionality of the structure. In addition, powder neutron diffraction experiments showed that throughout the two series, $Co_{3-x}Ni_xSn_2S_2$ ($0 \leq x \leq 3$) and $Co_{3-x}Fe_xSn_2S_2$ ($0 \leq x \leq 0.6$), transition-metal substitution occurs in a disordered fashion.

^{57}Fe Mössbauer spectroscopy measurements on materials in $Co_{3-x}Fe_xSn_2S_2$ ($0 \leq x \leq 0.6$), show two distinct sub spectra, which arise from the differences in the local environment of iron atoms at the disordered 9(*d*) site. Assignment of formal oxidation states is inconclusive, although the very different isomer shifts of the two doublets may be

indicative of a mixed-valent state of iron. ^{119}Sn Mössbauer data show that the two tin sites are not affected by iron substitution and retain the zero valent state, previously identified in the end-member phase, $Co_3Sn_2S_2$.[100] Physical property measurements have demonstrated that nickel substitution increases the metallic character of the material. This is consistent with the results of DFT calculations for the end-member phases ($M_3Sn_2S_2$, M = Co, Ni),[100,97] which indicate that with increasing electron count on going from M = Co to M = Ni, the half-occupied 24th band and unoccupied 25th band are progressively filled. There is a concomitant decrease in Seebeck coefficient with increasing the metallic character across the series. This, together with the simultaneous increase of thermal conductivity outweighs the decrease of resistivity, resulting in an overall reduction of ZT. By contrast, hole-doping through the introduction of iron, results in an improvement in TE performance. The electrical resistivity increases when iron is introduced, driving the material to a semiconducting state. At x = 0.5, the compound becomes an *n*-type semiconductor. Depopulation of the 24th band moves the valence band to lower energies and may shift E_F to a region of the DOS which is more highly structured. This may be the reason for the increase of $|S|$ which in combination with the reduction of thermal conductivity contributes to the rise in ZT: $Co_{2.6}Fe_{0.4}Sn_2S_2$ exhibiting the maximum value of ZT = 0.2 at 523 K. This improvement of TE performance in $Co_{3-x}Fe_xSn_2S_2$ ($0 \leq x \leq 0.6$) is promising for future research, showing new direction of chemical substitution in the shandite $Co_3Sn_2S_2$. The previous study[94] in $Co_3Sn_{2-x}In_xS_2$ revealed an enhancement of TE performance reaching power factors in the range 12 – 14 μW cm^{-1} K^{-2} at room temperature. The present work reveals that close to room temperature, $Co_{2.4}Fe_{0.6}Sn_2S_2$ exhibits a value of 10.3 μW cm^{-1} K^{-2} which is relatively high for a Te-free bulk material (Bi_2Te_3 alloys: ~36 μW cm^{-1} K^{-2}). In addition, compared to indium substitution,[94] the synthesis of $Co_{3-x}Fe_xSn_2S_2$ is a less costly procedure as iron is a cheaper metal than indium. Moreover, $Co_{2.5}Fe_{0.5}Sn_2S_2$ exhibits a higher ZT close to room temperature than that of other promising sulphides as Bi_2S_3,[41] $Pb_{0.0975}Na_{0.025}S$,[45] $NdGdS_3$,[114] $Cu_xMo_6S_8$,[115] which have been investigated recently. These materials exhibit their maximum values of ZT at elevated temperatures ($T \geq 700$ K), enabling them to be competitive with thermoelectrics for high-temperature waste heat recovery such as PbTe. Nevertheless, these materials present a $ZT \leq 0.11$ at 350 K. The present work provides an alternative route for the hole doping of the shandite $Co_3Sn_2S_2$, achieving an improvement in the TE performance of the bulk material, and as a result new routes arise for further research on the optimization of its TE properties.

Chapter 4 - Simultaneous substitution at both transition-metal and main-group sites in $Co_{3-x}Fe_xSn_{2-y}In_yS_2$

4.1 Introduction

In an effort to improve more the TE efficiency of the material, further hole doping was carried out in the already Fe-substituted shandite phases through the substitution of tin by indium, which has one less valence electron. A previous study[94] of $Co_3Sn_{2-x}In_xS_2$ revealed an enhancement of TE performance by tuning E_F within narrow *d*-bands. Therefore, simultaneous substitution at the transition-metal and main-group element sites may lead to an increase in Seebeck coefficient and consequently an improvement of figure-of-merit, ZT. A wide range of samples of general foumula $Co_{3-x}Fe_xSn_{2-y}In_yS_2$ with different combinations of x and y were synthesized in an effort to optimize the TE properties. The materials were synthesised in an analogous manner to that described in Section 3.2. All products were characterised by powder X-ray diffraction data as described in Section 3.3.1.

4.2 Hole doping in $Co_{2.5}Fe_{0.5}Sn_{2-y}In_yS_2$ ($0 \leq y \leq 0.6$)

The fact that the highest values of ZT close to room temperature are exhibited by $Co_{2.5}Fe_{0.5}Sn_2S_2$, lead to investigate firstly the $Co_{2.5}Fe_{0.5}Sn_{2-y}In_yS_2$ series, keeping the amount of iron constant at x = 0.5.

4.2.1 Powder X-ray diffraction for $Co_{2.5}Fe_{0.5}Sn_{2-y}In_yS_2$ ($0 \leq y \leq 0.6$)

Powder X-ray diffraction data for the $Co_{2.5}Fe_{0.5}Sn_{2-y}In_yS_2$ ($0 \leq y \leq 0.6$) series confirm the shandite structure with the space group $R\bar{3}m$ (Figure 4.1) which is adopted throughout the compositional range. Trace amounts of In_3S_4 were present in the samples. Rietveld refinements were carried out according to the procedure of Section 3.3.1 and using as the initial structural model, the lattice parameters and atomic coordinates of $Co_{2.5}Fe_{0.5}Sn_2S_2$. The thermal parameters of tin and indium atoms were constrained.

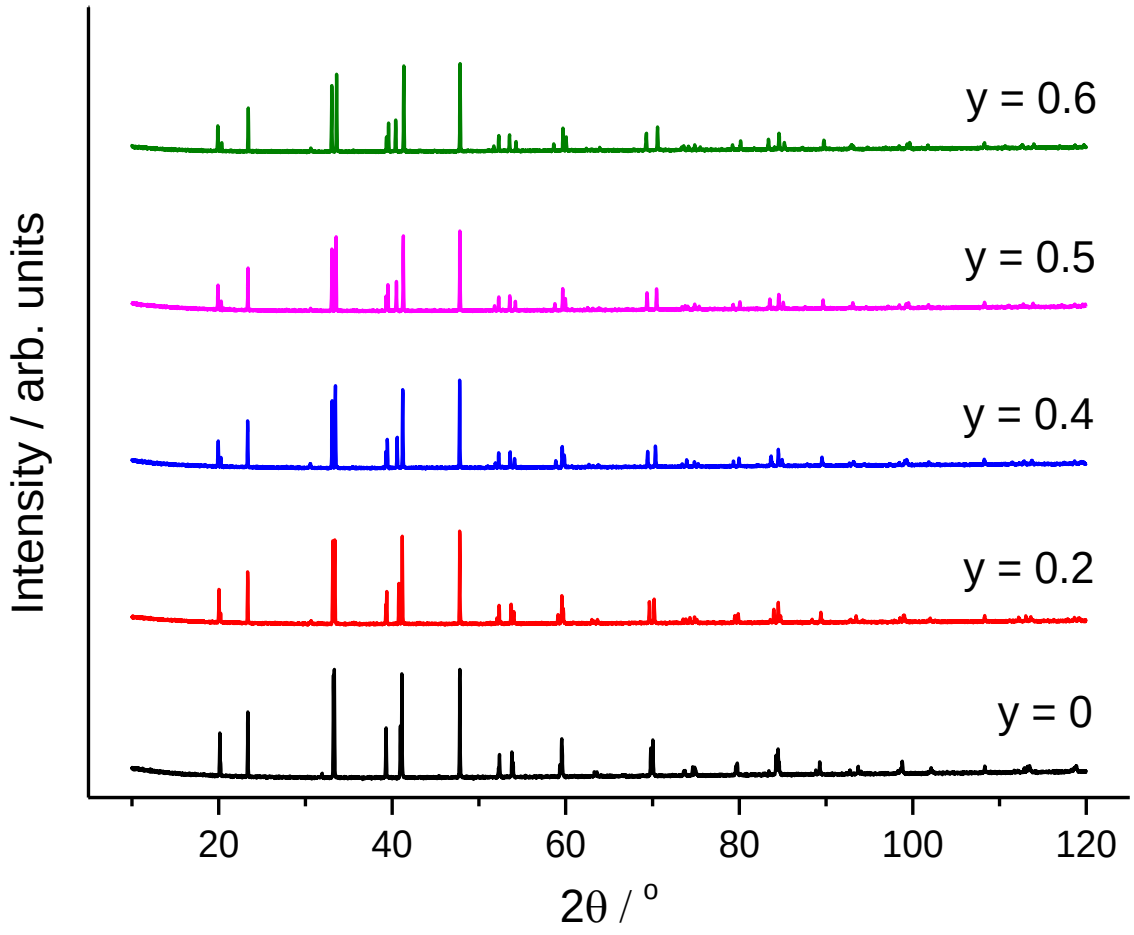

Figure 4.1 Powder X-ray diffraction data of $Co_{2.5}Fe_{0.5}Sn_{2-y}In_yS_2$ ($0 \leq y \leq 0.6$) over the range $10 \leq 2\theta / ° \leq 120$.

The similar X-ray scattering factors of indium and tin did not allow to extract conclusions about the distribution of In content at the main-group element sites. However, the neutron diffraction study[100] in $Co_3Sn_{2-x}In_xS_2$ series revealed a partial ordering at the inter-layer Sn(1) site. Assuming that the substitution of Sn by In in $Co_{2.5}Fe_{0.5}Sn_{2-y}In_yS_2$ ($0 \leq y \leq 0.6$) follows the same distribution with that observed in $Co_3Sn_{2-x}In_xS_2$ ($0 \leq x \leq 0.6$), the occupancy factors at the two main-group sites were set according to the results extracted by the neutron diffraction study. Each time, the refinement for a given sample was initiated using the refined model of the previous composition. Typical profiles are presented in Figures 4.2 and 4.3. The remaining patterns can be found in Appendix H. The refined model fits the experimental data well ($1.26 \leq \chi^2 \leq 1.47$, $2.8 \leq R_{wp} / \% \leq 3.1$). Figure 4.4 presents the unit cell parameters as a function of In composition determined by the Rietveld analysis. There is a rise in the lattice parameter *c*, which leads to an increase in the spacing between the kagome layers and consequently enhances the two-dimensional character of the structure.

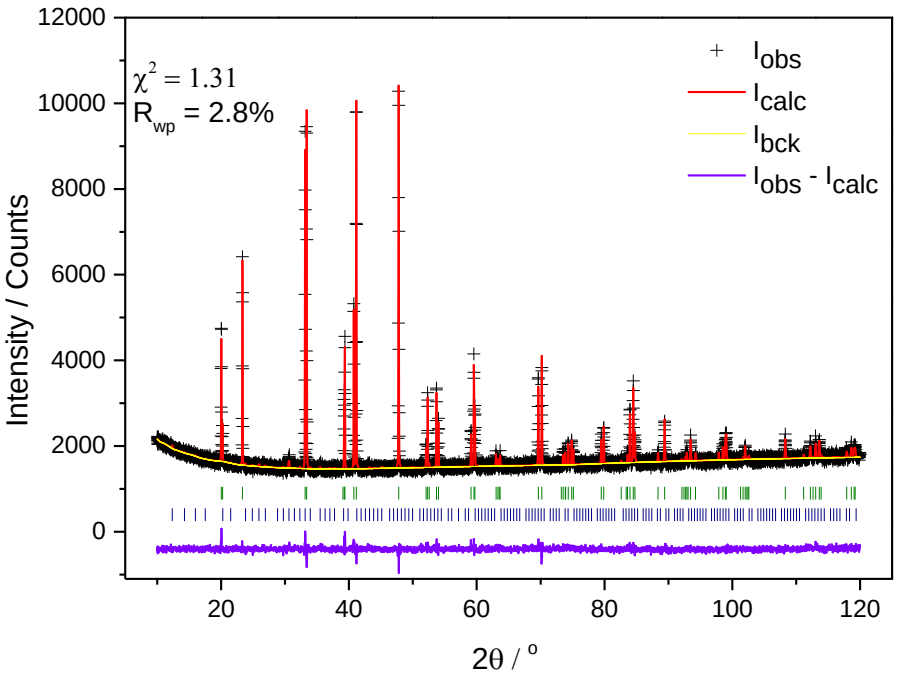

Figure 4.2 Final observed, calculated and difference profiles from Rietveld refinement for $Co_{2.5}Fe_{0.5}Sn_{1.8}In_{0.2}S_2$ using X-ray diffraction data. Reflection positions are marked. Olive markers, the shandite phase; Navy markers, In_3S_4 (~ 5.1 wt %).

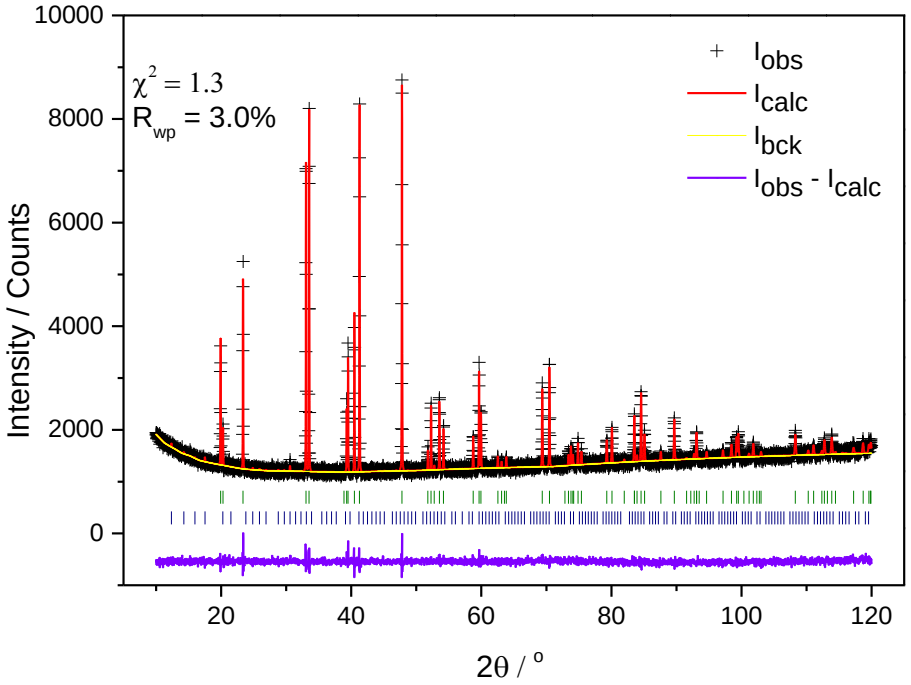

Figure 4.3 Final observed, calculated and difference profiles from Rietveld refinement for $Co_{2.5}Fe_{0.5}Sn_{1.5}In_{0.5}S_2$ using X-ray diffraction data. Reflection positions are marked. Olive markers, the shandite phase; navy markers, In_3S_4 (~ 2.5 wt %).

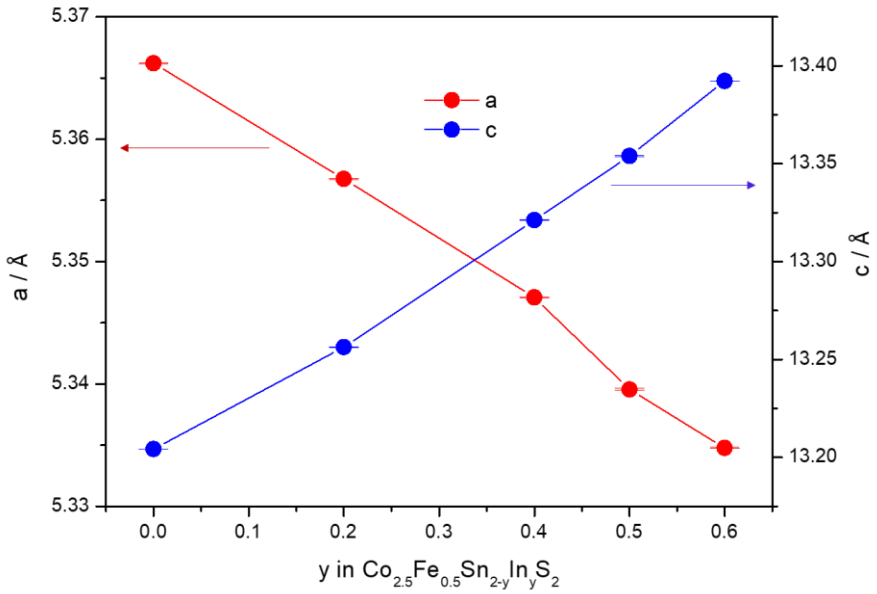

Figure 4.4 Lattice parameters determined by powder X-ray diffraction, for the series $Co_{2.5}Fe_{0.5}Sn_{2-y}In_yS_2$ ($0 \leq y \leq 0.6$).

Conversely, there is a small reduction in the lattice parameter *a*. A similar variation in lattice parameters with In content has been observed in the series $Co_3Sn_{2-x}In_xS_2$ ($x \leq 1$) by X-ray[94] and neutron[100] diffraction. The substitution of tin by the larger indium atom increases the volume and interlayer spacing between kagome sheets. However, the reduction in the α lattice parameter is associated with electronic rather than steric factors. According to DFT calculations,[100] the main contribution in the vicinity of Fermi level comes from the d_{xy} and $d_{x^2-y^2}$ states which participate in the intralayer interactions and have anti-bonding character. The progressive depopulation of these states through hole doping weakens the anti-bonding interactions, resulting in a small contraction of kagome layers.

4.2.2 Physical Property Measurements for $Co_{2.5}Fe_{0.5}Sn_{2-y}In_yS_2$ ($0 \leq y \leq 0.6$)

Electrical resistivity and Seebeck coefficient measurements were carried out on circular pellets, as described in Section 2.7.1.1. The pellets were fabricated by hot-pressing according to the procedure described in Section 2.5, exhibiting densities *ca*. 98 % of the crystallographic value. The introduction of holes through the substitution of Sn by In, increases the electrical resistivity (Figure 4.5) and the materials become more semiconducting.

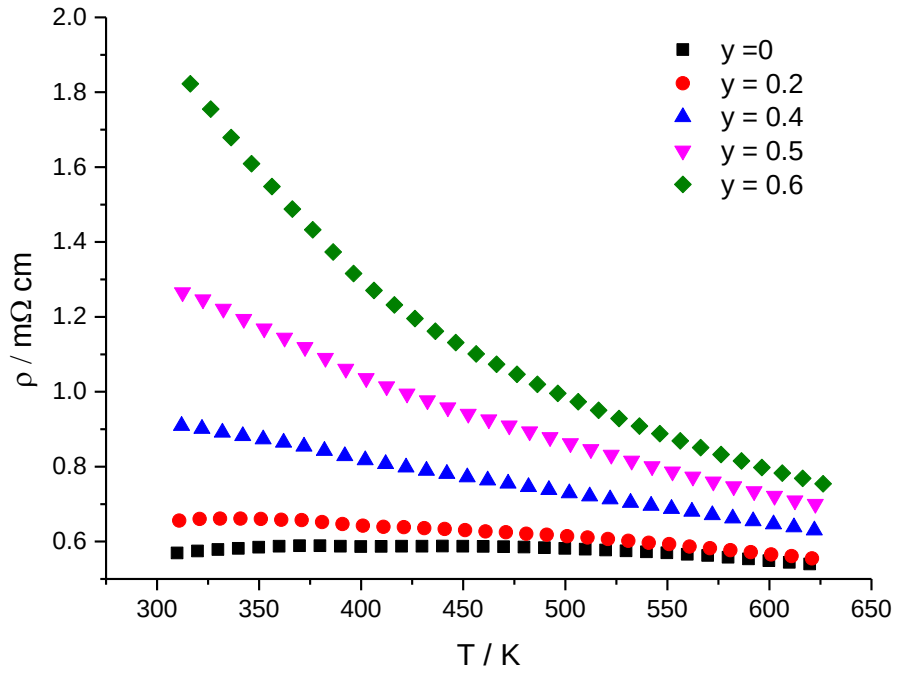

Figure 4.5 Electrical resistivity data as a function of temperature for $Co_{2.5}Fe_{0.5}Sn_{2-y}In_y S_2$ ($0 \leq y \leq 0.6$) in the temperature range $300 \leq T / K \leq 625$.

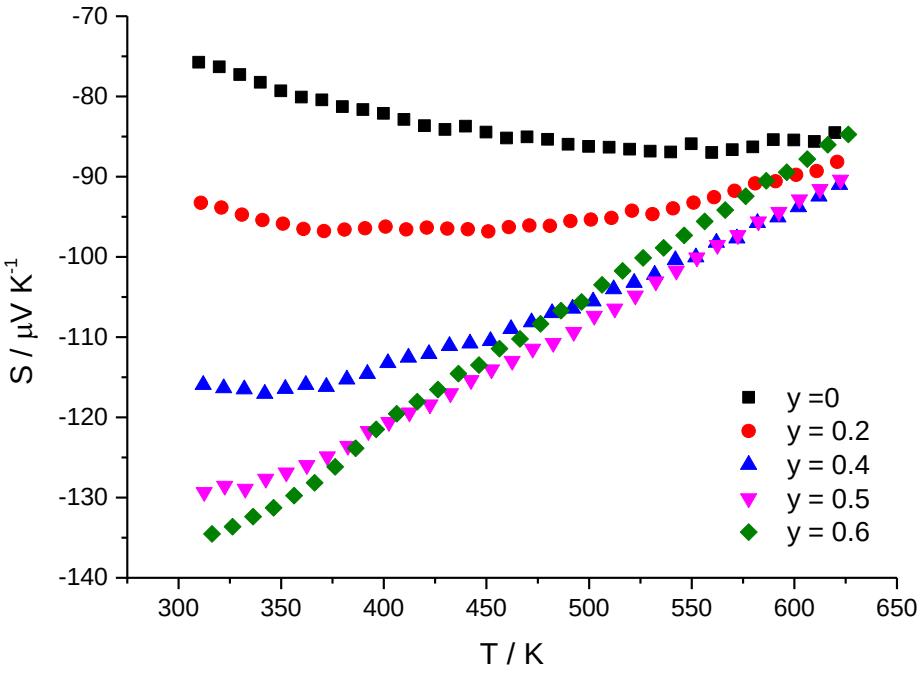

Figure 4.6 Seebeck coefficient data as a function of temperature for $Co_{2.5}Fe_{0.5}Sn_{2-y}In_yS_2$ ($0 \leq y \leq 0.6$) in the temperature range $300 \leq T / K \leq 625$.

There is a marked increase in |*S*| close to room temperature (Figure 4.6) as the In content is increased. The highest value of -135 μV K^{-1} which is exhibited by the most In-rich sample, with y = 0.6, corresponds to an increase of 78 % from that of In-free phase, $Co_{2.5}Fe_{0.5}Sn_2S_2$. The negative values indicate the *n*-type character of the materials. Thermal conductivity measurements were carried out on circular samples according to the procedure described in Section 2.7.2. In substitution causes a small reduction in κ (Figure 4.7) only for the most In-rich substituted samples (y = 0.5, 0.6) especially at temperatures close to ambient.

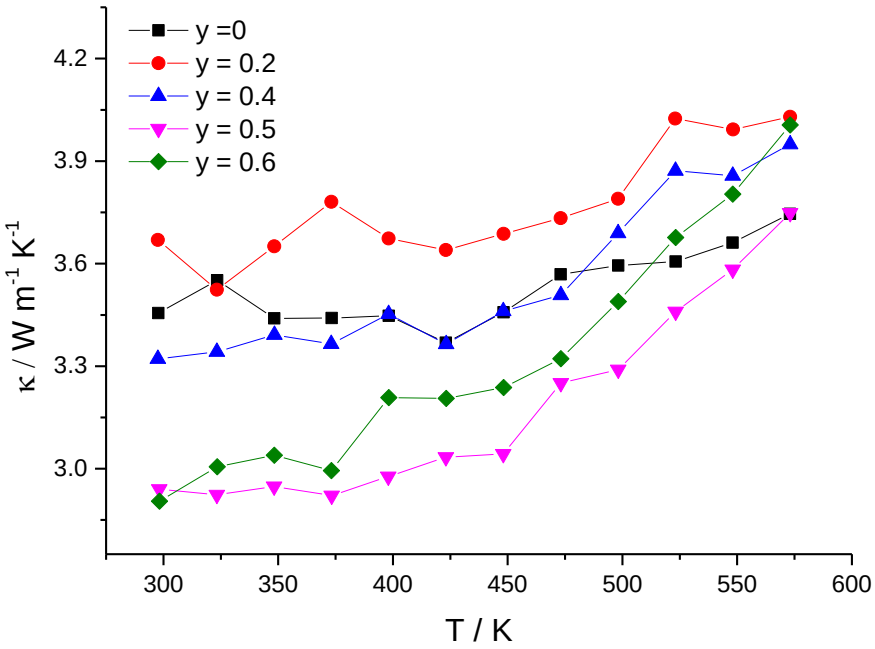

Figure 4.7 Thermal conductivity data as a function of temperature for $Co_{2.5}Fe_{0.5}Sn_{2-y}In_yS_2$ ($0 \leq y \leq 0.6$) in the temperature range $300 \leq T / K \leq 575$.

4.2.3 Thermoelectric Properties for $Co_{2.5}Fe_{0.5}Sn_{2-y}In_yS_2$ ($0 \leq y \leq 0.6$)

Using the physical property data of Section 4.2.2, the TE power factors and figures of merit were determined (Figures 4.8 and 4.9). There is a marked improvement of P.F. with In content for compositions up to y = 0.4 because the large increase in Seebeck coefficient offsets the relatively small rise in electrical resistivity. However, for the samples with larger amounts of In, y = 0.5 and 0.6, the P.F. is sharply reduced, with that of $Co_{2.5}Fe_{0.5}Sn_{1.4}In_{0.6}S_2$ being lower than of the In-free phase, due to the high electrical resistivity values. The maximum values of P.F., about 15.8 μW cm^{-1} K^{-2}, are exhibited by $Co_{2.5}Fe_{0.5}Sn_{1.6}In_{0.4}S_2$ in the temperature range 375 – 450 K.

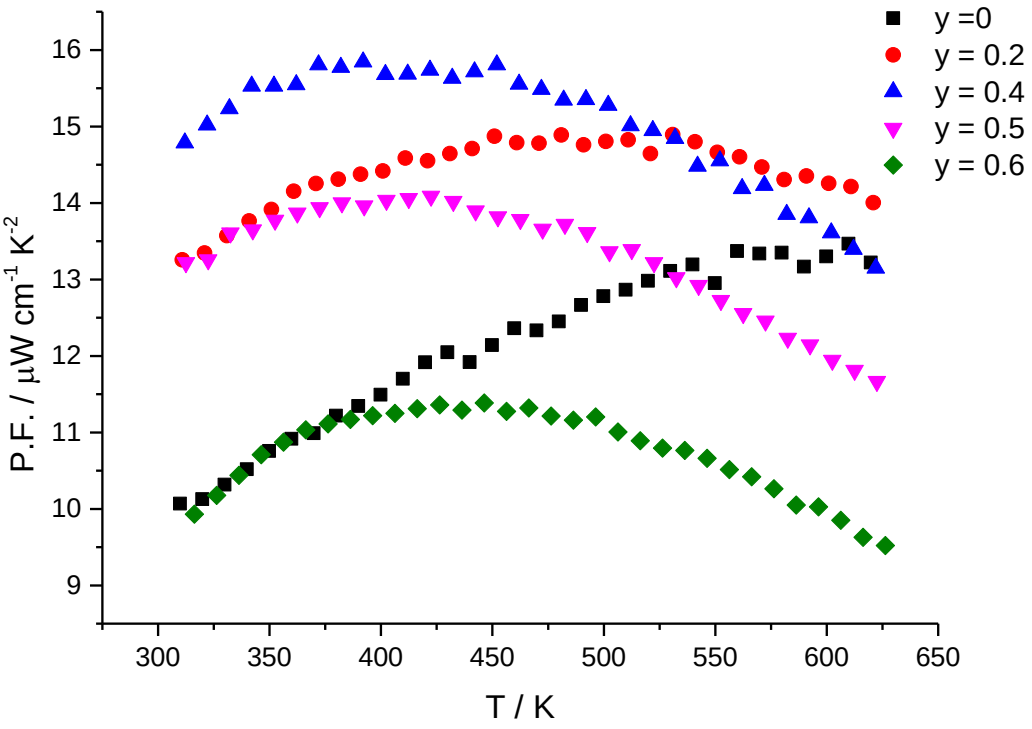

Figure 4.8 Power factor (P.F.) data for $Co_{2.5}Fe_{0.5}Sn_{2-y}In_yS_2$ ($0 \leq y \leq 0.6$) in the temperature range $300 \leq T / K \leq 625$.

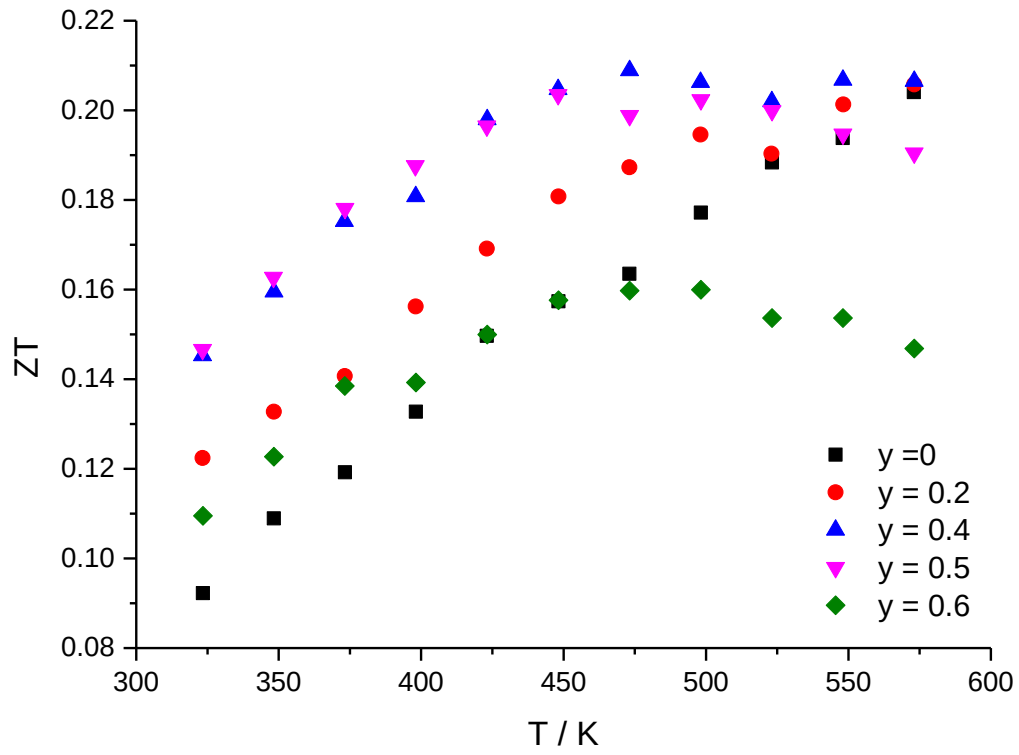

Figure 4.9 The figure-of-merit, ZT, for $Co_{2.5}Fe_{0.5}Sn_{2-y}In_yS_2$ ($0 \leq y \leq 0.6$) as a function of temperature.

The figure of merit, ZT, is improved especially for temperatures below 500 K (Figure 4.9). The maximum ZT value of 0.21 is exhibited by $Co_{2.5}Fe_{0.5}Sn_{1.6}In_{0.4}S_2$. This can be associated principally with the impact of the P.F., since the thermal conductivity, κ, for y = 0.4 is comparable with that of the In-free end-member phase, $Co_{2.5}Fe_{0.5}Sn_2S_2$.

4.3 Hole doping in $Co_{2.667}Fe_{0.333}Sn_{2-y}In_y S_2$ ($0 \leq y \leq 0.7$)

In an effort to explore further the impact of chemical substitution at both the transition-metal and main-group atom sites on the TE properties of the material, DFT calculations were carried out by Mr Alex Aziz and Dr Ricardo Crespo of this Department and the principal findings are included here with their permission. DFT calculations were performed using the Vienna Ab initio Simulation Package (VASP)[116] to determine the band structure for a wide range of different combinations of *x* and *y* compositions in the $Co_{3-x}Fe_xSn_{2-y}In_yS_2$ series. The results show that for x = 0.333 and y = 0.333, E_F might be tuned to regions of the DOS containing high and narrow peaks. The DOS for three selected samples of the $Co_{2.667}Fe_{0.333}Sn_{2-y}In_yS_2$ series are presented in Figures 4.10, 4.11 and 4.12.

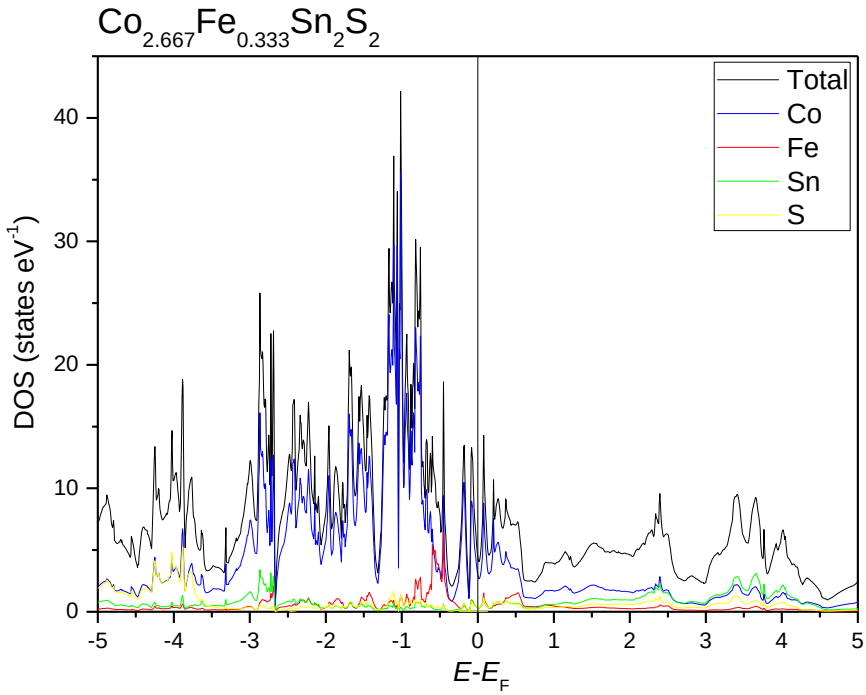

Figure 4.10 Total and partial DOS for $Co_{2.667}Fe_{0.333}Sn_2S_2$ determined by DFT calculations. Figure used with permission of Mr Alex Aziz and Dr Ricardo Grau-Crespo.

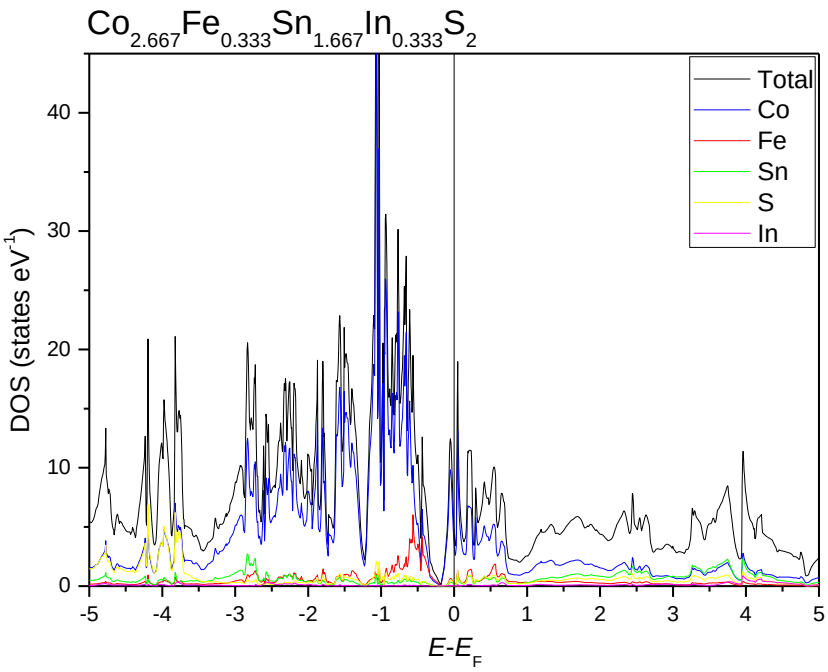

Figure 4.11 Total and partial DOS for $Co_{2.667}Fe_{0.333}Sn_{1.667}In_{0.333}S_2$ determined by DFT calculations. Figure used with permission of Mr Alex Aziz and Dr Ricardo Grau-Crespo.

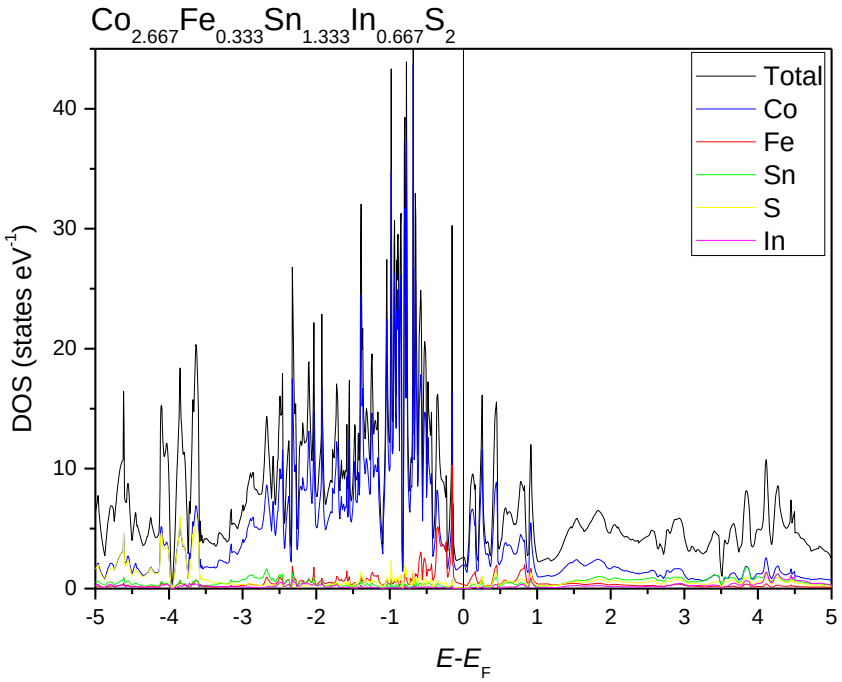

Figure 4.12 Total and partial DOS for $Co_{2.667}Fe_{0.333}Sn_{1.333}In_{0.667}S_2$ determined by DFT calculations. Figure used with permission of Mr Alex Aziz and Dr Ricardo Grau-Crespo.

The progressive depopulation of the half-occupied 24th *d* band shifts the E_F to lower energies. At a composition $Co_{2.667}Fe_{0.333}Sn_{1.333}In_{0.667}S_2$ the 24th *d* band is completely depopulated, and the E_F is located in the band gap, suggesting semiconducting behaviour. The results of band structure calculations for $Co_{2.667}Fe_{0.333}Sn_{1.333}In_{0.667}S_2$ are similar to those for Co_3SnInS_2,[100] which contains a similar number of holes and exhibits semiconducting behaviour. These results motivated an investigation of materials of general formula $Co_{2.667}Fe_{0.333}Sn_{2-y}In_yS_2$.

4.3.1 Powder X-ray diffraction for $Co_{2.667}Fe_{0.333}Sn_{2-y}In_yS_2$ ($0 \leq y \leq 0.7$)

The purity of the samples of $Co_{2.667}Fe_{0.333}Sn_{2-y}In_yS_2$ ($0 \leq y \leq 0.7$) series was determined by powder X-ray diffraction (Figure 4.13).

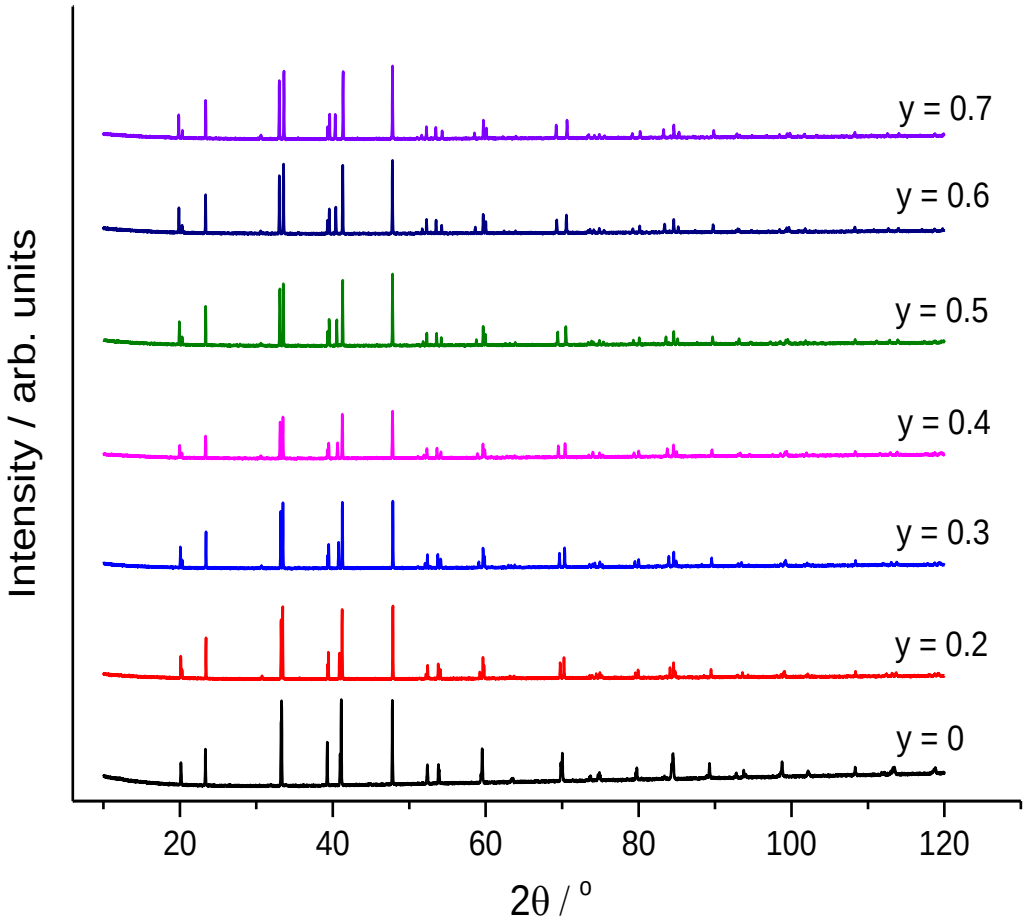

Figure 4.13 Powder X-ray diffraction data collected at room temperature for $Co_{2.667}Fe_{0.333}Sn_{2-y}In_yS_2$ ($0 \leq y \leq 0.7$) over the angular range $10 \leq 2\theta / ° \leq 120$.

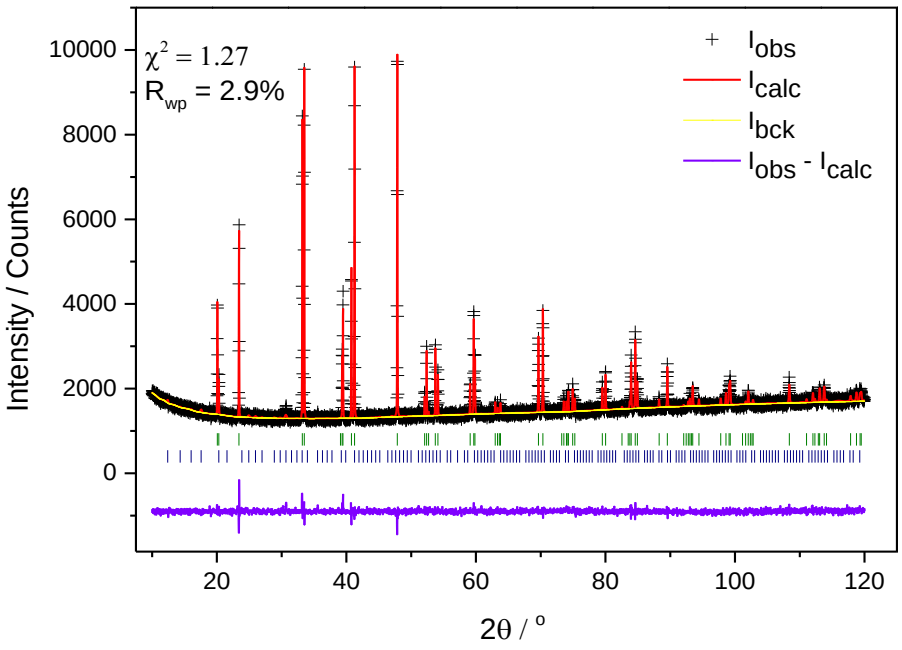

Figure 4.14 Final observed, calculated and difference profiles from Rietveld refinement for $Co_{2.667}Fe_{0.333}Sn_{1.7}In_{0.3}S_2$ using X-ray diffraction data. Reflection positions are marked. Olive markers, the shandite phase; navy markers, In_3S_4 (~ 5.2 wt %).

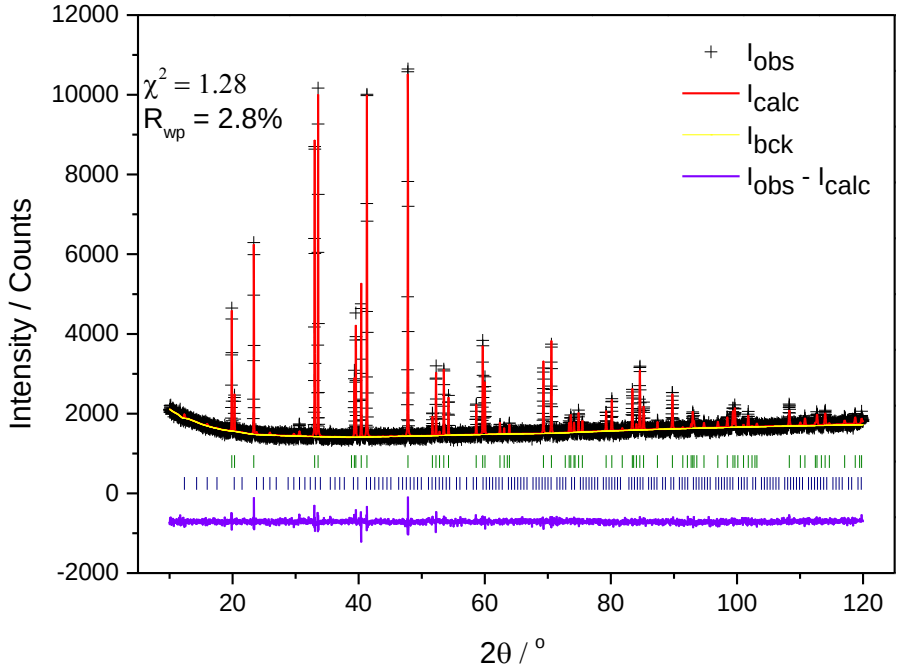

Figure 4.15 Final observed, calculated and difference profiles from Rietveld refinement for $Co_{2.667}Fe_{0.333}Sn_{1.4}In_{0.6}S_2$ using X-ray diffraction data. Reflection positions are marked. Olive markers, the shandite phase; navy markers, In_3S_4 (~ 4.4 wt %).

Data demonstrate that the shandite structure is adopted at all compositions with some traces of In_3S_4. Rietveld refinements were carried out according to the procedure of Section 4.2.1. Representative profiles are presented in Figures 4.14 and 4.15, while the remaining profiles are illustrated in Appendix H. As can be observed, the experimental data are described quite well ($1.27 \leq \chi^2 \leq 1.53$, $2.8 \leq R_{wp}$ / % ≤ 3.1) in the space group $R\bar{3}m$. In Figure 4.16, the lattice parameters α and c follow the same trend as described in 3.9.2.1 chapter, exhibiting similar values. The reduction of α lattice parameter creates a contraction of kagome layers, while the rise of c lattice parameter causes an increase in the interlayer spacing.

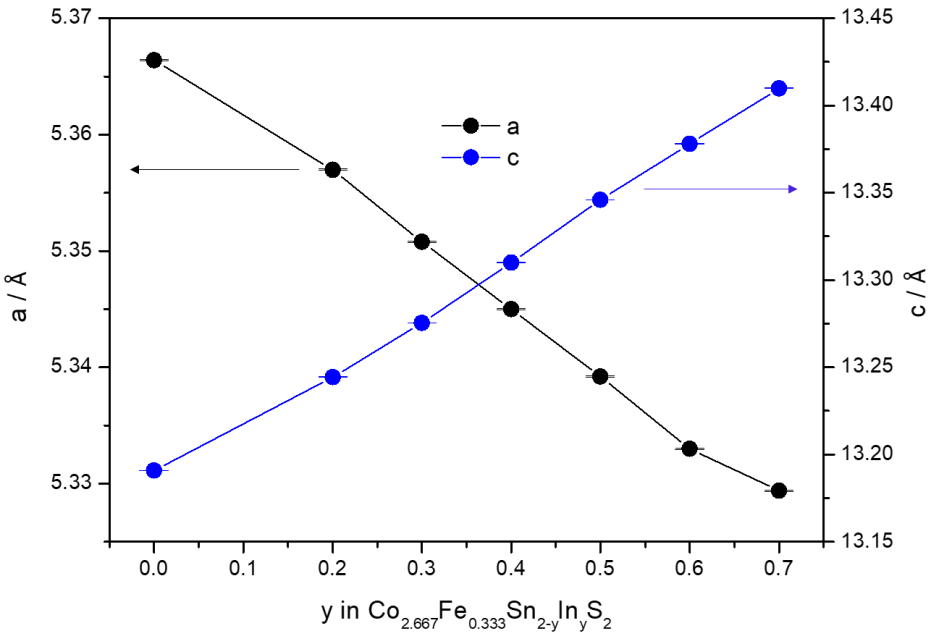

Figure 4.16 Lattice parameters determined by powder X-ray diffraction, for the series $Co_{2.667}Fe_{0.333}Sn_{2-y}In_yS_2$ ($0 \leq x \leq 0.7$).

4.3.2 Electrical transport properties for $Co_{2.667}Fe_{0.333}Sn_{2-y}In_yS_2$ ($0 \leq x \leq 0.7$)

Electrical transport property data reveal an increase in electrical resistivity with increased indium content (Figure 4.17). For $y \leq 0.2$, the materials exhibit a metallic behaviour as the electrical resistivity is increased slightly with the increase of temperature. For $y > 0.2$, ρ (T) reveals there is a transition to semiconducting behaviour.

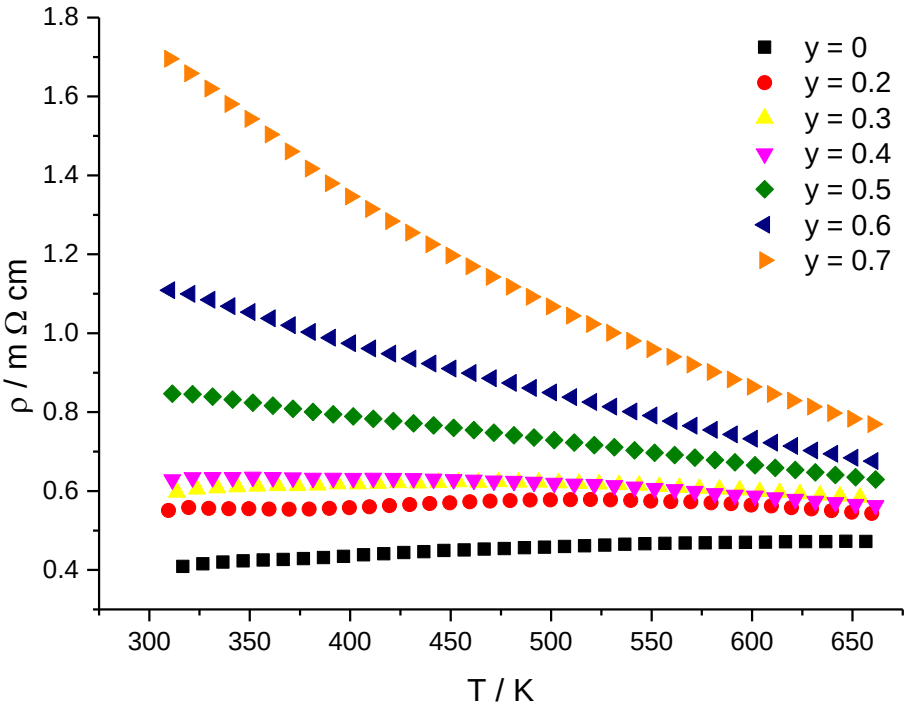

Figure 4.17 Electrical resistivity data for $Co_{2.667}Fe_{0.333}Sn_{2-y}In_y S_2$ ($0 \leq y \leq 0.7$) in the temperature range $300 \leq T / K \leq 650$.

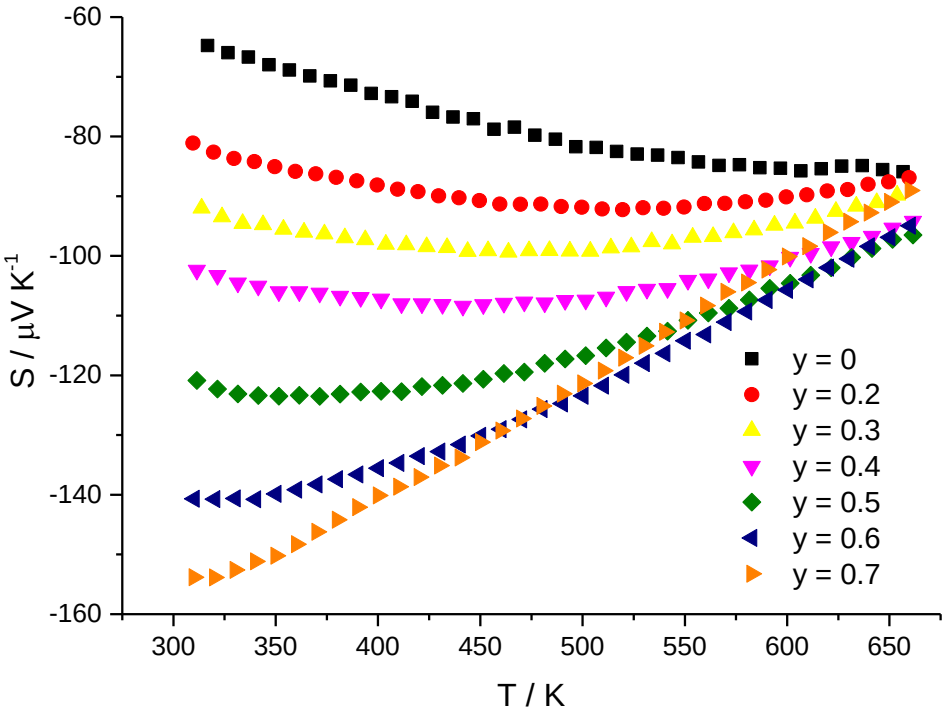

Figure 4.18 Seebeck coefficient data for $Co_{2.667}Fe_{0.333}Sn_{2-y}In_y S_2$ ($0 \leq y \leq 0.7$) in the temperature range $300 \leq T / K \leq 650$.

The negative values of the Seebeck coefficient of $Co_{2.667}Fe_{0.333}Sn_{2-y}In_yS_2$ ($0 \leq x \leq 0.7$) (Figure 4.18) demonstrate that *n*-type behaviour occurs at all compositions. It is notable that for this series there is a much greater compositional dependence of the Seebeck coefficient close to room temperature, compared to that of $Co_{2.5}Fe_{0.5}Sn_{2-y}In_yS_2$ ($0 \leq y \leq 0.6$). The value of -154 μV K^{-1} exhibited by $Co_{2.667}Fe_{0.333}Sn_{1.3}In_{0.7}S_2$ corresponds to an increase of *ca.* 140 % from that of the In-free phase.

There is a marked improvement of power factor (Figure 4.19) with increasing In content up to the composition with y = 0.6. For y = 0.7 the high increase in electrical resistivity outweighs the increase of Seebeck coefficient, resulting in an abrupt reduction of the power factor. The high electrical resistivity values for y = 0.7 sample agree with the predictions of DFT calculations which indicate that for a material with an In content 0.667, E_F is located in the energy band gap. The highest values of the power factor, *ca.* 19.2 μW cm^{-1} K^{-2}, are observed in the temperature range 400 - 450 K and exhibited by $Co_{2.667}Fe_{0.333}Sn_{1.5}In_{0.5}S_2$.

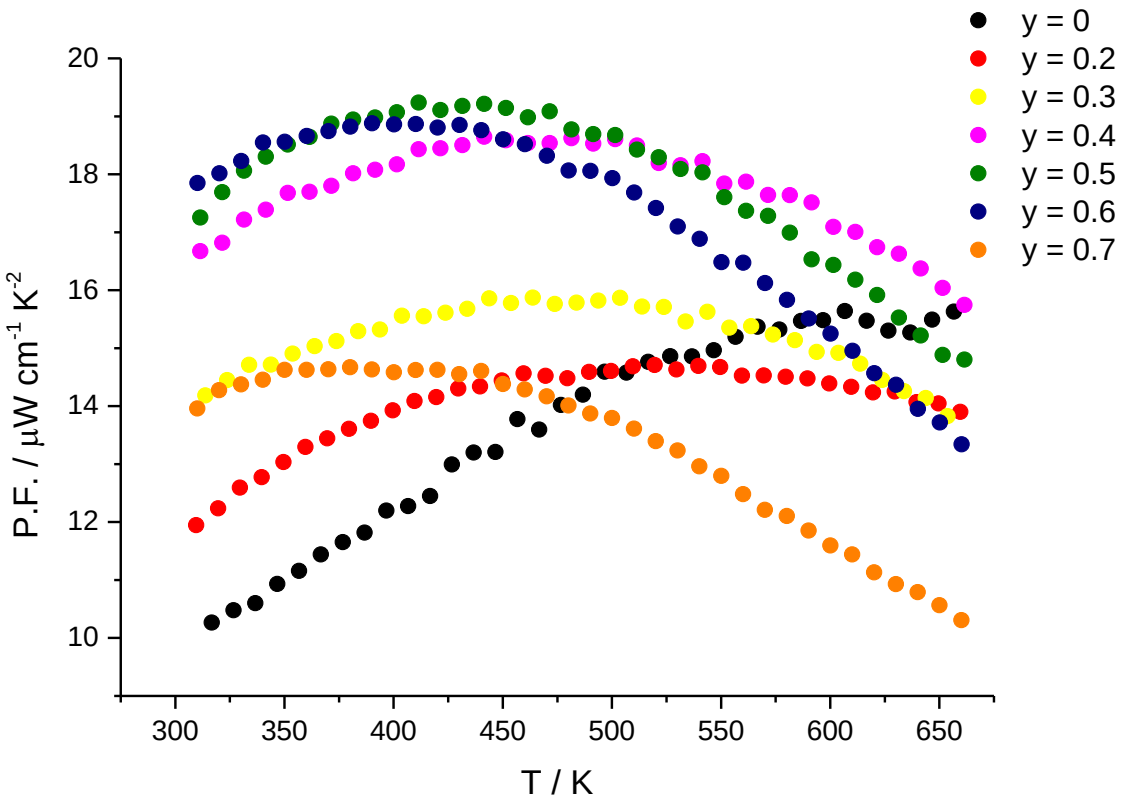

Figure 4.19 Power factor (P.F.) data for $Co_{2.667}Fe_{0.333}Sn_{2-y}In_y S_2$ ($0 \leq y \leq 0.7$) in the temperature range $300 \leq T / K \leq 650$.

Examination of the electrical resistivity and Seebeck coefficient as a function of In composition at a constant temperature (Figure 4.20) reveals that increasing the In content and consequently the number of holes drives the material to the semiconducting region with a characteristic increase of electrical resistivity and Seebeck coefficient. The optimum power factor is observed in the region where the ρ(T) and S(T) curves cross $0.4 \leq y \leq 0.6$.

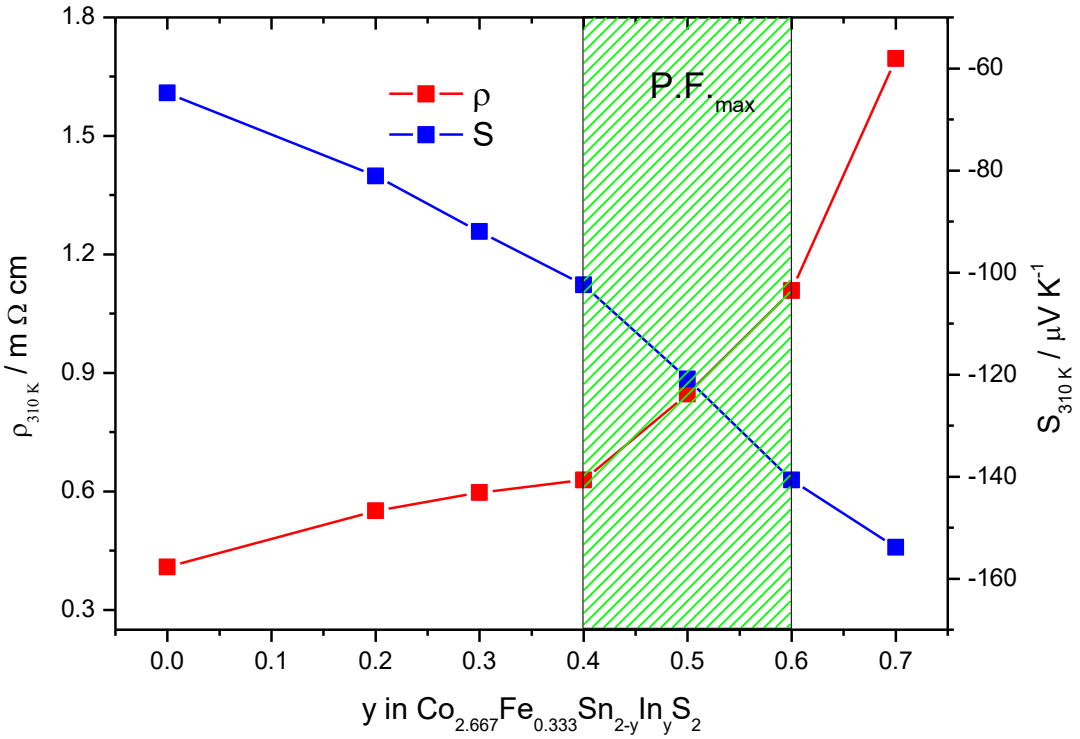

Figure 4.20 Electrical resistivity and Seebeck coefficient data in the series $Co_{2.667}Fe_{0.333}Sn_{2-y}In_y S_2$ ($0 \leq y \leq 0.7$) as a function of In content at the constant temperature of 310 K.

4.3.3 Thermal transport properties for $Co_{2.667}Fe_{0.333}Sn_{2-y}In_y S_2$ ($0 \leq y \leq 0.7$)

Thermal conductivity (κ) measurements were carried out as described in Section 2.7.2. The electronic contribution, κ_{el}, and hence the lattice contribution, κ_L, were determined using the Wiedemann-Franz law and the electrical resistivity data of Section 3.9.3.2. The thermal conductivity (Figure 4.21) is reduced with increasing In content as evidence by examination of Figure 4.22 which illustrates κ, κ_{el} and κ_L as a function of In composition at the constant temperature of 448 K.

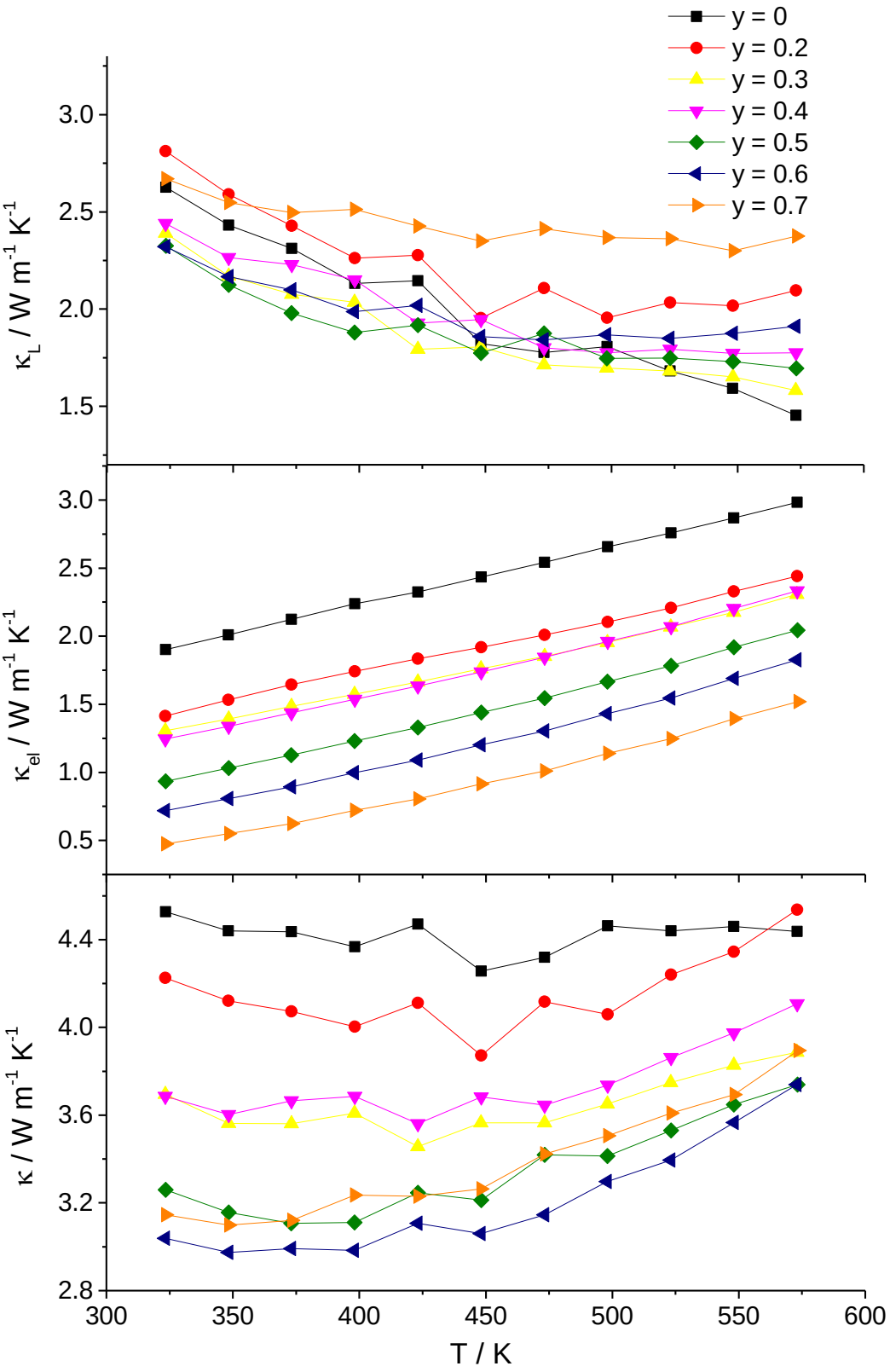

Figure 4.21 Thermal conductivity κ (bottom), electronic contribution, κ_e, (middle) and lattice contribution, κ_L, (top) as a function of temperature for $Co_{2.667}Fe_{0.333}Sn_{2-y}In_yS_2$ ($0 \leq y \leq 0.7$).

The total thermal conductivity is decreased mainly due to the reduction of electronic contribution with the In content, while the lattice contribution shows less dependence on composition. The largest differences in κ with respect to In content are observed close to room temperature. $Co_{2.667}Fe_{0.333}Sn_{1.4}In_{0.6}S_2$ exhibits the lowest values which correspond to a reduction of *ca.* 50 %.

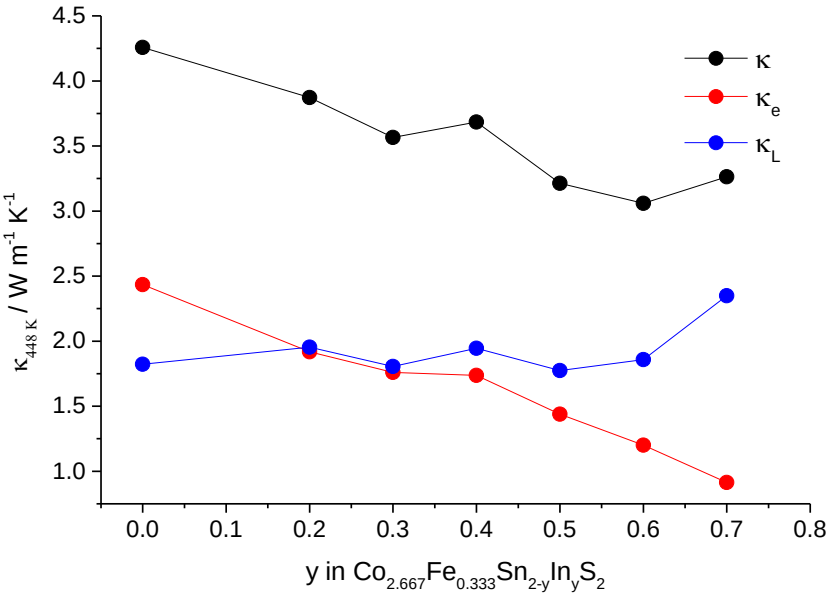

Figure 4.22 Compositional dependence of κ, κ_{el} and κ_L in $Co_{2.667}Fe_{0.333}Sn_{2-y}In_yS_2$ ($0 \leq y \leq 0.7$) at the constant temperature of 448 K.

4.3.4 Thermoelectric Figure-of-merit of $Co_{2.667}Fe_{0.333}Sn_{2-y}In_yS_2$ ($0 \leq y \leq 0.7$)

Using the physical property data of Section 4.3.3, the figures-of-merit for the series $Co_{2.667}Fe_{0.333}Sn_{2-y}In_yS_2$ ($0 \leq y \leq 0.7$) were determined. In substitution results in an improvement in TE performance of the series (Figure 4.23). The maximum ZT is exhibited by $Co_{2.667}Fe_{0.333}Sn_{1.4}In_{0.6}S_2$ at 473 K with the highest value of 0.28 which corresponds to an increase of 86 % compared to that of In-free phase. The figure-of-merit with respect to In content follows almost the same trend as that of the power factor. A gradual increase is observed up to y = 0.6, while for y = 0.7, ZT is reduced abruptly. The large increase in absolute value of Seebeck coefficient in combination with the reduction of thermal conductivity produces this marked improvement. Figure 4.24 presents ZT at 473 K as a function of the total number of holes per formula unit, x + y, which were introduced through the simultaneous Fe and In substitution in the initial $Co_3Sn_2S_2$ phase. The maximum ZT corresponds to x + y = 0.933.

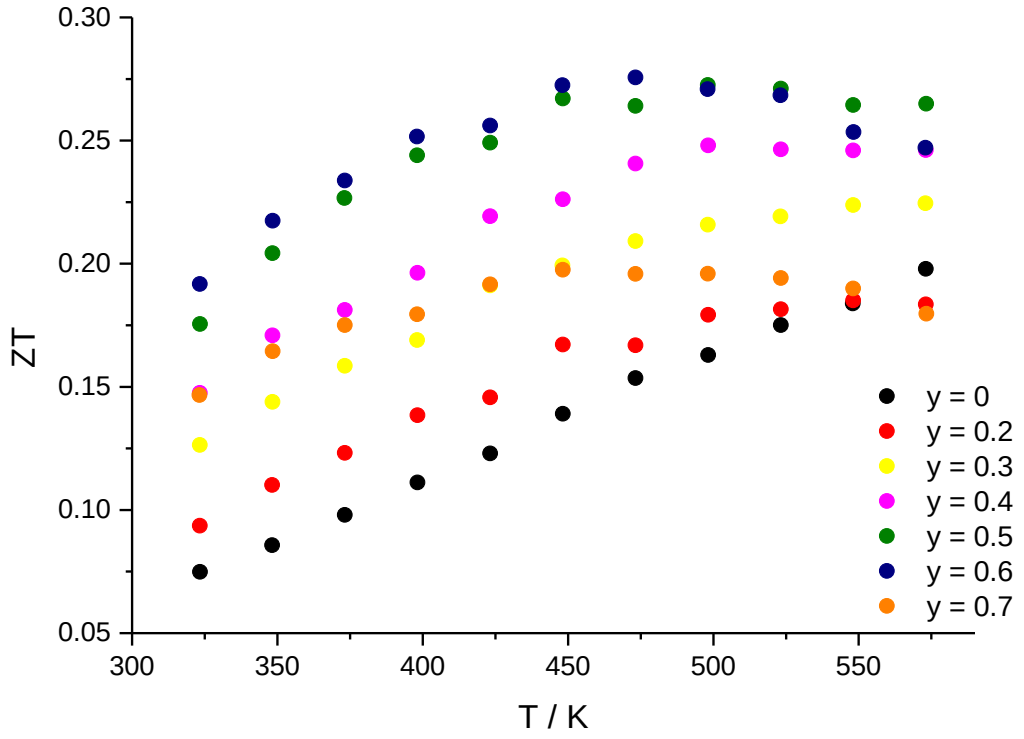

Figure 4.23 The figures-of-merit, ZT, for $Co_{2.667}Fe_{0.333}Sn_{2-y}In_yS_2$ ($0 \leq y \leq 0.7$) as a function of temperature.

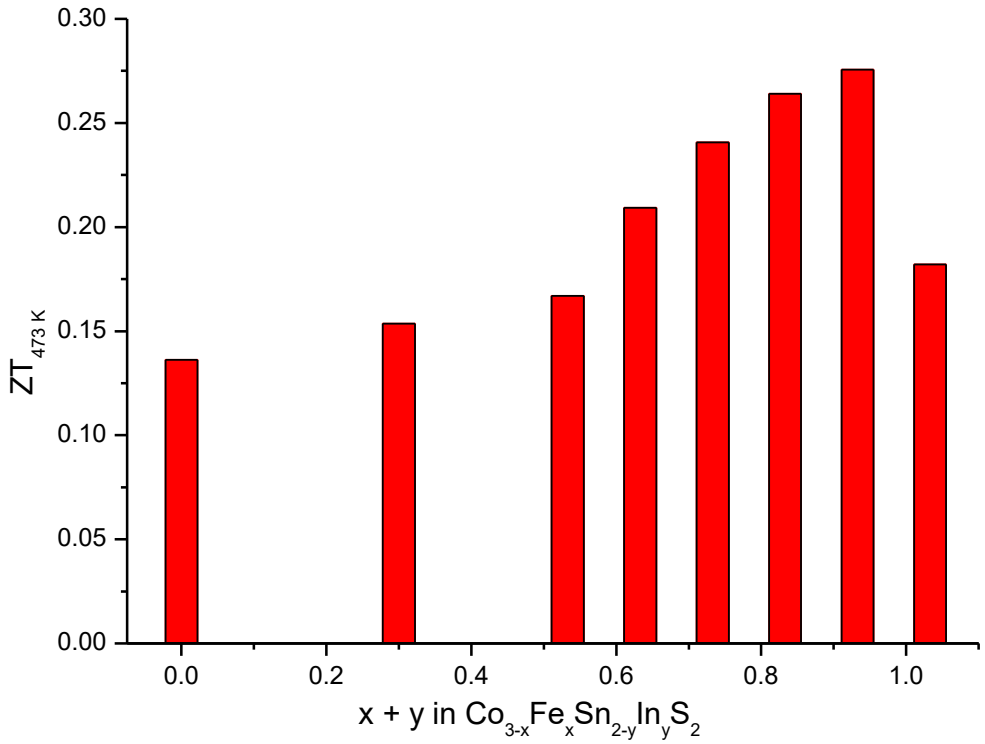

Figure 4.24 Figure-of-merit of $Co_{3-x}Fe_xSn_{2-y}In_yS_2$ ($x = 0.333$, $0 \leq y \leq 0.7$) at the constant temperature of 473 K as a function of x + y.

4.4 $Co_{3-x}Fe_xSn_{2-y}In_yS_2$, ($x + y \approx 0.9$)

Assuming that each replacement of Sn by In and Co by Fe generates one hole, the highest ZT values in both investigated series, $Co_{2.5}Fe_{0.5}Sn_{2-y}In_yS_2$ ($0 \leq y \leq 0.6$) and $Co_{2.667}Fe_{0.333}Sn_{2-y}In_yS_2$ ($0 \leq y \leq 0.7$), are exhibited by the samples with a total number of holes close to 0.9 per formula unit. It is notable that in the $Co_3Sn_{2-x}In_xS_2$ series,[94] the maximum ZT in the temperature range 400 – 500 K is achieved by samples with an indium content of $x = 0.8$ which is close to ≈ 0.9. The Co-end-member phase, $Co_3Sn_2S_2$, has 47 valence electrons and band structure calculations for this compound have shown that E_F crosses the narrow 24th valence band which is half-occupied. Hole doping through substitution with either indium or combination of iron and indium, causes a depopulation of the 24th band and a shift of E_F to lower energies. Hole doping with a total number of holes $x + y = 1$ per formula unit, reduces the valence electron count to 46 electrons and causes a complete depopulation of the half-occupied 24th band, shifting the E_F in the band gap. Therefore, when the material is doped with $x + y \approx 0.9$, E_F is moved towards the edge of the narrow 24th band. It is suggested that this crucial region may be the key to the large increase of Seebeck coefficient, through a more pronounced curvature in the density of states.

Furthermore, band structure calculations for $Co_3Sn_2S_2$ indicate that the 24th band is predominantly of *d* character. This means that the main contribution in the creation of this band comes from the *d* states of transition metal atoms, while *p* orbitals associated with the main group element do not contribute greatly in the formation of the band. Therefore, the substitution of cobalt by iron at the transition metal site may affect the density of states and the energy dependence of the 24th band. It is suggested here that the *d* states of iron atoms may shift the crucial region in which tuning of E_F may be used to optimize the Seebeck coefficient, to lower energies, closer to the edge of the 24th band. This could explain the observation that the highest ZT values in two investigated series of $Co_{3-x}Fe_xSn_{2-y}In_yS_2$ correspond to a hole content close to 0.9 per formula unit, an increase of 12.5 % compared to that one for the $Co_3Sn_{2-x}In_xS_2$ series.

However, the highest ZT values in $Co_{3-x}Fe_xSn_{2-y}In_yS_2$ is not only a matter of the number of holes. The amount of iron probably influences the energy dependence and the shape of the curvature at the edge of the 24th *d* band. Figure 4.25 shows electrical transport property data for three samples of $Co_{3-x}Fe_xSn_{2-y}In_yS_2$ with $x + y \approx 0.9$.

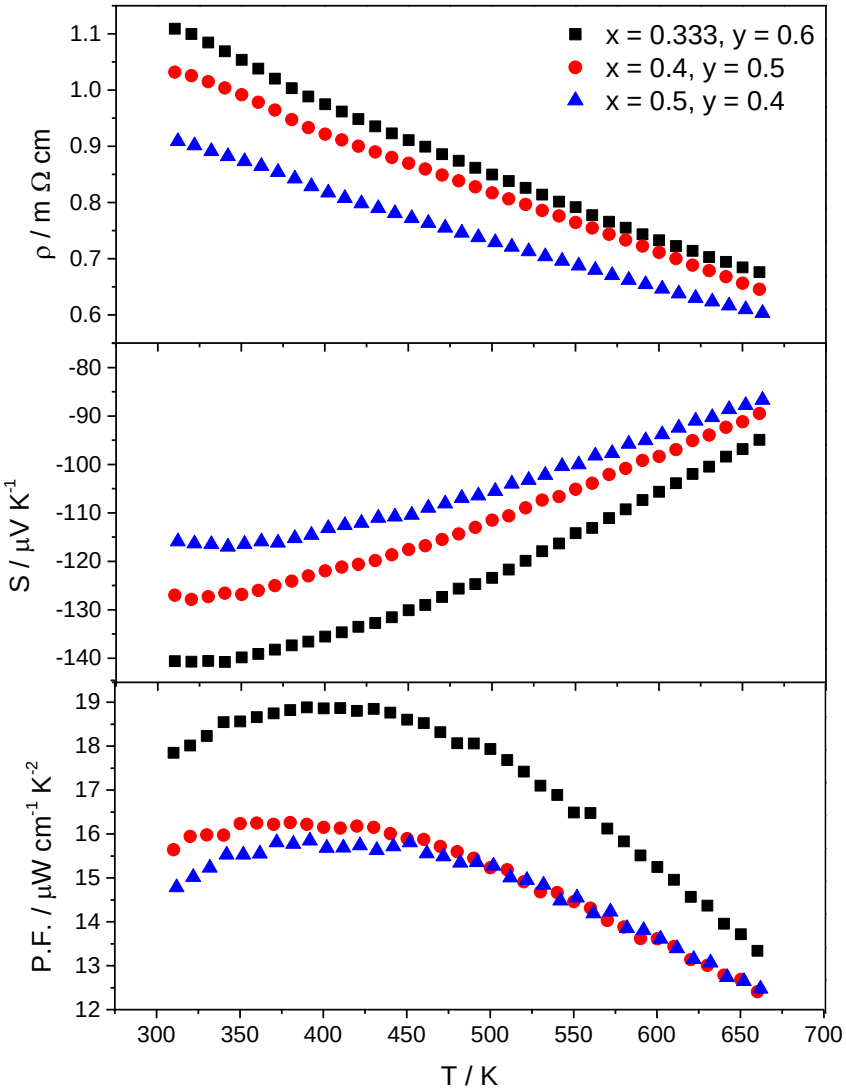

Figure 4.25 Electrical resistivity (top), Seebeck coefficient (middle) and power factor (bottom) data for $Co_{3-x}Fe_xSn_{2-y}In_yS_2$, ($x + y \approx 0.9$).

There are relatively small differences in electrical resistivity, especially for the samples with Fe content 0.333 and 0.4. However, the Seebeck coefficient shows more marked changes with composition. Although these three samples have almost the same level of doping, $Co_{2.667}Fe_{0.333}Sn_{1.4}In_{0.6}S_2$ exhibits the maximum Seebeck coefficient values. These results suggest an important role for iron in the optimization of Seebeck coefficient. Furthermore, the initial band structure calculations of Mr Alex Aziz of this Department support this view. It has been shown that the shandite $Co_{3-x}Fe_xSn_{2-y}In_yS_2$ series with x = 0.333 exhibit the highest Seebeck coefficient values. The specific amount of Fe may contribute to the sharpness of the DOS at the edge of the 24th *d* band.

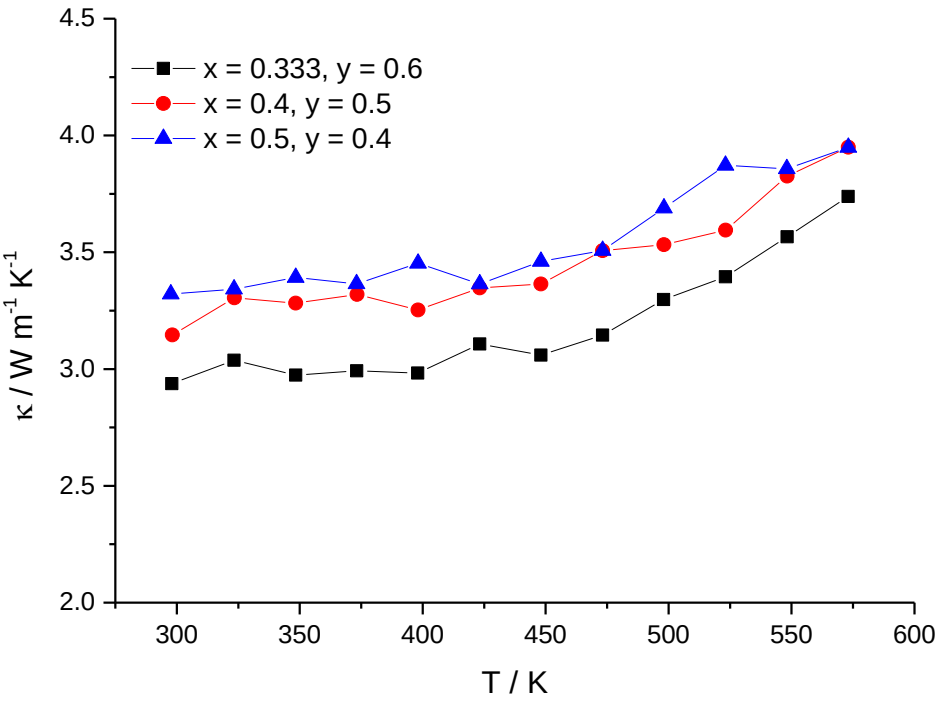

Figure 4.26 Thermal conductivity measurements for $Co_{3-x}Fe_xSn_{2-y}In_yS_2$, ($x + y \approx 0.9$).

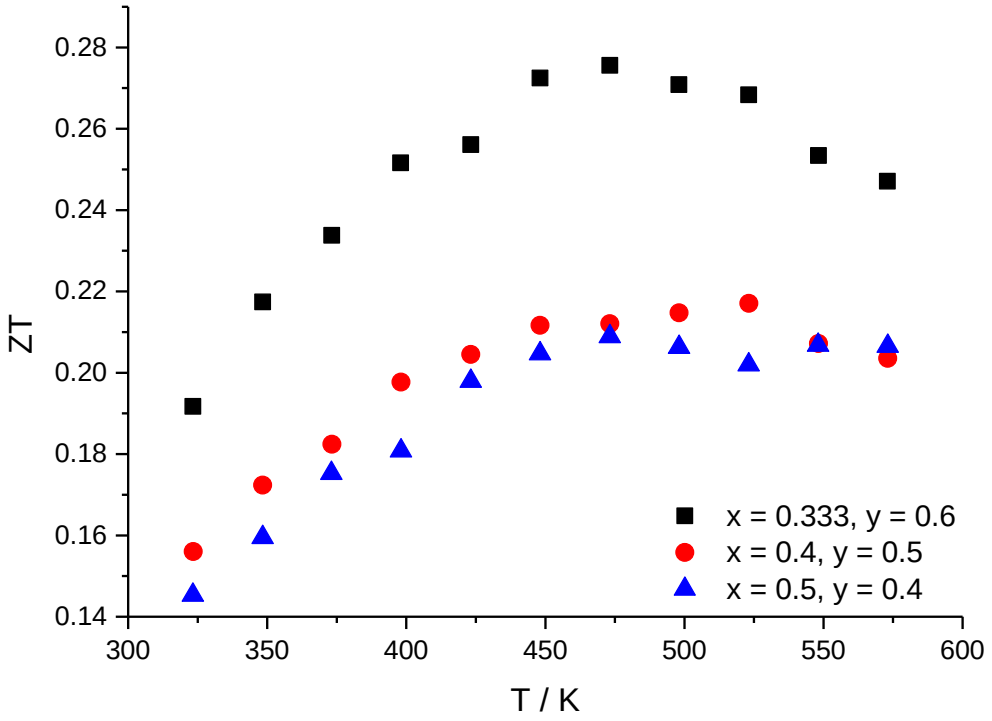

Figure 4.27 Figure-of-merit comparison for $Co_{3-x}Fe_xSn_{2-y}In_yS_2$, ($x + y \approx 0.9$).

Therefore, by tuning E_F at this region of density of states, a marked increase of Seebeck coefficient is achieved. The differences in the power factor values of $Co_{2.667}Fe_{0.333}Sn_{1.4}In_{0.6}S_2$ and the other two samples are notable. Figure 4.26 shows that there are no significant differences in thermal conductivity for these three samples with comparable doping levels. Further evidence for the importance of iron composition is provided by the fact that at 473 K, the ZT value of $Co_{2.667}Fe_{0.333}Sn_{1.4}In_{0.6}S_2$ (Figure 4.27) is almost 30 % higher than those of the other compounds. This increase in ZT comes mostly from the marked differences in the Seebeck coefficient, as the slightly lower thermal conductivity of $Co_{2.667}Fe_{0.333}Sn_{1.4}In_{0.6}S_2$ does not contribute greatly to this improvement.

4.5 Conclusions

In an effort to improve further the TE performance of the shandite sulphide, the simultaneous substitution of cobalt and tin by iron and indium respectively was carried out. Two series of general formula $Co_{3-x}Fe_xSn_{2-y}In_yS_2$ were prepared and powder X-ray diffraction demonstrated that the shandite structure was retained at all compositions. Rietveld refinements against powder X-ray diffraction data showed an increase in *c* lattice parameter with the increase of In content, leading to an increase in the spacing between the kagome layers. Initially, the $Co_{2.5}Fe_{0.5}Sn_{2-y}In_yS_2$ ($0 \leq y \leq 0.6$) series was investigated due to the fact that $Co_{2.5}Fe_{0.5}Sn_2S_2$ exhibited the highest ZT values close to room temperature. The TE properties of the $Co_{2.5}Fe_{0.5}Sn_{2-y}In_yS_2$ ($0 \leq y \leq 0.6$) series showed a small improvement in TE efficiency with the maximum ZT value of 0.21 exhibited by $Co_{2.5}Fe_{0.5}Sn_{1.6}In_{0.4}S_2$ at 473 K. Band structure calculations for $Co_{2.667}Fe_{0.333}Sn_{0.667}In_{0.333}S_2$ showed in the DOS narrow peaks close to E_F, suggesting that the investigation of the series $Co_{2.667}Fe_{0.333}Sn_{2-y}In_yS_2$ could increase the Seebeck coefficient by tuning the Fermi level to one of those peaks and improve the ZT.

The experimental results confirmed this prediction. Physical property measurements of $Co_{2.667}Fe_{0.333}Sn_{2-y}In_yS_2$ ($0 \leq y \leq 0.7$) reveal a large increase of 140 % in the Seebeck coefficient. $Co_{2.667}Fe_{0.333}Sn_{1.4}In_{0.6}S_2$ exhibits the highest ZT value of 0.28 at 473 K. This corresponds to an increase of 86 % over that of In-free phase. In both series investigated, the highest figure-of-merit is achieved, when the total hole content is close to 0.9 per formula unit. This number of holes optimizes the tuning of E_F in a region with a sharp curvature close to the edge of 24th valence band, resulting in a marked increase in Seebeck coefficient. This work also raises questions concerning the role of iron in the improvement of ZT in the series $Co_{2.667}Fe_{0.333}Sn_{2-y}In_yS_2$ ($0 \leq y \leq 0.7$). It is suggested

that the iron content affects the shape of the 24th *d* band in the DOS, providing a more pronounced curvature at the end of this band.

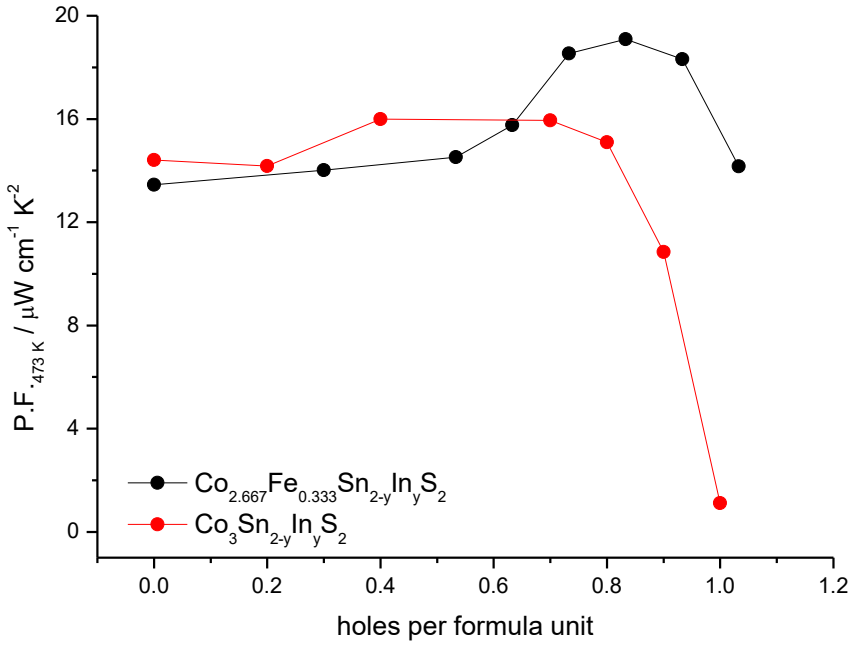

Figure 4.28 Power factors (P.F.) for $Co_{2.667}Fe_{0.333}Sn_{2-y}In_yS_2$ ($0 \leq y \leq 0.7$) and $Co_3Sn_{2-y}In_yS_2$ ($0 \leq y \leq 1$) as a function of the number of holes per formula unit at 473 K.

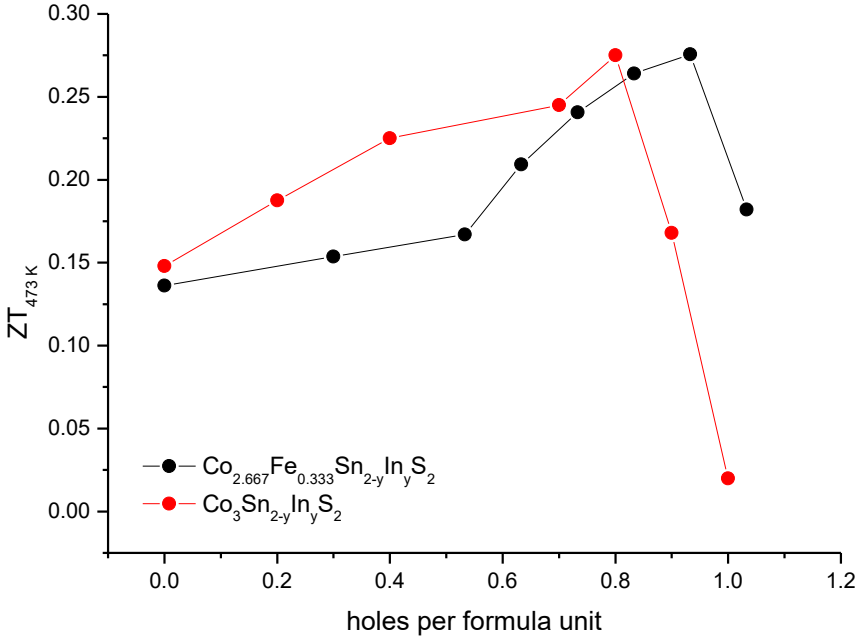

Figure 4.29 ZT of $Co_{2.667}Fe_{0.333}Sn_{2-y}In_yS_2$ ($0 \leq y \leq 0.7$) and $Co_3Sn_{2-y}In_yS_2$ ($0 \leq y \leq 1$) as a function of the number of holes per formula unit at 473 K.

Comparing the thermoelectric properties of $Co_{2.667}Fe_{0.333}Sn_{2-y}In_yS_2$ ($0 \leq y \leq 0.7$) and $Co_3Sn_{2-y}In_yS_2$ ($0 \leq y \leq 2$)[94] series as a function of number of holes per formula unit (Figures 4.28 and 4.29), useful conclusions are extracted about the benefits of the simultaneous substitution of iron and tin in the general improvement of the shandite sulphide as a candidate TE material. The series with the iron content of x = 0.333 exhibits higher power factors which reach 19.2 $\mu W\ cm^{-1}\ K^{-2}$ for y = 0.5: a particularly high value for a sulphide. ZT_{max} reaches almost the same values in both series (Figure 4.29). A slightly larger amount of hole doping in $Co_{2.667}Fe_{0.333}Sn_{2-y}In_yS_2$ ($0 \leq y \leq 0.7$) is required to achieve the maximum power factor and ZT values, increasing the number of holes per formula unit to 0.9333. However, the introduction of the iron content of x = 0.333 provides a less expensive synthesis route. Substituting an amount of Co by Fe which is a more earth-abundant element, and using less amount of In, the same levels of TE performance are reached. It is marked that for temperatures T ≤ 473 K, $Co_{2.667}Fe_{0.333}Sn_{1.4}In_{0.6}S_2$ exhibits a higher TE performance from other novel sulphides as Co_xTiS_2,[17] $Cu_{1-x}Co_xFeS_2$,[61] $Cu_{12}Sb_4S_{13}$,[65] PbS[45] and $LaGd_{1.02}S_3$.[58] This makes the shandite sulphide to occupy a more competitive position in Te-free, non-toxic thermoelectrics for low-grade waste-heat recovery.

Chapter 5 - Quaternary Chalcogenides

5.1 Introduction

The quaternary chalcogenides with the general formula A_2BCQ_4 (A = Cu, Ag; B = Zn, Cd; C = Sn, Ge; Q = S, Se) have attracted great interest for a wide range of environmentally friendly applications, such as solar cells,[117-119] candidate thermoelectrics[120-123] and photocatalysts for solar water splitting.[124] It is remarkable that thin film solar cells made from Cu_2ZnSnQ_4 (Q = S, Se) exhibit efficiencies of around 12.6%.[125,126] Although these compounds have been investigated for more than 40 years,[18] the detailed characterization of their crystal structure is still a disputed subject. The majority of reports describe these compounds at room temperature in either the stannite (space group $I\bar{4}2m$) or kesterite (space group $I\bar{4}$) derivatives of zinc-blende (Figure 1.5). The similarity of diffraction patterns of these two structures and the presence of elements with similar atomic numbers introduce ambiguity in the structural characterization using X-ray diffraction. Moreover, there is some confusion in the literature concerning the terms 'stannite' and 'kesterite'. Here, the term 'stannite' denotes only the ordered configuration crystallising in the space group $I\bar{4}2m$. If for instance an *A*/*B* disorder occurs in $I\bar{4}2m$ and *B* atoms occupy both *2a* and *4d* sites, this configuration is neither the stannite nor kesterite structure. In the special case, where all *B* atoms are located in z = 0.25 and 0.75 planes and have the same probability with *A* atoms to occupy either *2c* or *2d* sites, then a new symmetry is created where all *4d* sites are equivalent. Both Cu and Zn cations occupy 50 % of *4d* sites and the structure is described in the space group $I\bar{4}2m$ as fully disordered kesterite (Figure 5.1).[127]

The Cu_2ZnSnQ_4 (Q = S, Se) phases (CZTS and CZTSe) have been generally described in the kesterite structure.[75, 119, 128-131] However, there are many experimental X-ray diffraction studies which have characterized these compounds as stannite-type.[132, 123, 133] Chen et al. showed that for the CZTS and CZTSe phases the most stable configuration is the ordered kesterite structure but the small energy differences could lead to either the stannite or the disordered configurations being present in experimental samples.[118, 134]

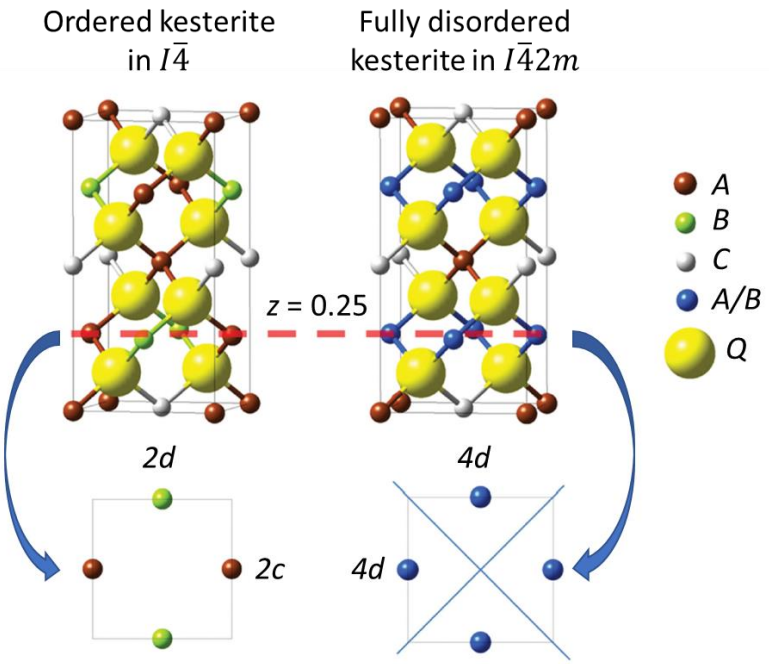

Figure 5.1 Illustration of ordered (left) and fully disordered (right) kesterite structure. Adapted from Bourdais et al.[127]

In 2011, a neutron diffraction study by Schorr[135] showed the existence of Cu/Zn disorder on the 2*c* and 2*d* sites in Cu_2ZnSnQ_4 (*Q* = S, Se). Paier et al.[136] have also suggested that cation disorder may be present within the Cu-Zn layer. Studies into the Ag analogues, $AgZnSnS_4$ (AZTS) and $AgZnSnSe_4$ (AZTSe), have indicated the kesterite structure in both experimental[130, 137] and computational work.[138] However, there is no reported study yet which provides an in-depth structural characterization, including possible cation ordering of Ag/Zn or Ag/Sn atoms.

The structural characterization of Cu_2ZnGeQ_4 (*Q* = S, Se) analogues (CZGS and CZGSe) has also been a contentious issue. Many reports suggest for these phases the zinc-blende stannite-type structure at room temperature,[74, 122, 124, 139, 130] while above 790 °C a phase transition to wurtzite-stannite structure has been observed for Cu_2ZnGeS_4, using X-ray diffraction.[140] However, first-principle calculations show clearly that both CZGS and CZGSe compounds are more stable in the kesterite structure.[18] Recently, Guc et al.[141] on the basis of polarized Raman spectroscopy and first-principle calculations, suggested that CZGS crystallizes in the kesterite structure, $I\bar{4}$. Another study describes the series $Cu_2ZnGeSe_{4-x}S_x$ in the space group $I\bar{4}2m$.[142] However, ^{63}Cu nuclear magnetic resonance (NMR) indicates two distinct sites for Cu atoms in CZGSe, which merge into one above 450 K. TGA/DSC analysis has also revealed an exothermic feature close to 450 K.[122] This corresponds to a phase transition,

from semiconducting to metallic behaviour, which has a marked influence in the transport properties of the material. This phase transition has not been identified yet and an in-depth structural investigation is necessary.

The lattice parameters of the kesterite and stannite derivatives are similar, which together with the similar X-ray scattering powers of the cations involved, makes the structural determination by powder X-ray diffraction ambiguous. Neutrons provide good contrast between the component cations (Table 2.1). Therefore, in the current investigation, powder neutron diffraction has been exploited to address the problem of establishing the correct ground state structures of the quaternary chalcogenides A_2ZnCQ_4 (*A* = Cu, Ag; *C* = Sn, Ge; *Q* = S, Se). Powder neutron diffraction has also been used to study the structure of Cu_2ZnGeQ_4 (*Q* = S, Se) as a function of temperature in order to investigate possible phase transition and the evolution of cation ordering.

Previous studies of the *p*-type semiconductor $Cu_2ZnGeSe_4$ have shown that hole doping enhances its thermoelectric properties. The introduction of holes through the substitution of Zn by Cu in $Cu_{2+x}Zn_{1-x}GeSe_4$ ($0 \leq x \leq 0.1$), results in a significant reduction in electrical resistivity due to the increase of the charge carrier concentration. The composition x = 0.075 exhibits the maximum ZT of 0.45 at 670 K.[122] An analogous improvement in the thermoelectric performance is achieved through the substitution of Ge by In, where the maximum value of ZT = 0.33 is obtained by $Cu_2ZnGe_{0.925}In_{0.075}Se_4$ at 673 K.[74] In the current work, hole doping is carried out through the chemical substitution of Ge by Cu in an effort to improve the thermoelectric performance of $Cu_2ZnGeSe_4$.

5.2 Synthesis

5.2.1 $Cu_2Zn*BQ*_4$ (*B* = Sn, Ge; *Q* = S, Se)

Appropriate mixtures of elemental copper (Sigma-Aldrich, powder, 99.999 %), zinc (Sigma-Aldrich, powder, < 150 µm, 99.995 %), germanium (Sigma-Aldrich, powder, ≥ 99.999 %), tin (Sigma-Aldrich, powder, ≥ 99 %), sulfur (Sigma-Aldrich, flakes, 99.99 %) and selenium (Sigma-Aldrich, pellets, < 5 mm, ≥ 99.99 %) were ground with an agate pestle and mortar and the mixture placed in a fused silica tube which was subsequently evacuated and sealed at 10^{-4} mbar as described in Section 2.1.1. Two firings followed for each compound with one intermediate grinding. The first firing for both selenide compounds and for Cu_2ZnSnS_4 was carried out at 650 ˚C for 48 hours, while the Cu_2ZnGeS_4 sulphide was reacted at the same temperature for 96 hours. The second firing of the selenides was carried out at 800 ˚C for 96 hours, while the synthesis

of sulphides, Cu_2ZnSnS_4 and Cu_2ZnGeS_4, required a second firing for 96 hours at 850 ˚C and 700 ˚C respectively. A heating / cooling rate of 2 ˚C min^{-1} was used in all cases.

5.2.2 Ag_2ZnSnS_4

Stoichiometric quantities of elemental silver (Sigma-Aldrich, powder, 99.99+ %), zinc (Sigma-Aldrich, powder, < 150 µm, 99.995 %), germanium (Sigma-Aldrich, powder, ≥ 99.999 %), tin (Sigma-Aldrich, powder, ≥ 99 %), sulfur (Sigma-Aldrich, flakes, 99.99 %) and selenium (Sigma-Aldrich, pellets, < 5 mm, ≥ 99.99 %) were ground together using an agate pestle and mortar. The resulting mixture was sealed under vacuum (10^{-4} mbar) into fused silica tubes. For the synthesis of Ag_2ZnSnS_4 one firing was necessary at 650 ˚C for 96 hours with a heating / cooling rate of 0.5 ˚C min^{-1}.

5.2.3 $Ag_2ZnSnSe_4$

A combination of mechanical alloying (Section 2.1.2) and thermal annealing was used for the synthesis of $Ag_2ZnSnSe_4$. Stoichiometric amounts of elemental silver (Sigma-Aldrich, powder, 99.99+ %), zinc (Sigma-Aldrich, powder, < 150 µm, 99.995 %), tin (Sigma-Aldrich, powder, ≥ 99 %) and selenium (Sigma-Aldrich, pellets, < 5 mm, ≥ 99.99 %) were mixed in a glove box and sealed under an Ar atmosphere into a stainless, steel jar of 25 ml together with 30 steel balls. The powdered mixture was milled for 4 h at 600 rpm. After milling, the collection of the powder was carried out in the glove box in order to avoid the oxidation of the sample. Subsequently, the powder was loaded and sealed in a silica tube under vacuum (10^{-4} mbar) in order to anneal the product for 30 min at 500 ˚C.

5.3 Structural Characterization

The initial structural characterization of the quaternary chalcogenides was carried out using powder X-ray diffraction. The data were collected at room temperature according to the description in Section 2.2. The purity of the samples was evaluated using the EVA software package. Traces of impurities were identified in some of them. The powder diffraction data for Cu_2ZnGeS_4 and $Cu_2ZnGeSe_4$ are consistent with the presence of a single phase. Small amounts of SnS and SnSe were present in the tin analogues, Cu_2ZnSnS_4 and $Cu_2ZnSnSe_4$, respectively. The powder diffraction pattern of Ag_2ZnSnS_4 shows no evidence for the presence of secondary phases, while in the

corresponding selenide, trace amounts of $SnSe_2$ and ZnSe were detected. Rietveld refinements were carried out for all materials using the powder X-ray diffraction data. However, the almost identical X-ray scattering factors of Cu^+ and Zn^{2+} cations and the similarity of the diffraction patterns arising from the space groups $I\bar{4}2m$ and $I\bar{4}$ did not allow the unambiguous identification of the particular zinc-blende derivative for the copper compounds. However, X-rays provide reasonable contrast between Ag^+ and Zn^{2+} cations and Rietveld refinements for Ag_2ZnSnQ_4 (Q = S, Se) indicate that ordered kesterite structure may be favoured in these cases, as it leads to a slightly lower goodness of fit parameter, χ^2.

5.3.1 Powder neutron diffraction study of A_2ZnCQ_4 at room temperature

Powder neutron diffraction data were collected at room temperature using the GEM diffractometer of the ISIS facility, Rutherford Appleton laboratory (Section 2.3.1). Multibank Rietveld refinements were conducted using the GSAS software package. Data from the high-resolution bank 6 (2θ = 154˚), bank 5 (2θ = 91˚), bank 4 (2θ = 63˚) and bank 3 (2θ = 35˚) were used. In order to exploit the Ag/Zn contrast provided by X-rays, the powder X-ray diffraction data of the silver compounds were included in the multibank neutron diffraction refinements (Figures 5.6 and 5.7). The combination of X-ray and neutron diffraction data in the Rietveld analysis is necessary for the silver-containing phases because the neutron scattering factors of Ag and Zn are similar (Table 2.1). In the Rietveld analysis, structural models in space groups $I\bar{4}2m$ and $I\bar{4}$ were investigated for all compounds. The crystallographic information for structural models in both space groups are presented in Tables 5.1. The refined lattice parameters and atomic coordinates of Q anions from the X-ray diffraction refinements were used for the initial structural models. The multibank Rietveld refinements were carried out according to the process described in Section 3.3.2.1. The background parameters were refined using the reciprocal interpolation function and the peak shape was modelled using the pseudo-Voigt function. All cation positions were examined for possible disorder, whilst constraining the thermal parameters of the elements on the same site to be equivalent. In each case where the possibility of disorder was investigated, two constraints were set on the occupancy factors: the sum of occupancy factors of cations on the same position was constrained at units and each position was assumed to be fully occupied. The resulting multibank Rietveld refinements of the quaternary compounds are illustrated in Figures 5.2 to 5.7. The refined lattice parameters, the calculated volume of the unit cell and atomic coordinates of the Q anions are presented in Table 5.2.

Table 5.1 Atomic coordinates of A_2ZnCQ_4 in $I\bar{4}2m$ and $I\bar{4}$ models.

Space Group $I\bar{4}2m$				
Atom	**Wyckoff Site**	**x**	**y**	**z**
A	4d	0	0.5	0.25
Zn	2a	0	0	0
C	2b	0	0	0.5
Q	8i	*x*	*x*	*z*
Space Group $I\bar{4}$				
Atom	**Wyckoff Site**	**x**	**y**	**z**
A	2c	0	0.5	0.25
Zn	2d	0	0.5	0.75
A	2a	0	0	0
C	2b	0	0	0.5
Q	8g	*x*	*y*	*z*

The site occupancy factors and isotropic thermal parameters for each position are presented in Table 5.3 and Table 5.4. Bond distances between cations and anions are presented in Table I1, Appendix I. The Rietveld analysis for Cu_2ZnGeQ_4 (Q = S, Se) revealed that their structures are better described in the space group $I\bar{4}$ than the space group $I\bar{4}2m$. This effectively excludes the possibility either of these two materials adopts the stannite-type structure. Investigating possible disorder on the cation positions, the refinement of the occupancy factors for the *2c* and *2d* positions showed disorder between the Cu and Zn cations. In Cu_2ZnGeS_4, the *2c* site is occupied by *ca.* 67 % of Cu and *ca.* 33 % of Zn and vice versa in *2d* position. Rietveld refinement provided no support for alternative disordering schemes (Cu/Zn on *2a* position, Cu/Ge or Zn/Ge on *2b* position were all attempted). In the selenide analogue, the *2c* position is occupied by *ca.* 71 % of Cu and *ca.* 28 % of Zn cations. The *2a* and *2b* positions are fully occupied by Cu and Ge cations respectively. Therefore, in both Cu_2ZnGeQ_4 (Q = S, Se) phases, their structures are characterized as disordered kesterites. The results for $Cu_2ZnGeSe_4$ are in a good agreement with a recent neutron diffraction study which also suggests a disordered kesterite structure for this material.[143] Comparing the unit cells of the two germanium-containing chalcogenides, it is evident that the substitution of sulphur by the larger selenium increases the lattice parameters, *a* and *c*, resulting in an increase of unit cell volume of *ca.* 16 %.

The refinements for both tin-containing chalcogenides, Cu_2ZnSnS_4 and $Cu_2ZnSnSe_4$, showed that their structures are best described in the space group $I\bar{4}$ with a small degree of disorder of Cu and Zn cations in the z = 0.25 and 0.75 planes. In Cu_2ZnSnS_4, the *2c* position is occupied by *ca.* 94.5 % of Cu and *ca*. 5.5 % of Zn cations. In the selenide analogue, the occupancy of Cu and Zn cations in the *2c* position is *ca.* 92 % and *ca.* 8 % respectively. In both cases, disorder in the other two cation sites are not observed.

Table 5.2 Refined lattice parameters, unit cell volume and refined atomic coordinates of *Q* (*Q* = S, Se) anions for A_2ZnCQ_4 (*A* = Cu, Ag; *C* = Sn, Ge; *Q* = S, Se).

Space group $I\bar{4}$						
	a / Å	c / Å	V / Å^3	*x(Q)*	*y(Q)*	*z(Q)*
CZGS	5.34333(2)	10.51126(6)	300.108(2)	0.246(3)	0.2650(9)	0.1224(2)
CZGSe	5.60873(2)	11.04297(6)	347.388(3)	0.2479(5)	0.2584(1)	0.1243(1)
CZTS	5.43218(3)	10.8308(1)	319.603(4)	0.2423(5)	0.2375(4)	0.1269(5)
CZTSe	5.69544(5)	11.3417(2)	367.902(6)	0.2382(5)	0.247(1)	0.1287(1)
AZTS	5.81261(3)	10.77886(7)	364.179(4)	0.243(1)	0.2216(3)	0.1289(3)
AZTSe	6.04419(3)	11.30653(9)	413.052(5)	0.2455(4)	0.2288(1)	0.1288(1)

Table 5.3 The refined site occupancy factors at each crystallographic position of A_2ZnCQ_4 (*A* = Cu, Ag; *C* = Sn, Ge; *Q* = S, Se).

Space group **$I\bar{4}$**					
	2c	*2d*	*2a*	*2b*	*8g*
CZGS	0.67(1) Cu 0.33(1) Zn	0.33(1) Cu 0.67(1) Zn	1.0(-) Cu	1.0(-) Ge	1.0(-) S
CZGSe	0.71(1) Cu 0.29(1) Zn	0.29(1) Cu 0.71(1) Zn	1.0(-) Cu	1.0(-) Ge	1.0(-) Se
CZTS	0.945(9) Cu 0.055(9) Zn	0.055(9) Cu 0.945(9) Zn	1.0(-) Cu	1.0(-) Sn	1.0(-) S
CZTSe	0.92(2) Cu 0.08(2) Zn	0.08(2) Cu 0.92(2) Zn	1.0(-) Cu	1.0(-) Sn	1.0(-) Se
AZTS	1.0(-) Ag	1.0(-) Zn	1.0(-) Sn	1.0(-) Sn	1.0(-) S
AZTSe	1.0(-) Ag	1.0(-) Zn	1.0(-) Sn	1.0(-) Sn	1.0(-) Se

Table 5.4 Refined thermal parameters on each crystallographic position of A_2ZnCQ_4 (A = Cu, Ag; C = Sn, Ge; Q = S, Se).

	Uiso(2c) *(Å²)*	*Uiso(2d)* *(Å²)*	*Uiso(2a)* *(Å²)*	*Uiso (2b)* *(Å²)*	*Uiso(8g)* *(Å²)*
CZGS	0.9(2)	1.4(3)	1.1(4)	0.9(3)	0.59(2)
CZGSe	1.40(2)	1.86(3)	1.72(2)	1.25(2)	0.967(3)
CZTS	1.86(2)	1.23(2)	1.83(2)	0.83(2)	0.93(1)
CZTSe	1.5(2)	2.2(3)	2.2(1)	0.9(1)	1.15(2)
AZTS	1.82(8)	1.5(1)	0.36(6)	2.67(8)	0.90(4)
AZTSe	2.18(5)	1.25(5)	0.82(3)	2.73(5)	0.961(6)

The *2a* and *2b* positions are fully occupied by copper and tin atoms respectively. In the neutron study of Schorr,[135] higher levels of Cu/Zn disorder were observed in the z = 0.25 and 0.75 planes. The site occupancy factors of Cu and Zn cations on the *2c* and *2d* sites depend on cooling conditions during the synthesis process. The quenched Cu_2ZnSnS_4 sample exhibited a Cu/Zn disorder of 50 %, while the sample which was treated with an applied cooling rate of 1 K h^{-1}, corresponded to a 30 % disorder. A recent powder neutron diffraction study on Cu_2ZnSnS_4 showed that the conditions for the final annealing step during the synthesis of the compound play a critical role in determining the extent of cation ordering in the z = 0.25 and 0.75 planes.[144] An order-disorder transition was revealed for CZTS samples annealed at different temperatures in the range of $473 \leq T / K \leq 623$. Annealing up to 513 K, an ordered arrangement is observed, while annealing above 553 K, results in a structure that is fully disordered. In the present case, a cooling rate of 2 K min^{-1} was applied after each firing for both CZTS and CZTSe. It is concluded that the synthesis process and conditions affect strongly the level of Cu/Zn disorder in the kesterite structure of tin chalcogenides. Their comparison with the germanium chalcogenides shows that the substitution of Ge by the larger Sn causes an increase of unit cell volume; *ca.* 6.5 % for the sulphide and *ca.* 6 % for the selenide.

Combining powder neutron and X-ray diffraction data, the Rietveld analysis for silver-containing phases revealed an ordered kesterite structure in each case. No Ag/Zn disorder was observed in the planes at z = 0.25 and 0.75 planes. The *2c* and *2a* sites are occupied exclusively by silver cations and the *2d* site is occupied only by zinc. Moreover, the refinement did not show any evidence for Ag/Sn disorder in the *2b* site of

Sn cations. Substituting the copper by the larger silver, an increase of the unit cell volume is observed for both sulphide (*ca.* 14 %) and selenide (*ca.* 12 %).

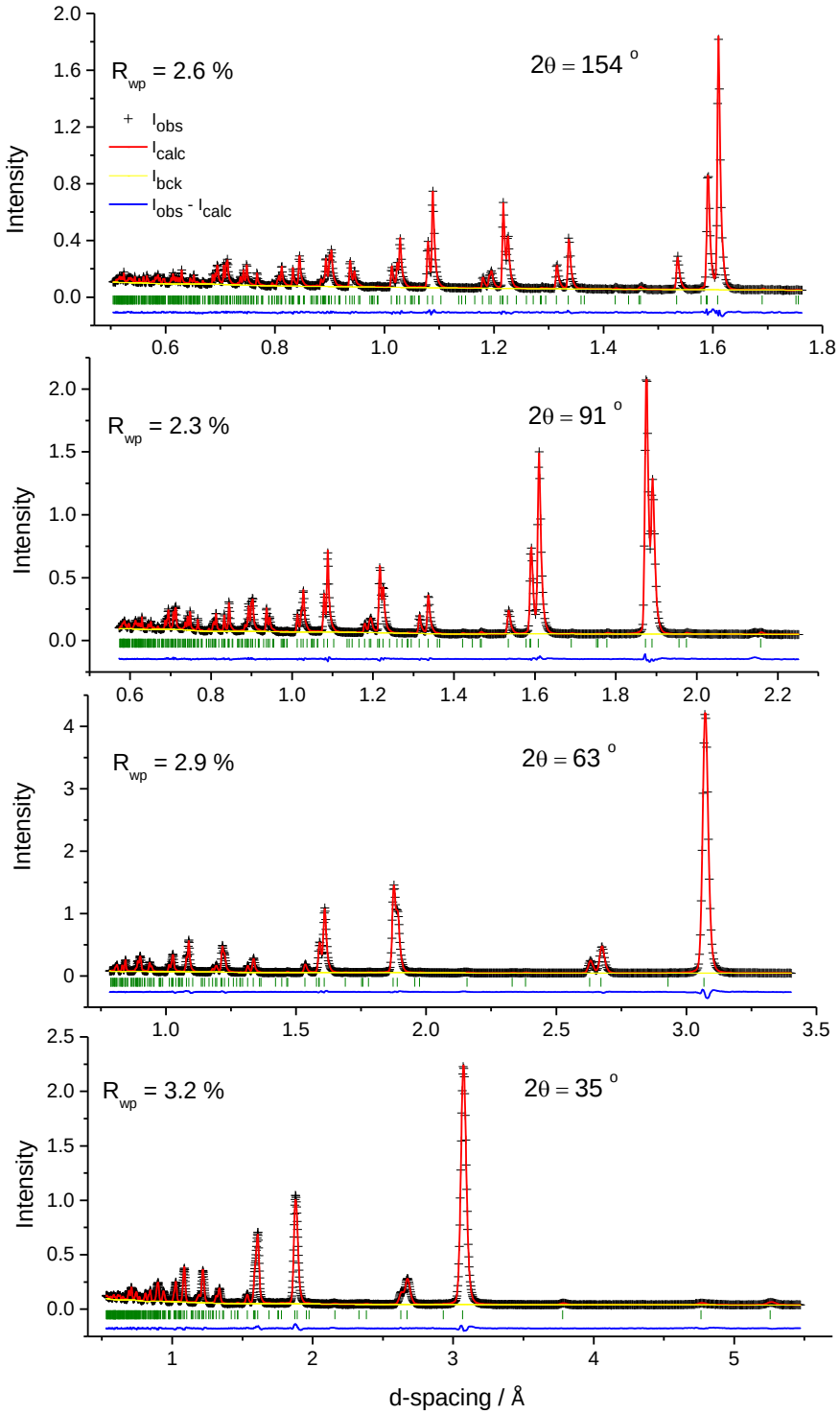

Figure 5.2 Multibank Rietveld refinement for Cu_2ZnGeS_4 using powder neutron diffraction data collected at room temperature (χ^2 = 2.8). Observed (black crosses), refined (red solid lines), difference (blue bottom line) and calculated background (yellow line) profiles. Reflection positions are marked by olive lines.

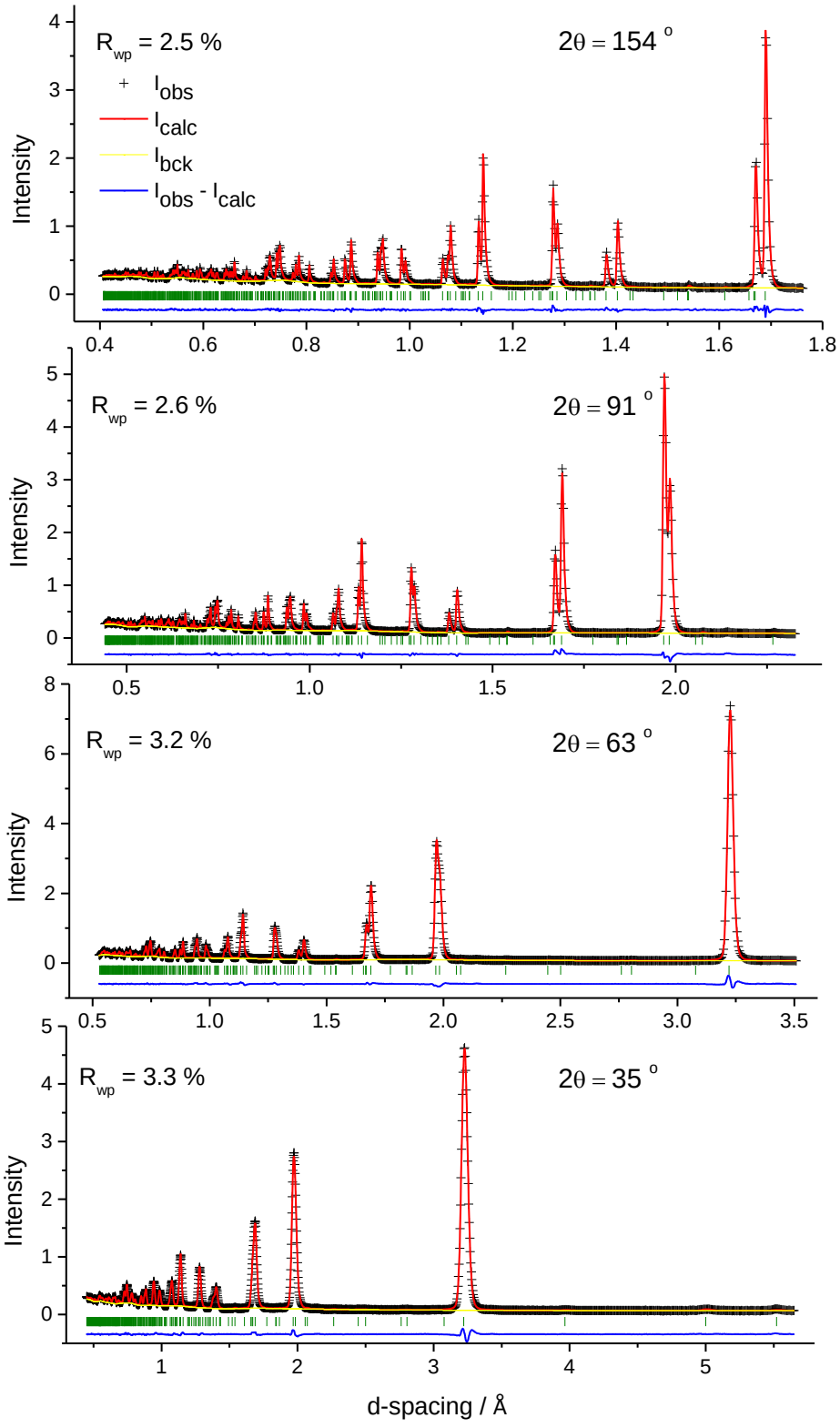

Figure 5.3 Multibank Rietveld refinement for $Cu_2ZnGeSe_4$ using powder neutron diffraction data collected at room temperature (χ^2 = 6.1). Observed (black crosses), refined (red solid lines), difference (blue bottom line) and calculated background (yellow line) profiles. Reflection positions are marked by olive lines.

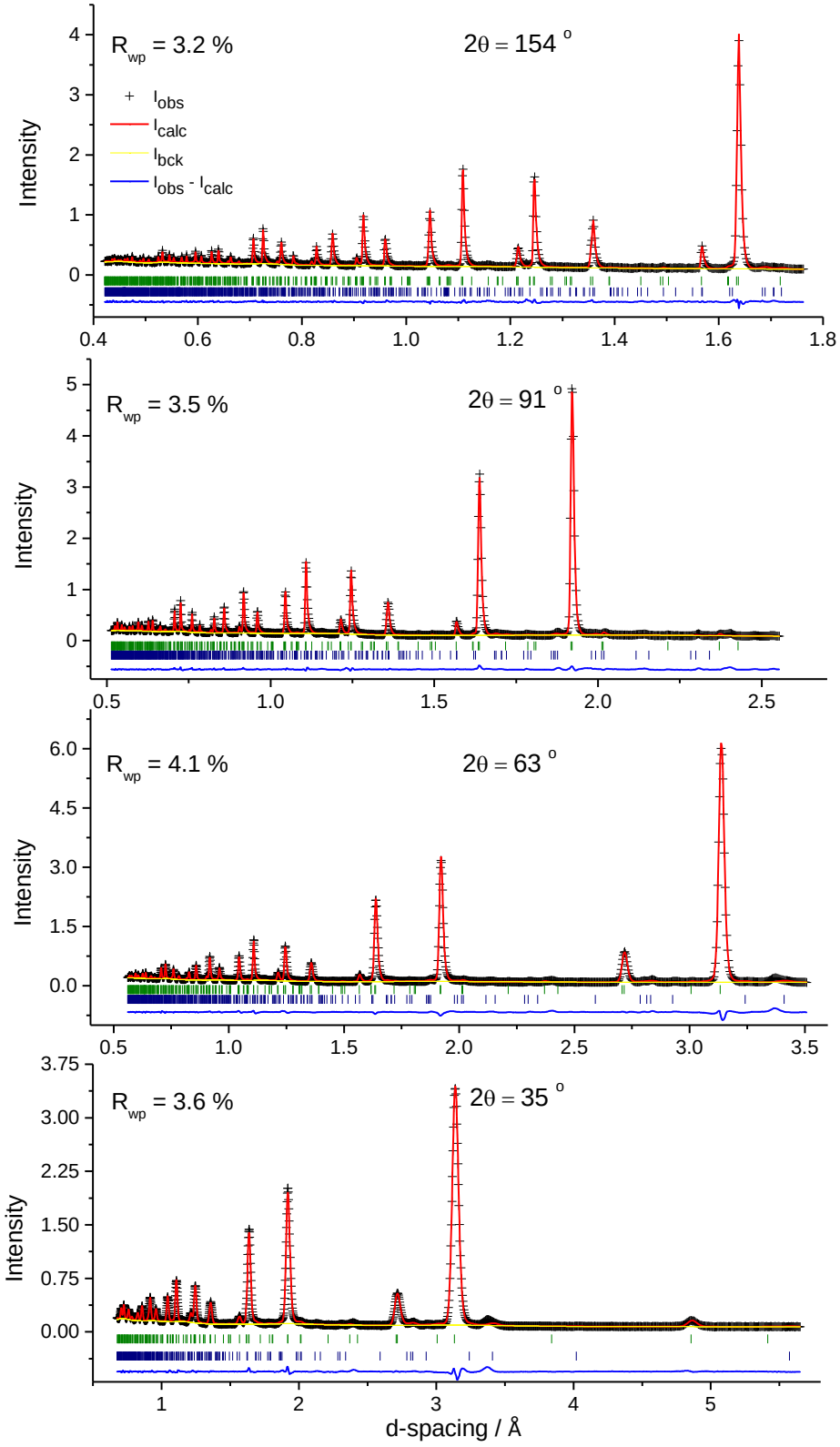

Figure 5.4 Multibank Rietveld refinement for Cu_2ZnSnS_4 using powder neutron diffraction data collected at room temperature (χ^2 = 8.7). Observed (black crosses), refined (red solid lines), difference (blue bottom line) and calculated background (yellow line) profiles. Reflection positions of Cu_2ZnSnS_4 phase are indicated by olive markers, while navy markers denote SnS (~ 5 wt %).

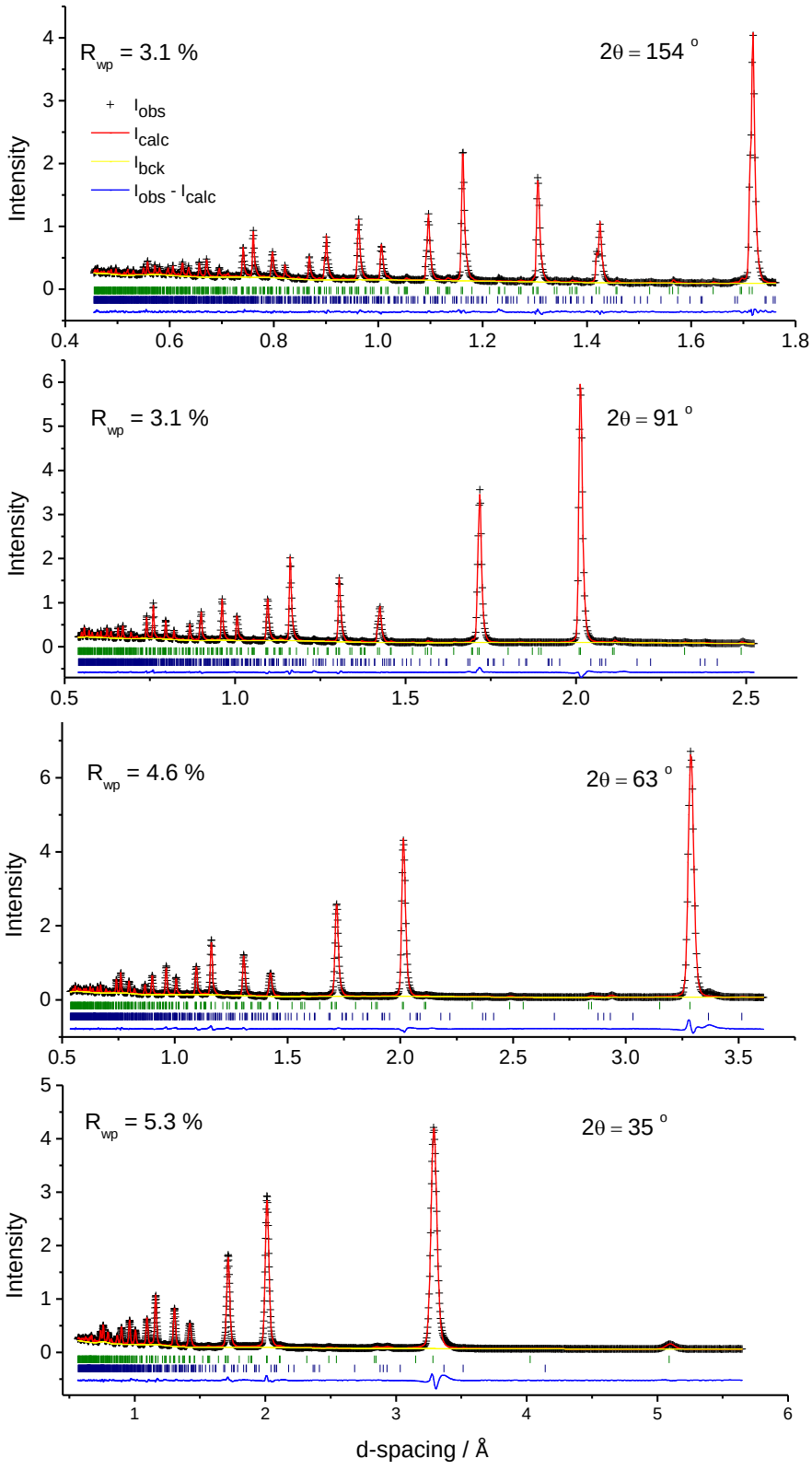

Figure 5.5 Multibank Rietveld refinement for $Cu_2ZnSnSe_4$ using powder neutron diffraction data collected at room temperature (χ^2 = 11.6). Observed (black crosses), refined (red solid lines), difference (blue bottom line) and calculated background (yellow line) profiles. Reflection positions of $Cu_2ZnSnSe_4$ phase are indicated by olive markers, while navy markers denote SnSe (~ 2 wt %).

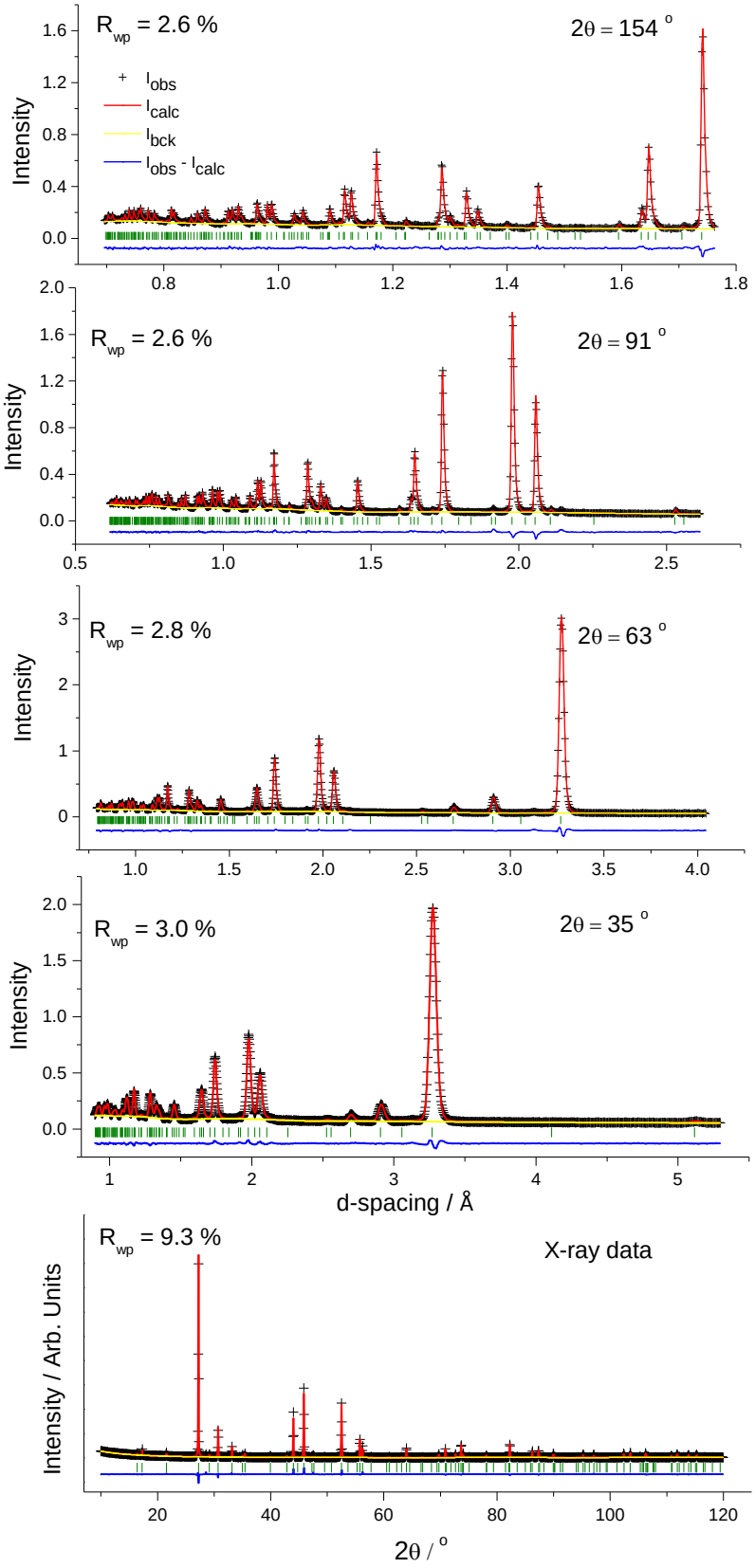

Figure 5.6 Multibank Rietveld refinement for Ag_2ZnSnS_4 combining powder neutron and X-ray diffraction data collected at room temperature (χ^2 = 3.2). Observed (black crosses), refined (red solid lines), difference (blue bottom line) and calculated background (yellow line) profiles. Reflection positions are marked by olive lines.

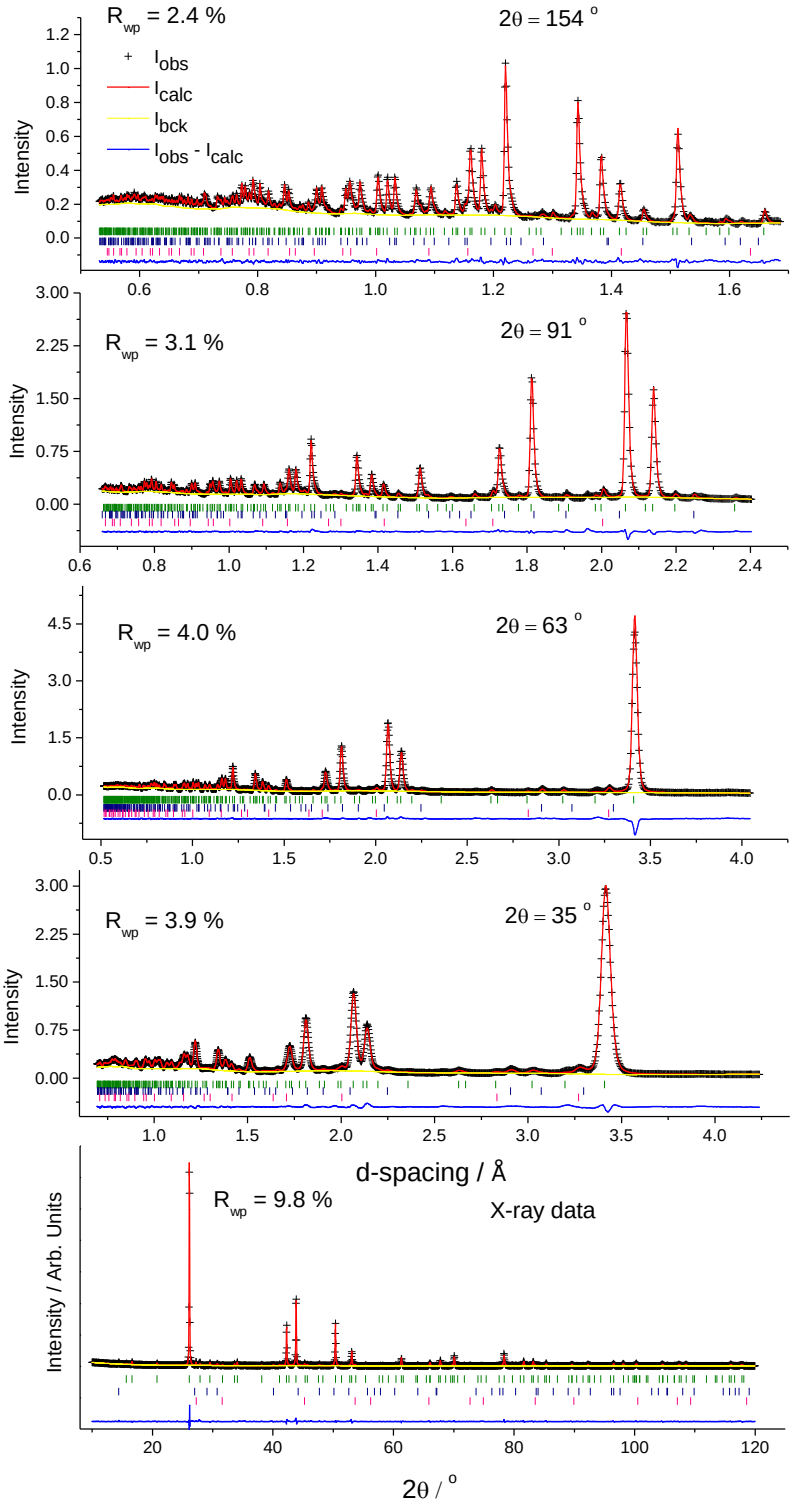

Figure 5.7 Multibank Rietveld refinement for $Ag_2ZnSnSe_4$ combining powder neutron and X-ray diffraction data collected at room temperature (χ^2 = 7.1). Observed (black crosses), refined (red solid lines), difference (blue bottom line) and calculated background (yellow line) profiles. Reflection positions of $Cu_2ZnSnSe_4$ phase are indicated by olive markers, while navy and pink markers denote SnSe (~ 1.6 wt %) and ZnSe (~ 1.9 wt %) respectively.

5.3.2 Powder neutron diffraction study of Cu_2ZnGeS_4 at high temperatures

Powder neutron diffraction data were collected for Cu_2ZnGeS_4 at temperatures, in the range $300 \leq T / K \leq 1173$, using the GEM diffractometer, as described in Section 2.3.1. The powdered sample was sealed under the vacuum of 10^{-4} mbar in a high purity quartz ampoule. Multibank Rietveld refinements were conducted using the data from the four detector banks $2\theta = 154^{\circ}$, 91°, 63° and 35°. The initial structural model was that established from the refinement against room temperature neutron diffraction data (Section 5.3.1). At each temperature, the refinement was initiated using the refined model obtained at the previous temperature.

The results from the refinements show that in the temperature range $300 \leq T / K \leq 1073$ no phase transition or any degradation of the sample is observed. The low values of refinement indexes ($1.3 \leq \chi^2 \leq 2.73$, $1.0 \leq R_{wp} / \% \leq 3.2$) indicate that the material is described well in the space group $I\bar{4}$. The thermal evolution of lattice and thermal parameters (Figures 5.8 and 5.9) show an increase in both as a function of temperature. The thermal expansion of the material results in an increase of the unit cell volume up to *ca* 3 %. Figure 5.10 illustrates the copper site occupancy factors in the temperature range $300 \leq T / K \leq 1073$.

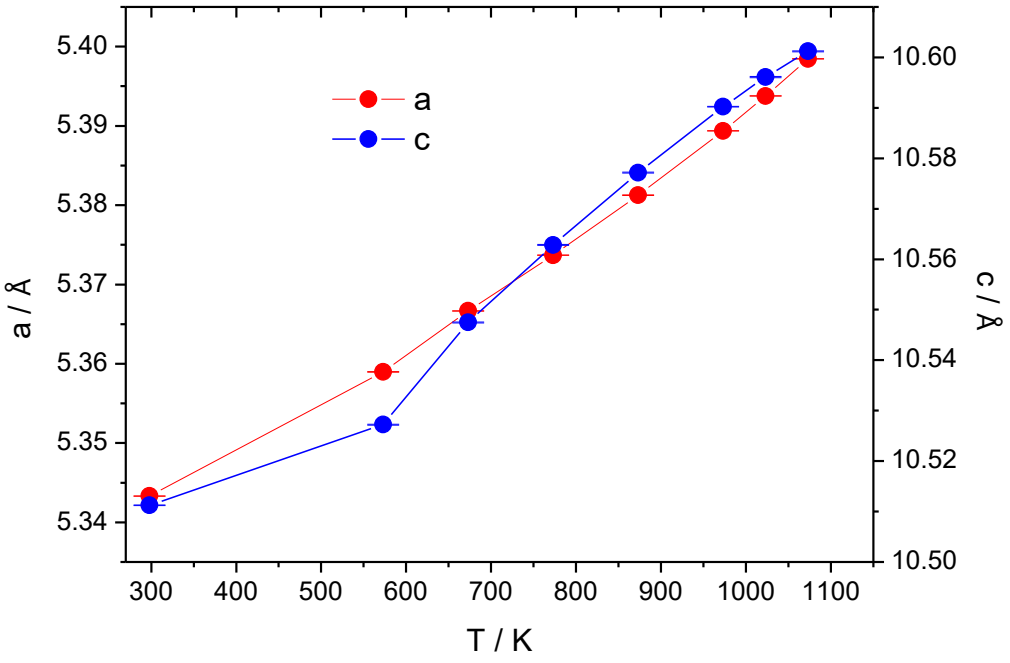

Figure 5.8 Refined lattice parameters of Cu_2ZnGeS_4 in the temperature range $300 \leq T / K \leq 1073$.

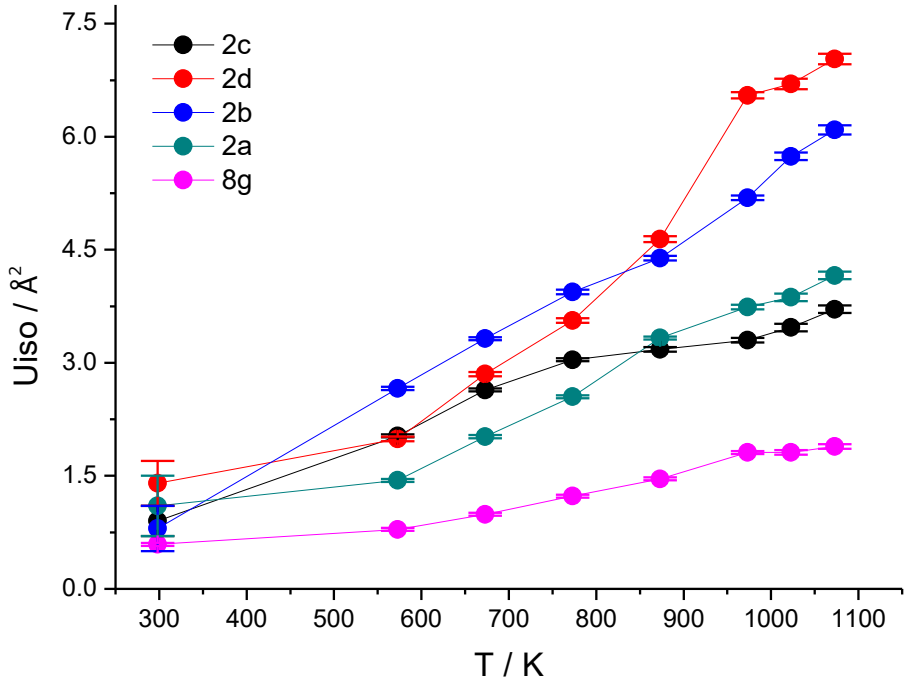

Figure 5.9 Refined thermal parameters of Cu_2ZnGeS_4 for each crystallographic position in the space group $I\bar{4}$ in the temperature range $300 \leq T / K \leq 1073$.

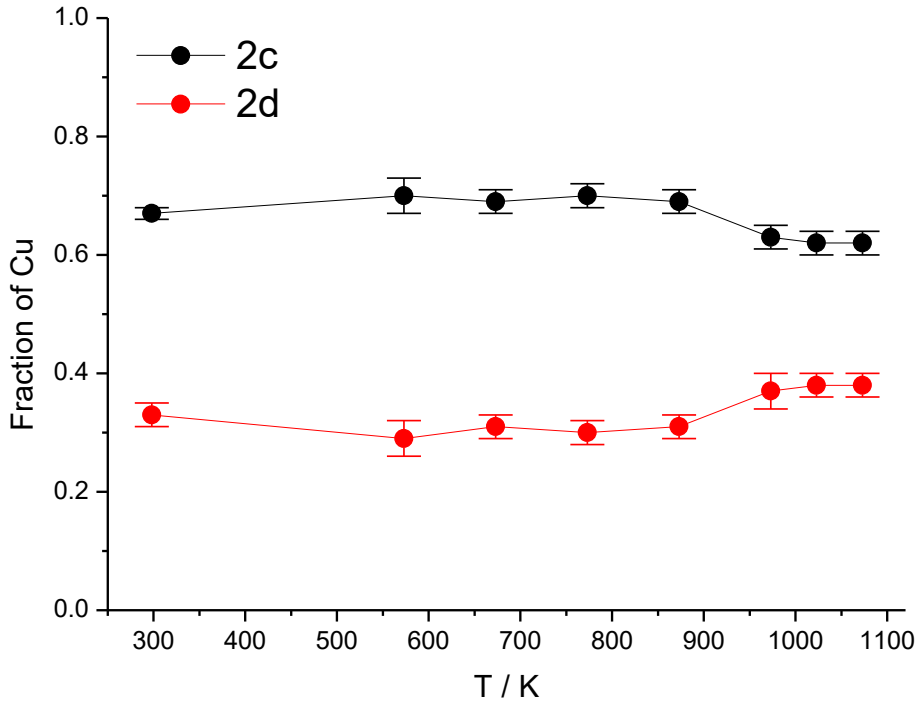

Figure 5.10 Temperature dependence of copper site occupancy factors in the two crystallographic positions, *2c* and *2d*, in the temperature range $300 \leq T / K \leq 1073$.

The Rietveld analysis reveals that the extend of Cu/Zn disorder in the planes at z = 0.25 and 0.75 is almost invariant up to 873 K, while in the range $973 \leq T / K \leq 1073$, the degree of disorder increases slightly, with copper and zinc cations to occupy *ca.* 62 % and *ca.* 38 % of the *2c* position respectively. The *2a* and *2b* positions remain fully ordered by the Cu and Ge cations respectively. At 1123 K, the neutron diffraction data (Figures 5.11 to 5.14) show clear differences in the observed peaks in the four detector banks, indicating a phase transition has occurred. Examining the case of wurtzite-stannite structure as reported in the X-ray diffraction study,[140] the multibank neutron diffraction refinement confirms this phase transition and the high-temperature phase is described well in the space group $Pmn2_1$ (χ^2 = 1.9, $1.3 \leq R_{wp} / \% \leq 2.2$). The refined parameters and the crystallographic positions of this structure are presented in Table 5.5, while the bond distances between cations and anions are presented in Table I2, Appendix I. The thermal parameters of each of the sulphur anions were constrained to the same value in order to avoid correlation problems during the refinement process. The possibility of disorder (Cu/Zn, Cu/Ge, Zn/Ge) was investigated in the high temperature phase. Rietveld analysis reveals that no such cation disorder occurs and Cu_2ZnGeS_4 adopts a fully ordered structure in the space group $Pmn2_1$ (Figure 5.15). In the wurtzite-stannite structure each cation is coordinated tetrahedrally by sulphur anions, while every S^{2-} is bonded to 2 Cu^+, 1 Zn^{2+} and 1 Ge^{+4} cations.

Table 5.5 The refined fractional coordinates, lattice and thermal parameters of Cu_2ZnGeS_4 at 1123 K, described in the space group $Pmn2_1$.

Space group *Pmn2₁*						
a = 7.5968(2) Å		**b = 6.5652(2) Å**		**c = 6.23870(6) Å**		
Atom	Wyckoff site	x	y	z	Occupancy	Uiso / Å^2
Zn	*2a*	0.0000	0.161(1)	0.507(3)	1.0	8.1(3)
Cu	*4b*	0.2488(5)	0.3344(7)	0.998(2)	1.0	5.5(1)
Ge	*2a*	0.0000	0.8178(7)	0.0000	1.0	5.2(2)
S	*2a*	0.0000	0.154(2)	0.104(2)	1.0	1.60(8)
S	*4b*	0.274(1)	0.339(2)	0.640(2)	1.0	1.60(8)
S	*2a*	0.0000	0.824(2)	0.620(2)	1.0	1.60(8)

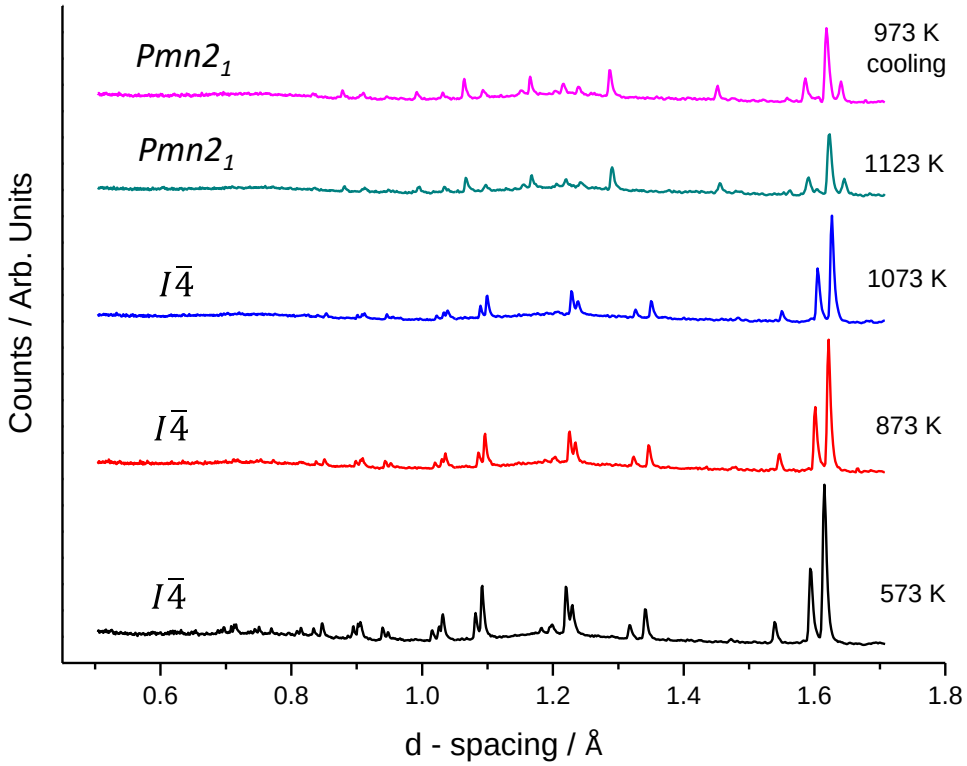

Figure 5.11 Neutron diffraction data of Cu_2ZnGeS_4 from bank 6 of 156˚ at high temperatures.

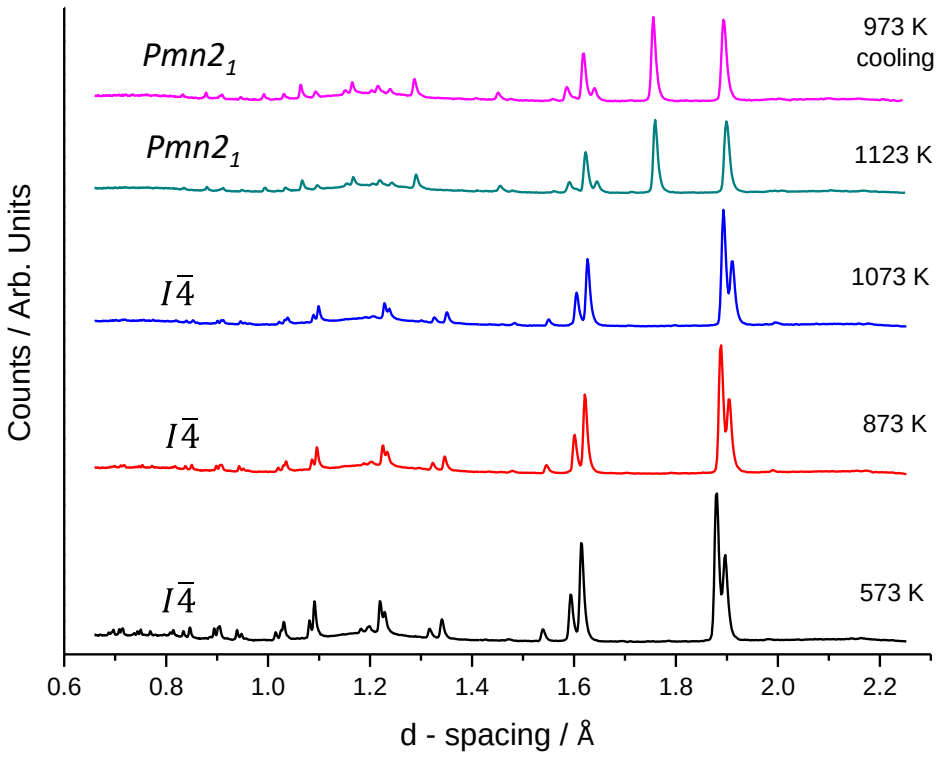

Figure 5.12 Neutron diffraction data of Cu_2ZnGeS_4 from bank 5 of 91˚ at high temperatures.

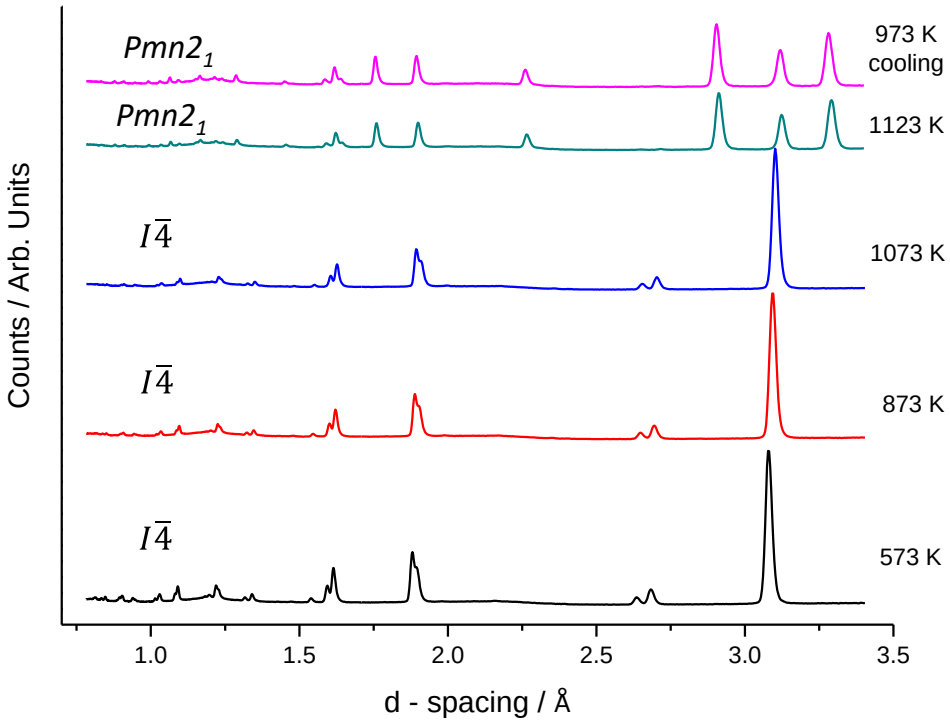

Figure 5.13 Neutron diffraction data of Cu_2ZnGeS_4 from bank 4 of 63˚ at high temperatures.

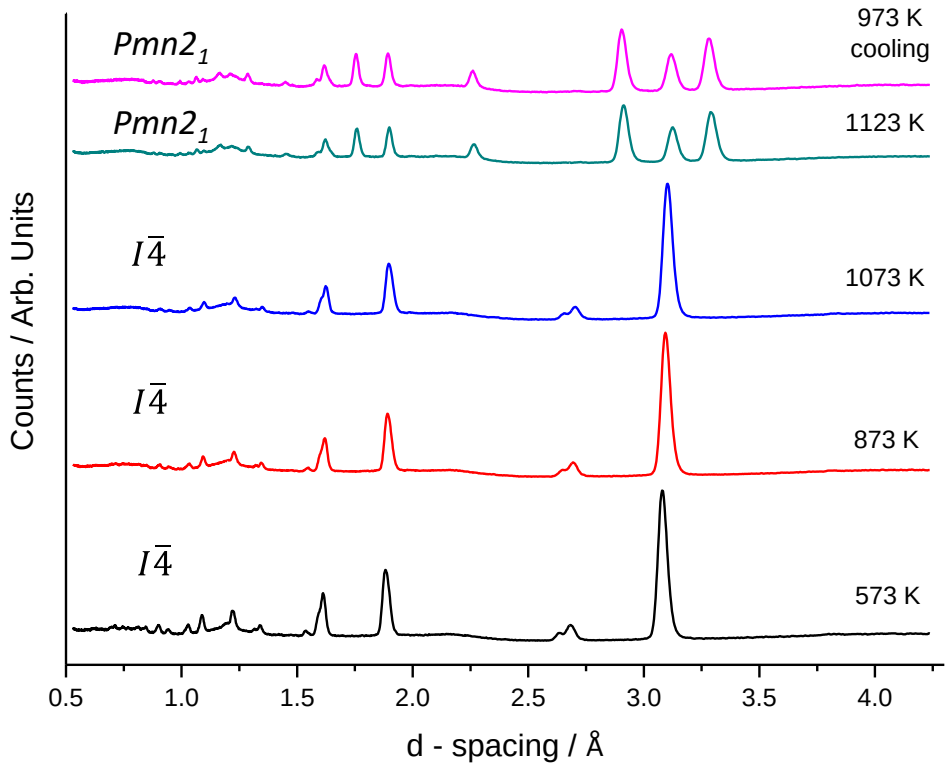

Figure 5.14 Neutron diffraction data of Cu_2ZnGeS_4 from bank 3 of 35˚ at high temperatures.

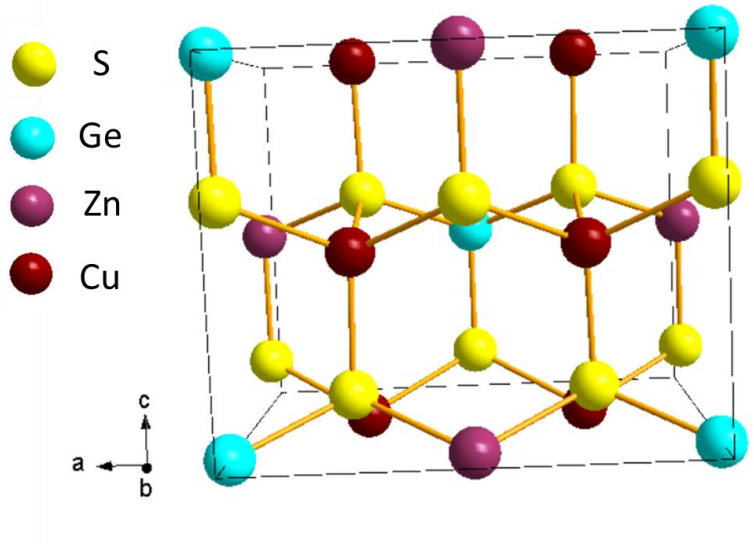

Figure 5.15 The wurtzite stannite structure of Cu_2ZnGeS_4 at 1123 K.

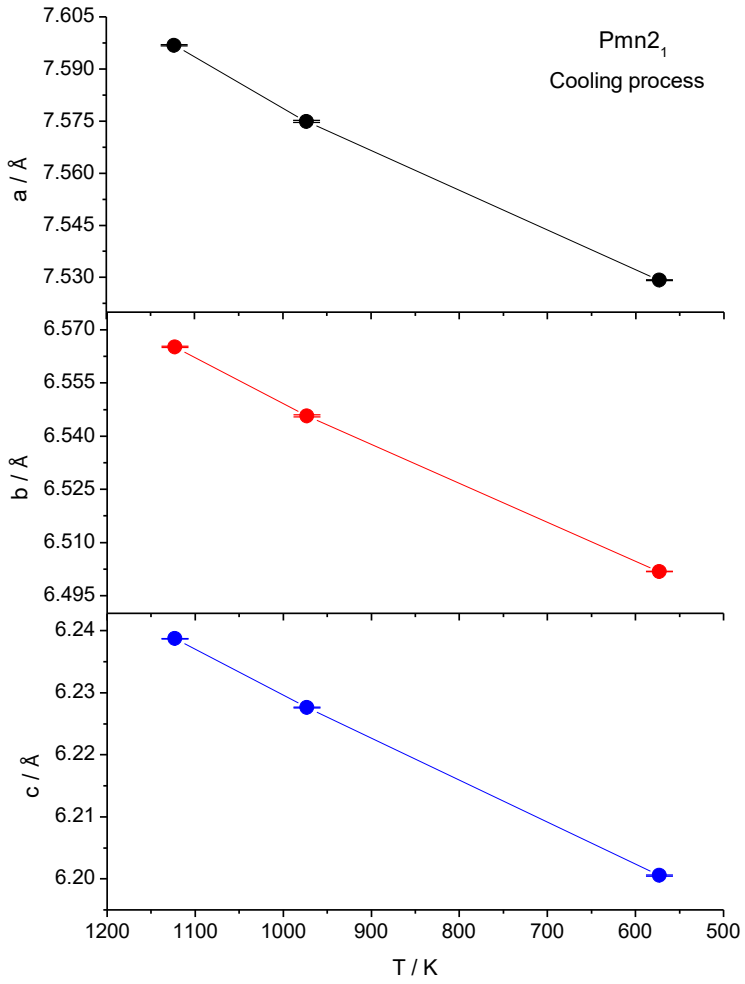

Figure 5.16 Refined lattice parameters of Cu_2ZnGeS_4 in the space group *Pmn2$_1$* during the cooling process.

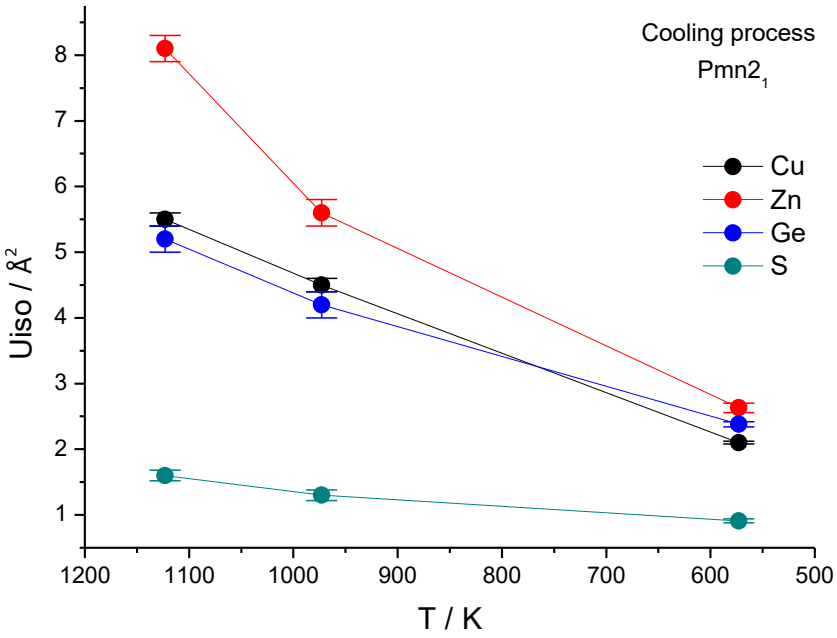

Figure 5.17 Refined thermal parameters of Cu_2ZnGeS_4 in the space group *Pmn2$_1$* during the cooling process.

Powder neutron diffraction data were also collected during the cooling (Figures 5.11 to 5.14). The Rietveld refinements demonstrate that the phase transition is irreversible and the high temperature phase with an ordered cation array persists for temperatures below 1073 K. The refined lattice and thermal parameters during the cooling process are presented in Figures 5.16 and 5.17 respectively. Cooling causes a thermal contraction in the unit cell, decreasing the lattice parameters, leading to a reduction in the unit cell volume of *ca.* 2.5 % between 1123 and 573 K.

5.4 Investigation of $Cu_2ZnGeSe_4$ at high temperatures

5.4.1 TGA / DSC analysis

Analysis of the thermal stability of $Cu_2ZnGeSe_4$ under N_2 flow was carried out in the temperature range $290 \leq T / K \leq 773$, as described in Section 2.9. TGA data (Figure 5.18) showed that no change in weight occurs up to 600 K. Above this temperature a slight decrease in mass is observed, reaching 0.4 % at 773 K, indicating that the selenium starts vaporising. DSC data (Figure 5.19) reveal that there is a slight change in the heat flow in the temperature range 437 – 512 K. The derivative of the heat flow shows clearly a variation at this temperature region, indicating a thermal effect which is

probably related with a phase transition. These results are in a good agreement with the reported DSC data of Zeier et al.[122]

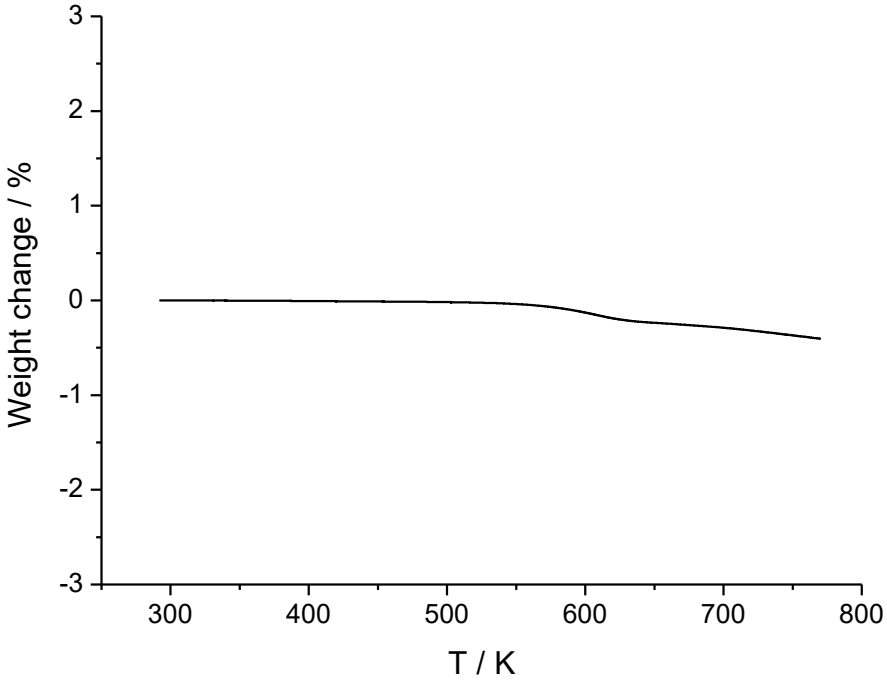

Figure 5.18 TGA data for $Cu_2ZnGeSe_4$ under N_2 flow.

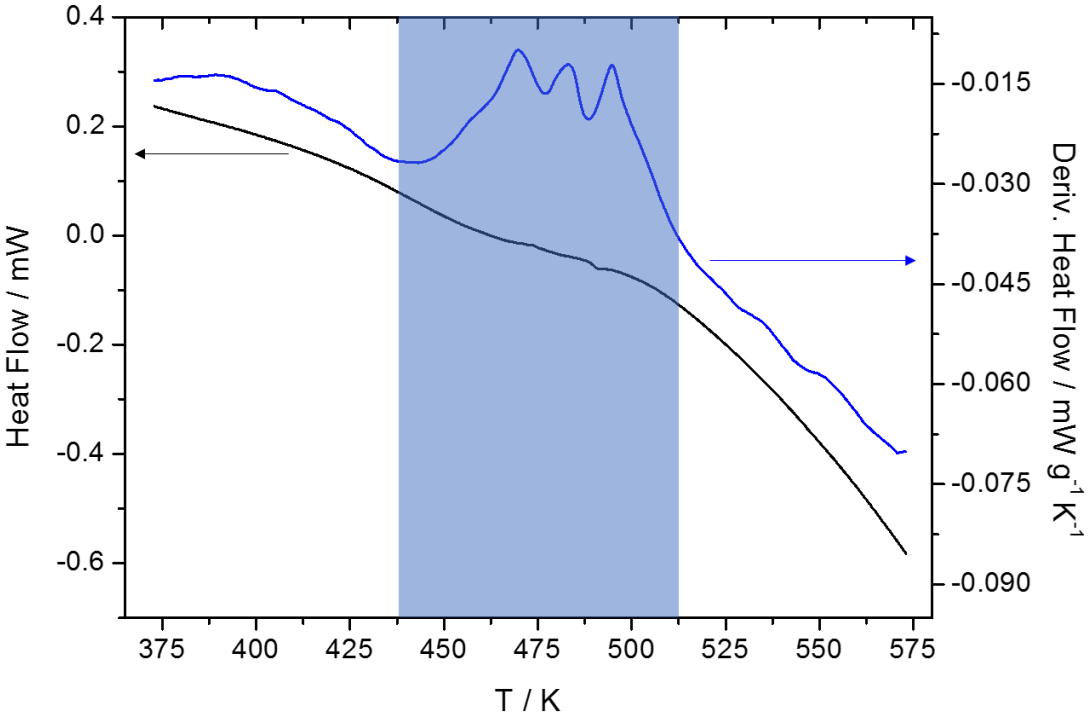

Figure 5.19 DSC data for $Cu_2ZnGeSe_4$ under N_2 flow.

5.4.2 Hot pressing of $Cu_2ZnGeSe_4$

The densification of $Cu_2ZnGeSe_4$ was carried out according to the hot-pressing process described in Section 2.5. A powered sample of 1.8 g was pressed under N_2 for 45 min at 65 bar and 600 ˚C. The resulting pellet exhibited a density of *ca.* 98.7 % of the crystallographic value. This percentage satisfied the demand for a good density and therefore, physical property measurements followed.

5.4.3 Electrical transport properties

Electrical resistivity and Seebeck coefficient measurements were conducted on the resulting pellet of $Cu_2ZnGeSe_4$ over the temperature range $300 \leq T / K \leq 655$ according to the procedure described in Section 2.7.1.1. In Figure 5.20, a pronounced change in ρ(T) is observed in the temperature range (shaded region) where the thermal effect was identified previously. The electrical resistivity data show clearly a decrease as a function of temperature up to 500 K, indicating the semiconducting behaviour of the material.

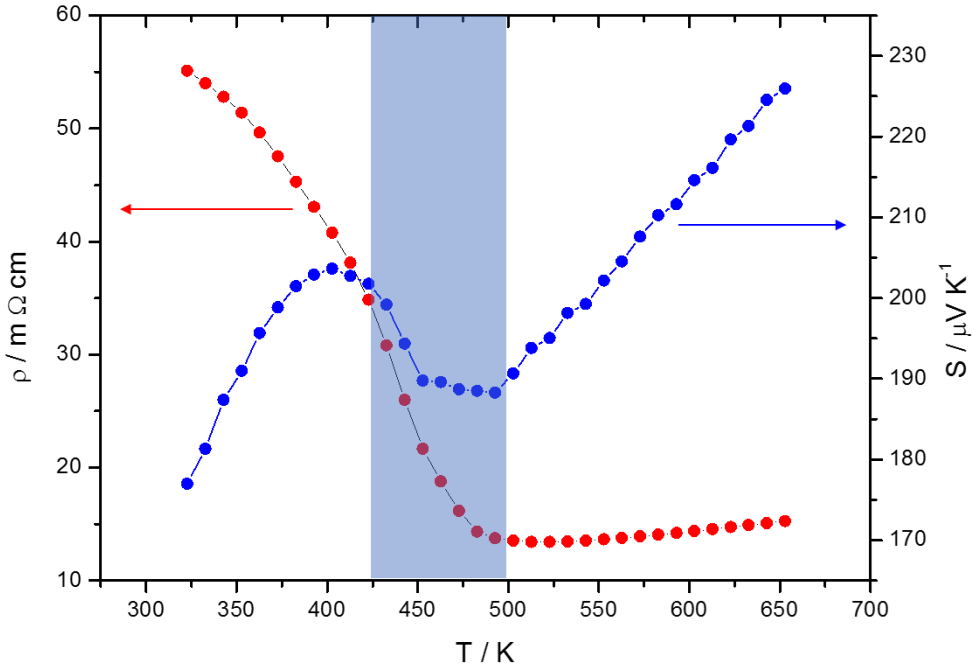

Figure 5.20 Electrical resistivity and Seebeck coefficient data of $Cu_2ZnGeSe_4$ as a function of temperature.

Above 500 K, a phase transformation occurs, and the material shows metallic ρ(T) behaviour, as the resistivity increases with rising temperature. The S(T) curve also shows a change in the shaded region of Figure 5.20. For T ≥ 500 K, the Seebeck coefficient increases almost linearly with increasing temperature, indicating the metallic behaviour of the material. The sharp decrease of electrical resistivity in the shaded temperature region results in a pronounced increase of power factor (Figure 5.21) and consequently, a strong influence on the thermoelectric performance of the material.

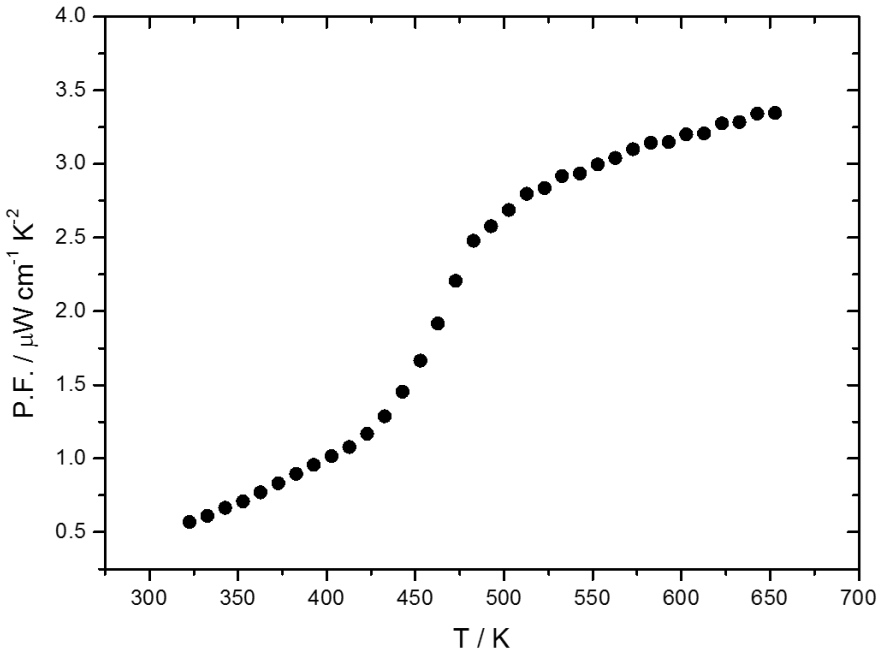

Figure 5.21 Power factor (P.F.) of $Cu_2ZnGeSe_4$ as a function of temperature.

The origin of anomalies in the electrical transport and thermal properties is unclear and a detailed structural investigation is necessary. Therefore, powder neutron diffraction experiments were conducted on $Cu_2ZnGeSe_4$ as a function of temperature through the region which these anomalies occur and the results are reported below.

5.4.4 Neutron diffraction study at high temperatures

Powder neutron diffraction data were collected for $Cu_2ZnGeSe_4$ as a function of temperature, using the POLARIS diffractometer at the ISIS facility, Rutherford

Appleton Laboratory, as described in Section 2.3.2. The powdered sample was sealed at 10^{-4} mbar into a high purity quartz ampoule, which was placed in a 8 mm diameter vanadium can. This was mounted inside a furnace which was evacuated to a pressure 10^{-4} Torr and data were collected over the temperature range $300 \leq T / K \leq 973$. Rietveld refinements were conducted using the data from bank 5 ($2\theta = 146.72^{\circ}$) and bank 4 ($2\theta = 92.59^{\circ}$). The results from the previous neutron diffraction refinement at room temperature were used as the initial structural model and the same refinement steps were applied for each temperature, according to the process described in Section 5.3.1. The background parameters were refined using the reciprocal interpolation function and the peak shape was modelled using the pseudo-Voigt function. The thermal parameters of all atoms were set to a single value in order to avoid correlation problems. The Rietveld refinements reveal that in the range $300 \leq T / K \leq 973$, the structure of $Cu_2ZnGeSe_4$ may be described in the space group $I\bar{4}$. No secondary phases are observed in this temperature range. The refined structural models provide a very good fit to the experimental data ($1.2 \leq R_{wp} / \% \leq 1.6$, $2.1 \leq \chi^2 \leq 3.5$). The shift of the peaks to higher values of d-space (Figures 5.22 and 5.23) with increasing temperature reflects the thermal expansion of the unit cell and the increase in lattice parameters (Figure 5.24). The unit cell volume increases *ca.* 2.6 % at 973 K. Figure 5.26 presents the refined occupancy factors of copper cations at the three crystallographic sites, *2c*, *2d* and *2a*, with the temperature evolution. Rietveld refinements reveal that on increasing the temperature of 450 K, the Cu/Zn disorder in the z = 0.25 and 0.75 planes is effectively constant, while the *2a* site remains fully occupied by Cu cations. The *2c* position is occupied by *ca.* 71 % of Cu and by *ca.* 29 % of Zn cations. At 473 K, the Cu/Zn distribution in the z = 0.25 and 0.75 planes becomes fully disordered. However, the site occupancy factor of copper at the *2c* and *2d* sites deviates from the expected value of 0.5 for a fully disordered structure, while simultaneously a slight decrease in the site occupancy factor is observed at the *2a* site. The reduction in the site occupancy factor values at the three Cu sites corresponds to the creation of copper vacancies, suggesting that at the disordering transition, Cu ions simultaneously start to migrate from their ideal crystallographic positions. On increasing the temperature, the site occupancy factors of Cu ions at the three crystallographic sites are reduced further, indicating an increase in the number of Cu vacancies.

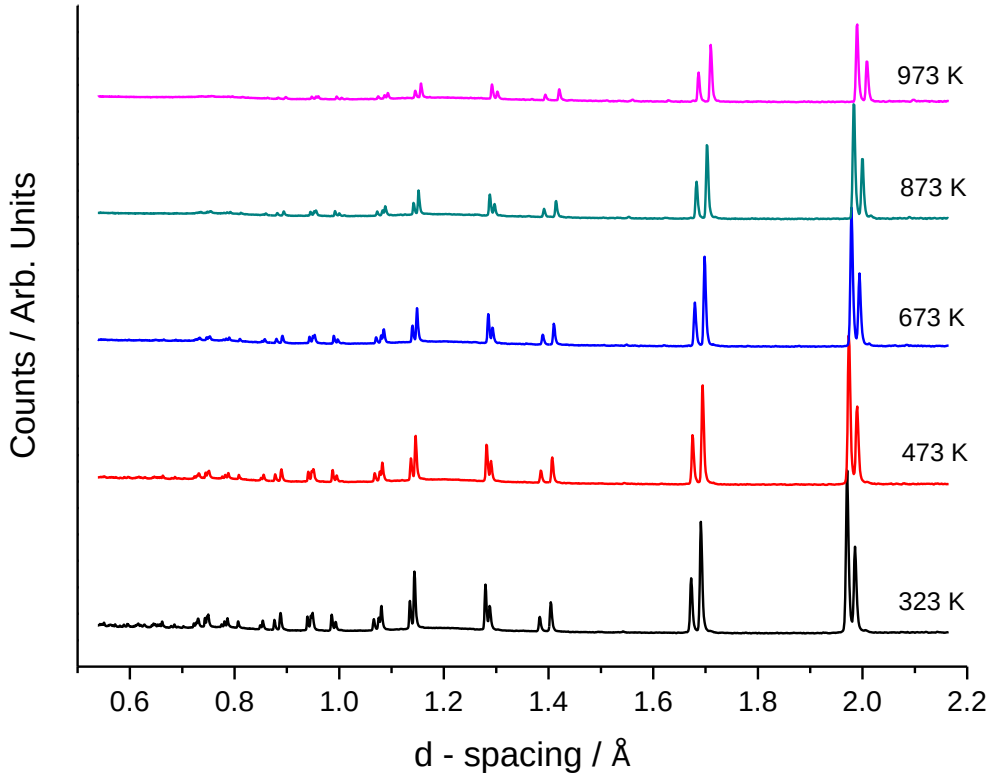

Figure 5.22 Neutron diffraction data of $Cu_2ZnGeSe_4$ from bank 5 of 146.72˚ at high temperatures.

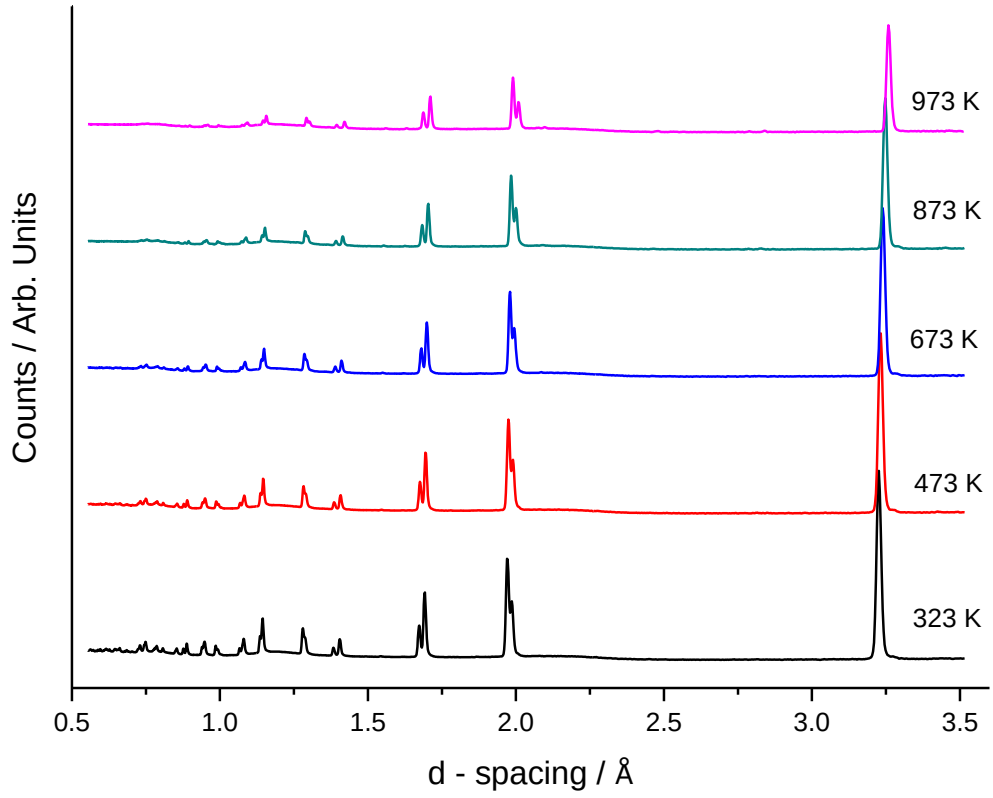

Figure 5.23 Neutron diffraction data of $Cu_2ZnGeSe_4$ from bank 4 of 92.59˚ at high temperatures.

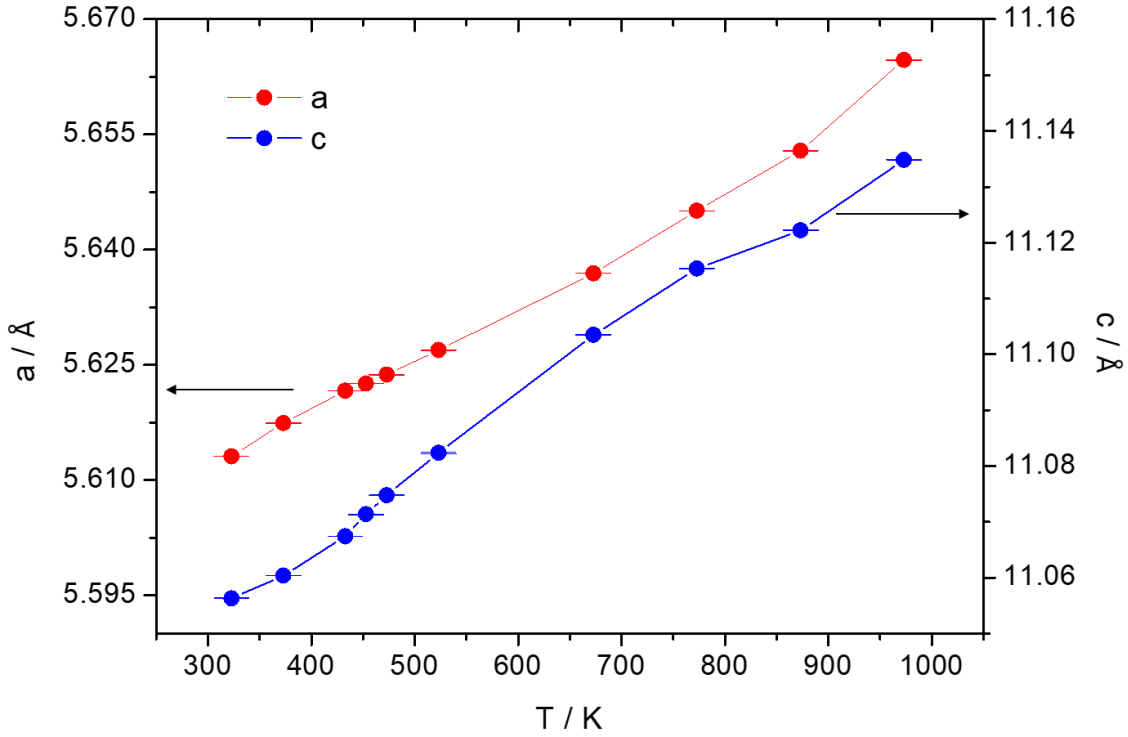

Figure 5.24 Refined lattice parameters of $Cu_2ZnGeSe_4$ in the temperature range $300 \leq T / K \leq 973$.

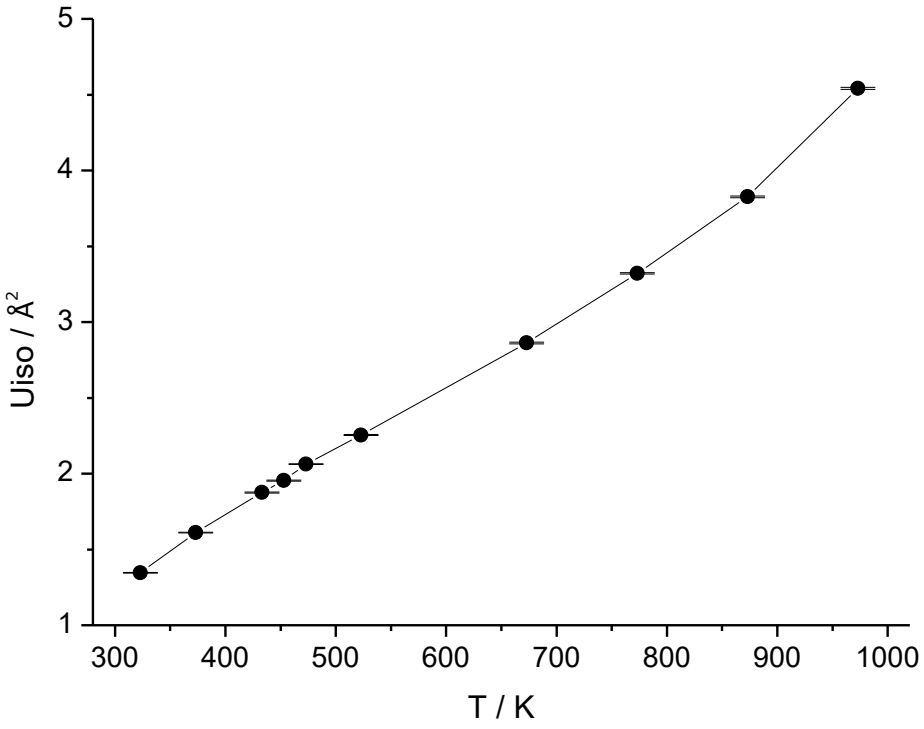

Figure 5.25 Refined overall thermal parameter of $Cu_2ZnGeSe_4$ in the space group $I\bar{4}$ in the temperature range $300 \leq T / K \leq 973$.

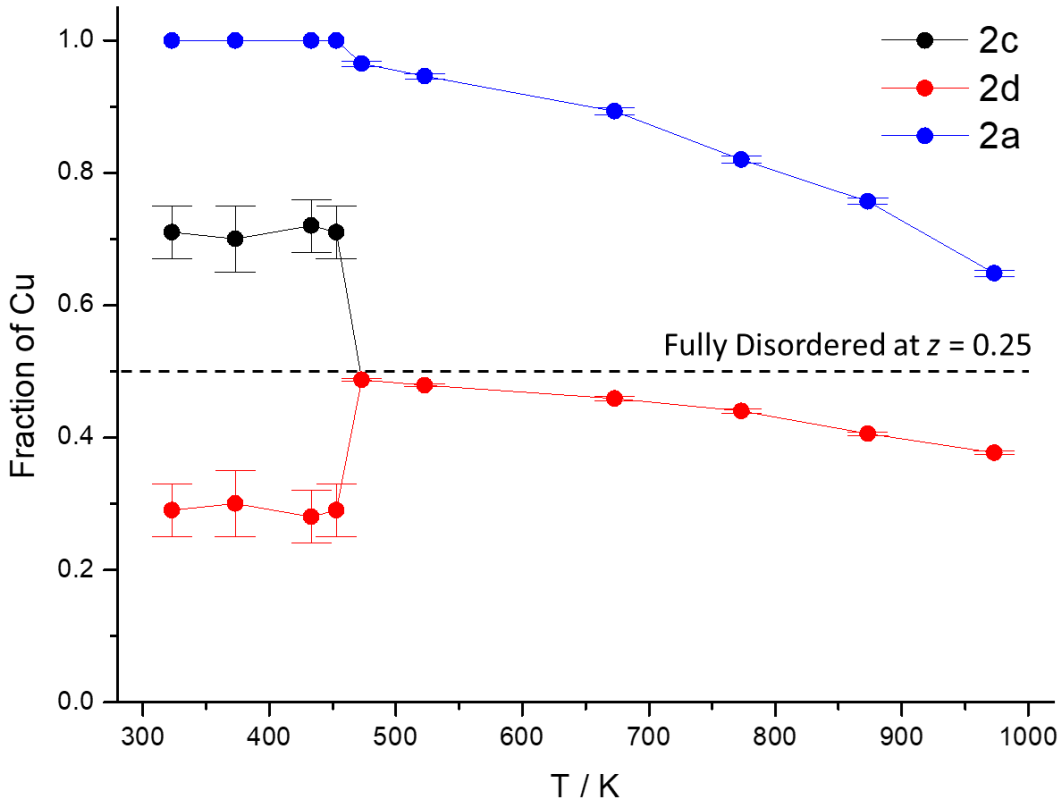

Figure 5.26 Temperature dependence of copper site occupancy factors in the three crystallographic positions *2c*, *2d* and *2a* of $Cu_2ZnGeSe_4$ in the temperature range $300 \leq T / K \leq 973$.

Initially, conclusions for Cu vacancies at the three Cu sites extracted at high temperatures. At 973 K, a wide range of different models were examined, investigating all possible cases of cation disorder. The structural models which were assessed are below:

- Stannite ($I\bar{4}2m$).
- Ordered kesterite ($I\bar{4}$).

  Disordered kesterite models ($I\bar{4}$) setting:
- partial Cu/Zn disorder in the z = 0.25 and 0.75 planes (*2c* and *2d* sites).
- fully Cu/Zn disorder in the z = 0.25 and 0.75 planes.
- Cu/Zn disorder at *2a* and *2d* sites.
- fully Cu/Zn disorder at the three crystallographic sites, *2a*, *2c* and *2d*.
- Cu/Ge disorder at *2c* and *2b* sites.
- Zn/Ge disorder at *2d* and *2b* sites

All structural models corresponded to complete occupation of all cation sites. The differences in the quality of the refinements were negligible. However, refining the

occupancy factors of Cu and Zn cations at *2c* and *2d* sites in the partially disordered kesterite model, the program corresponded to full Cu/Zn ordering in the z = 0.25 and 0.75 planes (with R_{wp} = 1.23 and 1.25 % for histograms of bank 5 and 4 respectively, χ^2 = 2.236). A disorder-to-order transition on heating would not be a thermodynamically favourable process. Therefore, further investigation of the structure at high temperatures focused on the introduction of copper vacancies. This time, the site occupancy factors of Cu ions at *2c*, *2d* and *2a* sites were allowed to refine independently from the occupancy factors of the other cations which were set to their nominal values. The results showed an improvement of the refinements with both the R-factors and χ^2 values reduced. There was a clear reduction in the site occupancy factor values of Cu ions at the three crystallographic positions, indicating copper vacancies. The best agreement (R_{wp} = 1.19 and 1.20 % for histograms of bank 5 and 4 respectively, χ^2 = 2.064) was obtained for a structure with Cu/Zn disorder in the z = 0.25 and 0.75 planes, with the Zn atoms occupying 50 % of *2c* and *2d* positions and Cu ions occupying *ca.* 38 % of *2c* and *2d* positions and *ca.* 65 % of the *2a* position. The site occupancy factors of Cu at *2c* and *2d* positions were constrained to the same value in these refinements.

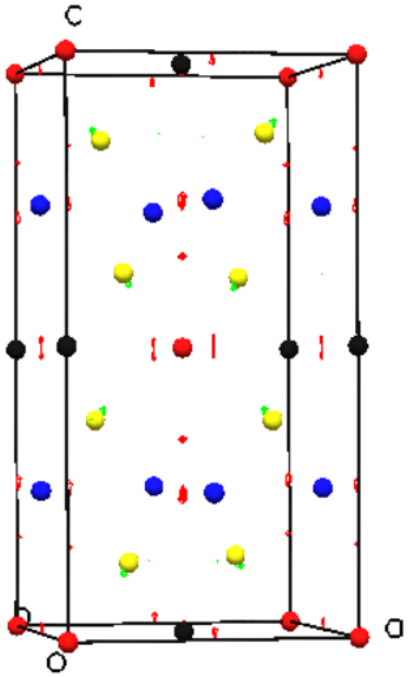

Figure 5.27 Illustration of difference Fourier map of $Cu_2ZnGeSe_4$ at 973 K plotted using DrawXTL software. Red, black and yellow spheres denote Cu, Ge and Se atoms respectively and blue spheres Cu/Zn cations in z = 0.25 plane. The red and green spots denote the residual nuclear density in the supercell.

The results show an appreciable percentage of Cu vacancies at the three sites (total percentage 29.5 %), indicating probably more than one interstitial sites. Difference Fourier maps calculated for this structural model reveal residual nuclear density in the unit cell (Figure 5.27). By determining the position of the maxima in this residual nuclear density, efforts were made to introduce interstitial Cu ions into the refinement. However, inclusion of interstitial copper cations did not result in an improvement in the quality of the refinement. Therefore, it may be concluded that the interstitial copper ions are not localised at a particular crystallographic position but are distributed throughout the structure, consistent with an appreciable ion mobility. At lower temperatures in the range $473 \leq T / K \leq 973$, the refinements demonstrate that the data for $Cu_2ZnGeSe_4$ are best described by a structure in which the *2a* site is incompletely occupied by Cu cations and the *2c* and *2d* positions are 50 % occupied by Zn cations while copper occupies less than 50 % of the *2c* and *2d* sites, indicating that copper ion vacancies are present at lower temperatures, albeit at a lower level (Figure 5.26). Below 473 K, Rietveld analysis provided no evidence for the presence of copper cation vacancies at any of the three (*2c*, *2d* and *2a*) sites.

From the neutron study of $Cu_2ZnGeSe_4$ in the range $300 \leq T / K \leq 973$, it is concluded that a partial order-to-fully disorder transition occurs at 473 K which is accompanied by the creation of Cu vacancies. A fraction of the Cu cations may become mobile above the temperature of 473 K because the thermal energy is sufficient enough to overcome the bonding attractive forces between copper and selenium ions, resulting in the release of Cu^+ in the structure. It is suggested that the creation of copper vacancies at 473 K is probably related with the semiconductor-to-metal transition observed close to this temperature (Figure 5.20), inducing changes in the band structure of the material. Moreover, it is possible the Cu ion mobility to contribute positively in the increase in total electrical conductivity. This may explain the pronounced decrease in electrical resistivity which is observed close to 473 K (Figure 5.20).

5.5 Hole Doping in $Cu_{2+x}ZnGe_{1-x}Se_4$ ($0 \leq x \leq 0.15$)

Hole doping was carried out in $Cu_2ZnGeSe_4$ through the chemical substitution of germanium by copper, targeting the improvement of electrical transport properties and the thermoelectric performance of the material. The series $Cu_{2+x}ZnGe_{1-x}Se_4$ ($0 \leq x \leq 0.15$) was synthesized according to the process used for the end-member phase and described in Section 5.1.

5.5.1 Characterization using powder X-ray diffraction

Powder X-ray diffraction data were collected for the series $Cu_{2+x}ZnGe_{1-x}Se_4$ ($0 \leq x \leq 0.15$) according to the process described in Section 2.2. The experimental patterns of the series are presented in Figure 5.28, confirming that all compositions adopt the kesterite structure. Trace amounts of ZnSe and CuSe were identified through the EVA software package. Rietveld refinements were carried out using as the initial structural model the refined lattice parameters and atomic coordinates of the germanium end-member phase. The background parameters were refined using the cosine fourier series and the peak shape was modelled using the pseudo-Voigt function. The refinements followed the procedure outlined in Section 2.4. For a given composition in the series, refinement was initiated using for the initial structural model, the refined model for the previous composition in the series. The thermal parameters of Cu and Ge atoms which occupy the same crystallographic position were constrained to be equivalent, while site occupancy factors were set at their nominal values.

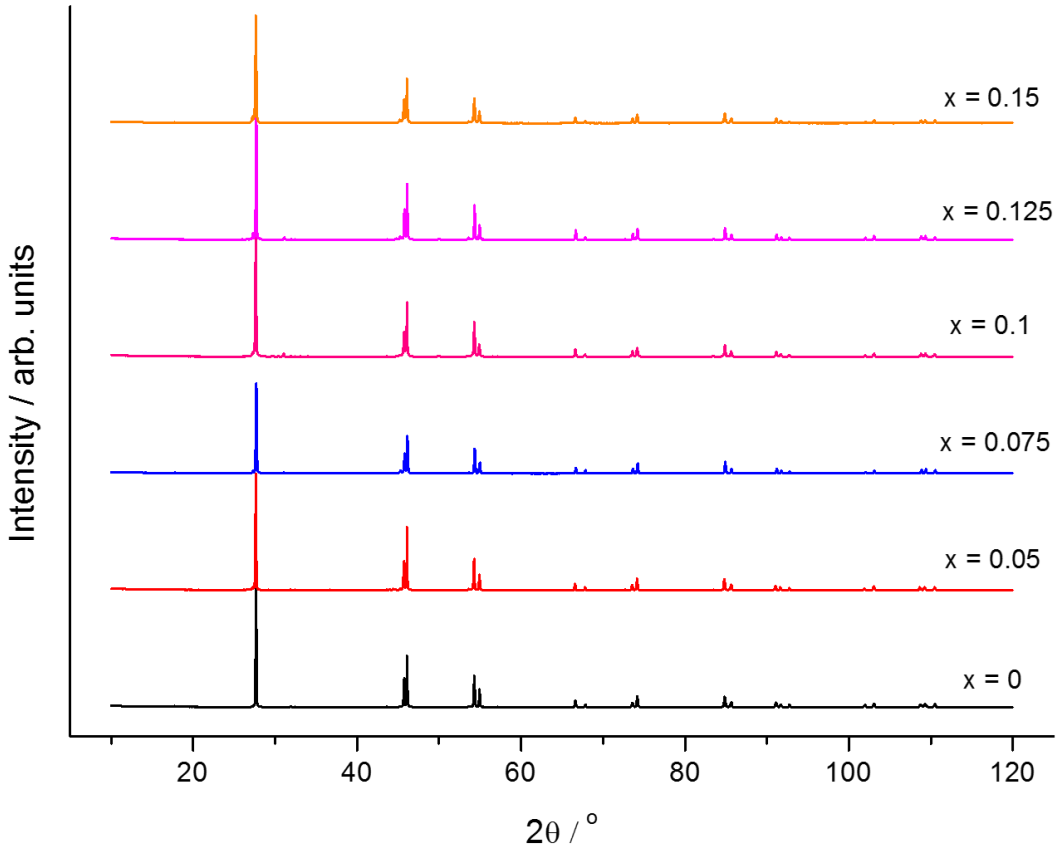

Figure 5.28 Powder X-ray diffraction data for $Cu_{2+x}ZnGe_{1-x}Se_4$ ($0 \leq x \leq 0.15$) over the range $10 \leq 2\theta / ° \leq 120$.

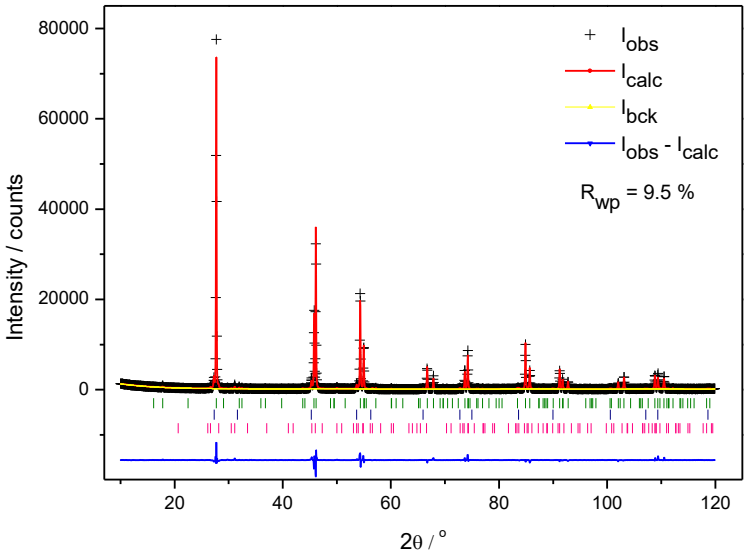

Figure 5.29 Rietveld refinement for $Cu_{2.075}ZnGe_{0.925}Se_4$ using X-ray diffraction data ($\chi^2 = 5.5$). Observed (black crosses), refined (red solid lines) and difference (blue bottom line) profiles. Olive markers correspond to the $Cu_{2.075}ZnGe_{0.925}Se_4$ phase, while navy and pink markers correspond to traces of ZnSe (~ 3.8 wt %) and CuSe (~ 3.2 wt %) respectively.

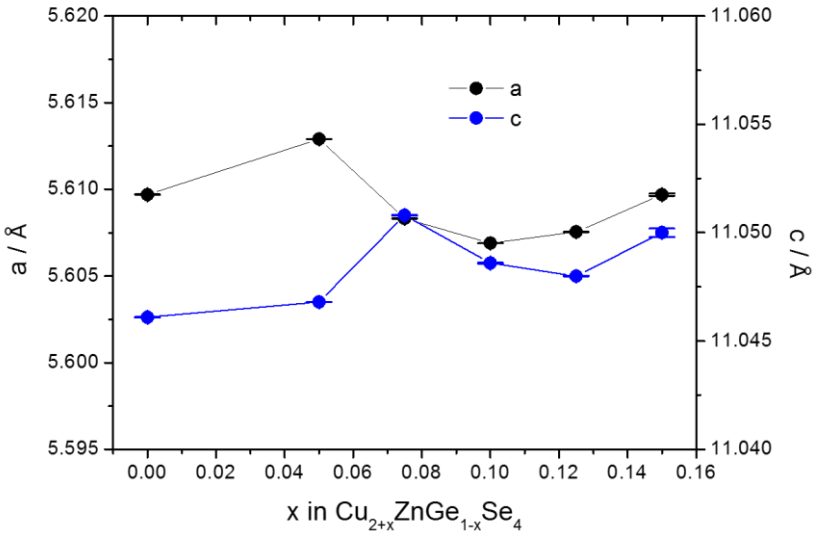

Figure 5.30 Refined lattice parameters for the series $Cu_{2+x}ZnGe_{1-x}Se_4$ ($0 \leq x \leq 0.15$).

The results from the refinements show that all materials throughout the series $Cu_{2+x}ZnGe_{1-x}Se_4$ ($0 \leq x \leq 0.15$) can be described in the space group $I\bar{4}$. A representative refinement is presented in Figure 5.29, while the remaining refinements are provided in Appendix J. The small amounts of substitution of Ge by Cu causes some slight fluctuations in *a* and *c* lattice parameters for $x \leq 0.15$ (Figure 5.30), without affecting greatly the dimensions of the unit cell.

5.5.2 Electrical transport properties for $Cu_{2+x}ZnGe_{1-x}Se_4$ ($0 \leq x \leq 0.15$)

Electrical resistivity and Seebeck coefficient measurements were carried out on circular pellets of $Cu_{2+x}ZnGe_{1-x}Se_4$ ($0 \leq x \leq 0.15$) over the temperature range $300 \leq T / K \leq 655$ as described in Section 2.7.1.1. The substitution of Ge atoms by Cu provides two holes and significantly affects the electrical transport properties of the material. The electrical resistivity (Figure 5.31) presents a sharp reduction for the sample with x = 0.075 especially for temperatures below 400 K. At higher levels of substitution, it remains correspondingly low. Hole doping drives the material from the semiconducting to the metallic region for $x \geq 0.075$ and $T \leq 400$ K as evidenced by the change in sign of the gradient $d\rho / dT$. Above the critical temperature of 473 K, all samples exhibit metal-like $\rho(T)$. A large reduction is also observed in the Seebeck coefficient with the increase of copper content (Figure 5.32), especially for x = 0.05. All samples exhibit positive Seebeck coefficient values, indicating that holes are the dominant charge carriers throughout the series. Both resistivity and Seebeck coefficient data indicate a phase transformation in the temperature range 450 – 473 K analogous to that characterised for the end-member phase and described in Section 5.4.3.

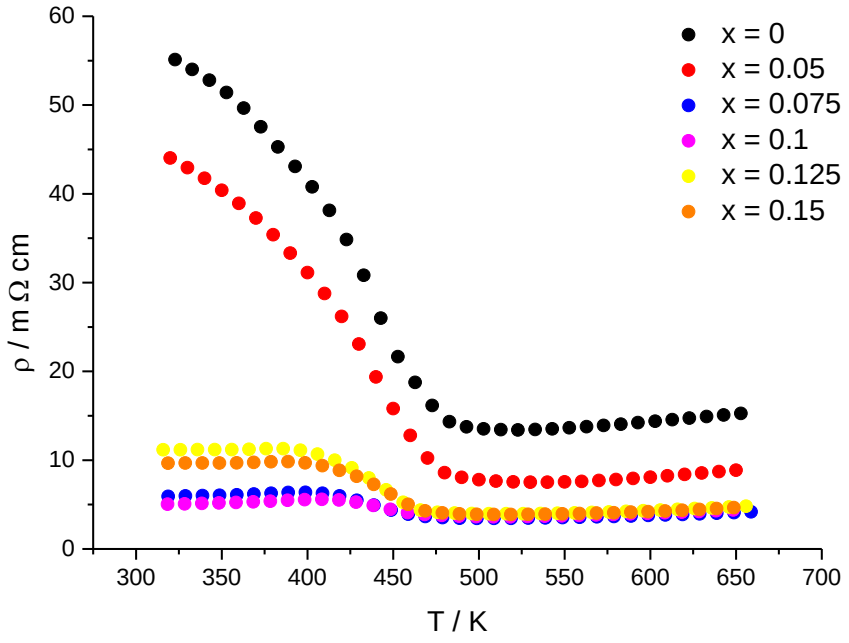

Figure 5.31 Electrical resistivity data as a function of temperature for $Cu_{2+x}ZnGe_{1-x}Se_4$ ($0 \leq x \leq 0.15$) in the temperature range $300 \leq T / K \leq 655$.

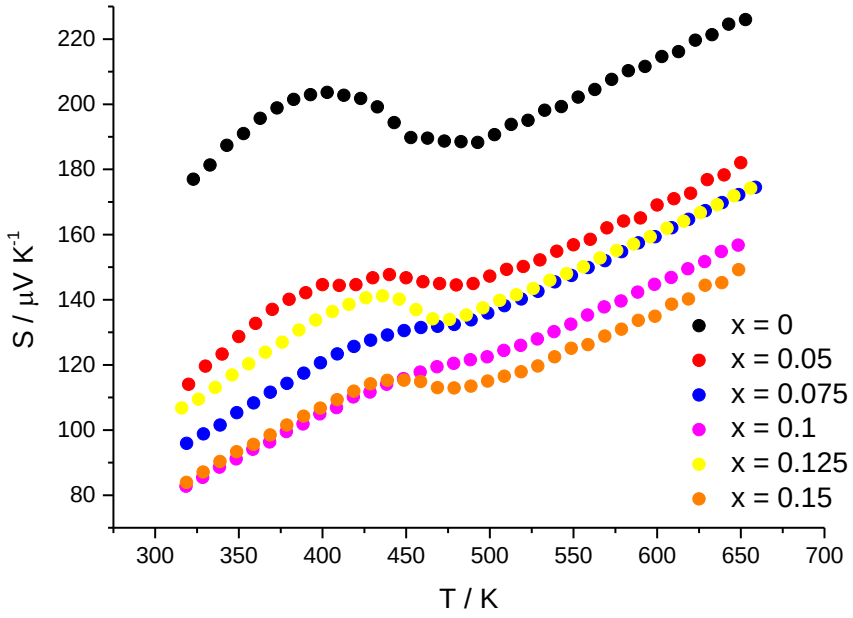

Figure 5.32 Seebeck coefficient data as a function of temperature for $Cu_{2+x}ZnGe_{1-x}Se_4$ ($0 \leq x \leq 0.15$) in the temperature range $300 \leq T / K \leq 655$.

With increasing copper content, the signature of the phase transition becomes less pronounced in both the resistivity and Seebeck coefficient data and the critical temperature of phase transformation shows a slight shift to lower temperatures.

5.5.3 Thermal conductivity for $Cu_{2+x}ZnGe_{1-x}Se_4$ ($0 \leq x \leq 0.15$)

Measurements of the thermal conductivity, κ, were carried out on circular pellets of the series $Cu_{2+x}ZnGe_{1-x}Se_4$ ($0 \leq x \leq 0.15$), according to the procedure described in Section 2.7.2. The electronic contribution, κ_{el}, to the thermal conductivity, was determined by using the Wiedemann-Franz law and the lattice contribution, κ_L, by subtraction. The electrical resistivity data of Section 5.5.2 were used for the determination of κ_{el}. Thermal conductivity data for the series $Cu_{2+x}ZnGe_{1-x}Se_4$ ($0 \leq x \leq 0.15$) are presented in Figure 5.33. The substitution of germanium by copper increases the thermal conductivity of the material. All doped samples exhibit higher values of total κ than those of the Ge-end-member phase in the temperature range 300 – 573 K. Moreover, all samples exhibit a local maximum at 473 K which may be related with the phase transformation. The temperature dependence of electronic thermal conductivity follows the trend of electrical conductivity. Close to room temperature where the electrical conductivity is 'poor', all samples exhibit low values of κ_e. In the temperature region

close to critical temperature of 473 K, the rise of the electronic thermal conductivity is more intense as a function of temperature.

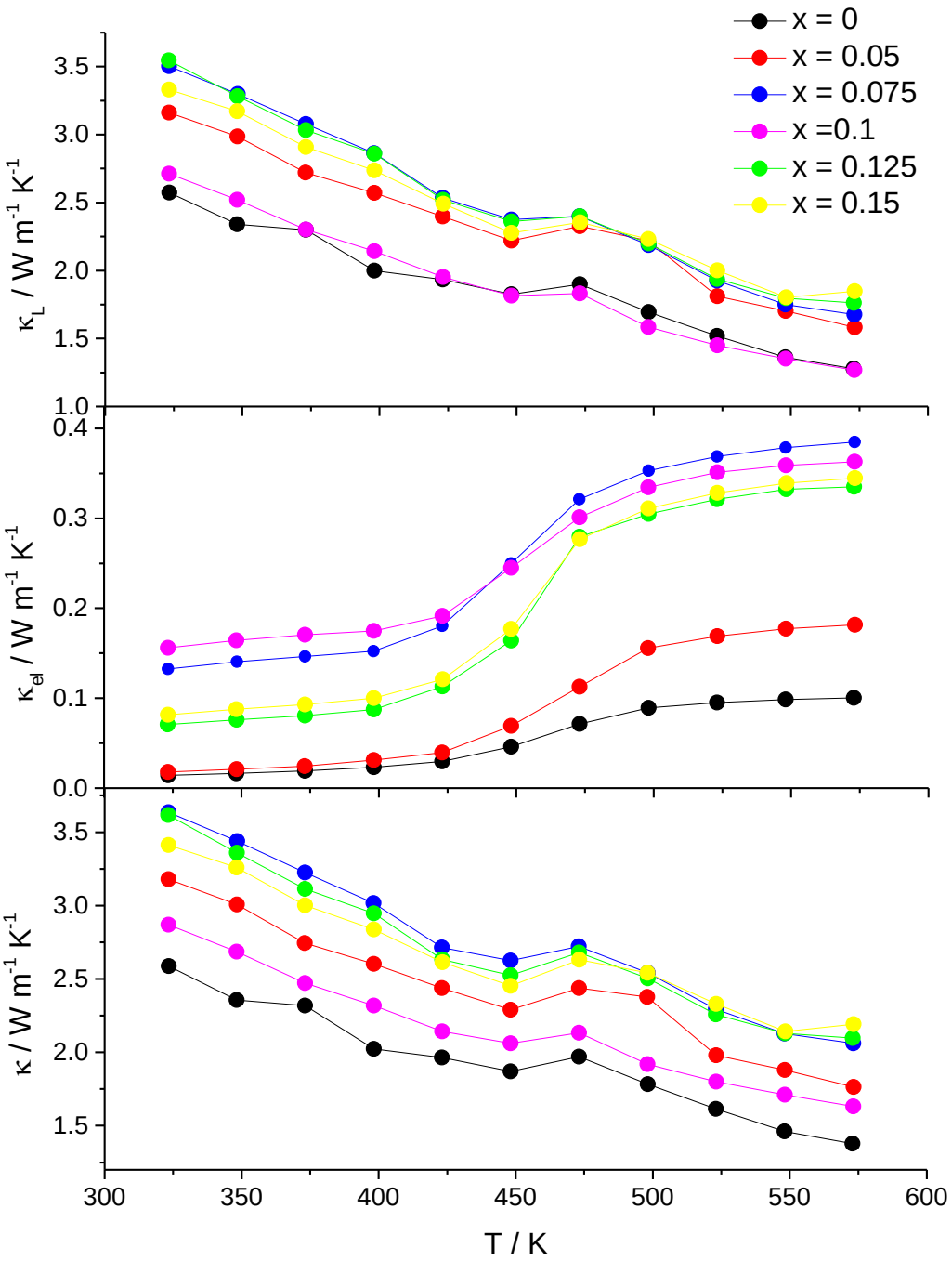

Figure 5.33 Thermal conductivity κ (bottom), electronic contribution, κ_e, (middle) and lattice contribution, κ_L, (top) as a function of temperature for $Cu_{2+x}ZnGe_{1-x}Se_4$ ($0 \leq x \leq 0.15$) in the range $300 \leq T / K \leq 573$.

Most of the doped samples also exhibit slightly higher values of lattice thermal conductivity compared with those of the Ge-end-member phase. This might be explained by the fact that the substitution of Ge by Cu increases the number of atoms with similar atomic masses, Cu and Zn, and reduces simultaneously the number of heavier cations Ge^{4+}, resulting in a less distorted structure. Generally, across the series $Cu_{2+x}ZnGe_{1-x}Se_4$ ($0 \leq x \leq 0.15$), the total thermal conductivity is determined principally by the lattice contribution, while the electronic thermal conductivity contributes only slightly to κ.

5.5.4 Thermoelectric properties for $Cu_{2+x}ZnGe_{1-x}Se_4$ ($0 \leq x \leq 0.15$)

The electrical resistivity, Seebeck coefficient and thermal conductivity data were used to determine the thermoelectric power factor (Figure 5.34) and figure of merit ZT (Figure 5.35) of the series $Cu_{2+x}ZnGe_{1-x}Se_4$ ($0 \leq x \leq 0.15$). Hole doping through the substitution of Ge by Cu improves the power factor of the material because the increase in electrical conductivity offsets the reduction in Seebeck coefficient.

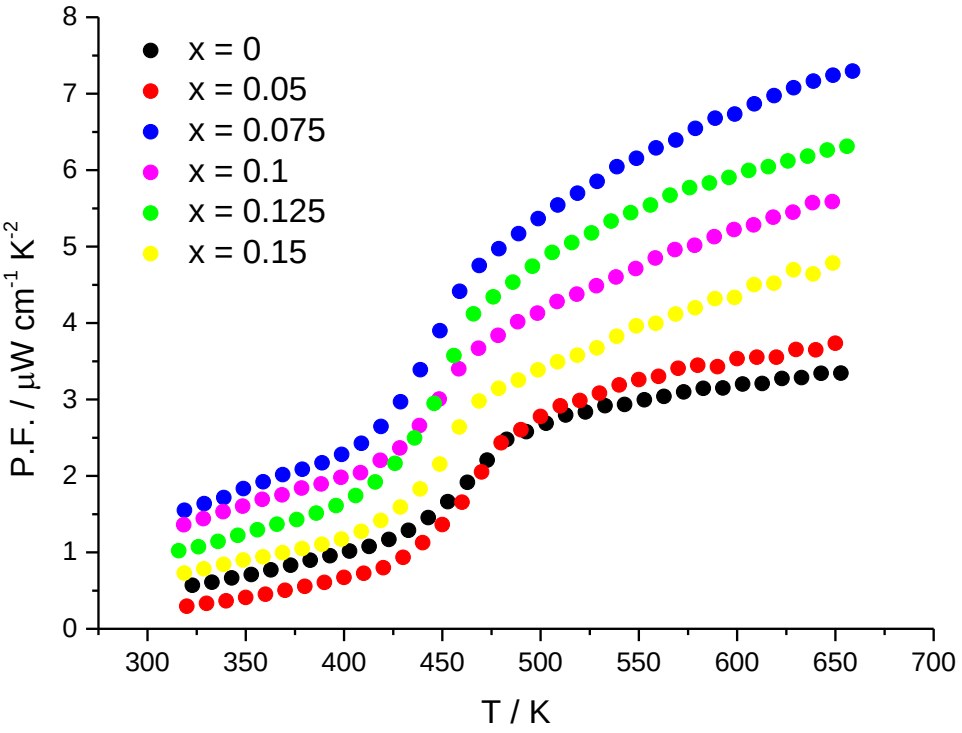

Figure 5.34 Power factor (P.F.) data for $Cu_{2+x}ZnGe_{1-x}Se_4$ ($0 \leq x \leq 0.15$) in the temperature range $300 \leq T / K \leq 655$.

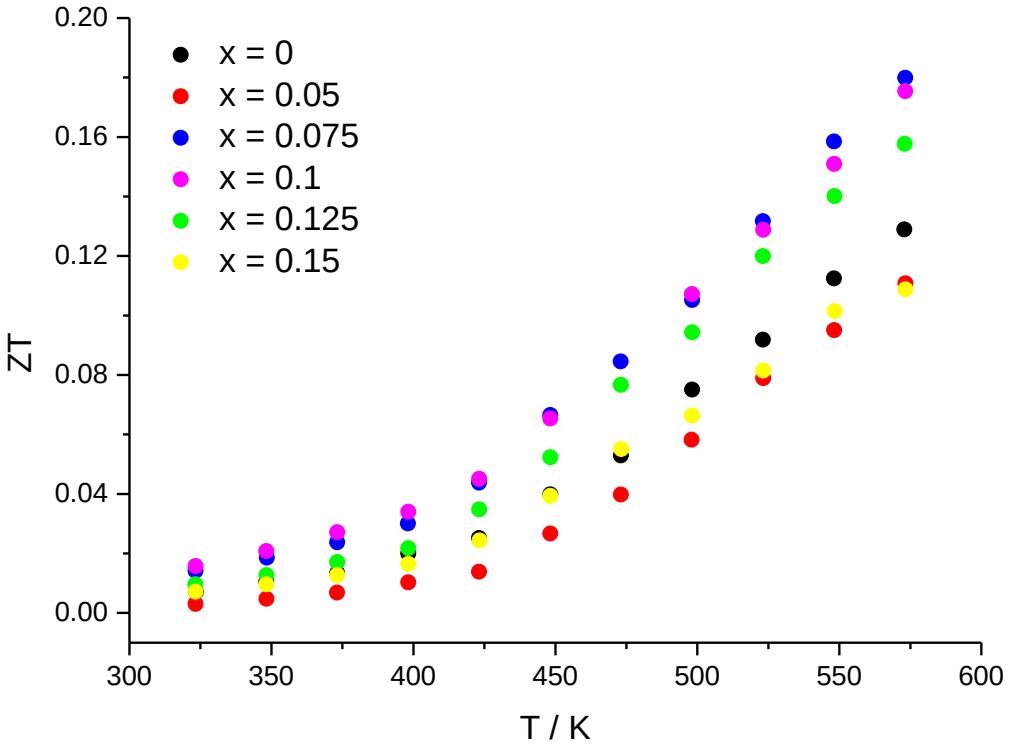

Figure 5.35 Figure-of-merit, ZT, for $Cu_{2+x}ZnGe_{1-x}Se_4$ ($0 \leq x \leq 0.15$) in the temperature range $300 \leq T / K \leq 573$.

All doped samples with $x \geq 0.075$ exhibit higher power factors than those of the Ge-end-member phase in the temperature range 300 – 655 K, with the highest differences being observed above the temperature of 473 K. The power factor exhibits a marked increase with maximum values being observed for x = 0.075, while for higher levels of substitution it is reduced. It is remarkable that $Cu_{2.075}ZnGe_{0.925}Se_4$ exhibits at 655 K a power factor of 7.3 μW cm^{-1} K^{-2}, which corresponds to an increase of *ca*. 120 % from that of the end-member $Cu_2ZnGeSe_4$.

The thermoelectric figure-of-merit of the material is improved through the substitution of Ge by Cu for $0.075 \leq x \leq 0.125$. The maximum ZT values are reached by the samples with the lowest electrical resistivities. The improvement in electrical conductivity is sufficient to offset both the decrease in Seebeck coefficient and the increase in thermal conductivity, arising from a larger electronic component. The maximum ZT of 0.18 is exhibited by $Cu_{2.075}ZnGe_{0.925}Se_4$ at 573 K and corresponds to an increase of 38.5 % compared to that of the stoichiometric end-member phase. Limitation of the thermal diffusivity instrument did not allow measurements of thermal conductivity above 573 K. If the rising trend in ZT as a function of temperature was to continue to higher temperatures, even higher ZT values may be possible.

5.6 Conclusions

In this chapter, structural investigations were conducted on quaternary chalcogenides A_2ZnCQ_4 (A = Cu, Ag; C = Sn, Ge; Q = S, Se) through the collection of powder neutron diffraction data at ISIS facility, Rutherford Appleton Laboratory. The multibank Rietveld refinements revealed that all compounds are best described in the space group $I\bar{4}$, which allows the possibility of a stannite-type structure ($I\bar{4}2m$) to be excluded. For all copper-containing materials, Cu/Zn disorder is observed in the z = 0.25 and 0.75 planes and as a result these structures are considered to be disordered kesterites. The highest extent of Cu/Zn disorder is exhibited by the copper-germanium compounds. In Cu_2ZnGeS_4, the *2c* position is occupied by *ca*. 67 % of Cu and *ca*. 33 % of Zn, while in $Cu_2ZnGeSe_4$, the occupancy factors of Cu and Zn cations in the *2c* site are *ca*. 71 % and *ca*. 29 % respectively. The tin analogues are less disordered with the *2c* position occupied by *ca.* 5.5 % and *ca.* 8 % of Zn cations in the sulphide and selenide respectively. By contrast, the silver compounds crystallize in a fully ordered structure. The *2c* position is occupied only by Ag cations and the *2d* only by Zn cations. These structures are described as ordered kesterites.

Powder neutron diffraction data were also collected at elevated temperatures for the Cu_2ZnGeQ_4 (Q = S, Se) phases. For the sulphide, Rietveld analysis showed that the Cu/Zn disorder in the z = 0.25 and 0.75 planes is not affected greatly up to a temperature of 873 K, while in the temperature range $973 \leq T / K \leq 1073$ an increase of the degree of disorder is observed with the *2c* position being occupied by *ca.* 62 % of Cu^{+} and *ca*. 38 % of Zn^{+2} at 1073 K. An irreversible phase transition from the zinc-blende kesterite ($I\bar{4}$) to the wurtzite stannite structure ($Pmn2_1$) is observed at 1123 K. The high-temperature phase exhibits complete cation ordering which remains during the cooling process. For $Cu_2ZnGeSe_4$, the neutron study reveals at $T \geq 473$ K full Cu/Zn disorder in in the z = 0.25 and 0.75 planes and the creation of Cu vacancies at the three crystallographic positions, *2a*, *2c* and 2d. The number of Cu vacancies increases with increasing temperature, reaching 29.5 % at 973 K. It is suggested that Cu vacancies probably induce changes in the band structure. This results in a semiconducting-to-metallic transition in the behaviour of the material which occurs at 500 K. TGA/DSC analysis of $Cu_2ZnGeSe_4$ showed in the temperature range $400 \leq T / K \leq 500$ a thermal feature which is associated with the phase transformation.

In an effort to improve the thermoelectric properties of the *p*-type semiconductor $Cu_2ZnGeSe_4$, hole doping was carried out through the chemical substitution of Ge by

Cu. Powder X-ray diffraction data showed that all samples across the series $Cu_{2+x}ZnGe_{1-x}Se_4$ ($0 \leq x \leq 0.15$) crystallize in the space group $I\bar{4}$ with small levels of ZnSe and CuSe impurities. Physical property measurements reveal a marked reduction in electrical resistivity with increasing Cu content. For $x \geq 0.075$ the behaviour of the material changes from semiconducting to metallic in the range $300 \leq T / K \leq 400$. The improvement of electrical conductivity outweighs the decrease in Seebeck coefficient, resulting in a pronounced increase of the thermoelectric power factor. Although the substitution of Ge by Cu causes a small increase in thermal conductivity, an improvement of the thermoelectric figure-of-merit is achieved with the maximum value of 0.18 exhibited by $Cu_{2.075}ZnGe_{0.925}Se_4$ at 573 K.

Chapter 6 - Conclusions

In this thesis, research was carried out on two families of chalcogenide materials, the shandite sulphides and the quaternary chalcogenides. Structural investigations were conducted on polycrystalline compounds using powder X-ray and neutron diffraction. Physical properties were measured, and the thermoelectric figure-of-merit was determined. Doping strategies through chemical substitution were applied in order to improve the thermoelectric performance of the materials.

6.1 Shandite sulphides

The shandite $Co_3Sn_2S_2$ is a pseudo-two-dimensional mixed-metal sulphide and has attracted interest for its thermoelectric properties. The low-dimensionality of the structure provides a more structured density of states with narrow peaks close to the Fermi level. In an effort to achieve an increase in Seebeck coefficient by tuning E_F within these narrow *d*-bands, electron and hole doping was examined through the substitution of Co by its neighbouring elements, Ni and Fe, synthesising the two series, $Co_{3-x}Ni_xSn_2S_2$ ($0 \leq x \leq 3$) and $Co_{3-x}Fe_xSn_2S_2$ ($0 \leq x \leq 0.6$). In the case of Ni substitution, powder X-ray diffraction showed an expansion of the kagome layer, while the substitution of Co by Fe causes a slight increase of spacing between the layers. Neutron diffraction studies revealed that across the two series, the transition-metal site is fully disordered. ^{119}Sn and ^{57}Fe Mössbauer spectroscopy measurements were conducted on the series $Co_{3-x}Fe_xSn_2S_2$ ($0 \leq x \leq 0.6$). The two tin sites retain their zero valent state across the series, while two distinct sub spectra are observed for iron atoms. This is likely to be associated with the differences of the local electronic environment of iron atoms which are located at the *9d* site with a disordered fashion. Electron doping enhances the metallic character of the material as nickel content increases, while hole doping drives the material to become *n*-type semiconductor. A metal-to-semiconductor transition occurs for iron substitution at x = 0.5. Ni substitution causes a reduction in Seebeck coefficient which is mainly responsible for the decrease of the ZT across the series. On the other hand, the depopulation of the 24th *d*-band through Fe substitution results in an increase in $|S|$ which probably comes from the shift of E_F to a region of the density of states which shows a more pronounced curvature. This, together with the simultaneous reduction of thermal conductivity improves the thermoelectric

performance of the material. $Co_{2.6}Fe_{0.4}Sn_2S_2$ exhibits the maximum ZT value of 0.2 at 523 K.

Attempts were carried out to increase further the thermoelectric figure-of-merit of the shandite $Co_3Sn_2S_2$, introducing more holes by simultaneous chemical substitution at both transition-metal and main-group metal sites. Substituting tin by indium in the already iron-doped material, the number of holes was increased, shifting the Fermi level to even lower energies. Two series were investigated, $Co_{2.5}Fe_{0.5}Sn_{2-y}In_yS_2$ ($0 \leq y \leq 0.6$) and $Co_{2.667}Fe_{0.333}Sn_{2-y}In_yS_2$ ($0 \leq y \leq 0.7$), keeping constant the iron content and increasing gradually the indium composition. The phase purity of the samples was tested by powder X-ray diffraction. Traces of In_3S_4 were identified. Rietveld refinements revealed an increase of spacing between the kagome layers as In content was increased, enhancing the two-dimensionality of the structure. Electrical and thermal transport properties were measured, and the thermoelectric figure-of-merit was determined across the two series. The material becomes more semiconducting with the increase of indium substitution. The thermoelectric performance is improved in both series with the maximum ZT values to be observed for a total number of holes per formula unit *ca*. 0.9. However, $Co_{2.667}Fe_{0.333}Sn_{2-y}In_yS_2$ ($0 \leq y \leq 0.7$) presents a more pronounced improvement in the thermoelectric efficiency because across the series a high increase in the Seebeck coefficient occurs. DFT calculations were carried out by Mr Alex Aziz for the determination of DOS for a wide range of iron and indium substituted samples. The DOS of $Co_{2.667}Fe_{0.333}Sn_{0.667}In_{0.333}S_2$ shows sharp peaks close to E_F. According to the Mott relation, the tuning of E_F in this sharply-structured region of DOS is the key for this remarkable rise in Seebeck coefficient (*ca.* 140 %). Comparing the thermoelectric properties of $Co_{2.667}Fe_{0.333}Sn_{2-y}In_yS_2$ ($0 \leq y \leq 0.7$) with those of $Co_3Sn_{2-y}In_yS_2$ ($0 \leq y \leq 2$), it is concluded that the iron-doped series exhibits higher power factor values at 473 K, while both series reach similar maxima of figure-of-merit. Therefore, the iron substitution by x = 0.333 provides the same thermoelectric performance, reducing in parallel the synthesis cost of the material. It is notable that $Co_{2.667}Fe_{0.333}Sn_{1.5}In_{0.5}S_2$ exhibits the highest reported power factor (19.2 $\mu W\ cm^{-1}\ K^{-2}$) for a bulk sulphide in the temperature range 400 - 450 K, while $Co_{2.667}Fe_{0.333}Sn_{1.4}In_{0.6}S_2$ reaches the maximum ZT of 0.28 at 473 K. Table 6.1 presents the TE properties of selected materials described in Chapters 3 and 4, illustrating the gradual progress achieved in the TE performance of the shandite sulphides. It is remarkable that through the simultaneous substitution at the transition-metal and main-group sites in $Co_3Sn_2S_2$ the figure-of-merit doubled.

Table 6.1 Thermoelectric properties at 473 K of shandite sulphides

Material	ρ / $m\Omega$ *cm*	S / $\mu V\,K^{-1}$	κ / $W\,m^{-1}\,K^{-1}$	*ZT*
$Ni_3Sn_2S_2$	0.06	-21.9	21.80	0.02
$Co_3Sn_2S_2$	0.38	-71.2	4.67	0.14
$Co_{2.6}Fe_{0.4}Sn_2S_2$	0.53	-85.4	3.85	0.17
$Co_{2.5}Fe_{0.5}Sn_{1.6}In_{0.4}S_2$	0.75	-108.1	3.51	0.21
$Co_{2.667}Fe_{0.333}Sn_{1.4}In_{0.6}S_2$	0.89	-127.4	3.15	0.28

6.2 Quaternary Chalcogenides

Powder neutron diffraction studies were carried out on quaternary sulphides and selenides of general formula A_2ZnCQ_4 (*A* = Cu, Ag; *C* = Sn, Ge; *Q* = S, Se). These compounds exhibit exceptional properties for many sustainable applications. However, their structural characterization remains an ambiguous issue due to the presence of cations with similar atomic masses. For this reason, structural investigations with neutrons are necessary because they can provide a good contrast between the neighbouring elements involved in the structure. The Rietveld analysis revealed that these compounds are crystallized in the kesterite structure with the space group $I\bar{4}$. Possible cation ordering was examined for all samples. The multibank refinements showed a Cu/Zn disorder at the *z* = 0.25 and 0.75 planes for all copper-containing phases, while the structures of silver compounds are ordered with Ag and Zn cations occupying the *2c* and *2d* position respectively. Neutron diffraction experiments were also carried out at high temperatures for the Cu_2ZnGeQ_4 (*Q* = S, Se) phases. For the sulphide, the Rietveld refinements show an increase in the Cu/Zn disorder in the temperature range $973 \leq T / K \leq 1073$, with the *2c* position being occupied by *ca.* 62 % of Cu^+ and *ca.* 38 % of Zn^{+2}. An irreversible phase transition from the zinc-blende kesterite ($I\bar{4}$) to the wurtzite-stannite structure ($Pmn2_1$) is revealed at 1123 K. For $Cu_2ZnGeSe_4$, at 473 K the *z* = 0.25 and 0.75 planes become fully disordered and simultaneously Cu vacancies start being created at the three cupper sites, *2a*, *2c* and 2*d*. As the temperature increases, a gradual increase of Cu vacancies is observed at the three sites. At 973 K, 29.5 % of the total copper content has been released as mobile Cu^+ ions in the solid. Probably, the creation of copper vacancies affects the band structure of the material. This may explain the semiconductor-to-metal transformation which is observed at 500 K. TGA/DSC analysis of $Cu_2ZnGeSe_4$ reveals a slight variation in the

heat flow in the temperature region around 473 K, supporting the neutron diffraction results. Hole doping was carried out in $Cu_{2+x}ZnGe_{1-x}Se_4$ ($0 \leq x \leq 0.15$) in order to improve the thermoelectric performance of the material. Powder X-ray diffraction data are well-described in the space group $I\bar{4}$, although some traces of ZnSe and CuSe are evident. The substitution of Ge by Cu increases the number of holes, improving greatly the electrical transport properties of the material. A large reduction in electrical resistivity is accomplished by the increase of copper content and for x = 0.075 a semiconducting-to-metallic transition is observed. The increase in electrical conductivity outweighs the decrease of the Seebeck coefficient and the small rise of thermal conductivity, resulting in an improvement of thermoelectric performance of the material. $Cu_{2.075}ZnGe_{0.925}Se_4$ exhibits the maximum ZT value of 0.18 at 573 K.

6.3 Future work

In this thesis, an improvement in the thermoelectric performance of shandite sulphides was achieved through the chemical substitution at the transition-metal and main-group metal sites. $Co_{2.667}Fe_{0.333}Sn_{1.4}In_{0.6}S_2$ has the potential to be a promising sulphide for low-temperature thermoelectric applications. This material exhibits adequate electrical transport properties with a relatively low electrical resistivity and a sufficient Seebeck coefficient, particularly at temperatures close to ambient. This results in a power factor of 19.2 $\mu W\ cm^{-1}\ K^{-2}$ at 400 K which is a high value for an earth-abundant bulk thermoelectric material and can be competitive with those of state-of-the-art bulk bismuth telluride alloys. However, its thermal conductivity still remains at high values, decreasing markedly the overall performance and keeping the ZT in low levels. For this reason, efforts should be carried out in the future for the reduction of κ. Nanocompositing is a good strategy to increase phonon scattering in the lattice matrix and to achieve an effective decrease in lattice thermal conductivity.

The structural investigations using powder neutron diffraction, in quaternary chalcogenides lead to important conclusions about their superstructure, the cation ordering and phase transition phenomena which occur at elevated temperatures. This study will support future research of these materials for a wide range of environmentally friendly applications. Moreover, there are no reports about the thermoelectric properties of silver analogues. Investigations of these compounds as possible candidate thermoelectrics may lead to promising results in the future. The neutron diffraction study of $Cu_2ZnGeSe_4$ in the temperature range $300 \leq T / K \leq 973$, reveals the creation of copper vacancies for $T \geq 473$ K, assuming that Cu ions are released and become mobile

in the structure. Ionic conductivity measurements would be useful as future work, in order to check possible contribution in the total electrical conductivity. In addition, DFT calculations and X-ray photoelectron spectroscopy experiments would shed further light on the semiconductor-to-metal transition and the possible effect of copper vacancies on the band structure of the material.

References

1. U.S. Department of Energy, Energy Information Administration, Report# DOE/EIA-0484 (2009), International Energy Outlook 2009, Washington: Government Printing Office, 2009.
2. P. K. Choubey, K.-S. Chung, M.-S. Kim, J.-C. Lee, R. R. Srivastava, *Miner. Eng.*, 2017, **110**, 104.
3. A. J. Jacobson, *Chem. Mater*., 2010, **22**, 660.
4. A. González, E. Goikolea, J. A. Barrena, R. Mysyk, *Renew. Sust. Energ. Rev.*, 2016, **58**, 1189.
5. W. A. Badawy, *J. Adv. Res.*, 2015, **6**, 123.
6. P. Vaqueiro and A. V. Powell, *J. Mater. Chem.*, 2010, **20**, 9577.
7. D. M. Rowe, *Renew. Energ.*, 1999, **16**, 1251.
8. L. E. Bell, *Science*, 2008, **321**, 1457.
9. D. M. Rowe, *Thermoelectrics Handbook Macro to Nano*, Taylor & Francis Group, 2006.
10. J. R. Sootsman, D. Y. Chung, M. G. Kanatzidis, *Angew. Chem. Int. Ed.*, 2009, **48**, 8616.
11. A. J. Minnich, M. S. Dresselhaus, Z. F. Ren, G. Chen, *Energy Environ. Sci.*, 2009, **2**, 466.
12. G. J. Snyder and E. S. Toberer, *Nat. Mater*., 2008, **7**, 105.
13. H.J. Goldsmid and J.W. Sharp, *J. Electron. Mater.*, 1999, **28**, 869.
14. R. J. D. Tille, *Understanding solids: the science of materials*, John Wiley & Sons, West Sussex, 2004.
15. R. Agarwal and C. M. Lieber, *Appl. Phys. A*, 2006, **85**, 209.
16. A. Madhukar, *Solid State Commun.*, 1975, **16**, 383.

17. G. Guélou, P. Vaqueiro, J. Prado-Gonjal, T. Barbier, S. He´bert, E. Guilmeau, W. Kockelmannc and A. V. Powell, *J. Mater. Chem. C*, 2016, **4**, 1871.
18. S. Chen, A. Walsh, Y. Luo, J.-H. Yang, X. G. Gong, and S.-H. Wei, *Phys. Rev. B*, 2010, **82**, 195203.
19. P. A. Cox, *The Electronic Structure and Chemistry of Solids*, 1987**.**
20. C. N. Rao and J. Gopalakrishnan, *New Directions in Solid State Chemistry*, Cambridge University Press, Cambridge, 2nd edn., 1997.
21. N. F. Mott and E. A. Davis, *Electronic Processes in Non-Crystalline Materials*, Clarendon Press, Oxford, 1979.
22. B. C. Sales, D. Mandrus, R. K. Williams, *Science*, 1996, **272**, 1325.
23. K. Kishimoto, S. Utsunomiya, K. Akai, H. Asada, T. Koyanagi, *J. Alloys Compd.*, 2016, 1.
24. R. P. Hermann, R. Jin, W. Schweika, F. Grandjean, D. Mandrus, B. C. Sales and G. J. Long, *Phys. Rev. Lett.*, 2003, **90**, 135505-1.
25. K. Biswas, J. He, I. D. Blum, C.-I. Wu, T. P. Hogan, D. N. Seidman, V. P. Dravid, M. G. Kanatzidis, *Nature*, 2012, **489**, 414.
26. C. Wood, *Rep. Prog. Phys.*, 1988, **51**, 459.
27. K. Biswas, J. He, Q. Zhang, G. Wang, C. Uher, V. P. Dravid and M. G. Kanatzidis, *Nature*, 2011, **3**, 160.
28. B. Poudel, Q. Hao, Y. Ma, Y. Lan, A. Minnich, B. Yu, X. Yan, D. Wang, A. Muto, D. Vashaee, X. Chen, J. Liu, M. S. Dresselhaus, G. Chen, Z. Ren, *Science*, 2008, **320**, 634.
29. I. Terasaki, Y. Sasago and K. Uchinokura, *Phys. Rev. B*, 1997, **56**, R12685.
30. M. S. Dresselhaus, G. Chen, M. Y. Tang, R. Yang, H. Lee, D. Wang, Z. Ren, J.-P. Fleurial, P. Gogna, *Adv. Mater.*, 2007, **19**, 1043.
31. A. I. Hochbaum, R. Chen, R. D. Delgado, W. Liang, E. C. Garnett, M. Najarian, A. Majumdar, P. Yang, *Nature*, 2008, **451**, 163.
32. A. I. Boukai, Y. Bunimovich, J. Tahir-Kheli, J.-K. Yu, W. A. Goddard, J. R. Heath, *Nature*, 2008, **451**, 168.
33. E. A. Skrabek and D. S. Trimmer, *CRC Handbook of Thermoelectrics*, CRC, Boca Raton, 1995.
34. C. B. Vining, W. Laskow, J. O. Hanson, R. R. Vanderbeck, P. D. Gorsuch, *J. Appl. Phys.*, 1991, **69**, 4333.
35. Wright, D. A., *Nature*, **181**, 1958, 834.

36. O. Ben-Yehuda, R. Shuker, Y. Gelbstein, Z. Dashevsky and M. P. Dariel, *J. Appl. Phys.*, 2007, **101**, 113707.
37. J. R. Drabble and C. H. I. Goodmann, *J. Phys. Chem. Solid*, 1958, **5**, 142.
38. R. Venkatasubramanian, E. Siivola, T. Colpitts, B. O'Quinn, *Nature*, 2001, **413**, 597.
39. M. H. Ettenberg, W. A. Jesser and F. D. Rosi, *Proc. 15th Int. Conf. on Thermoelectrics*, IEEE, Piscataway, NJ, 1996.
40. A. Kyono and M. Kimata, *Am. Mineral.*, 2004, **89**, 932.
41. D. Guo, C. Hu, C. Zhang, *Mater. Res. Bull.*, 2013, **48**, 1984.
42. B. Chen, C. Uher, L. Iordanidis and M. G. Kanatzidis, *Chem. Mater.*, 1997, **9**, 1655.
43. L.-D. Zhao, B.-P. Zhang, W,-S. Liu, H.-L. Zhang, J.-F. Li, *J. Solid State Chem.*, 2008, **181**, 3278.
44. K. Biswas, L. Zhao and M. G. Kanatzidis, *Adv. Energy Mater.*, 2012, **2**, 634.
45. L.-D. Zhao, J. He, C.-I. Wu, T. P. Hogan, X. Zhou, C. Uher, V.P. Dravid, M. G. Kanatzidis, *J. Am. Chem. Soc.*, 2012, **134**, 7902.
46. S. Johnsen, J. Q. He, J., J. Androulakis,V. P. Dravid, I. Todorov, D.-Y. Chung, M. G. Kanatzidis, *J. Am. Chem. Soc.*, 2011, **133**, 3460.
47. L.-D. Zhao, S.-H. Lo, J. Q. He, H. Li, K. Biswas, J. Androulakis, C.-I. Wu, T. P. Hogan, D.-Y. Chung, V. P. Dravid, M. G. Kanatzidis, *J. Am. Chem. Soc.*, 2011, **133**, 20476.
48. Cox, P. A., *The Elements: Their Origin, Abundance, and Distribution,* Oxford University Press, Oxford, 1989.
49. K. F. Hsu, S. Loo, F. Guo, W. Chen, J. S. Dyck, C. Uher, T. Hogan, E. K. Polychroniadis, M. G. Kanatzidis, *Science*, 2004, **303**, 818.
50. S. N. Girard, J. Q. He, X. Y. Zhou, D. Shoemaker, C. M Jaworski, C. Uher, V. P. Dravid, J. P. Heremans, M. G. Kanatzidis, *J. Am. Chem. Soc.*, 2011, **133**, 16588.
51. J. Androulakis, I.Todorov, J. Q. He, D.-Y. Chung, V. P. Dravid, M. G. Kanatzids, *J. Am. Chem. Soc*., 2011, **133**, 10920.
52. H. Wang, Y. Z. Pei, A. D. Lalonde, G. Snyder, *J. Adv. Mater.*, 2011, **23**, 1366.
53. A. M. Schmidt, M. A. McGuirea, F. Gascoin, G. J. Snyder, F. J. DiSalvo, *J. Alloys Compd.*, 2007, **431**, 262.
54. T. Caillat, J. P. Fleural, G. J. Snyder, *Solid State Sci.*, 1999, **1**, 535.
55. M. A. McGuire, C. Ranjan and F.J. DiSalvo, *Inorg. Chem*., 2006, **45**, 2718.

56. M. Ohta, H. Yuan, S. Hirai, Y. Yajima, T. Nishimura, K. Shimakage, *J. Alloys Compd.*, 2008, **451**, 627.
57. M. Ohta and S. Hirai, *J. Electron. Mater.* 2009, **38**, 1287.
58. M. Ohta, S. Hirai and T. Kuzuya, *J. Electron. Mater.*, 2011, **40**, 537.
59. T. Takeshita, K. A. Gschneidner, Jr. and B. J. Beaudry, *J. Appl. Phys.*, 1985, **57**, 4633.
60. K. Suekuni, K. Tsuruta, T. Ariga and M. Koyano, *Appl. Phys. Express 5*, 2012, **5**, 051201-1.
61. D. Berthebaud, O.I. Lebedev, A. Maignan, *J. Materiomics*, 2015, **1**, 68.
62. Y. He, T. Day, T. Zhang, H. Liu, X. Shi, L. Chen and G. Jeffrey Snyder, *Adv. Mater.*, 2014, **26**, 3974.
63. B. Yua, W. Liua, S. Chena, H. Wanga, H. Wanga, G. Chenb, Z. Rena, *Nano Energy*, 2012, **1**, 472.
64. X. Lu, D. T. Morelli, Y. Xia and V. Ozolins, *Chem. Mater.*, 2015, **27**, 408.
65. J. Heo, G. Laurita, S. Muir, M. A. Subramanian and D. A. Keszler, *Chem. Mater.*, 2014, **26**, 2047.
66. R. Chetty, A. Bali, M. H. Naik, G. Rogl, P. Rogl, M. Jain, S. Suwas and R. C. Mallik, *Acta Mater.*, 2015, **100,** 266.
67. P. Qiu, T. Zhang, Y. Qiu, X. Shi and L. Chen, *Energy Environ. Sci.*, 2014, **7**, 4000.
68. R Weihrich and I. Anusca, *Z. Anorg. Allg. Chem.*, 2006, **632**, 1531.
69. P. Vaqueiro and G. G. Sobany, *Solid State Sci.*, 2009, **11**, 513.
70. Y.S. Dedkov, M. Holder, S.L. Molodtsov and H.Rosner, *J. Phys.*, 2008, **100**, 1742.
71. X. Y. Shi, F. Q. Huang, M. L. Liu, and L. D. Chen, *Appl. Phys. Lett.*, 2009, **94**, 122103.
72. M.-L. Liu, I-W. Chen, F.-Q. Huang and L.-D.Chen, *Adv. Mater.*, 2009, **21**, 3808.
73. R. Chetty, J. Dadda, J. de Boor, E. Müller, R. C. Mallik, *Intermetallics*, 2015, **57**, 156.
74. R. Chetty, A. Bali, O.E. Femi, K. Chattopadhyay and R.C. Mallik, *J. Electron. Mater.*, 2016, **45**, 1625.
75. K. Wei, L. Beauchemin, H. Wang, W. D. Porter, J. Martin, G. S. Nolas, *J. Alloys Compd.*, 2015, **650,** 844.
76. J. S. Benjamin, *Metall. Trans.*, 1970, **1**, 2943.

77. C. C. Koch, *Nanostruct. Mater.*, 1993, **2**, 109 - 129.
78. B. S. Murty and S. Ranganathan, *Int. Mater. Rev.*, 1998, **43**, 101.
79. A. R. West, *Basic Solid State Chemistry, Second Edition*, John Wiley & Sons Ltd, 1999.
80. *Bruker AXS GmbH, "EVA",* Karlsruhe, Germany, 2007.
81. A. C. Larson and R. B. von Dreele"General Structure Analysis System (GSAS)", Los Alamos National Laboratory Report LAUR, 2004, 86-748.
82. L. E. Smart and E. A. Moore, *Solid State Chemistry: An Introduction, Fourth Edition*, CRC Press, 2012.
83. https://www.ncnr.nist.gov/resources/n-lengths/list.html
84. *http://www.stfc.ac.uk/news/uk-science-facility-praised-by-international-review/.*
85. http://wwwisis2.isis.rl.ac.uk/disordered/gem/gem_home.htm.
86. A. C. Hannon, *Nucl. Instrum. Meth. A*, 2005, **551**, 88.
87. http://www.isis.stfc.ac.uk/instruments/polaris/polaris-upgrade-poster11575.pdf.
88. *http://www.isis.stfc.ac.uk/instruments/polaris/polaris4643.html*.
89. H. Rietveld, *J. Appl. Cryst.*, 1969, **2**, 65.
90. R. A. Young, *The Rietveld Method*, Oxford University Press, Oxford, 1993.
91. C. Howard, *J. App. Cryst.*, 1982, **15**, 615.
92. P. Thompson, D. E. Cox, J. B. Hastings, *J. Appl. Cryst.*, 1987, **20**, 79.
93. P. Gütlich, *Lecture Notes "Mössbauer Spectroscopy"*, Online: http://obelix.physik.uni-bielefeld.de/~schnack/molmag/material/Guetlich-Moessbauer_Lectures_web.pdf.
94. J. Corps, P. Vaqueiro and A.V. Powell, *J. Mater. Chem. A*, 2013, **1**, 6553.
95. T. Kubodera, H. Okabe, Y. Kamihara and M. Matoba, *Physica B*, 2006, **378 - 380**, 1142.
96. R. Weihrich, I. Anusca and M. Zabel, *Z. Anorg. Allg. Chem.*, 2005, **631**, 1463.
97. P. Gütlich, K.-J. Range, C. Felser, C. Schultz-Münzenberg, W. Tremel, D. Walcher, and M. Waldeck, *Angew. Chem., Int. Ed.*, 1999, **38**, 2381.
98. J. Rothballer, F. Bachhuber, F. Pielnhofer, F. M. Schappacher, R. Pöttgen, R. Weihrich, *Eur. J. Inorg. Chem.*, 2013, 248.
99. A. Umetani, E. Nagoshi, T. Kubodera, M. Matoba, *Physica B*, 2008, **403**, 1356.
100. J. Corps, P. Vaqueiro, A. Aziz, R. Grau-Crespo, W. Kockelmann, J.C. Jumas, A.V. Powell, *Chem. Mater.*, 2015, **27**, 3946.

101. Y. Sakai, R. Tanakadate, M. Matoba, I. Yamada, N. Nishiyama, T. Irifune, K. Funakoshi, T. Kunimoto, Y. Higo and Y. Kamihara, *J. Phys. Soc. Jpn.*, 2015, **84**, 044705.
102. M. A. Kassem, Y. Tabata, T. Waki, H. Nakamura, *J. Solid State Chem.*, 2016, **233**, 8.
103. M. A. Kassem, Y. Tabata, T. Waki, H. Nakamura, *J. Phys. Soc. Jpn.*, 2016, **85**, 064706.
104. P. Mangelis, P. Vaqueiro, J.-C. Jumas, I. da Silva, R. I. Smith, A. V. Powell, *J. Solid State Chem.*, 2017, **251**, 204.
105. P. E. Lippens, *Phys. Rev. B*, 1999, **60**, 4576.
106. E. Fluck, W. Kerler, and W. Neuwirth, *Angew. Chem. Int. Ed.*, 1963, **2**, 277.
107. N. N. Greenwood and H. J. Whitfield, *J. Chem. Soc. (A)*, 1968, 1697.
108. L. Häggström, T. Ericsson, R. Wäppling, E. Karlsson and K. Chandra, *J. Phys. Colloq.*, 1974, **35(C6)**, 603.
109. G. N. Goncharov, Yu. M. Ostaneich and S.B. Tornilov, *Izv. Akad. Nauk. SSSR, Ser. Geol.*, 1970, **8**, 79.
110. A. A. Temperly and H. W. Lefevre, *J. Phys. Chem. Solids*, 1966, **27**, 85.
111. C. Boekema, A. M. Krupski, M. Varasteh, K. Parvin, F. van Til, F. van der Woude, G. A. Sawatzki, *J. Magn. Magn. Mater.*, 2004, **272**, 559.
112. K. Forcher, W. Lottermoiser and G. Amthauer, *Neu Jb Mineral, Abh.*, 1988, **160**, 25.
113. F. Di Benedetto, G. P. Bernardini, D. Borrini, W. Lottermoser, G. Tippelt, G. Amthauer, *Phys. Chem. Miner.*, 2005, **31**, 683.
114. M. Ohtaa, T. Kuzuyab, H. Sasakib, T. Kawasakib, S. Hirai, *J. Alloys Compd.*, 2009, **484**, 268.
115. M. Ohta, H. Obara and A. Yamamoto, *Mater. Trans.*, 2009, **50**, 2129.
116. G. Kresse and J. Furthmüller, *Comput. Mater. Sci.*, 1996, **6**, 15.
117. Q. Guo, G. M. Ford, W. C. Yang, B. C. Walker, E. A. Stach, H. W. Hillhouse, and R. Agrawal, *J. Am. Chem. Soc.*, 2010, **132,** 17384.
118. S. Chen, X. G. Gong, A. Walsh, and S.-H. Wei, *Appl. Phys. Lett.*, 2009, **94**, 041903.
119. S. Delbos, *EPJ Photovolt.*, 2012, **3**, 35004.
120. C. Sevik and T. Cagin, *Phys. Rev. B*, 2010, **82**, 045202.
121. C. P. Heinrich, T. W. Day, W. G. Zeier, G. J. Snyder and W. Tremel, *J. Am. Chem. Soc*., 2014, **136**, 442.

122. W. G. Zeier, A. LaLonde, Z. M. Gibbs, C. P. Heinrich, M. Panthöfer, G. J. Snyder and W. Tremel, *J. Am. Chem. Soc.*, 2012, **134**, 7147.
123. Ch. Raju, M. Falmbigl, P. Rogl, X. Yan, E. Bauer, J. Horky, M. Zehetbauer and R. C. Mallik, *AIP Adv.*, 2013, **3**, 032106.
124. I. Tsuji, Y. Shimodaira, H. Kato, H. Kobayashi and A. Kudo, *Chem. Mater.*, 2010, **22**, 1402.
125. J. Kim, H. Hiroi, T. K. Todorov, O. Gunawan, M. Kuwahara, T. Gokmen, D. Nair, M. Hopstaken, B. Shin, Y. S. Lee, W. Wang, H. Sugimoto, and D. B. Mitzi, *Adv. Mater.*, 2014, **26,** 7427.
126. W. Wang, M. T. Winkler, O. Gunawan, T. Gokmen, T. K. Todorov, Y. Zhu, and D. B. Mitzi, *Adv. Energy Mater.*, 2014, **4**, 1301465.
127. S. Bourdais, C. Chone, B. Delatouche, A. Jacob, G. Larramona, C. Moisan, A. Lafond, F. Donatini, G. Rey, S. Siebentritt, A. Walsh, and G. Dennler, *Adv. Energy Mater.*, 2016, **6**, 1502276.
128. S. R. Hall, J. T. Szymanski and J. M. Stewart, *Can. Mineral.*, 1978, **16,** 131.
129. J. M. Skelton, A. J. Jackson, M. Dimitrievska, S. K. Wallace and A. Walsh, *APL Mater.*, 2015, **3**, 041102.
130. W. Gong, T. Tabata, K. Takei, M. Morihama, T. Maeda and T. Wada, *Phys. Status Solidi C*, 2015, **12**, 700.
131. R. Chetty, M. Falmbigl, P. Rogl, P. Heinrich, E. Royanian, E. Bauer, S. Suwas and R. C. Mallik, *Phys. Status Solidi A*, 2013, **210**, 2471.
132. D. Zou, G. Nie, Y. Li, Y. Xu, J. Lin, H. Zheng and J. Li, *RSC Adv.*, 2015, **5**, 24908.
133. Y. Dong, H. Wang and G. S. Nolas, *Inorg. Chem.*, 2013, **52**, 14364.
134. S. Chen, A. Walsh, J.-H. Yang, X. G. Gong, L. Sun, P.-X. Yang, J.-H. Chu, and S.-H. Wei, *Phys. Rev. B*, 2011, **83**, 125201.
135. S. Schorr, *Sol. Energ. Mat. Sol. C.*, 2011, 95, 1482.
136. J. Paier, R. Asahi, A. Nagoya and G. Kresse, *Phys. Rev. B*, 2009, **79**, 115126.
137. C. H. Ma, H. F. Guo, K. Z. Zhang, N. Y. Yuan and J. N. Ding, *Mater. Lett.*, 2017, **186,** 390.
138. T. Jing, Y. Dai, X. C. Ma, W. Wei, and B. B. Huang, *J. Phys. Chem. C*, 2015, **119,** 27900.
139. W. G. Zeier, H. Zhu, Z. M. Gibbs, G. Ceder, W. Tremel and G. J. Snyder, J. *Mater. Chem. C*, 2014, **2**, 10189.
140. K. Doverspike, K. Dwight and A. Wold, *Chem. Mater.*, 1990, **2**, 194.

141. M. Guc, A. P. Litvinchuk, S. Levcenko, M. Y. Valakh, I. V. Bodnar, V. M. Dzhagan, V. Izquierdo-Roca, E. Arushanov and A. Perez-Rodrigueza, *RSC Adv.*, 2016, **6,** 13278.
142. W. G. Zeier, C. P. Heinrich, T. Day, C. Panithipongwut, G. Kieslich, G. Brunklaus, G. J. Snyder and W. Tremel, *Mater. Chem. A*, 2014, **2**, 1790.
143. G. Gurieva, D. M. Többens, M. Ya. Valakh, S. Schorr, *J. Phys. Chem. Solids*, 2016, **99**, 100.
144. A. Ritscher, M. Hoelzel, M. Lerch, *J. Solid Sate Chem.*, 2016, **238**, 68.

Appendix A – d-spacing equations

Equations for X-ray diffraction d-spacing calculations:

Orthorhombic:
$$\frac{1}{d_{hkl}^{\ 2}} = \frac{h^2}{a^2} + \frac{k^2}{b^2} + \frac{l^2}{c^2}$$

Tetragonal:
$$\frac{1}{d_{hkl}^{\ 2}} = \frac{h^2 + k^2}{a^2} + \frac{l^2}{c^2}$$

Cubic:
$$\frac{1}{d_{hkl}^{\ 2}} = \frac{h^2 + k^2 + l^2}{a^2}$$

Hexagonal:
$$\frac{1}{d_{hkl}^{\ 2}} = \frac{4}{3}\left(\frac{h^2 + hk + k^2}{a^2}\right) + \frac{l^2}{c^2}$$

Monoclinic:
$$\frac{1}{d_{hkl}^{\ 2}} = \frac{1}{\sin^2 \beta}\left(\frac{h^2}{a^2} + \frac{k^2 \sin^2 \beta}{b^2} + \frac{l^2}{c^2} - \frac{2hl\cos\beta}{ac}\right)$$

Rhombohedral:
$$\frac{1}{d_{hkl}^{\ 2}} = \frac{\left(h^2 + k^2 + l^2\right)\sin^2\alpha + 2\left(hk + kl + hl\right)\left(\cos^2\alpha - \cos\alpha\right)}{a^2\left(1 - 3\cos^2\alpha + 2\cos^3\alpha\right)}$$

Triclinic:
$$\frac{1}{d_{hkl}^{\ 2}} = \frac{1}{V^2}\left(S_{11}h^2 + S_{22}k^2 + S_{33}l^2 + 2S_{12}hk + 2S_{23}kl + 2S_{13}hl\right)$$

where

$$S_{11} = b^2c^2\sin^2\alpha$$
$$S_{22} = a^2c^2\sin^2\beta$$
$$S_{33} = a^2b^2\sin^2\gamma$$
$$S_{12} = abc^2\left(\cos\alpha\cos\beta - \cos\gamma\right)$$
$$S_{23} = a^2bc\left(\cos\beta\cos\gamma - \cos\alpha\right)$$
$$S_{13} = ab^2c\left(\cos\alpha\cos\gamma - \cos\beta\right)$$
$$V = abc\sqrt{1 - \cos^2\alpha - \cos^2\beta - \cos^2\gamma + 2\cos\alpha\cos\beta\cos\gamma}$$

Appendix B – Powder X-ray diffraction refinements for $Co_{3-x}Ni_xSn_2S_2$ ($0 \leq x \leq 3$)

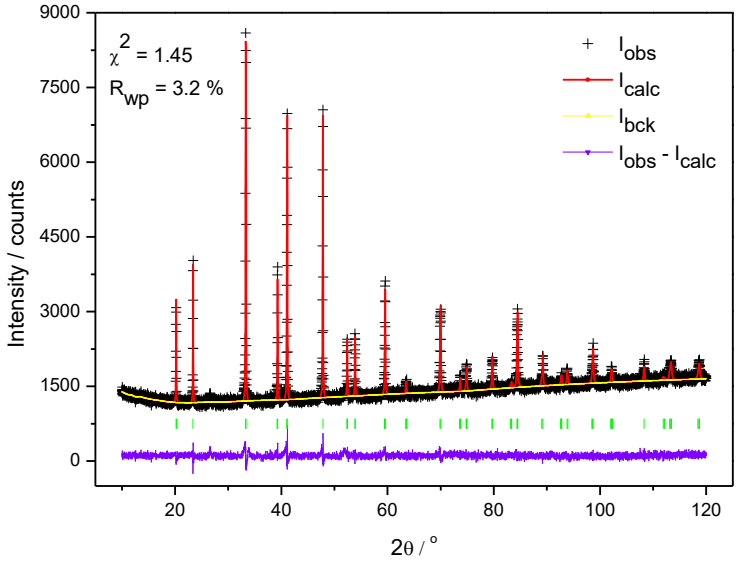

Figure B1 Rietveld refinement for $Co_{2.85}Ni_{0.15}Sn_2S_2$ using X-ray diffraction data. Observed (black crosses), refined (red solid lines) and difference (blue bottom line) profiles. Reflection positions are marked by green lines.

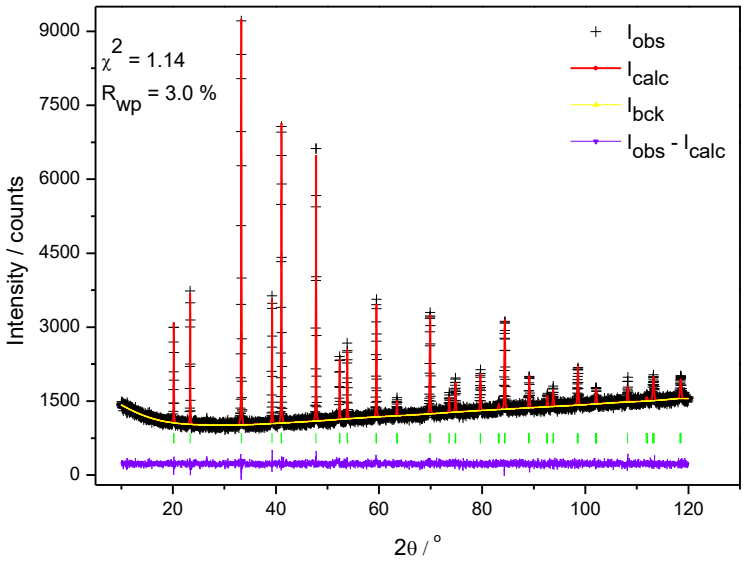

Figure B2 Rietveld refinement for $Co_{2.7}Ni_{0.3}Sn_2S_2$ using X-ray diffraction data. Observed (black crosses), refined (red solid lines) and difference (blue bottom line) profiles. Reflection positions are marked by green lines.

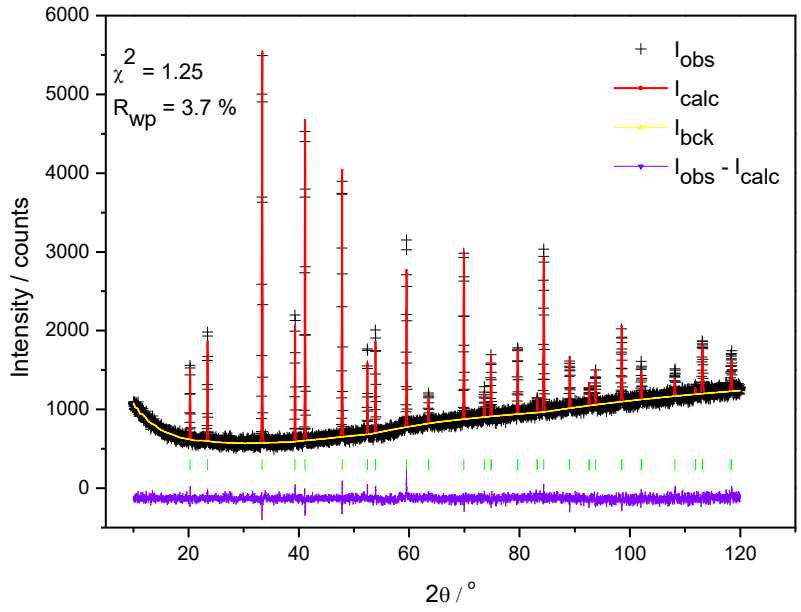

Figure B3 Rietveld refinement for $Co_{2.5}Ni_{0.5}Sn_2S_2$ using X-ray diffraction data. Observed (black crosses), refined (red solid lines) and difference (blue bottom line) profiles. Reflection positions are marked by green lines.

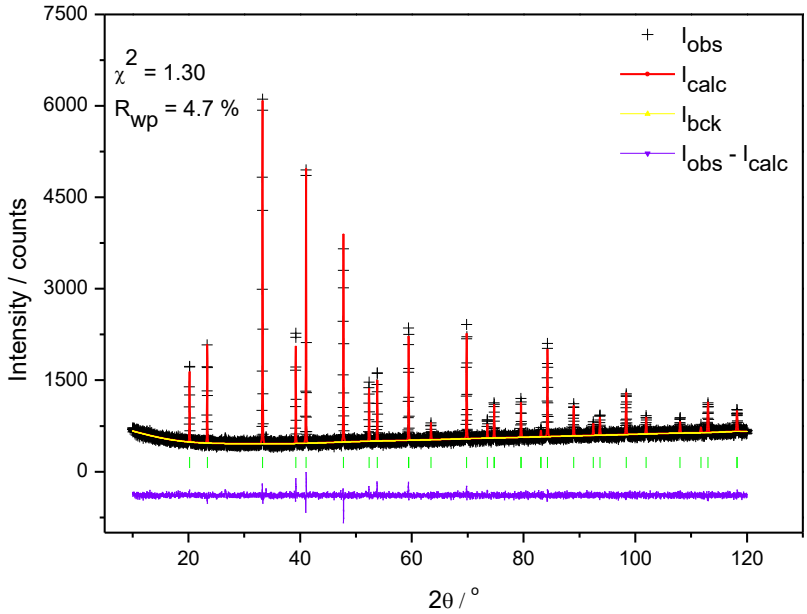

Figure B4 Rietveld refinement for $Co_{2.4}Ni_{0.6}Sn_2S_2$ using X-ray diffraction data. Observed (black crosses), refined (red solid lines) and difference (blue bottom line) profiles. Reflection positions are marked by green lines.

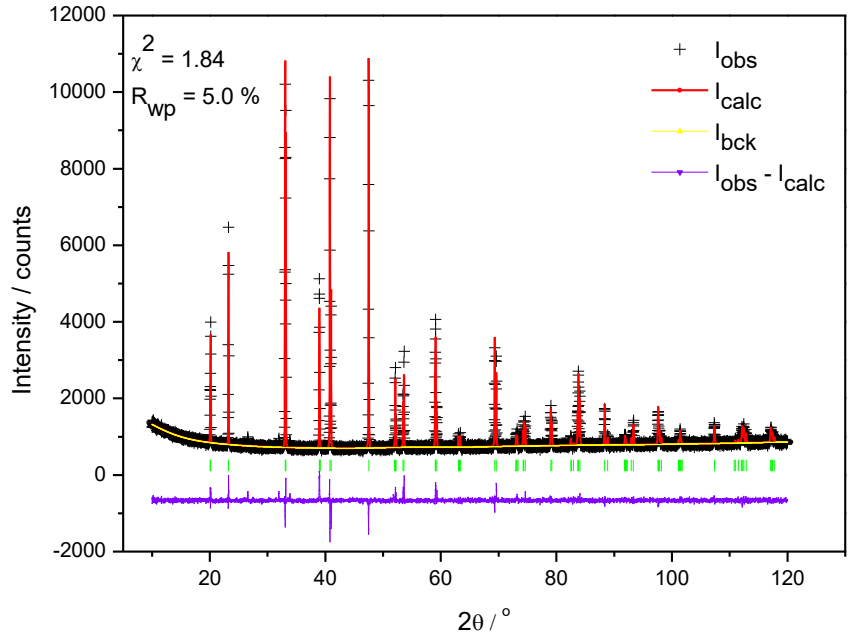

Figure B5 Rietveld refinement for $Co_{1.5}Ni_{1.5}Sn_2S_2$ using X-ray diffraction data. Observed (black crosses), refined (red solid lines) and difference (blue bottom line) profiles. Reflection positions are marked by green lines.

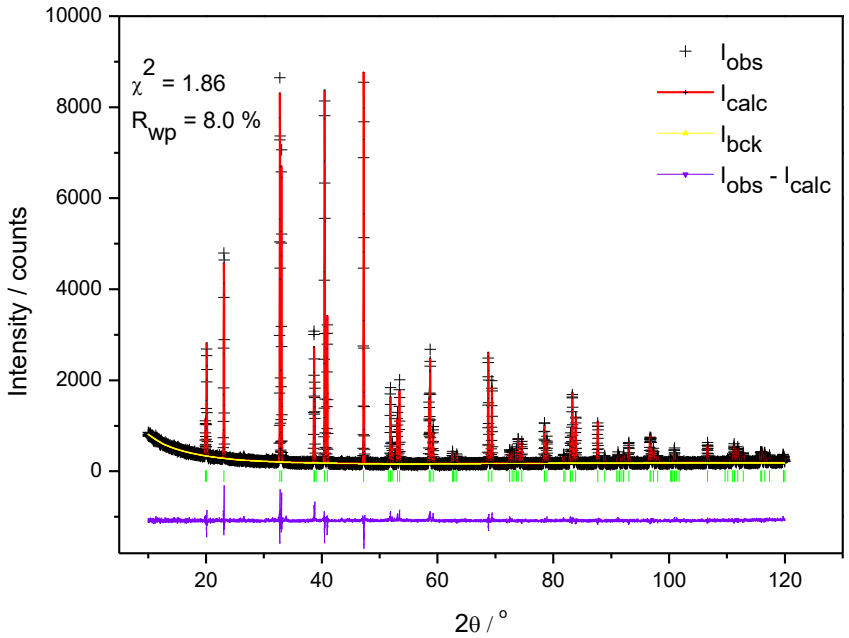

Figure B6 Rietveld refinement for $Co_{0.5}Ni_{2.5}Sn_2S_2$ using X-ray diffraction data. Observed (black crosses), refined (red solid lines) and difference (blue bottom line) profiles. Reflection positions are marked by green lines.

Appendix C – Powder X-ray diffraction refinements for $Co_{3-x}Fe_xSn_2S_2$ ($0 \leq x \leq 0.6$)

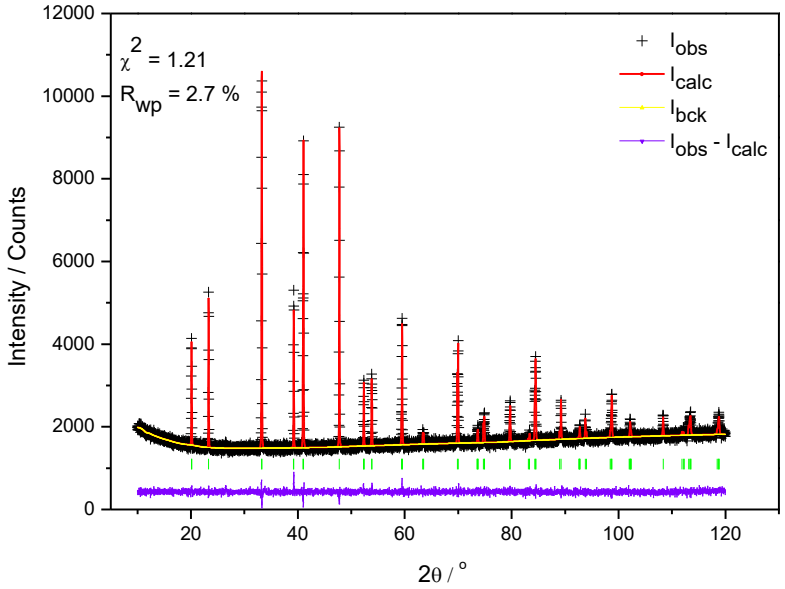

Figure C1 Rietveld refinement for $Co_{2.9}Fe_{0.1}Sn_2S_2$ using X-ray diffraction data. Observed (black crosses), refined (red solid lines) and difference (blue bottom line) profiles. Reflection positions are marked by green lines.

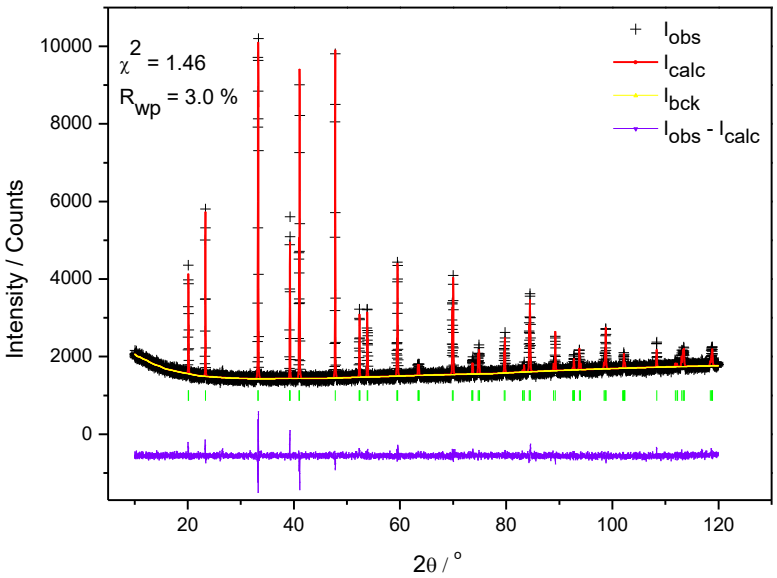

Figure C2 Rietveld refinement for $Co_{2.8}Fe_{0.2}Sn_2S_2$ using X-ray diffraction data. Observed (black crosses), refined (red solid lines) and difference (blue bottom line) profiles. Reflection positions are marked by green lines.

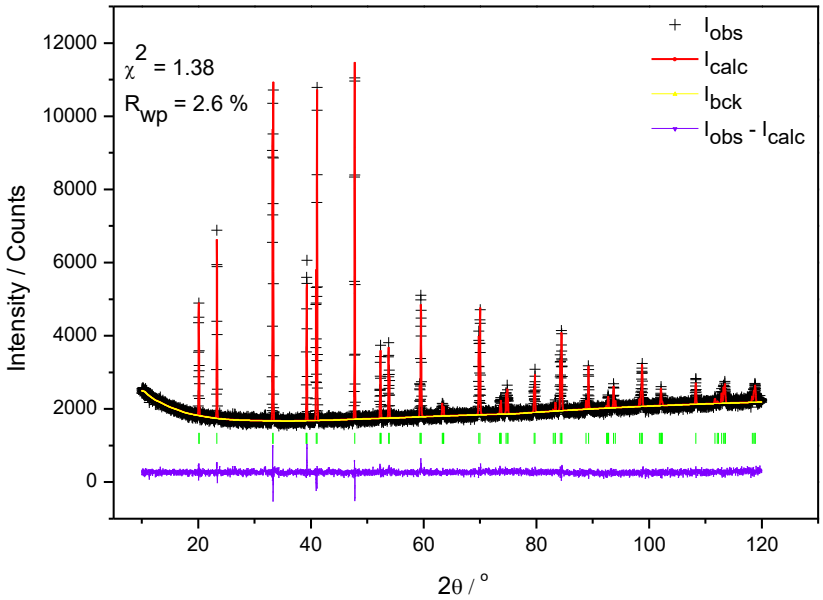

Figure C3 Rietveld refinement for $Co_{2.6}Fe_{0.4}Sn_2S_2$ using X-ray diffraction data. Observed (black crosses), refined (red solid lines) and difference (blue bottom line) profiles. Reflection positions are marked by green lines.

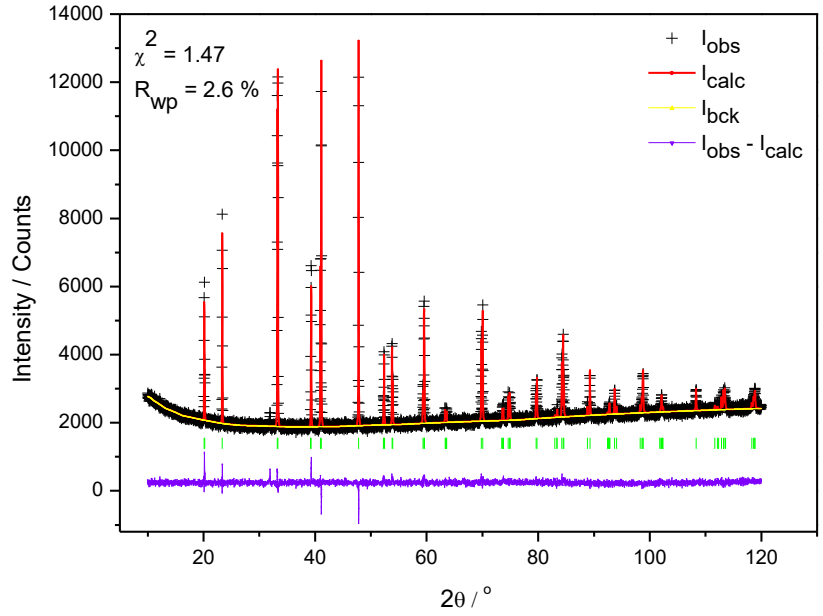

Figure C4 Rietveld refinement for $Co_{2.5}Fe_{0.5}Sn_2S_2$ using X-ray diffraction data. Observed (black crosses), refined (red solid lines) and difference (blue bottom line) profiles. Reflection positions are marked by green lines.

Appendix D – Powder Neutron diffraction refinements for $Co_{3-x}Ni_xSn_2S_2$ ($0 \leq x \leq 3$)

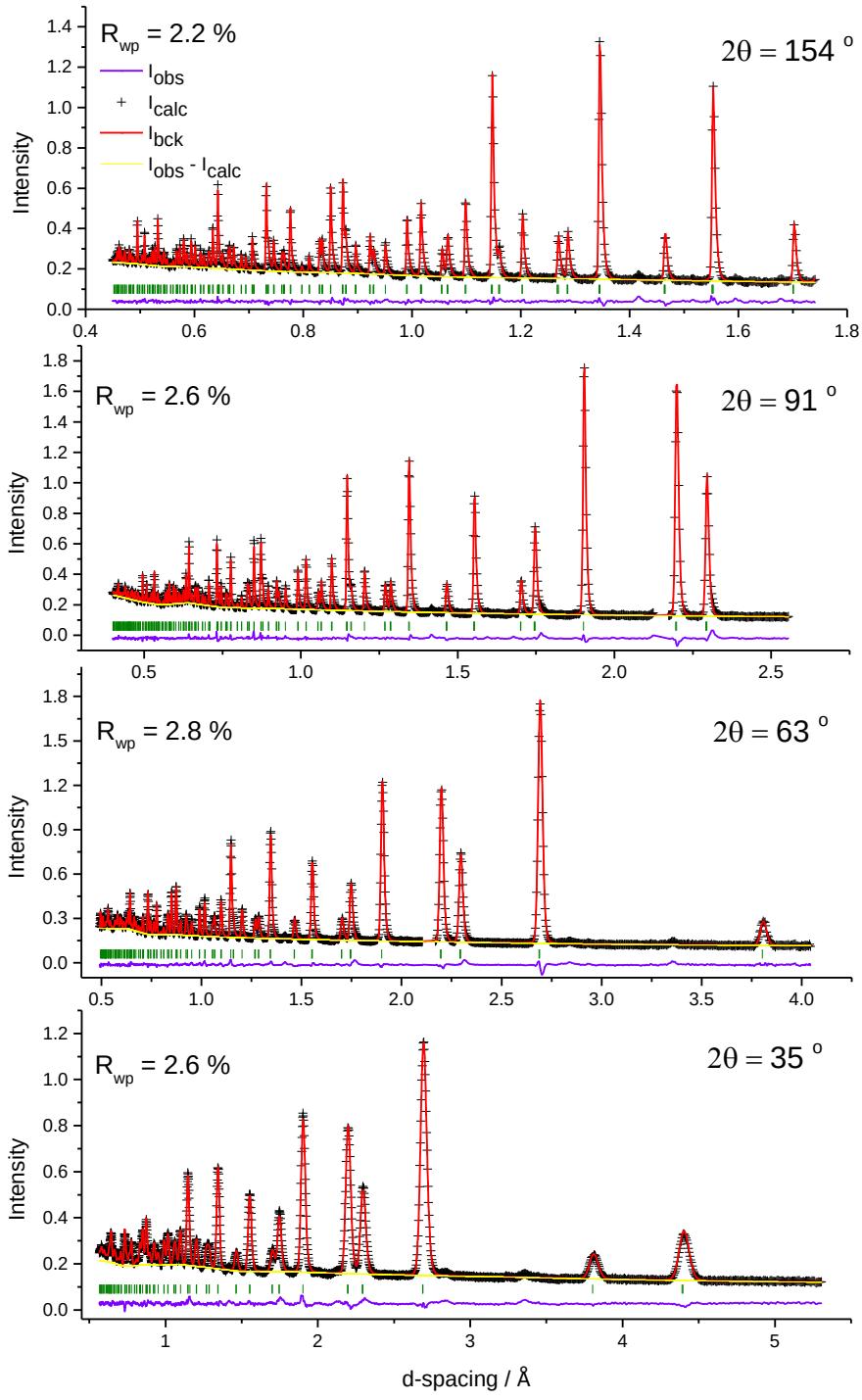

Figure D1 Multibank Rietveld refinement for $Co_{2.667}Ni_{0.333}Sn_2S_2$ using powder neutron diffraction data collected at room temperature ($\chi^2 = 3.7$). Observed (black crosses), refined (red solid lines) and difference (blue bottom line) profiles. Reflection positions are marked by olive lines.

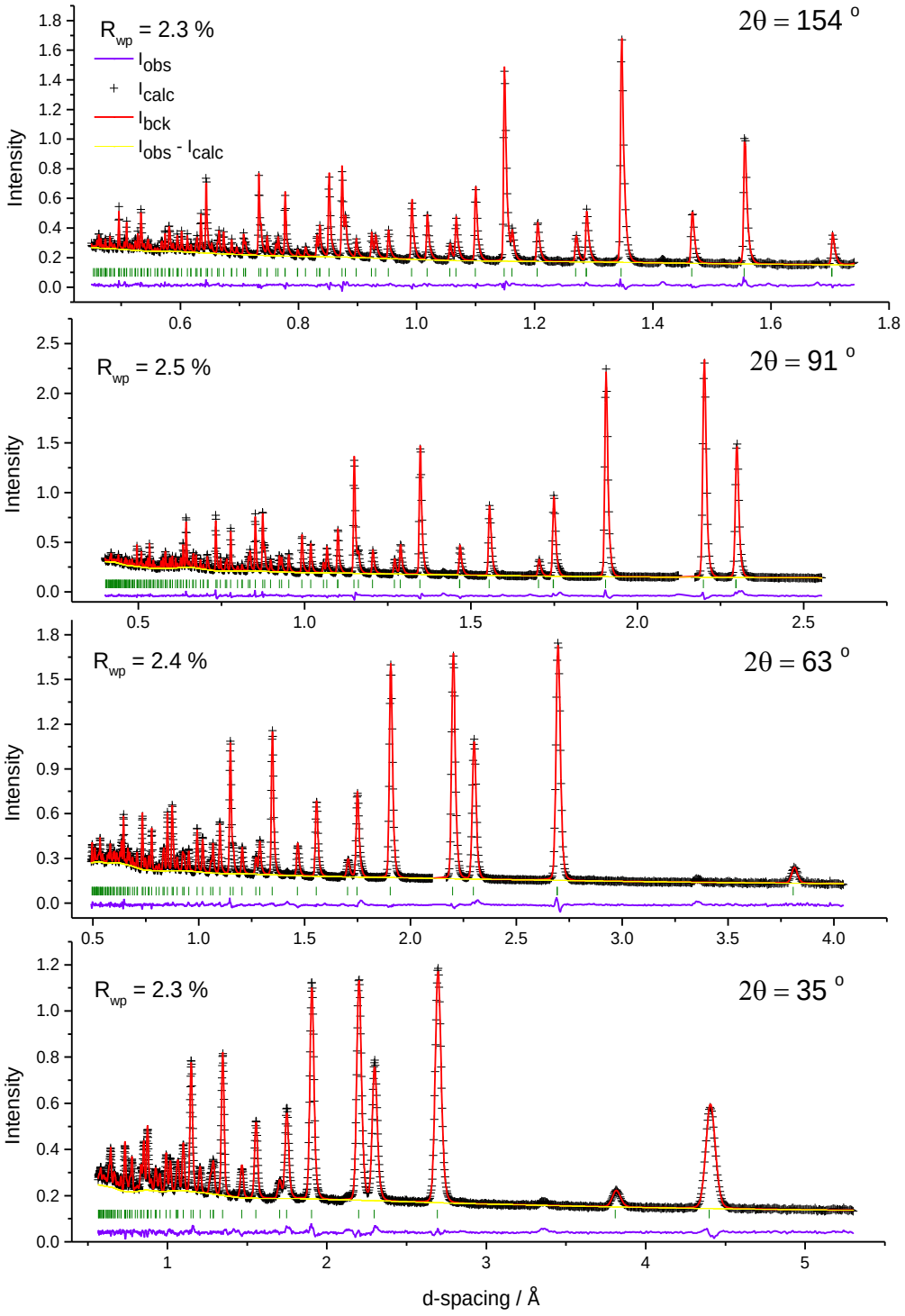

Figure D2 Multibank Rietveld refinement for $Co_{2.334}Ni_{0.666}Sn_2S_2$ using powder neutron diffraction data collected at room temperature (χ^2 = 3.5). Observed (black crosses), refined (red solid lines) and difference (blue bottom line) profiles. Reflection positions are marked by olive lines.

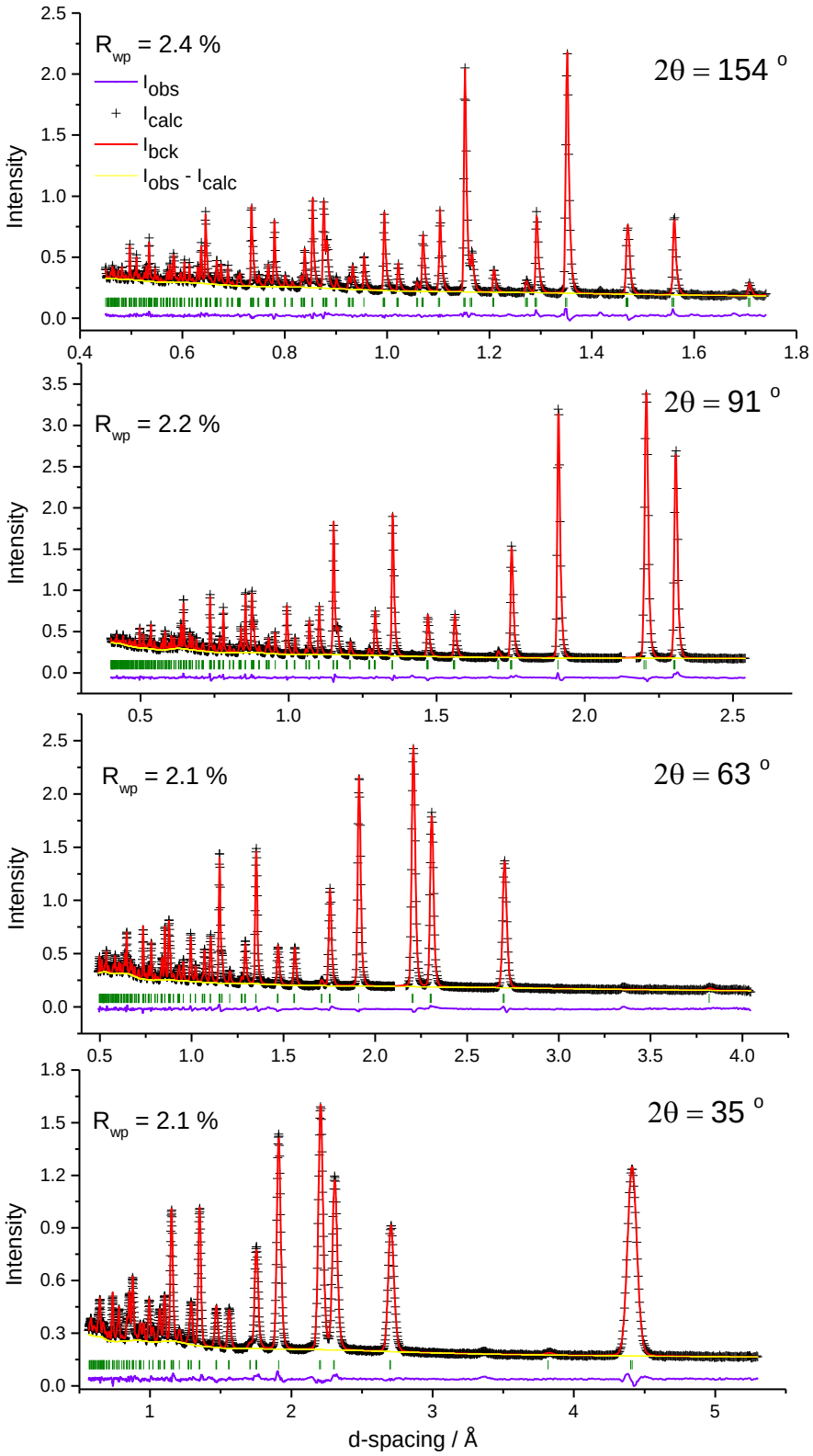

Figure D3 Multibank Rietveld refinement for $Co_{1.667}Ni_{1.333}Sn_2S_2$ using powder neutron diffraction data collected at room temperature (χ^2 = 3.9). Observed (black crosses), refined (red solid lines) and difference (blue bottom line) profiles. Reflection positions are marked by olive lines.

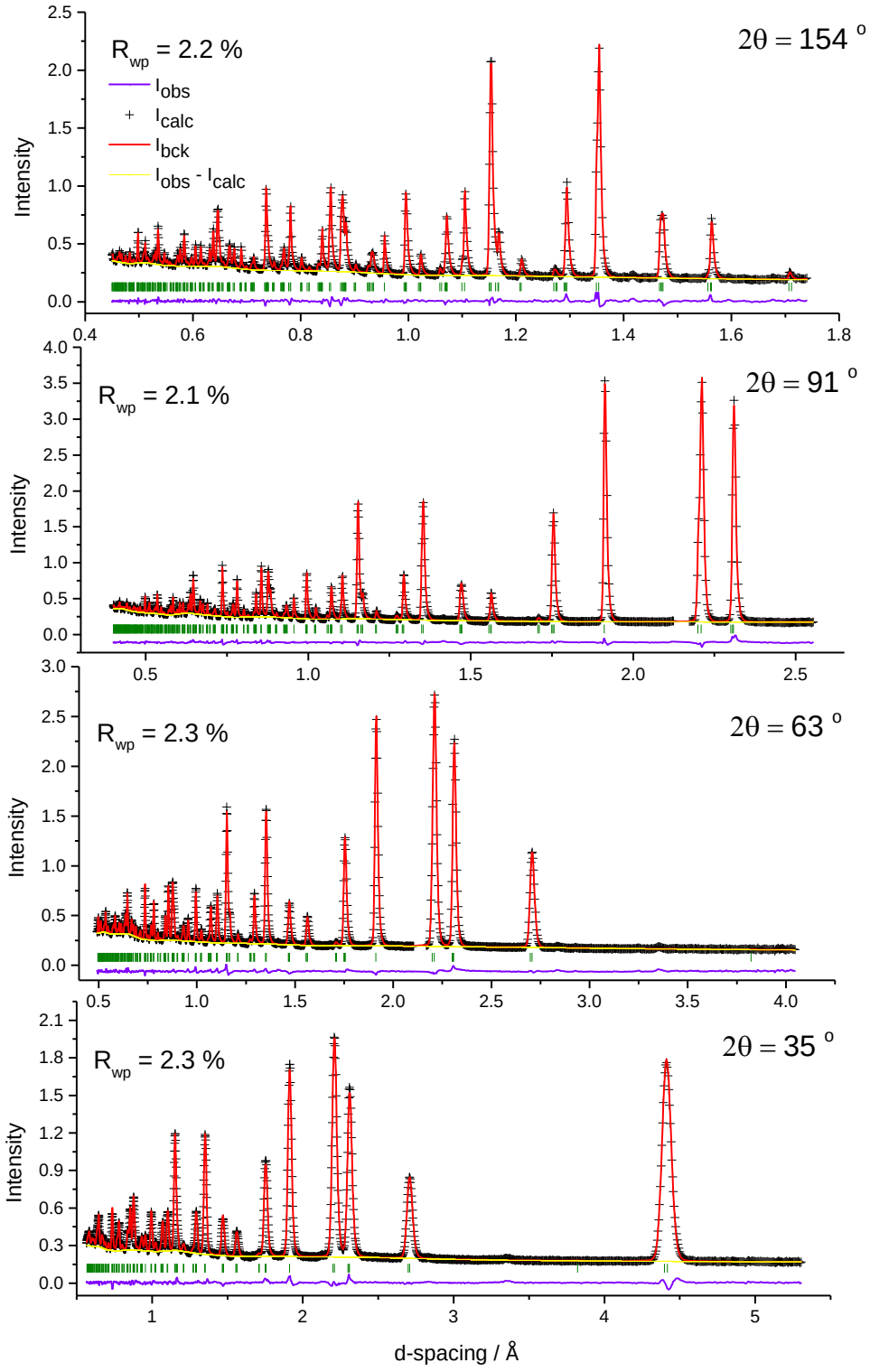

Figure D4 Multibank Rietveld refinement for $Co_{1.334}Ni_{1.666}Sn_2S_2$ using powder neutron diffraction data collected at room temperature (χ^2 = 3.9). Observed (black crosses), refined (red solid lines) and difference (blue bottom line) profiles. Reflection positions are marked by olive lines.

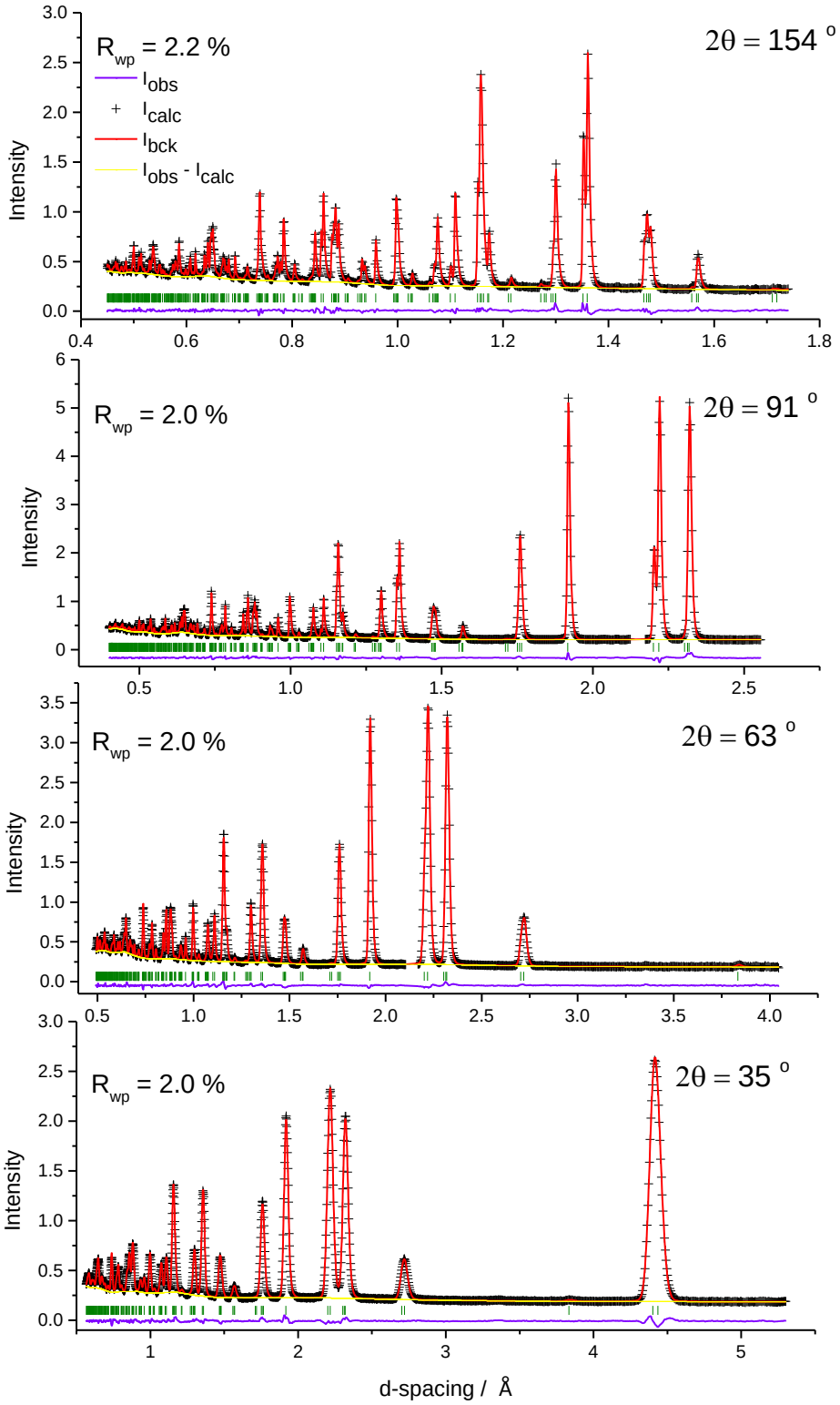

Figure D5 Multibank Rietveld refinement for $Co_{0.667}Ni_{2.333}Sn_2S_2$. using powder neutron diffraction data collected at room temperature (χ^2 = 3.9). Observed (black crosses), refined (red solid lines) and difference (blue bottom line) profiles. Reflection positions are marked by olive lines.

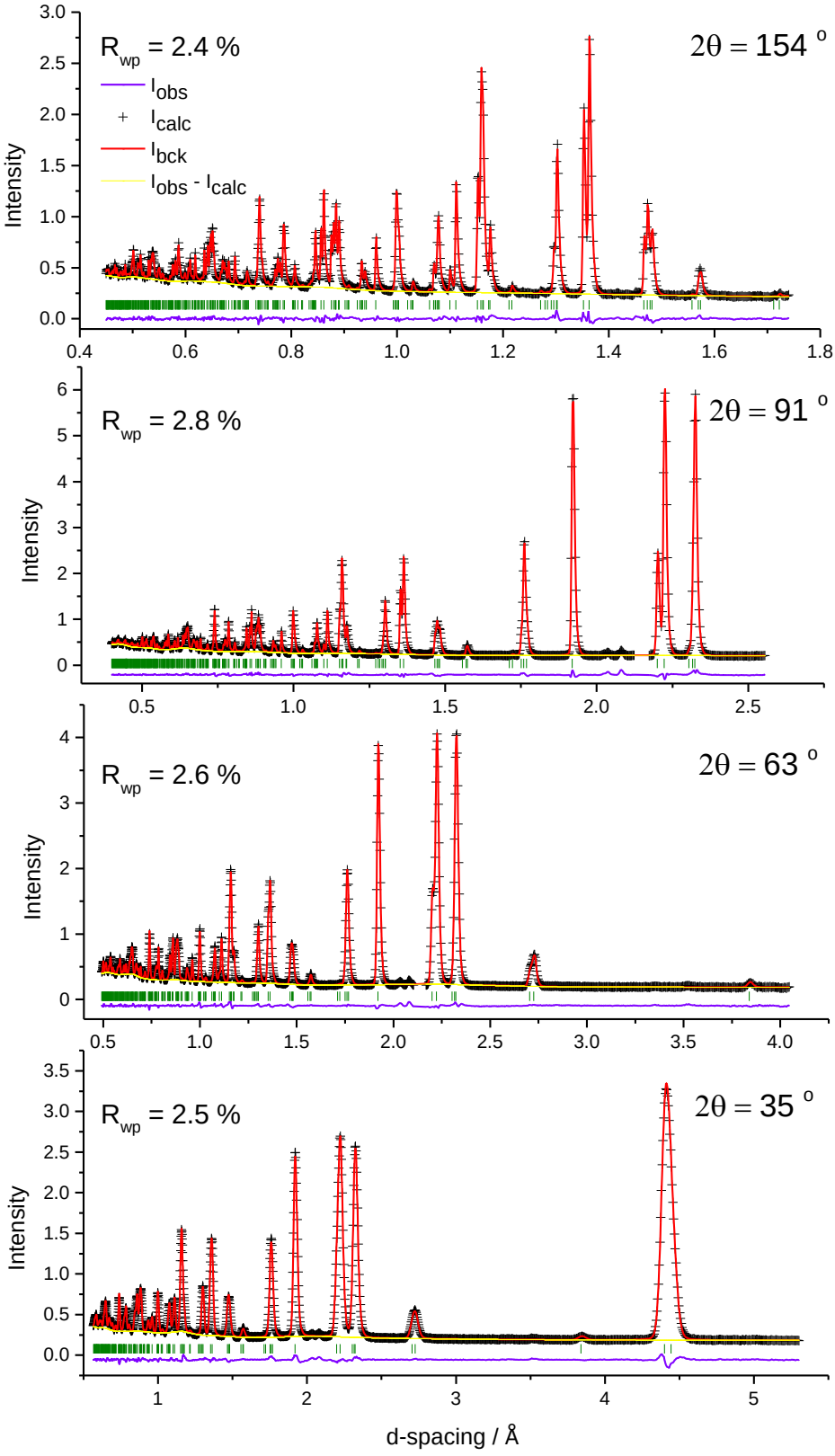

Figure D6 Multibank Rietveld refinement for $Co_{0.334}Ni_{2.666}Sn_2S_2$. using powder neutron diffraction data collected at room temperature (χ^2 = 7.0). Observed (black crosses), refined (red solid lines) and difference (blue bottom line) profiles. Reflection positions are marked by olive lines.

Appendix E – Neutron diffraction data for $CoNi_2Sn_2S_2$ at elevated temperatures.

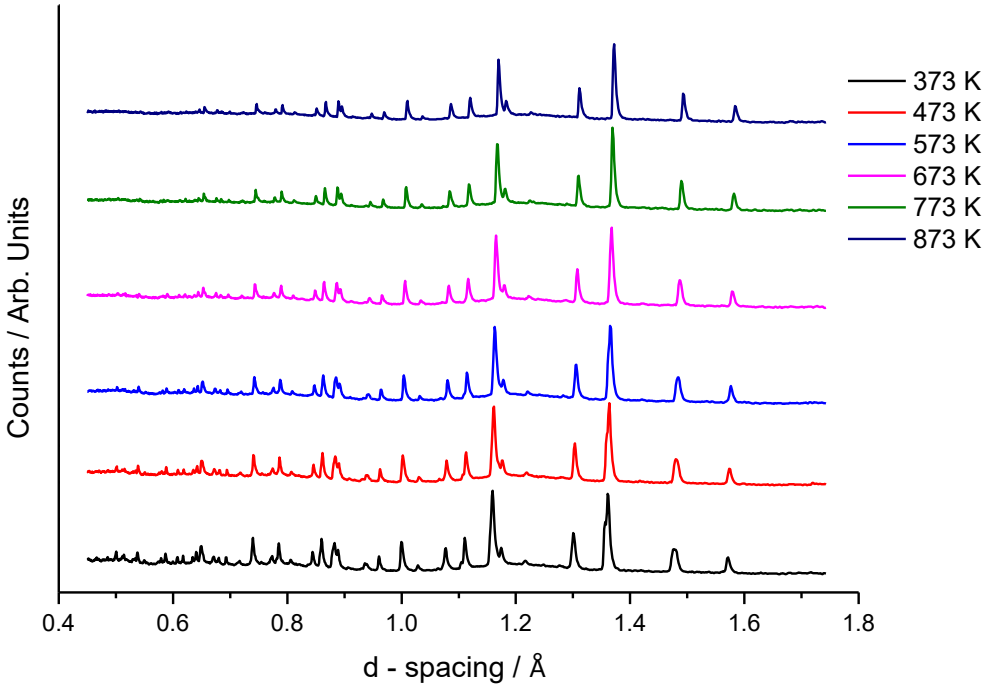

Figure E1 Neutron diffraction data of $CoNi_2Sn_2S_2$ from bank 6 of 154˚ at elevated temperatures.

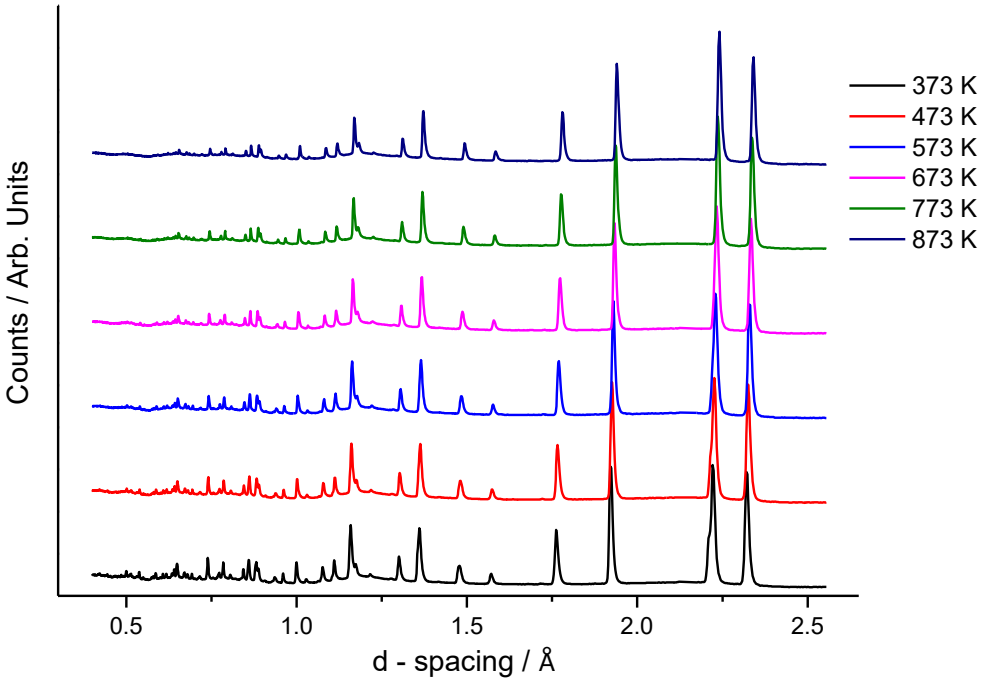

Figure E2 Neutron diffraction data of $Co_2NiSn_2S_2$ from bank 5 of 91˚ at elevated temperatures.

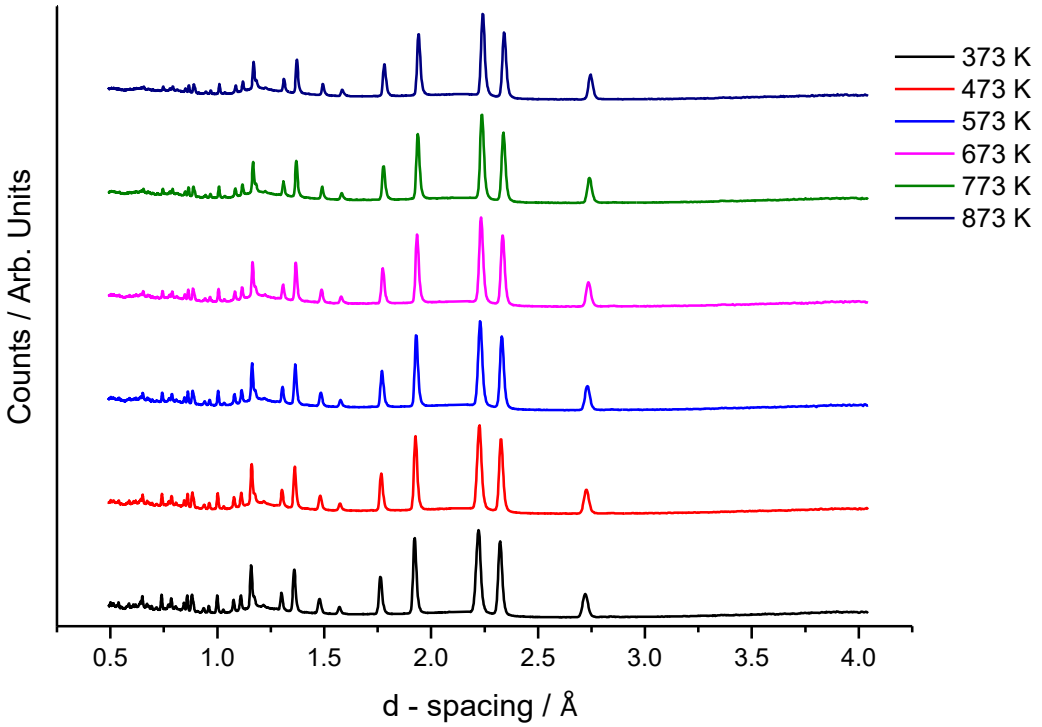

Figure E3 Neutron diffraction data of $CoNi_2Sn_2S_2$ from bank 4 of 63˚ at elevated temperatures.

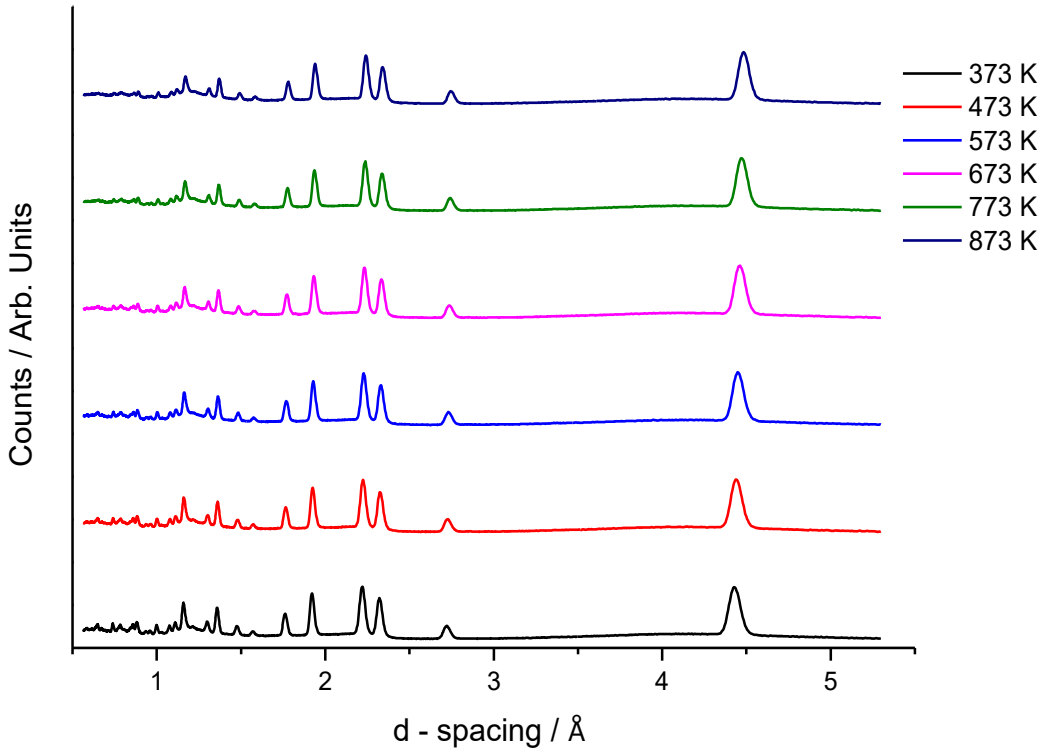

Figure E4 Neutron diffraction data of $CoNi_2Sn_2S_2$ from bank 3 of 35˚ at elevated temperatures.

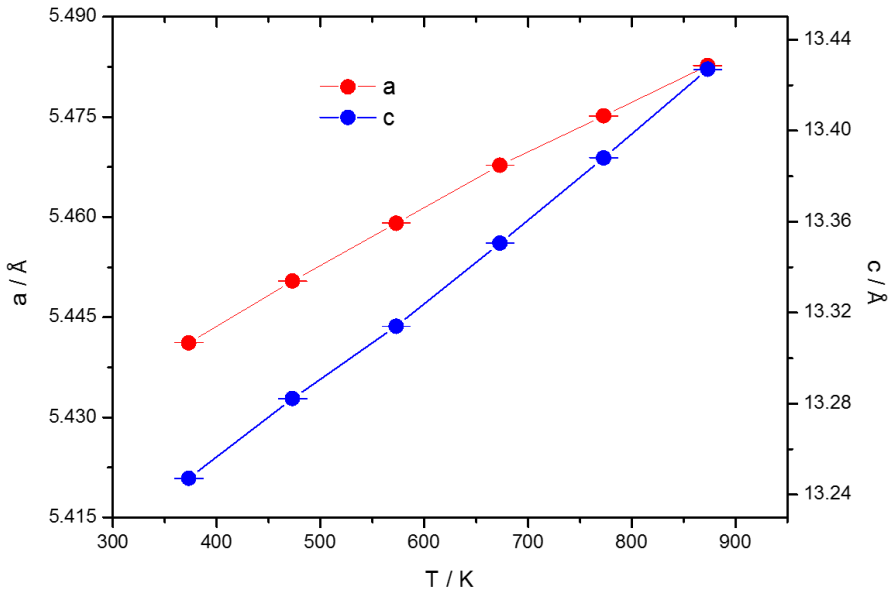

Figure E5 Lattice parameters of $CoNi_2Sn_2S_2$ as a function of temperature.

Appendix F - Mössbauer spectroscopy data for $Co_{3-x}Fe_xSn_2S_2$ ($0 \leq x \leq 0.6$)

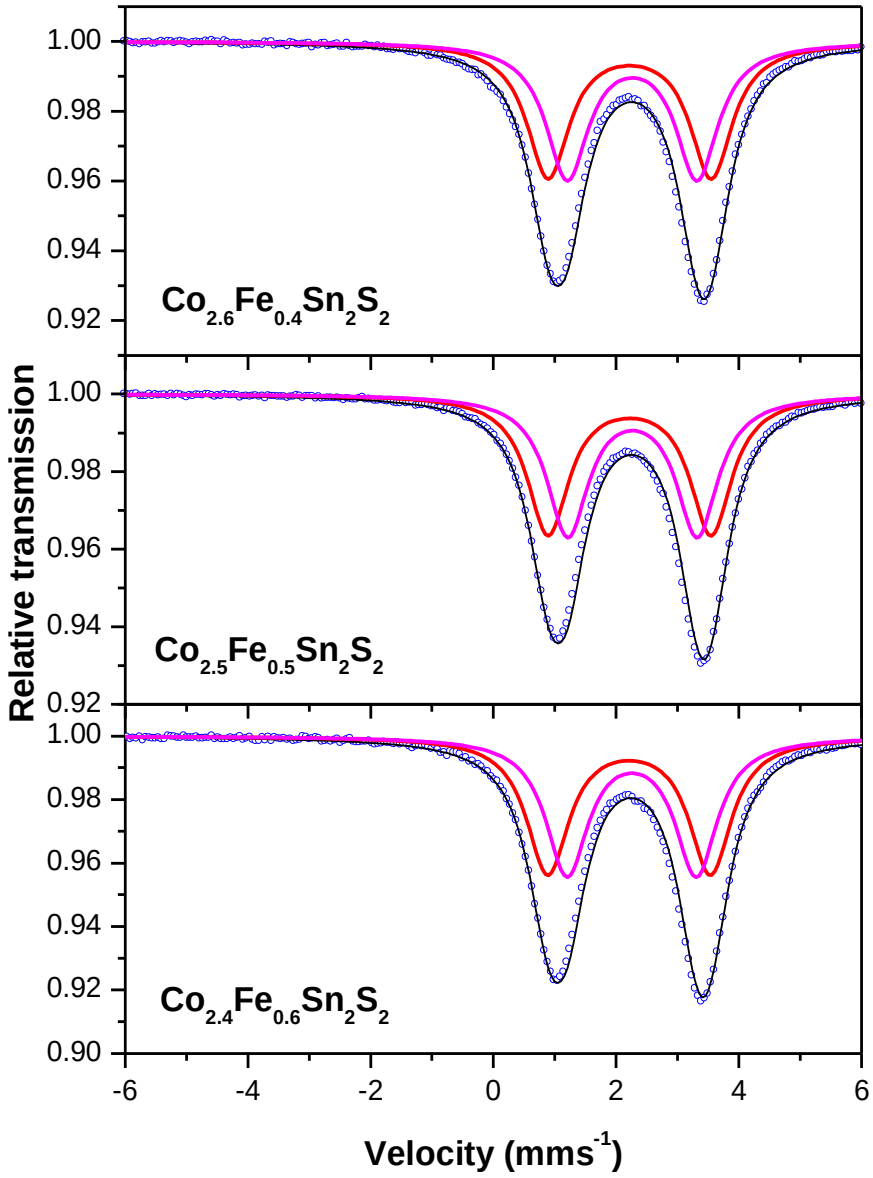

Figure F1 ^{119}Sn Mössbauer spectroscopy data collected at room temperature for the samples $Co_{3-x}Fe_xSn_2S_2$ ($0.4 \leq x \leq 0.6$).

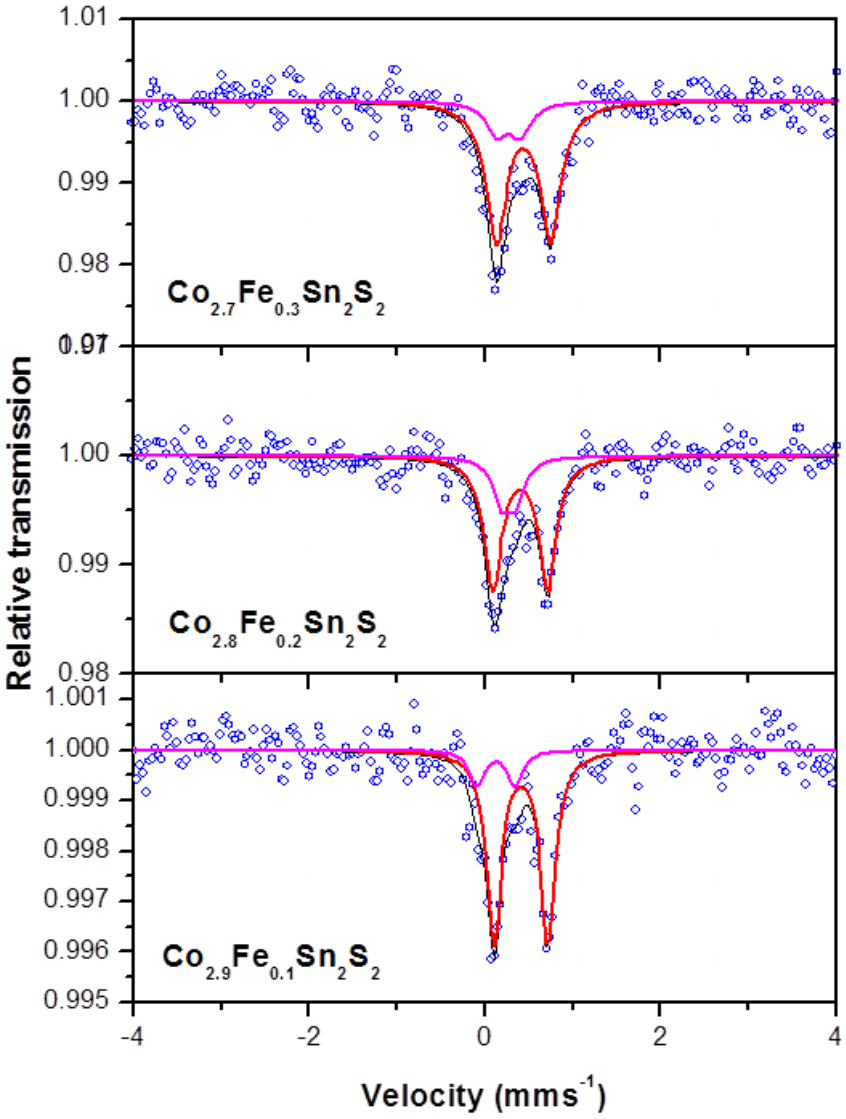

Figure F2 ^{57}Fe Mössbauer spectroscopy data for three samples of the series $Co_{3-x}Fe_xSn_2S_2$ ($0.1 \leq x \leq 0.3$).

Appendix G – Probability calculations for the local environment of Fe atoms

In the kagome layer, every Fe atom is surrounded by 4 transition metal atoms which can be either Co or Fe. The probability of any of the 4 neighbours being occupied by Fe is:

$$x' = \frac{5}{4} x_f$$

where $x_f = x / 3$ is the Fe composition per formula unit.

The probability of a transition metal site not being occupied by Fe is:

$$(1 - x')$$

The probability of n Fe atoms among 4 neighbours is:

$$P(\text{occupied})^n \, P(\text{vacant})^{4-n} \, N^o$$

where $N^o = \frac{4!}{(4-n)!n!}$ is the number of possible combinations.

Finally, the probability of n Fe atoms being any of the 4 neighbour sites is:

$$(x')^n \, (1-x')^{4-n} \, \frac{4!}{(4-n)!n!}$$

Appendix H – Powder X-ray diffraction refinements for $Co_{3-x}Fe_xSn_{2-y}In_yS_2$

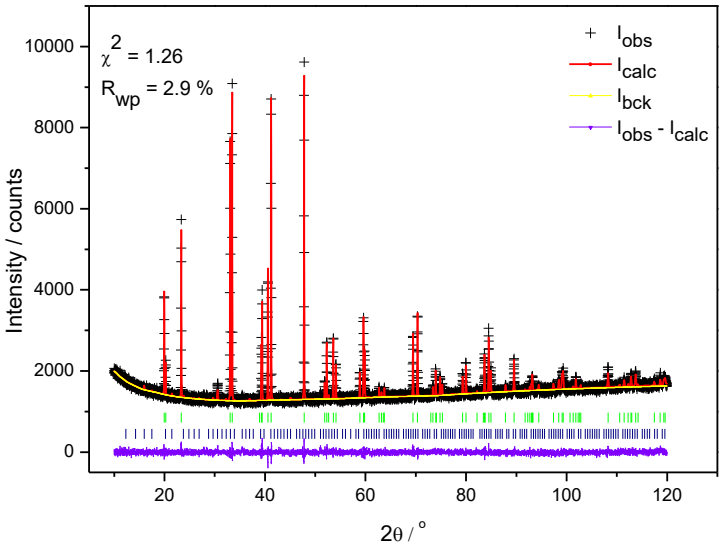

Figure H1 Rietveld refinement for $Co_{2.5}Fe_{0.5}Sn_{1.6}In_{0.4}S_2$ using X-ray diffraction data. Observed (black crosses), refined (red solid lines) and difference (blue bottom line) profiles. Green markers correspond to the shandite phase, while navy markers correspond to small amount of In_3S_4 (~ 8.5 wt %).

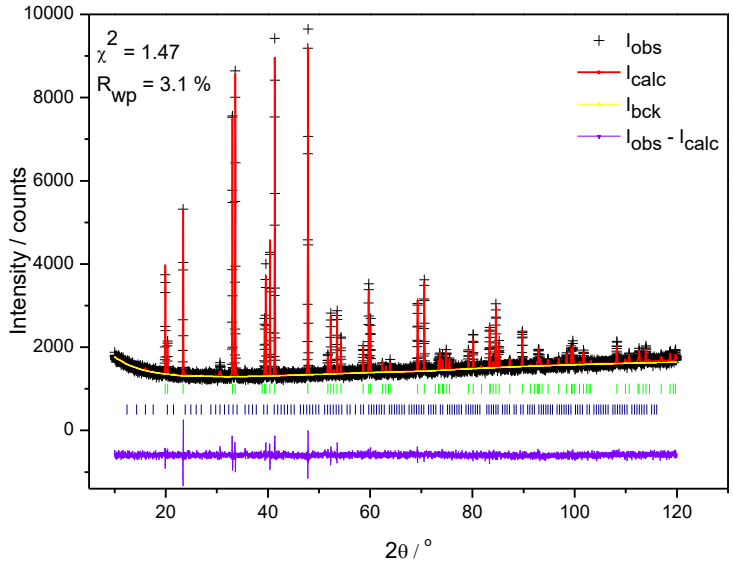

Figure H2 Rietveld refinement for $Co_{2.5}Fe_{0.5}Sn_{1.4}In_{0.6}S_2$ using X-ray diffraction data. Observed (black crosses), refined (red solid lines) and difference (blue bottom line) profiles. Green markers correspond to the shandite phase, while navy markers correspond to small amount of In_3S_4 (~ 8.8 wt %).

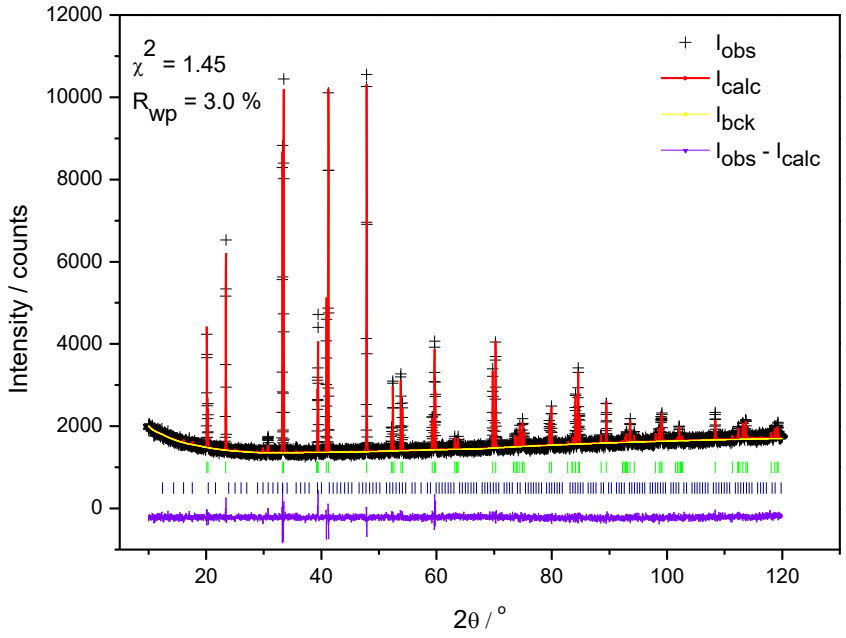

Figure H3 Rietveld refinement for $Co_{2.667}Fe_{0.333}Sn_{1.8}In_{0.2}S_2$ using X-ray diffraction data. Observed (black crosses), refined (red solid lines) and difference (blue bottom line) profiles. Green markers correspond to the shandite phase, while navy markers correspond to small amount of In_3S_4 (~ 5.8 wt %).

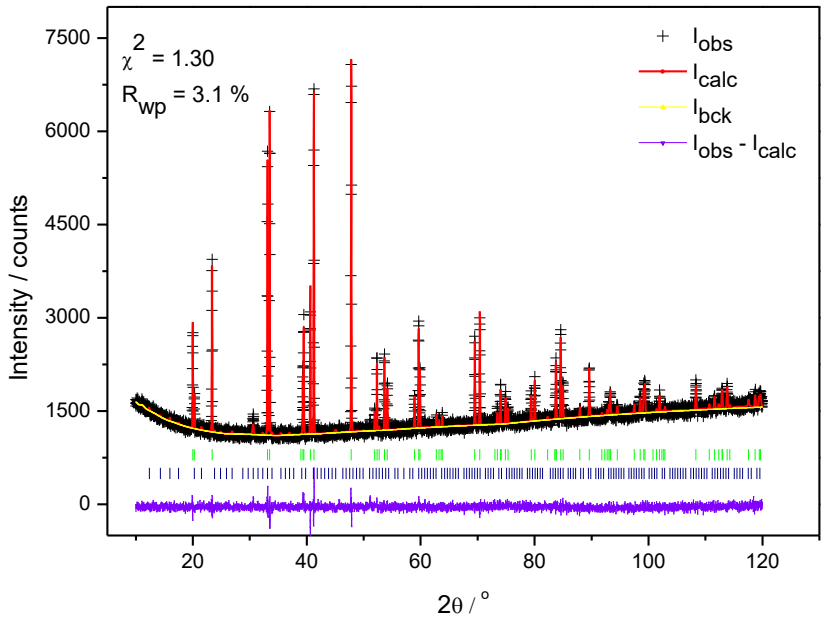

Figure H4 Rietveld refinement for $Co_{2.667}Fe_{0.333}Sn_{1.6}In_{0.4}S_2$ using X-ray diffraction data. Observed (black crosses), refined (red solid lines) and difference (blue bottom line) profiles. Green markers correspond to the shandite phase, while navy markers correspond to small amount of In_3S_4 (~ 7.3 wt %).

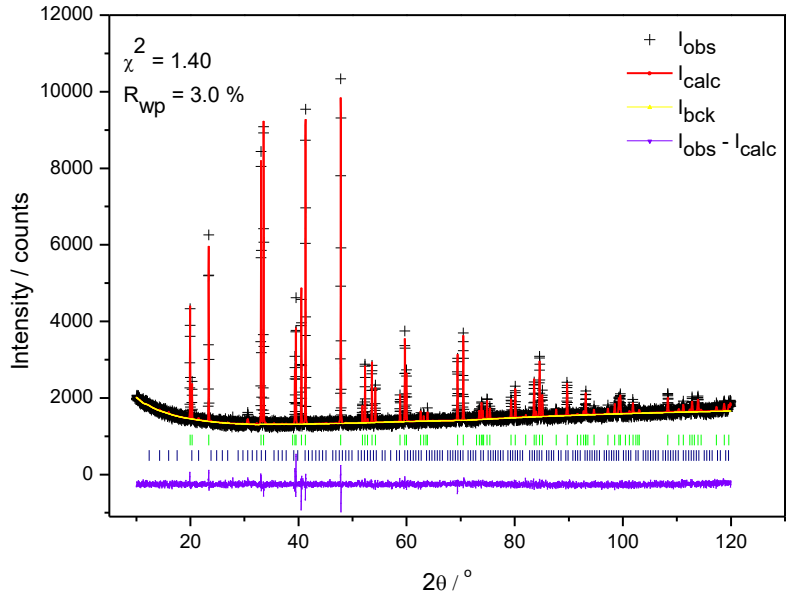

Figure H5 Rietveld refinement for $Co_{2.667}Fe_{0.333}Sn_{1.5}In_{0.5}S_2$ using X-ray diffraction data. Observed (black crosses), refined (red solid lines) and difference (blue bottom line) profiles. Green markers correspond to the shandite phase, while navy markers correspond to small amount of In_3S_4 (~ 5.2 wt %).

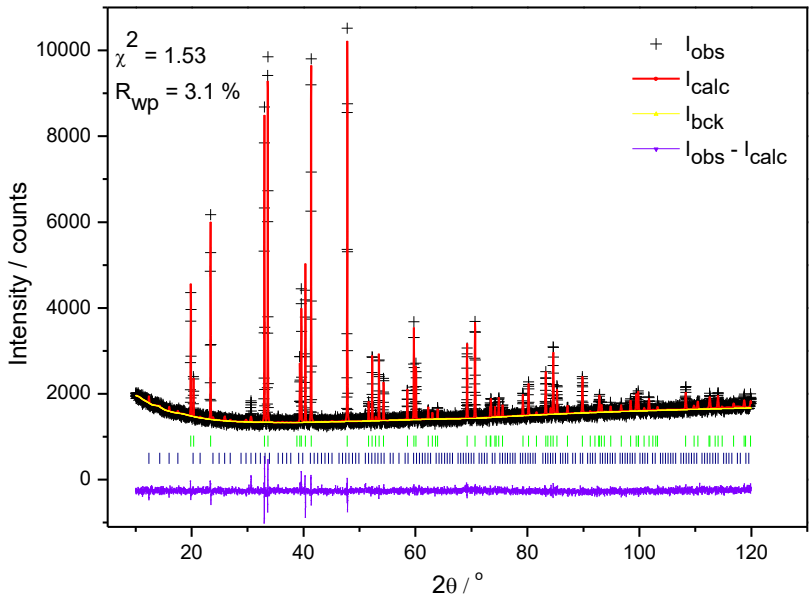

Figure H6 Rietveld refinement for $Co_{2.667}Fe_{0.333}Sn_{1.3}In_{0.7}S_2$ using X-ray diffraction data. Observed (black crosses), refined (red solid lines) and difference (blue bottom line) profiles. Green markers correspond to the shandite phase, while navy markers correspond to small amount of In_3S_4 (~ 5.1 wt %).

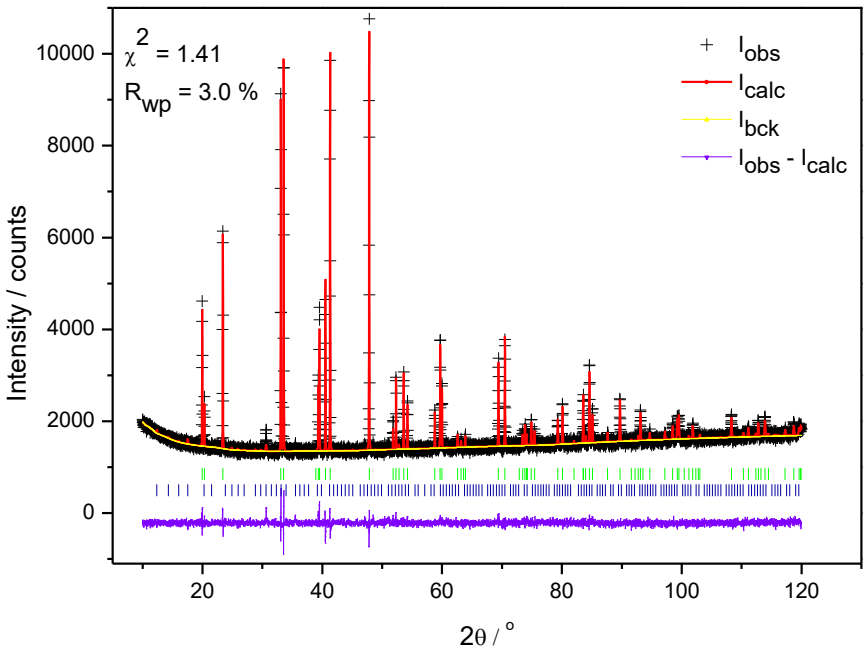

Figure H7 Rietveld refinement for $Co_{2.6}Fe_{0.4}Sn_{1.5}In_{0.5}S_2$ using X-ray diffraction data. Observed (black crosses), refined (red solid lines) and difference (blue bottom line) profiles. Green markers correspond to the shandite phase, while navy markers correspond to small amount of In_3S_4 (~ 5.0 wt %).

Appendix I – Neutron diffraction refinement results for quaternary chalcogenides.

Table I1 Bond distances between cations and anions of A_2ZnCQ_4 (A = Cu, Ag; C = Sn, Ge; Q = S, Se). Data collected at room temperature.

	A – Q (Å) A at *2a* site	*A*/Zn – Q (Å) *A*/*Zn* at *2c* site	*A*/Zn – Q (Å) *A*/Zn at *2d* site	C – Q (Å)
CZGS	2.320(11)	2.259(7)	2.376(7)	2.253(12)
CZGSe	2.4330(19)	2.3866(19)	2.4544(19)	2.3918(19)
CZTS	2.299(4)	2.355(4)	2.324(4)	2.425(4)
CZTSe	2.409(5)	2.4399(31)	2.470(5)	2.5350(30)
AZTS	2.584(5)	2.533(4)	2.346(4)	2.382(4)
AZTSe	2.4973(16)	2.6011(16)	2.4810(17)	2.6785(16)

Table I2 Bond distances between cations and anions in the wurtzite-stannite structure of Cu_2ZnGeS_4 at 1123 K.

Bond lengths / Å	
Cu – S(1)	2.299(8)
Cu – S(2)	2.325(8)
Cu – S(3)	2.248(6)
Zn – S(1)	2.319(15)
Zn – S(2)	2.514(13)
Zn – S(3)	2.540(10)
Ge – S(1)	2.370(12)
Ge – S(2)	2.299(15)
Ge – S(3)	2.188(9)

Appendix J – X-ray diffraction refinements for $Cu_{2+x}ZnGe_{1-x}Se_4$ ($0 \leq x \leq 0.15$)

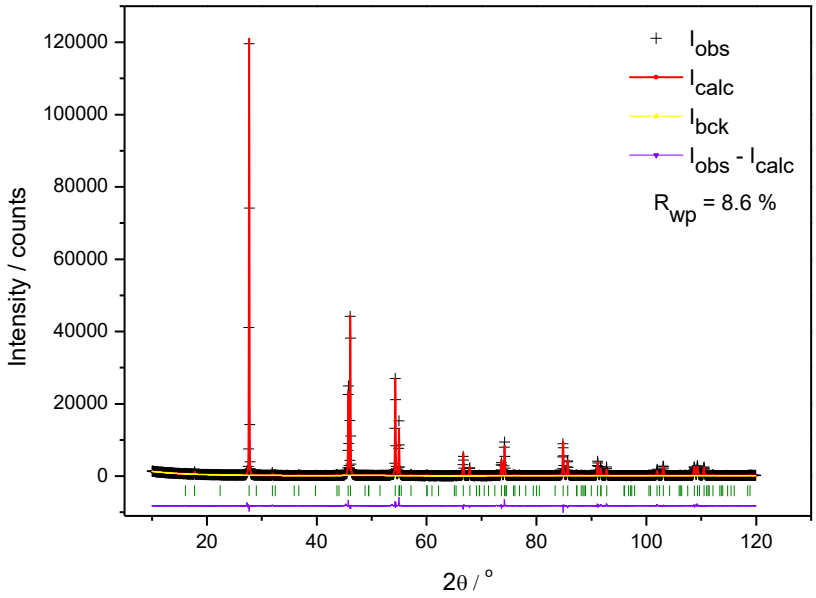

Figure J1 Rietveld refinement for $Cu_2ZnGeSe_4$ using X-ray diffraction data ($\chi^2 = 4.7$). Observed (black crosses), refined (red solid lines) and difference (blue bottom line) profiles. Olive markers correspond to the $Cu_2ZnGeSe_4$ phase.

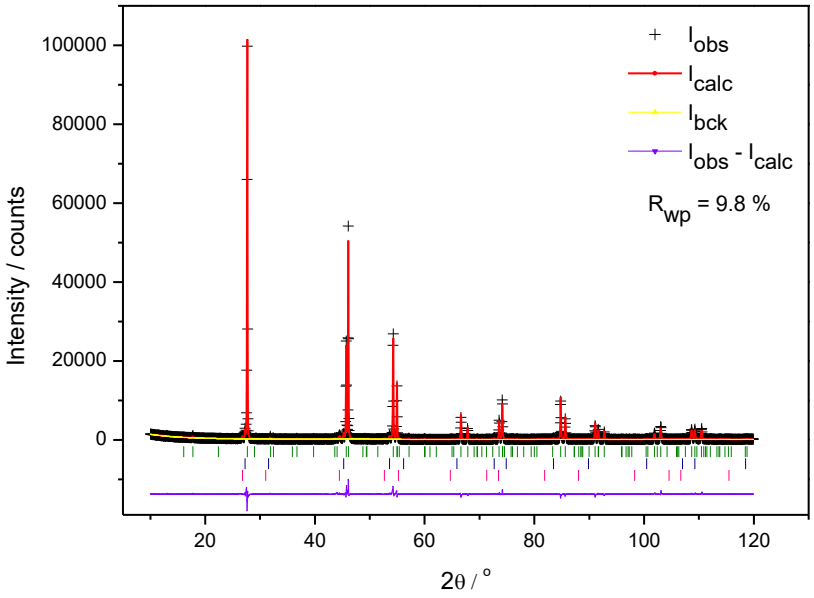

Figure J2 Rietveld refinement for $Cu_{2.05}ZnGe_{0.95}Se_4$ using X-ray diffraction data ($\chi^2 = 6.3$). Observed (black crosses), refined (red solid lines) and difference (blue bottom line) profiles. Olive markers correspond to the $Cu_{2.05}ZnGe_{0.95}Se_4$ phase, while navy and pink markers correspond to traces of ZnSe (~ 2.8 wt%) and CuSe (~ 2.9 wt %) respectively.

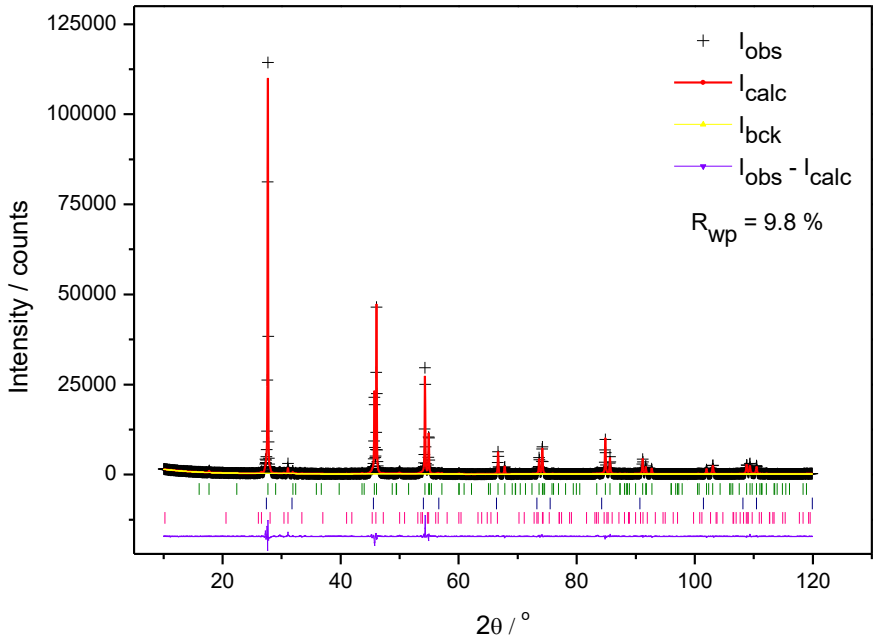

Figure J3 Rietveld refinement for $Cu_{2.1}ZnGe_{0.9}Se_4$ using X-ray diffraction data (χ^2 = 7.3). Observed (black crosses), refined (red solid lines) and difference (blue bottom line) profiles. Olive markers correspond to the $Cu_{2.1}ZnGe_{0.9}Se_4$ phase, while navy and pink markers correspond to traces of ZnSe (~ 8.5 wt%) and CuSe (~ 5.0 wt%) respectively.

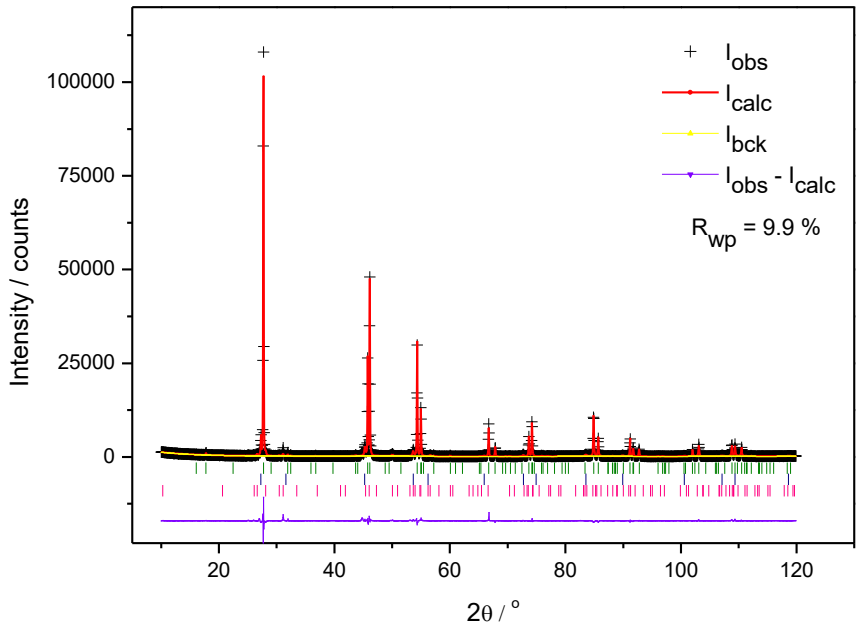

Figure J4 Rietveld refinement for $Cu_{2.125}ZnGe_{0.875}Se_4$ using X-ray diffraction data (χ^2 = 6.9). Observed (black crosses), refined (red solid lines) and difference (blue bottom line) profiles. Olive markers correspond to the $Cu_{2.125}ZnGe_{0.875}Se_4$ phase, while navy and pink markers correspond to traces of ZnSe (~ 6.2 wt%) and CuSe (~ 4.8 wt%) respectively.

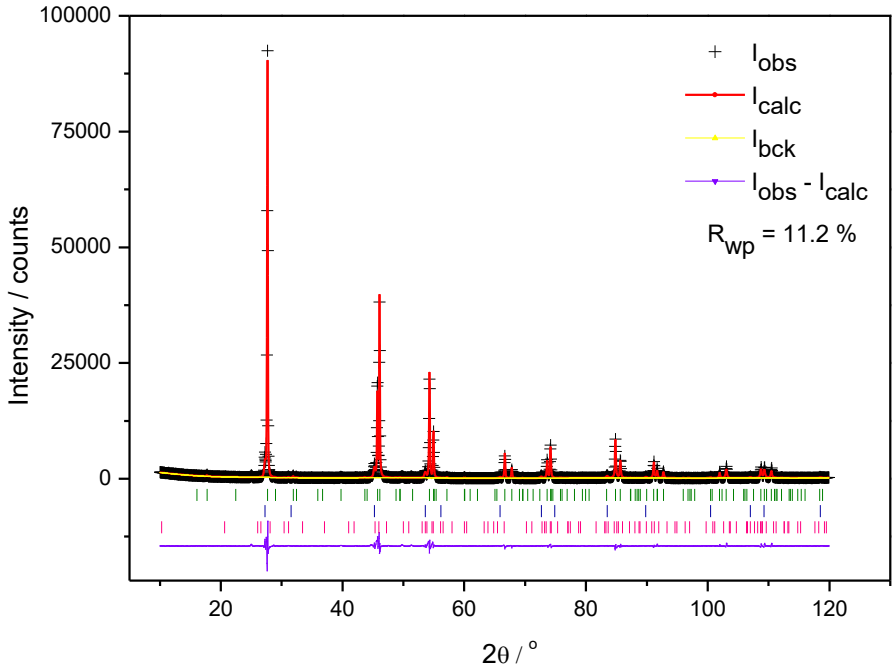

Figure J5 Rietveld refinement for $Cu_{2.15}ZnGe_{0.85}Se_4$ using X-ray diffraction data (χ^2 = 8.9). Observed (black crosses), refined (red solid lines) and difference (blue bottom line) profiles. Olive markers correspond to the $Cu_{2.15}ZnGe_{0.85}Se_4$ phase, while navy and pink markers correspond to traces of ZnSe (~ 7.4 wt%) and CuSe (~ 0.5 wt%) respectively.